High Performance Intermetallic and Ceramic Formed by SHS Process

By

Tri Widodo Besar RIYADI

Submitted in Partial Fulfilment of the Requirements

for the Degree Doctor of Philosophy

Supervised by:

Professor Tao Zhang

Faculty of Science, Engineering and Computing

Kingston University, London

July 2013

KP 0924353 4

Acknowledgement

This research would not have been possible without the support of many people. I would like to express my deep gratitude to Professor Tao Zhang, the director of studies, for his patient guidance, enthusiastic encouragement, deep care in my financial situation, and useful advices of this research. I would also like to thank the members of the supervisory committee, Mr. Denis Merchant and Dr. Homa Hadavinia for their help and valuable support on this project. Special thanks should be given to Jackie Deacon as research coordinator. I would like to convey thanks to Faculty boards, Prof. Andy Augosti for providing the financial means and the laboratory facilities. I am particularly grateful for the assistance given by Mr. Alex Vein, Mr. Barry, Mr. Dean, Mr. Lau, Mr. John and Mr. Martin. My grateful thanks are also extended to Dr. Xiaomeng Zhu for his help in doing the XRD tests in Shenzhen Harbin Institute of Technology China, Dr. Jiming Gao for his help in doing Vickers indentations test in Southbank University London, Mr. Richard Giddens for his help in doing SEM tests, and Mr. Simon Crust for his help in doing laser Raman microspectroscopy. I also take this opportunity to thank the William Rowland and Huntsman UK companies for their assistance in providing the raw materials.

I am highly indebted to Ministry of Education and Culture the Government of Indonesia and University of Muhammadiyah Surakarta for the full scholarship and the opportunity.

Lastly, I wish to express my love and gratitude to my mother, my wife, my daughters, my friends, brothers and sisters for their constant encouragement without which this task would not be possible.

Abstract

In this study, a new method to fabricate high performance intermetallic and ceramic materials and coatings was developed using the SHS process. Induction heating was used as an ignition source to initiate the SHS reaction of Ni/Al and preheat the steel substrate, while titanium was used as an underlayer to facilitate the adhesion between the coatings and the substrate. The reactions were performed in a reaction chamber with an atmosphere of argon gas, while the combustion temperatures were measured using type-K thermocouple and infrared pyrometer. The microstructure characterizations of synthesized products were conducted using SEM, XRD and laser Raman microspectroscopy. Vickers indentation tester was used to evaluate the microhardness and the adhesion strength of the coatings.

In the fabrication of NiAl coating, the formation of NiAl was initiated by the melting of Al and subsequently reacted with Ni to form NiAl after receiving the heat generated by induction heating. The synthesized product formed a liquid phase during the reaction and partly diffused into the Ti underlayer. The heat released by Ni/Al reaction then promoted the melting of Ti and further reactions between Ti and Ni/Al to produce Ti_3Al–Ti_2Ni composites, whereas the unreacted Ti formed an alloy with the coating material. The heat released by Ni/Al reaction and that generated by induction heating were also responsible for the formation of metallurgical bonding in the interface between the underlayer and the substrate. The effects of current variations, underlayer thickness, compaction pressure and melting point of underlayer on the microstructure of synthesized products were investigated. The mechanical properties and thermal shock resistance of synthesized products were also studied.

To investigate the effect of reactant compositions on the combustion temperature, microstructure and mechanical properties of synthesized products, NiAl–TiC–Al_2O_3 composites were fabricated using a low cost TiO_2. The

microstructure of synthesized product showed that the reaction of Ni/Al and TiO_2/Al/C was complete. Two reaction stages were observed from the temperature profiles which represent the exothermic reaction of TiO_2/Al/C system and the phase transformation of Ni/Al system. An increase in the TiO_2/Al/C content increased the combustion temperature. However, the maximum temperature was still lower than the melting point of TiC and Al_2O_3 indicating that both products were formed in the solid state during the reaction. An increase in the TiO_2/Al/C content produced a higher porosity in the product due to the increase of the solid TiC and Al_2O_3 particles compared with that of the liquid NiAl. The Ni/Al reactions acted as an exothermic agent to the ignition of TiO_2/Al/C reaction, and increased the liquid content for improving the density of synthesized product. The microhardness of synthesized product also increased with an increase in the TiO_2/Al/C content due to the increased content of the ceramic particles.

In the fabrication of TiC intermetallic composite coating, induction heating was successfully used to initiate the exothermic reaction of the reactants composed of multilayer configurations of Ti/C, Ni/Al and Ti. The synthesized product was inhomogeneously composed of TiC/Ti_3Al/Ti_2Ni, while a small amount of TiO_2 oxides and unreacted C were also observed. The hardness of TiC/Ti_3Al/Ti_2Ni was 1135.48 ± 139.58 HV, indicating that a hard TiC intermetallic composite coating was successfully synthesized using induction heating.

Keywords: SHS coating, Induction heating, Intermetallic, Ceramic

Table of Contents

Acknowledgement ii

Abstract iii

Table of Contents v

List of Figures x

List of Tables xv

List of Symbols xvii

Chapter 1. Introduction 1

1.1. Background and motivation 1

1.2. Aims and objectives 4

1.3. Outlines of the report 5

Chapter 2. Literature Survey 6

2.1. Intermetallic and ceramic materials 6

2.1.1. Intermetallics 6

2.1.1.1. Ni–Al and related phases 7

2.1.1.2. Ti–Al and related phases 8

2.1.1.3. Fe–Al and related phases 9

2.1.1.4. Ti–Ni and related phases 10

2.1.1.5. Al–Ni–Ti and related phases 11

2.1.2. Ceramics 11

2.2. SHS coating 13

2.2.1. Introduction to SHS coating 13

2.2.2. Ignition techniques 17

2.2.3. Processing routes of SHS coating 20

2.2.3.1. In situ SHS with casting route 20

2.2.3.2. Combined SHS with laser technology 22

2.2.3.3. SHS assisted with Concentrated Solar Energy 25

2.2.3.4. Combined SHS with microwave 28

2.2.3.5. Combined SHS with induction furnace 29

2.2.3.6. Combined SHS with thermal spraying 32
2.2.3.7. Combined SHS with magnetron sputtering 33
2.2.3.8. SHS and centrifugal casting technology 35
2.2.4. Post treatment 36
2.2.4.1. Remelting 36
2.2.4.2. Annealing 36
2.2.4.3. Densification 37
2.2.5. Bonding to substrate 39
2.2.5.1. General description 39
2.2.5.2. Type of adhesion in coating 39
2.2.5.3. Factors affecting the adhesion strength 40
2.2.5.4. General improvement for adhesion strength 41
2.2.5.5. Adhesion Improvement in SHS process 42
2.3. Processing parameters in SHS process 44
2.3.1. Grain size 44
2.3.2. Thermal conductivity 48
2.3.3. Green density 51
2.3.4. Heating rate 53
2.3.5. Reactant composition 55
2.3.6. Evolution of gas 56
2.3.7. Gravity 57
2.4. Adiabatic combustion temperature 58
2.5. Heat transfer in SHS process 61
2.6. Application of SHS products 65
2.6.1. Oxidation and corrosion resistance coating in high temperature 65
2.6.2. Wear resistance for high temperature application 66
2.6.3. Cutting tool and insert coatings 66
2.6.4. Bio medical application 66
2.6.5. Protective coating in dangerous environment 67
2.6.6. For repairing gas turbine component 67
2.6.7. Fabrication ceramic–lined compound copper pipe 68
2.7. Induction heating 68

2.7.1. Introduction 68
2.7.2. Theoretical considérations 69
2.7.3. Application of induction heating 69
2.8. Summary 70
Chapter 3. Experimental Procedures 74
3.1. Preparation of starting material and substrate 74
3.1.1. Material selections 74
3.1.2. Sample compositions 76
3.1.3. Powder mixing 77
3.1.4. Powder compaction 78
3.1.5. Preparation of substrate....80
3.2. Preparation of tools and equipments 81
3.2.1. Reaction chamber 81
3.2.2. Induction heating 82
3.2.2.1. Coil selections 82
3.2.2.2. Selection of heating parameters 83
3.2.3. Temperature monitoring and emissivity calibration 83
3.2.3.1. Emissivity of NiAl 84
3.2.3.2. Emissivity of titanium 87
3.2.3.3. Emissivity of steel substrate 89
3.3. Preparation of SHS process 90
3.3.1. Fabrication of NiAl coating 90
3.3.1.1. Variation of underlayer thickness 91
3.3.1.2. Variation of compaction pressure 92
3.3.1.3. Variation of melting temperature of the underlayer 93
3.3.1.4. Variation of heating rate....93
3.3.2. SHS process of NiAl–TiC–Al_2O_3 composite 93
3.3.3. Fabrication of TiC intermetallic matrix composite coating 94
3.4. Microstructure characterization 95
3.5. Properties evaluation 98
3.5.1. Hardness test 98
3.5.2. Adhesion strength 99

3.5.3. Thermal shock test 99
3.6. Summary 101
Chapter 4. Combustion Behaviour and Microstructure Characterization of NiAl Coating 102
4.1. Introductions 102
4.2. Experimental procedures 103
4.3. Results and discussion 105
4.3.1. Calculation of the adiabatic temperature 105
4.3.2. Measurement of temperature profile 109
4.3.2.1. Temperature profile of Ni/Al reaction 109
4.3.2.2. Temperature profile of Ti 112
4.3.2.3. Temperature profile of steel substrate 113
4.3.3. Microstructure characterization..... 115
4.3.3.1. Phase identification 115
4.3.3.2. SEM micrograph 121
4.3.3.3. Element distribution across the interfaces.....131
4.3.3.4. Formation mechanism of the synthesized products 134
4.3.3.5. Effect of underlayer thickness on the microstructure of synthesized products 141
4.3.3.6. Effect of heating rates on the microstructure of synthesized products 141
4.3.3.7. Effect of compaction pressure on the microstructure of synthesized products 145
4.3.3.8. Effect of the melting points of underlayer material on the microstructure of synthesized products 148
4.4. Summary 155
Chapter 5. Mechanical Propreties and Thermal Shock Behaviour of NiAl Coating 157
5.1. Introductions 157
5.2. Experimental procedures 161
5.2.1. Combustion synthesis of Ni/Al 161
5.2.2. Evaluation of the mechanical properties 161

5.2.3. Investigation of the thermal shock behaviour 162
5.3. Results and discussion 163
5.3.1. Microhardness distributions 163
5.3.2. Adhesion strength 168
5.3.3. Thermal shock behaviour 170
5.4. Summary 180
Chapter 6. SHS Process of NiAl–TiC–Al_2O_3 Composite 183
6.1. Introduction 183
6.2. Experimental procedures 185
6.3. Results and discussion 187
6.3.1. Combustion behaviour 187
6.3.1.1. Mechanism of reactions 187
6.3.1.2. Measurement of combustion temperature 189
6.3.2. Microstructure characterizations 193
6.3.2.1. X-rays diffraction spectra 193
6.3.2.2. Scanning Electron Microscopy (SEM) 196
6.3.2.3. Laser Raman microspectroscopy 205
6.3.3. Evaluation of the mechanical properties 216
6.4. Summary 218
Chapter 7. Fabrication of TiC Intermetallic Matrix Composite Coating..... 220
7.1. Introduction 220
7.2. Experimental procedures 222
7.3. Results and discussion 223
7.3.1. Microstructure analysis 223
7.3.2. Formation mechanisms 236
7.3.3. Mechanical properties 238
7.4. Summary 240
Chapter 8. Conclusions and Further Work 241
8.1. Conclusions 241
8.2. Further work 245
References 248

List of Figures

Fig. 2.1. Schematic diagram of the SHS coating 17
Fig. 2.2. Intermediate layer Ni–Al–Ti between NiAl coating and Ti substrate [11] 37
Fig. 2.3. The effect of particle size (ro) on wave velocity (V) [49] 46
Fig. 2.4. Ignition energy for the SHS of NiAl as a function of (a) effective thermal conductivity; and (b) sample porosity [100] 49
Fig. 2.5. Thermal conduction as a function of green density [105] 51
Fig. 2.6. Velocity of combustion propagation as a function of green density [105] 51
Fig. 2.7. The effect of green density on the combustion behaviour [102] 52
Fig. 2.8. The effect of green density on the heating rate [17] 53
Fig. 2.9. Temperature versus time diagram showing the heating rates [75] 54
Fig. 2.10. Microstructure of W–Al system described the phenomenon of settling 58
Fig. 2.11. Temperature profile for SHS process of Ni/Al obtained by: (a) experiment; and (b) simulation [123] 64
Fig. 2.12. The effect of porosity on propagation velocity for the SHS process of Ni/Al with grain size = 50 μm [123] 65
Fig. 3.1. SEM micrographs of reactant powders: (a) Al; (b) Ni; (c) Ti; (d) C; and (e) TiO_2 76
Fig. 3.2. Schematic diagram of powder compaction 79
Fig. 3.3. Schematic diagram of the experimental set up 82
Fig. 3.4. Temperature profile of the Ni/Al reaction 87
Fig. 3.5. Temperature profile of the Ni/Al reaction using various emissivities 87
Fig. 3.6. Temperature profile of Ti using various emissivities 88
Fig. 3.7. Enlarged temperature profile of Ti using selected emissivities 89
Fig. 3.8. Temperature profile of the steel substrate using $\varepsilon = 0.8$ 90
Fig. 3.9. Schematic picture of the Ni/Al + $3TiO_2$/4Al/3C without substrate 94
Fig. 3.10. Schematic picture of the Ni/Al + $3TiO_2$/4Al/3C with substrate 94

Fig. 3.11. Raman spectra for TiN, TiC, and TiC1-xNx [141] 98
Fig. 3.12. Temperature calibration of furnace 101
Fig. 4.1. Schematic configuration of the coating, underlayer and substrate 104
Fig. 4.2. The enthalpy versus temperature diagram of Ni/Al 107
Fig. 4.3. The effect of preheating temperature on: (a) adiabatic temperature of NiAl; (b) fraction of melted NiAl 108
Fig. 4.4. Temperature profile of NiAl/Ti using varied currents of induction heating 111
Fig. 4.5. Schematic configuration of Ti/NiAl.....112
Fig. 4.6. Temperature profile of Ti underlayer heated by Ni/Al reaction 113
Fig. 4.7. Temperature profile of the steel substrate heated by induction heating with various currents 114
Fig. 4.8. XRD spectra of the sample with underlayer thickness of 0.31 mm observed at: (a) 40 μm; and (b) 70 μm below the surface 116
Fig. 4.9. XRD spectra of the sample with underlayer thickness of 0.53 mm observed at: (a) 40 μm; and (b) 600 μm below the surface 118
Fig. 4.10. XRD spectra of the sample with underlayer thickness of 0.83 mm observed at: (a) 40 μm; (b) 400 μm; and (c) 500 μm below the surface.....120
Fig. 4.11. Back scattered SEM micrograph of the sample using underlayer thickness of 0.31 mm 123
Fig. 4.12. Back scattered SEM micrograph of the sample using underlayer thickness of 0.53 mm 124
Fig. 4.13. Back scattered SEM micrograph of the sample using underlayer thickness of 0.83 mm 125
Fig. 4.14. Back scattered SEM micrograph of microstructure in the underlayer of the sample with underlayer thickness of: (a) 0.53 mm; and (b) 0.31 mm.....127
Fig. 4.15. Back scattered SEM micrograph of microstructure across the interface between underlayer and coating in the sample with underlayer thickness of 0.31 mm 128

Fig. 4.16. Microstructure at the interface between underlayer and substrate obtained by: (a) back scattered images, (b) secondary images in the sample with underlayer thickness of 0.31 mm.....131
Fig. 4.17. Element distribution at the interfaces; (a) between underlayer and coating; (b) between substrate and underlayer in the sample with underlayer thickness of 0.31 mm 134
Fig. 4.18. Phase diagram of Ni–Al binary systems [2] 136
Fig. 4.19. Phase diagram of Ti–Ni binary system [33] 137
Fig. 4.20. Phase diagram of Ti–Al binary system [27] 138
Fig. 4.21. Back scattered SEM micrograph of products synthesized by heating rates of (a) 46.6 K/s; (b) 57.0 K/s; and (c) 85.5 K/s 144
Fig. 4.22. Back scattered SEM micrograph of synthesized product prepared by compaction pressure of: (a) 100 MPa; and (b) 150 MPa 147
Fig. 4.23. Back scattered SEM micrograph of synthesized product using Al underlayer: (a) image across the coating, underlayer and the substrate; (b) high magnification image at the underlayer.....150
Fig. 4.24. Back scattered SEM micrograph of synthesized product using Ni as underlayer.....153
Fig. 5.1. Microhardness distribution across the samples with different underlayer thicknesses: (a) 0.31 mm; (b) 0.53 mm; and (c) 0.83 mm ..166
Fig. 5.2. Indentation pictures across the samples with varied underlayer thicknesses: (a) 0.31 mm; (b) 0.53 mm; and (c) 0.83 mm 168
Fig. 5.3. Indentation at the interface between underlayer and the substrate using indenter load of 20 N 169
Fig. 5.4. Temperature history of coating surface during thermal shock 171
Fig. 5.5. The surface morphology of the coating surface: (a) before; and (b) after thermals shock test with 8 times repetitions.....172
Fig. 5.6. Thermal cracks developed across the samples with underlayer thicknesses of: (a) 0.31 mm; (b) 0.53 mm; and (c) 0.83 mm.....177
Fig. 5.7. Optical micrograph of the interface between underlayer and substrate after indentation using loads: (a) 1 N; (b) 5 N; (c) 10 N; and (d) 20 N.....179

Fig. 5.8. Raman spectra of oxides in the substrate 180
Fig. 6.1. Temperature profiles of the SHS process of NiAl–TiC–Al_2O_3 obtained by 10, 20, 30, and 40 wt. % TiO_2/Al/C.....193
Fig. 6.2. X-ray diffraction spectra of the synthesized products prepared by Ni/Al with: (a) 0; (b) 10; (c) 20; (d) 30; and (c) 40 wt.% of TiO_2/Al/C 196
Fig. 6.3. SEM micrograph of NiAl–TiC–Al_2O_3 composites prepared by Ni/Al with: (a) 0; (b) 10; (c) 20; (d) 30; and (e) 40 wt.% of TiO_2/Al/C 199
Fig. 6.4. Element composition using EDX of the samples in Fig. 6.3 at positions: (a) spot A; (b) spot B; and (c) spot C 200
Fig. 6.5. Enlarged SEM micrograph of the sample with (a) 30 wt.% ; and (b) 10 wt.% of TiO_2/Al/C.....203
Fig. 6.6. Raman spectra of TiO_2.....206
Fig. 6.7. Raman spectra of calcined alumina (Al_2O_3).....207
Fig. 6.8. Raman spectra of Ti/C mixture.....208
Fig. 6.9. Raman spectra of TiC formed by SHS process.....209
Fig. 6.10. Raman spectra of Ni/Al mixture 210
Fig. 6.11. Raman spectra of NiAl product obtained from Ni/Al mixture 211
Fig. 6.12. Raman spectra of compressed powder of Ni/Al + 3TiO_2/4Al/3C mixtures 212
Fig. 6.13. Locations of Raman test on the cross sectional area 213
Fig. 6.14. Raman spectra at position: (a) A; and (b) B in Fig. 6.13 214
Fig. 6.15. Locations of Raman test on the coating surface 215
Fig. 6.16. Raman spectra at the coating surface at position C in Fig. 6.15 216
Fig. 6.17. Microhardness of synthesized products prepared (x) Ni/Al + (1-x) TiO_2/Al/C with x = 0, 10, 20, 30 and 40 wt. %.....217
Fig. 6.18. Impressions of Vickers indentation in the samples with 10 wt. % TiO_2/Al/C 217
Fig. 7.1. Schematic configuration of the TiC intermetallic coating 222
Fig. 7.2. X-ray diffraction spectra of TiC composite system.....224
Fig. 7.3. Typical SEM micrograph of TiC composite coating: (a) image across the coating and substrate; (b) enlarge image of the coating; (c) high magnification image of the coating surface 228

Fig. 7.4 EDX spectra of: (a) spot A; (b) spot B; (c) spot C; and (d) spot D shown in Fig. 7.3(b) 231
Fig. 7.5. Microstructure across the interface in the TiC system 232
Fig. 7.6. EDX spectra of the spot E shown in Fig. 7.5 232
Fig. 7.7. Element distribution across the synthesized product of TiC system 234
Fig. 7.8. Line scan EDS analysis of: (a) Ti; (b) Al; (c) Ni; and (d) Fe shown in Fig. 7.7 236
Fig. 7.9. Microhardness comparison of different systems 239
Fig. 7.10. Indentation on the coating surface of TiC composite coating 239

List of Tables

Table 2.1. Properties of selected intermetallics [22] 7
Table 2.2. Advantages and disadvantages of ignition systems 18
Table 2.3. The effect of scanning speed on the coating microhardness [10] 23
Table 2.4. The effect of particle size on the SHS process parameters [102] 45
Table 2.5. The effect of reactant composition on the adiabatic temperature 55
Table 2.6. The adiabatic temperature of some SHS reactions 60
Table 3.1. Powder materials data 75
Table 3.2. Calculation result of compaction pressure 80
Table 3.3. Thickness variations of underlayer 91
Table 3.4. Thickness of underlayer with varied compaction pressure 92
Table 3.5. Density of Ti underlayer after compaction 92
Table 4.1. Thermodynamic properties of Al, Ni, and NiAl [120] 106
Table 4.2. Equations used for enthalpy calculations 106
Table 4.3. Chemical composition (in wt.%) of the phases in Fig. 4.11 124
Table 4.4. Chemical composition (in at.%) of the phases in Fig. 4.11 124
Table 4.5. Chemical composition (in wt.%) of the phases in Fig. 4.12 124
Table 4.6. Chemical composition (in at.%) of the phases in Fig. 4.12 125
Table 4.7. Chemical composition (in wt.%) of the phases in Fig. 4.14 127
Table 4.8. Chemical composition (in at.%) of the phases in Fig. 4.14 127
Table 4.9. Chemical composition (in wt.%) of the phases in Fig. 4.15 129
Table 4.10. Chemical composition (in at.%) of the phases in Fig. 4.15 129
Table 4.11. Chemical composition (in wt.%) of the phases in Fig. 4.16 131
Table 4.12. Chemical composition (in at.%) of the phases in Fig. 4.16 131
Table 4.13. Chemical composition (in wt.%) of the phases in Fig. 4.23(a) and (b) 151
Table 4.14. Chemical composition (in at.%) of the phases in Fig. 4.23(a) and (b) 151
Table 4.15. Chemical composition (in wt.%) of the phases in Fig. 4.24 153
Table 4.16. Chemical composition (in at.%) of the phases in Fig. 4.24 153

Table 5.1. Thermal expansion coefficient (CTE) of several materials.....176
Table 5.2. Type of oxide in the steel substrate.....180
Table 6.1. Variation of the weight fractions of reactants.....186
Table 6.2. Theoretical weight fraction of the reaction products.....186
Table 6.3. Heat of formation at 298 K for different systems.....189
Table 6.4. Chemical composition (in wt.%) of the spot A, B and C in Fig. 6.5 204
Table 6.5. Chemical composition (in at.%) of the spot A, B and C in Fig. 6.5 204
Table 6.6. Material properties of NiAl, TiC, and Al_2O_3 [186].....205
Table 7.1. Chemical composition (in wt.%) of the phases in Fig. 7.3(b).....229
Table 7.2. Chemical composition (in at.%) of the phases in Fig. 7.3(b).....229

List of Symbol

a = Stoichiometric ratio

C = Initial mass fraction of the reactant in the mixture

C_p = Heat capacity

D_1 = Diameter of coil (effective diameter)

D_2 = Diameter of the sample

E_c = Modulus Young of coating

E = Activation energy

E_{ig} = Ignition energy

$f(\eta)$ = kinetic function

ρ_1 = Electrical resistivity of the coil

ρ_2 = Electrical resistivity of the sample

μ_o = Magnetic permeability of free space

μ_r = Magnetic permeability of the sample relative to free space

H_L = Latent heat of phase transformation

HV = Vickers hardness

ΔH = Enthalpy of reactions

$\Delta H(R_i)$ = Enthalpy of reactants

$\Delta (P_j)$ = Enthalpy of products

ΔH_{298} = Enthalpy formation in the standard state at 298 K

$\Delta H(T_{ig})$ = Enthalpy of at the ignition point

k = Thermal conductivity

k/k_{bulk} = Effective thermal conductivity

K_o = Constant

n_i, n_j = Molar number of reactant and product components

R_i, P_j = Identification for reactant and product

r = Radius

R = Gas constant (8.314 J/mol.K)

ρ = Density

Q = Heat transferred into or out of the system

T = Temperature

T_a = Ambient temperature

T_{ad} = Adiabatic temperature

T_c = Combustion temperature

T_{ig} = Ignition temperature

T_{pre} = Preheating temperature

T_{trans} = Transition temperature

T_{max} = Maximum combustion temperature

t = Time

t_μ = Time lag of ignition

t_σ = Time range of ignition

v = Wave velocity

W = Work done by the system

Φ = Reaction rate

ω = Frequency of electrical generator

σ_c = Developed thermal stress in coating

$\Delta\alpha$ = Thermal expansion coefficient mismatches

ν = Poison ratio

Chapter 1

Introduction

This chapter provides the background and objectives of this research. The importance of advance materials used as protective coatings in high temperature environments to have high oxidation and corrosion resistance and techniques to produce these coatings are discussed in this chapter. A brief synopsis of the literature related to intermetallic and ceramic materials with their synthesis processes are described. Subsequently, the problem and knowledge gap in the field of research, including the aim and objectives of the present study are stated. The outline of the thesis report is also presented.

1.1. Background and motivation

Carbon steels have been widely used as a structural material in engineering applications at room temperature due to their low prices. However, one of the most critical challenges for engineering materials used in high temperature application is the risk of oxidation and corrosion. In a high-temperature environment such as in the heat exchangers and turbines of thermal power plants, steel mills, hot-work tool steels and extruders, carbon steel cannot provide sufficient oxidation and corrosion resistance. The formation of oxide scale caused by these harmful reactions can lead to the degradation of the mechanical properties of materials. The protection by advanced coatings is therefore required as assurance that the components can withstand high gas temperatures [1].

In the last few decades, intermetallics have been widely studied because they offer significant advantages in their physical and mechanical properties such as, high melting point, low density, and good oxidation and corrosion resistance. As a result they are considered to be a promising advanced material for use in high temperature applications. Among the various intermetallic compounds, much research has been devoted to the development of NiAl due to its high strength and

excellent oxidation resistance at elevated temperature [2]. The intermetallics of titanium aluminide systems such as Ti_3Al and TiAl have also offered greater potential for high temperature application and in a variety of structural applications such as in space, aircraft engines, and automobile applications. Compared with conventional titanium alloys, Ti_3Al and TiAl have low density, high specific strength, high specific stiffness, and high oxidation resistance [3].

Ceramics have attracted wide interest as advance materials for high temperature applications due to their advantages such as high modulus, high hardness, high melting temperature, and high corrosion resistance. It is apparent that Ceramics represent the best choice of material for use in high temperature applications, particularly, to provide corrosion resistance [4]. Of a broad range of ceramics typically inorganic materials such as oxides, borides, carbides, and nitrides, titanium carbide has developed into one of the most interesting ceramics since it has high strength and good wear resistance at elevated temperature. Having such outstanding properties, the titanium carbide particle has been widely investigated as an ideal candidate for the reinforcing phase in intermetallic matrix composite [5]. The combination of intermetallic and ceramic has attracted the greatest attention in the production of a high performance composite material which has good oxidation and wear resistance in high a temperature application [6].

There are several processing techniques to synthesize intermetallic and ceramic materials. However, most traditional techniques may lead to the complexity of process and expensive equipment due to the requirement of a relatively high temperature process. The Self propagation high temperature synthesis (SHS) process offers significant advantages to fabricate intermetallic and ceramic materials since it produces high exothermic reaction and a short processing time. Recent research has shown that the synthesized material formed by the SHS process can be applied directly on metal substrates to fabricate coatings in one step using the heat generated during SHS reaction. Combining the SHS and coating fabrication into one processing step can then be more efficient. Some studies have reported the successful fabrication of coating from the synthesized product formed by the SHS process. The application of combined SHS with casting was used in the

fabrication of $MoSi_2$–MoS_2 composite coating [7] and Ni_3Al–TiC composite coating [8]. Laser techniques are used to simultaneously ignite the SHS reaction and fabricate the coating for surface modifications such as laser cladding and laser surface alloying [9][10]. A Microwave technique was used to ignite SHS of Ni/Al powders which were subsequently applied as a coating on Ti substrate [11][12]. The observation of available studies has reported that the combined SHS process and coating fabrication offers numerous advantages such as, simple equipment, low energy consumption, and high processing time efficiency [13].

Despite the proven experimental success of the fabrication of coatings which combined with the SHS process, its application to prepare high performance coatings has a number of limitations. The main aspect to be addressed is that the SHS process, in most cases, produces porous product [14]. The application of porous product as a protective coating in a high temperature environment is unacceptable since the pores can allow hot air from outside to infiltrate into the substrate and generate an oxidation reaction. Although extensive research has been carried out on the reduction of porosity in the synthesized product formed by the SHS process, the preparation of densified product by common SHS process is still difficult [15]. An additional problem arising in the process is that the high combustion temperature released by the SHS process can produce thermal shock at the interface of the coating–substrate which may cause the detachment of the coating from the substrate. In addition, temperature changes during cooling from the high combustion temperature of the SHS process and during subsequent service can generate thermal stress in the coating which leads to thermal cracks in the surface resulting in poor adhesion strength. So far, there has been a lack of a joining technique for dissimilar advance materials in high temperature application [16]. The science of SHS reaction and the fabrication technique of coatings with high density and strong bonding to the substrate for high temperature application, using SHS process need to be investigated.

Recently, induction heating has been successfully used as the ignition source to initiate the SHS process of NiAl and NiAl based ceramic composites [17][18][19]. The heating process is capable of providing high heat intensity and a fast heating

process on a large area of samples in a magnetic field. The heating process is fast because the power goes directly to the material being heated and is concentrated at the surface of the substrate. These advantages are the motivation for the present study which seeks to expand its application to fabricate coatings, particularly, with improved density and adherence. To date, there has only been very limited research about the use of induction heating to initiate the SHS process and coating fabrication in one processing route.

1.2. Aims and objectives

The aim of this work is to develop a new method to fabricate high performance intermetallic and ceramic materials and coatings formed using SHS process. This method involves the use of induction heating as the external heat source which serves not only to ignite the SHS process, but also to help the fabrication of the coating. In particular, the objectives of this work are described as follows:

- To study the application of induction heating to fabricate NiAl coatings formed by the SHS process. The effect of processing parameter on the combustion behaviour, microstructure, and mechanical properties of the synthesized product are investigated. The formation mechanism of the synthesized product is also analysed.

- To study the method to improve the adhesion between the coating and the substrate, and examine the microstructure and the adhesion performance of the coating after experiencing high temperature treatment.

- To study the effect of the processing parameter on the combustion behaviour, microstructure, and mechanical property of NiAl–TiC–Al_2O_3 composite.

- To study the fabrication of hard composite coating of TiC.

1.3. Outlines of the report

The thesis is divided into eight chapters. Chapter 1 is an introductory which outlines the motivation and purpose to apply the induction heating technique as a new method to fabricate coatings combined with the SHS process. Chapter 2 reviews the literatures involved in the fabrication of coatings using the SHS process such as the discussion of materials used as advance protective coatings, the varied methods of combined SHS and coating processing routes, the processing parameters affecting the process, the performance of the coatings, and the application of coatings formed by the SHS process. The chapter concludes by defining the problem and highlighting the knowledge deficiencies within the field of research.

Chapter 3 describes the materials and experimental details for the present research. The content describes the preparation of the raw material, the tools and equipment used for experiment, the preparation to perform the SHS process and coating production, and the preparation for products characterizations. The next four chapters present the results and discussions of the research. Chapter 4 discusses the combustion behaviour and the microstructure of the synthesized NiAl coating. In this chapter, the formation mechanism of the synthesized product is analysed. Chapter 5 is focused on the evaluation of the mechanical properties of the synthesized product. Chapter 6 is concerned with the fabrication of NiAl–TiC–Al_2O_3 composite material. Chapter 7 analyses the production of hard TiC coating.

Finally, Chapter 8 considers the conclusion and direction for future research based on the present work. The conclusion provides a summary and analysis of the findings of the study to develop a new method to produce high performance material and coatings for high temperature applications. The implication of the findings for future research is also described.

Chapter 2

Literature Survey

This chapter presents a review of current developments in processing routes to fabricate advance protective coatings using SHS process. It begins with a short overview of intermetallic and ceramic materials which offer significant advantages for high temperature applications, followed by a description of the SHS process, its attractiveness to synthesize intermetallic and ceramic materials, and the approaches to fabricate coatings using the SHS process. Different processing routes to fabricate coating formed by SHS process using different heat sources are also discussed. The chapter continues with discussion on the factors affecting the coating performances such as densification, post treatment, and bonding to substrate. The processing parameters which affect the SHS process including thermodynamic calculations and heat transfer are reported. The applications of coating synthesized by the SHS process for industrial application and environmental interest are also presented. In addition, the introduction of induction heating as an effective heat source to initiate the SHS process is also described. To conclude, this chapter gives a brief summary of the review, followed by a discussion on the research opportunities and research plan for the present work.

2.1. Intermetallic and ceramic materials

2.1.1. Intermetallics

Intermetallics is a short general term used to describe an intermetallic compound or phase which is used to refer the mixture of two or more metals in a specific proportion that forms a class of advance materials or chemical compounds which contain different crystalline structures from those of their constituents [20]. Intermetallic compounds have a particular chemical compound with a definite atomic formula based on the chemical composition of their constituents, such as NiAl, Ti_3Al, and $MoSi_2$. The biggest advantage of intermetallics is that they possess

long-range ordered crystal structures which help the difficulty in dislocation motion. This factor allows intermetallics to have good properties such as high melting point and great strength in high temperature, but results in poor properties in ambient temperature such as the britlleness and fracture toughness [21]. The melting point and density of various intermetallics are listed in Table 2.1. Further studies have shown that the brittleness of intermetallics at room temperature such as found in Fe_3Al and Ni_3Al can be reduced by alloying and microstructural control [21]. In high temperature applications, intermetallics such as titanium aluminide and $MoSi_2$ also have a problem with insufficient creep resistance. However, this problem can be improved by alloying or composite formation [21].

Table 2.1. Properties of selected intermetallics [22]

Intermetallic compounds	Melting point (°C)	Density (g/cm^3)
NiAl	1640	5.86
Ni_3Al	1390	7.50
FeAl	1250	5.56
Fe_3Al	1540	6.72
TiAl	1460	3.91
Ti_3Al	1600	4.2
$TiAl_3$	1350	3.4

Amongst the intermetallic systems, much research has been devoted to study aluminide intermetallics based on transition metals such as Ti, Fe, and Ni, due to their excellent properties for oxidation resistance. Most intermetallics which contain aluminium are attractive for oxidation resistance since atom Al will react with O_2 to produce α–Al_2O_3 at temperature above 1000 °C that protects inner surface layers from oxidation [6]. The discussion of several intermetallic systems which mainly composed of Ti, Ni, Fe, and Al, is reported here.

2.1.1.1. Ni–Al and related phases

Among a variety of intermetallic compounds, NiAl and Ni_3Al have long been considered as candidates for high-temperature applications due to their high melting temperature and excellent oxidation resistance [23]. The melting temperature of NiAl phase which is 1911 K, is higher than that of its based

elements; Ni (1728 K) and Al (933 K) [24]. This indicates that the atomic bonding between the unlike Ni and Al atoms is much stronger than that between the alike Al atoms and Ni atoms. The crystal structure of NiAl is also clearly different from its constituent. NiAl has bcc structure with atomic ordering or known as B2 structure, while Ni and Al have fcc structure [20]. The difference of the crystal structures between NiAl phase and its constituent show that NiAl is chemical compound of metal.

Despite its excellent properties, the performance of NiAl is hindered by its low ductility or high brittleness particularly at ambient temperature. NiAl also suffers from insufficient creep resistance at elevated temperature [2]. This brittleness is related to its low cohesive strength of its grain boundary. Low ductility of intermetallic is generally dependent on the slip system which is insufficient to meet Von Misses criterion. Thus, there is no plastic deformation in the polycrystalline form. By adding with other particles, it is expected to make segregation to the grain boundaries, and then changes the fracture mode [23]. Several investigations have been carried out to increase the balance of NiAl properties in elevated and ambient temperatures by microalloying, compositing, and applying different processing techniques [21]. A number of pure elements have been investigated as particle addition such as Fe, Mn, and Mo to improve the ductility of NiAl [25]. A variety of ceramics such as TiC and TiB_2 have also been tried to improve its property [5][26]. TiB_2 is less studied since it incorporates with an expensive element.

2.1.1.2. Ti–Al and related phases

The intermetallics of titanium aluminide systems, in particular, Ti_3Al and TiAl, have offered greater potential for high temperature applications since they have better properties such as low density, high specific strength, high specific stiffness, and high oxidation resistance compared to conventional titanium alloys [27]. Titanium aluminides have the potential for serving in a variety of structural applications such as in space, aircraft engines, and automobiles. For space applications, the realization of a hypersonic vehicle has implied a specific material

which requires low structural weight, high thermal stability, and compatibility for high temperature. For aircraft engine applications, the development of a small and efficient turbine requires high strength to weight ratio and increased turbine entry temperature in order to produce higher thrust. In automobiles, weight saving gained through the use of lightweight material is a benefit for improved fuel consumption. Ti_3Al and TiAl having low density and high thermal conductivity are attractive for automobile industries which require heat resistance for rotating engine component at high speed [27].

Fabrication of Ti_3Al and TiAl can be prepared by different routes such as ingot metallurgy, reactive sintering or SHS process, and explosive shock-wave consolidation, as has been reviewed by S. Djanarthany et al. [27]. In the SHS process, elemental powders of Ti and Al are usually compressed and ignited by an external heat source to initiate the synthesis process. The reaction mechanism is initiated by the melting of Al which triggers the reaction between Ti and Al to produce a high exothermic reaction. A study has demonstrated that at the first stage of Ti/Al reaction, liquid Al was melted and subsequently spread over the surface of Ti particles to form a layer which covered Ti in the core. The next step was the reaction between $TiAl_3$ and Ti in the core to produce TiAl at a temperature near 1330 °C. In the final stage, Ti was reduced and TiAl changed to form Ti_3Al. The final product was generally not pure, but took the form of a mixture of $TiAl_3$, TiAl, and Ti_3Al which were porous [28]. Briefly, the sequence of Ti_3Al formation is described in Eq. (2.1)

$$Ti + Al_{(liquid)} \rightarrow Ti + TiAl_3 \rightarrow Ti + TiAl_3 + TiAl \rightarrow Ti_3Al \qquad (2.1)$$

2.1.1.3. Fe–Al and related phases

The iron aluminides FeAl and Fe_3Al are attractive intermetallics for a broad range of applications due to their low cost, good corrosion and oxidation resistance, and are easy to fabricate [23]. In addition, they also have good resistance to carburization, sulfidation, and wear properties [21]. FeAl and Fe_3Al have high temperature properties compared to many structural alloys due to the formation of

an alumina protective coating, but they exhibit brittle fracture and low ductility at ambient temperature resulting in the fabrication difficulty using conventional techniques such as ingot metallurgy. Reactive synthesis using powder metallurgy has been used to overcome this problem by producing near net shape forming product with commensurate energy savings [29]. However, the sintering of Fe–Al is still a challenge due to the porosity caused by the Kirkendall effect or the difference of diffusion rate between Fe and Al in their counterparts [30]. Further studies have been carried out to reduce their porosities by adding metal or ceramic to form intermetallic composite materials [31][32].

According to the phase diagram of Fe–Al, there are varied Fe–Al phases which can be formed during the sintering process of Fe–Al mixture depending on the temperature. The variation of processing temperature in the reaction of Fe–Al system was investigated by H. Gao et al. [29]. The processing temperature below 500 °C has shown no reaction. Increasing the processing temperature from 500 °C to 600 °C, intermediate phases such as Fe_3Al, Fe_2Al_5, $FeAl_3$, and $FeAl_2$ were initially formed. Increasing the reaction temperature from 700 °C to 1000 °C, all the intermediate phases were removed and FeAl became visible.

2.1.1.4. Ti–Ni and related phases

Nickel–titanium systems offer potential use for protective coatings since they have good oxidation and corrosion resistance. These materials are also characterized by good wear resistance since they have a low friction coefficient. However, like other intermetallic systems, Ti–Ni systems have a lack of toughness and ductility at room temperatures [33].

Among the Ti–Ni intermetallic compounds, NiTi is the most popular and is used in a variety of different fields. The porous structure of NiTi makes this material suitable for biomedical applications. NiTi shape memory alloys have been widely used as the biomaterial for implantations due to their biocompatibility [34]. Porous NiTi is mostly fabricated by powder metallurgy using reaction synthesis, metal injection molding, and plasma sintering. However, SHS is advantageous since it

offers energy saving [35]. A study has reported about an investigation into the effects of pressure, preheating temperature, and heating rate on the microstructure and porosity of the NiTi formed by SHS process of Ti–Ni powders [35]. The results showed that the porosity of NiTi could achieve 59.7 vol. %.

2.1.1.5. Al–Ni–Ti and related phases

Advanced aluminide materials such as NiAl and TiAl have received special attention for high temperature application due to their advantages such as high corrosion and oxidation resistance, low density, and high strength [21]. Due to the brittleness of common intermetallics, the mixing with other metals is often carried out to improve their ductility at room temperature. The addition of Ti into Ni–Al system has been observed to improve its creep strength due to an atomic mismatch within the solubility range and semicoherent precipitation of $AlNi_2Ti$ beyond the solubility range, while the addition of Ni into the Ti–Al system has improved the ductility at room temperature whilst maintaining its creep and oxidation resistance at high temperature [36]. Different modern processing routes have also been studied to produce intermetallics of nickel and titanium aluminide such as the application of NiAl for coating on Ti substrate which was fabricated by using microwave [11]. High energy supplied by microwaves could initiate the combustion synthesis of Ni/Al until achieving the melting point of the synthesized product. The liquid phase of synthesized NiAl then reacted with Ti substrate at the interface to form a Al–Ni–Ti system. It was reported that Ti_2Ni was formed at the intermediate layer. TiAl based intermetallic has also been joined on the Ni with Ti underlayer using diffusion brazing [37]. During the brazing, Ti underlayer was melted and reacted with TiAl based metal to form different products binary and ternary systems such as TiNi, Ti_2Ni, $AlNi_2Ti$, Al_3Ni_2Ti, TiAl, and Ti_3Al at the brazing zone.

2.1.2. Ceramics

There has been a lot of interest in ceramic materials such as TiC, TiB_2, WC, SiC, and Al_2O_3 as hard protective coatings in a wide range of industrial applications since they have high hardness and high wear resistance [38][39][40][41]. Of these

materials, titanium carbide has developed into the most interesting ceramic for high temperature application due to its high modulus, high hardness, high melting temperature, and high corrosion resistance [40]. However, the application of single phase ceramic in high temperature is limited due to its poor fracture toughness. Therefore, the TiC particle has been widely investigated as a candidate for use in the reinforcing phase for various composite materials such as metallic matrix composite [42], intermetallic matrix composite [5], and ceramic matrix composite [43]. Some studies have observed the reinforcement of TiC in the NiAl/TiC composite system [5][44][45]. Such composites have showed high wear resistance due to the high hardness of TiC. The studies have also shown that the combination of high hardness and the excellent stability of TiC at high temperature, together with the strong atomic bonds of the nickel aluminides, has produced composites that have excellent wear resistant at room and high temperatures [18].

Alumina ceramic systems such as TiC–Al_2O_3 have also been widely found in high temperature applications since they have high hardness and low density. It was also reported that the binary ceramic composites of TiC–Al_2O_3 could improve the fracture toughness of the individual ceramic materials, either TiC or Al_2O_3 [46]. Further investigations have showed that ternary ceramic composites exhibited higher fracture toughness than those of binary ceramic composites. The addition of 10 % ZrO_2 into Al_2O_3–TiC prepared from TiO_2, Al, and C using combustion synthesis and followed by hot pressing was able to increase the fracture toughness of Al_2O_3–TiC–10 wt.% ZrO_2 by approximately 20% more than that of Al_2O_3–TiC composite [47].

There are many processing techniques to produce ceramic. Generally, ceramic matrix composite is prepared from elemental powder using mechanical densification. Several studies were carried out to produce ceramic using pressureless sintering, hot pressing, and hot isostatic pressing [48]. However, due to their high degree of covalent bonding and low self diffusion, densification is difficult. In addition, the high melting temperature of ceramics requires a long exposure at high temperature for the sintering process to achieve full density. High

temperatures in the processing route of ceramic also influence the microstructure of the product, such as grain growth [40].

High energy ball milling has been investigated to be powerful method to induce the synthesis of a TiC system producing nanocrystalline product. Fabrication of Al_2O_3–TiC nanocomposites using mechanical ball milling was reported by E. Mohammad Sharifi et al. [48]. The effect of milling time and heat treatment was observed. The result showed that the reactant powder composed by $Al/TiO_2/C$ had experienced a SHS process after 40 hours of milling and the crystal of synthesized Al_2O_3–TiC was less than 10 nm. Annealing at 900 °C has kept the size of product. However, the crystallite size of the product was bigger after increasing the annealing temperature to 1200 °C.

Combustion synthesis has offered an alternative to produce ceramic via a short and simple process [49]. However, the product synthesized by the SHS process is usually porous [14]. The additional application of pressure is sometimes required during the synthesis process in order to improve the density of product [47]. The addition of liquid metal as diluents was also studied to increase the density of product by reducing the combustion temperature [50]. Different techniques to produce high density product of ceramic using a relatively low temperature were carried out by spark plasma sintering (SPS) [51]. The sintering process in the SPS technique is very short due to the heating process which is accomplished through spark discharge generated by instantaneous pulsed direct current. Other techniques to improve the density of ceramic have also been carried out by combining the SHS process with pressure obtained from the dynamic compaction using high explosive detonation [40].

2.2. SHS Coating

2.2.1. Introduction to SHS coating

Self propagation high temperature synthesis (SHS) is a type of combustion synthesis which transforms reactants into products in a highly exothermic reaction. The combustion process is initiated by heating the front part of the sample to its

ignition temperature using an external heat source. After the reaction is ignited, the heat produced by combustion reaction then propagates and heats up the adjacent layer to the ignition temperature so that the combustion wave can self propagate through the whole sample. Another type of combustion synthesis is known as thermal explosion or simultaneous combustion in which the combustion of the whole part of the compact occurs simultaneously once the ignition point is achieved [52][49].

Over the past four decades the SHS process has become very attractive since it offers several significant advantages. The combustion reaction is highly exothermic ensuring the combustion process proceeds to completion. The high temperature of combustion synthesis can reach a temperature above the low boiling point of some impurities in the element. The combustion reaction can therefore boil off the impurities to produce a better purity of product. The combustion rate is also very rapid resulting in better homogenization of the product. This is due to the fact that the heating rate affects the completeness of the reaction. When using the same ignition energy, the reaction front in a rapid heating propagates faster such as occurs in high density pellet. The rapid heating hence reduces the heat loss and results in the completeness of reaction to obtain homogeneous microstructure. Since the reaction occurs in a short time, the operation becomes more effective. From a technological point of view, a short combustion process would produce high productivity, and therefore less power consumption [52]. Another benefit is that SHS process is self sustaining. After the heat due to ignition is imparted, the combustion reaction will self-propagate by itself. The heat from the combustion of the front layer will produce an ignition heat to other layers. The additional heat source required by other types of process to maintain the combustion process can therefore be eliminated thus making the process very efficient. Given these significant advantages, the SHS process has been considered as an alternative to conventional furnace technology which requires complex process preparation and expensive equipment [49].

Recent development of the SHS process has made it more attractive since it can be applied for the fabrication of coatings [13]. A number of external heat

sources have been used to initiate the SHS reaction and deposit the SHS product onto the substrate to fabricate the coating. With the current approach, the processing route which combines the fabrication of material synthesized by using the SHS process and the deposition of coating on the substrate is referred to as SHS coating. Various ignition techniques such as microwave [53] and laser technology [54] have been used to initiate the SHS reaction. These heat sources have been subsequently combined to fabricate coating from the synthesized product. In the synthesis processing stage, the heat supplied from the external heat source is used to increase the temperature of the synthesized material from its initial temperature to ignition temperature. After reaching the ignition point, the combustion wave will self-propagate through the whole sample. The use of the external heat source can then be eliminated. The heat release produced by SHS reaction can reach very high temperature such as in the combustion synthesis of intermetallics and ceramics. Taking advantage of the reaction process, the heat produced by the SHS reaction can then be used to increase the substrate temperature in order to help adhesion on the deposition of the synthesized product on the substrate [7]. By using SHS process to fabricate coating the process of material fabrication and coating deposition onto the substrate is simplified into one step.

SHS coating or the fabrication of a coating combined with the SHS reaction might be carried out according to the following approaches:

- Using the heat released by the SHS reaction to deposit coating material on the substrate. The exothermic heat produced by the SHS reaction is utilized to increase the temperature of substrate and to create adhesion between coating and substrate. In this method, an external heat source is only used as an igniter to initiate the SHS reaction. After ignition, the external heat source is switched off and does not play a role in the coating deposition. This method offers some advantages such as the simplicity of the process, since the ignition and coating application is conducted in one step, and the relatively low energy requirement since there is no need to use additional heat for the application of the coating. However, the bonding strength might be very dependent on the energy provided by SHS reaction. A study has identified that the energy affecting the

bond strength is influenced by the mass of reactant. Lower mass has produced less energy and shorter heating time to facilitate the formation of the bonding at the interfaces [55].

- The heat used for coating deposition is obtained from the heat release produced by the SHS reaction and the additional heat from an external source. In this method, the external heat is not only used to initiate SHS but also to help adhesion by increasing the substrate temperature and maintaining the molten phase of the SHS product. This method has produced better bond strength [11]. Since there is additional heat to help coating deposition, more energy consumption from the external heat source is necessary. The combination of the initiation of the SHS process and coating deposition on the substrate in one place is often referred to as one step process, or *in situ* process.

- The ignition process and coating deposition are carried out in different places. This means that there are two processes which occur in a different time period. The first being the production of material using the SHS method, and the second by applying the material synthesized by SHS to fabricate the coating. The heat used to ignite the SHS process and to deposit the coating might also be obtained from different sources. An example of this method might be found in the fabrication of coating by plasma spraying, where the SHS product is usually firstly milled to become classified powder, and then deposited into the substrate by plasma spraying [56].

Fig. 2.1 shows the schematic of the processing route of the SHS coating. The reactant powder can be applied on the substrate by using dry or wet techniques. The main process of SHS coating involves the ignition process and coating deposition. Many ignition techniques obtained from external heat source can be used not only to initiate the SHS reaction, but also to help the deposition of the coating on the substrate and to be used as a heat source for post treatment. SHS processes are followed by post treatments such as by using annealing and remelting to improve the coating performance. Densification or sintering additives might also be used to reduce the product's porosity.

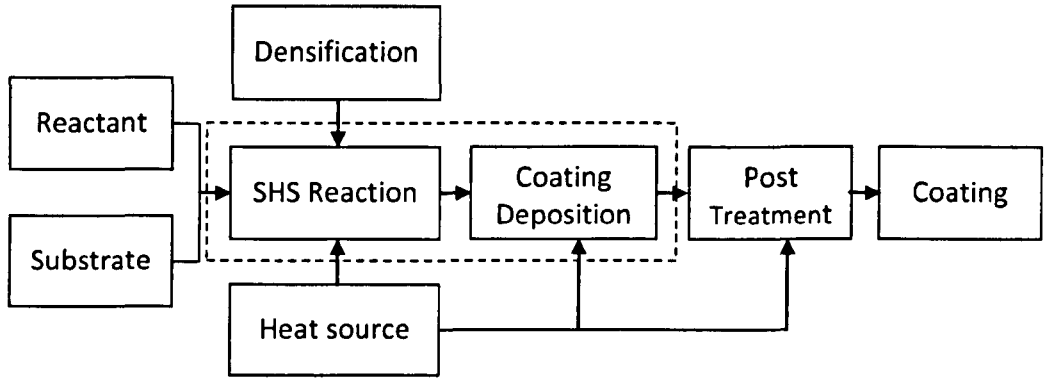

Fig. 2.1. Schematic diagram of the SHS coating

Fig. 2.1 also describes that the main component of the SHS coating processing route is SHS reaction and coating deposition. The following paragraphs will review each of the processes identified in Fig. 2.1, especially with respect to ignition techniques, different SHS coating processes, post treatment and densification.

2.2.2. Ignition techniques

The ignition system plays a vital role in the SHS process since it significantly affects the whole process by providing sufficient energy to initiate a combustion process. The control and repeatability of the ignition operating system is also extremely important with respect to safety. Some heat sources such as electric discharge through a heated tungsten wire or coil, radiant heat flux, resistance heating coil, reactive gas, and chemical oven have long been successfully used to ignite combustion synthesis. The use of these techniques has been discussed by J.J. Moore [49].

The high power density of a laser has been used as an efficient tool for ignition in combustion synthesis by heating the local surface layer of the sample until its ignition temperature is achieved. Y. X. Li et al. [54] have taken laser beam as heat source to ignite the combustion synthesis of TiCx from elemental powders of Al–Ti–C. Meanwhile, microwave energy has been investigated by Duangduen Atong and David E. Clark as a method to ignite the combustion synthesis of composite

Al_2O_3–TiC [53]. The casting process has been used to initiate the combustion synthesis of TiC/Ni_3Al [8]. In the casting technique, reactant powders positioned in the mould will be ignited to initiate the synthesis reaction by the heat of the molten liquid metal poured into the mould. Other investigations have also shown that concentrated solar energy converged by a Fresnel lens has been used as power source to initiate the SHS process of NiAl [55]. A solar spot can generate a high temperature on the material surface and is capable of igniting a sample of Ni/Al to reach its ignition temperature at 913 K. More recently, induction heating has been successfully observed by Zhu et al. as an efficient tool for ignition in the combustion synthesis of NiAl/Al_2O_3 [19] and NiAl/TiC [18]. An electric field has also been used as an ignition source for combustion synthesis [57]. During the field activated combustion synthesis (FACS) reaction, the applied electric field is used to initiate the ignition by providing the heat resulting from the Joule effect. The heat has also contributed to the propagation of combustion velocity during the SHS reaction. Another method which has been tried to ignite the combustion synthesis is through the use of an oxygen-acetylene flame [58]. This method has been used in the fabrication of ceramic-lined compound copper pipe (CLCCP) by SHS and centrifugal casting technology.

With many available and thoroughly investigated techniques used as ignition systems in combustion synthesis, careful consideration towards the technological and economic aspects of each ignition technique is crucial in order to obtain the optimum option. Table 2.2 presents an analysis of the advantages and disadvantages of some ignition techniques used in combustion synthesis.

Table 2.2. Advantages and disadvantages of ignition systems

Ignition technique	Advantages	Disadvantages	Ref.
Laser	- High ignition power, high heat intensity, and high heating rate - Well defined surface location - Repeatability and easy control of its ignition parameter	- High initial cost - Complicated process - Unsuitable for applications with large heating areas	[54]

Microwave	- Provide rapid and volumetric heating process - Heat is generated internally within the material and flows towards the outside - Less processing time and energy consumption	- Non uniform heating - Low reproducibility - Only for materials which have good absorptivity to microwave energy	[53]
Casting routes	- In situ reaction - No additional ignition instrument	- The supplying heat depends on the melting temperature of the molten metal	[8]
Concentrated solar energy	- No contact area between heat source and sample - Fairly fast heating - Environment friendly and energy saving	- Heat source is affected by the lens	[55]
Induction heating	- No contact area between heat source and sample - Capable of heating a large area providing it has a magnetic field - High heat intensity and fast heating - Well defined surface location - High accuracy and repeatability - Clean process and environmental friendly - Easy control of ignition parameters	- Only for material which is electrically and magnetically conductive	[19] [18] [17]

Based on the considerations listed in Table 2.2, the use of microwave and induction heating might be advantageous to increase the effectiveness and completeness of the reaction since the heating comes from inside the body of the material. The use of induction heating might be of greater interest for an efficient external source in combustion synthesis when its capability for fast heating and process cleanliness is considered. Fast heating produced by induction heating will facilitate a high heating rate to achieve the required ignition temperature in a shorter time over a larger area. This means that induction heating is helpful in enhancing the efficiency of the production process.

2.2.3. Processing routes of SHS coating

Several processing routes which combine SHS reaction and coating deposition have been found in many recent works. Their important features are discussed as follows:

2.2.3.1. In situ SHS with casting route

The casting route has been utilized to synthesize material and to fabricate the coating in one process. The SHS process in the casting route is initiated by using the heat from the molten steel which is poured into a sand mould. The reactant which is pasted on the sand mould obtains the heat energy used to initiate SHS reaction from the molten steel. The heat produced by the SHS process is used to help adhesion through the diffusion process of Fe atoms from the molten steel into the coating to produce metallurgical bonding between coating and the substrate. In this case, the reactant is converted into coating product, while the substrate comes from the molten steel [7][8].

The application of combined SHS with casting route has been found in the fabrication of $MoSi_2$–MoS_2 composite coating on the steel substrate [7]. Using the same technique, Ni_3Al–TiC composite has also been synthesized in situ by one step reaction synthesis from the mixture of 3Ni–Al–Ti–C powders in liquid steel and followed by a densification procedure [8]. In the SHS casting process of Ni_3Al–TiC, the starting material which is composed of 3Ni–Al–Ti–C powders is first compressed to form a compacted pellet. The pellet is then pasted on the sand mould while the molten steel is prepared by using an induction furnace. The high temperature liquid steel is then poured into the mould and heats the sand mould and pellet. The SHS reaction of the reactant system is initiated by the high temperature of the liquid steel poured into the mould. As obtained by a differential scanning calorimetry (DSC) curve, the synthesis reaction is composed of two reactions, 3Ni–Al, and 3Ni–Al–Ti–C. The first reaction is to produce Ni_3Al. This reaction produces high heat release which is then used as heat source to initiate the second reaction to form TiC. In this case, heat release produced by Ni_3Al reaction is used as an igniter for the SHS reaction of 3Ni–Al–Ti–C system. Due to the relatively high combustion

temperature, the synthesized product is in the liquid phase for a while. The liquid product is in contact with the steel substrate, and the high temperature of the liquid product will cause the Fe atoms on the steel substrate to melt. Due to the concentration difference of Fe atoms in the two liquids, Fe atoms will diffuse from steel surface into the liquid of synthesized product to form a new interphase at the interface. The diffusion process continues until the coating and substrate begin to solidify. When all phases are completely solidified, the interphase formed at the interface produces metallurgical bonding. The formation of metallurgical bonding at the interface also has the benefit that it helps to reduce the concentration of thermal stress due to the high temperature of the SHS process which can generate cracks. It is generally known that cracks can be found in synthesized product formed using the SHS process due to the high thermal stresses induced through thermal expansion mismatches such as found in ceramic composites [49]. During the process, the liquid steel also permeates into the porous product synthesized by SHS. It is widely known that the SHS process can generate porous product. High combustion temperatures and short process times can produce porous product as a result of the intrinsic and extrinsic sources such the gas entrapment from low boiling point impurities [2]. Due to the capillary attraction, the liquid steel would infiltrate into the porous product. The Fe infiltration can then reduce the porosity of the composite product.

It might be assumed that the casting route is an advantageous method to produce SHS coatings by the relatively easy process of igniting the reaction by using the heat from molten steel poured into the preform pasted on the sand mould. Another benefit is that Fe atoms on the molten steel can diffuse into the coatings product to form a new interphase at the interface and produce metallurgical bonding. However, it was evident that there were some Fe atoms which diffused into the coating product to form dilution. The infiltration of steel metal into the coating might become a disadvantage since it can reduce the hardness of synthesized product. The infiltration of metal can also decrease the combustion temperature which is critical to produce pure product.

2.2.3.2. Combined SHS with laser technology

Materials synthesized by SHS can be coated on a substrate surface by using laser technology. Lasers have been used to simultaneously ignite the SHS reaction and fabricate the coating in one process. A laser is capable of producing fast heating which has been used as an efficient tool for surface modification such laser cladding and laser surface alloying [9][10]. The high cooling rate in laser processing has been observed to produce product of very fine grain size which results in an increase of hardness [9]. A strong bond between the substrate and coating layer can also be achieved by using a laser. During laser heating, the molten phase of the coating and substrate causes the atoms in the coating and substrate to diffuse amongst each other. Using this method has allowed the production of diffusion bonding which increases the bonding strength at the interface. Through the use of a laser is also possible to tailor the coating properties by varying the laser processing variables, such as scanning speed, power density, and beam size [59]. In general, it is reported that the use of lasers to ignite the SHS process and fabricate coatings on the substrate provides a significant saving on the amount of laser density due to the addition of heat from exothermic reaction [60].

In the coating processing route which combines SHS with laser cladding, the reaction synthesis process is initiated by inducing the heat source produced by laser beam onto the reactant powder preplaced on the substrate. The powder mixtures might be placed on the substrate or by injecting them into the trailing edge of the molten pool [59]. The ignition of the SHS reaction through the use of a laser can only exist in the laser scanned area. Once the reaction is ignited, the combustion wave front will self propagate along the reactant powder on the substrate until completion. Synthesized product formed by the SHS process is then used as cladding material. Subsequently, the high power density of the laser beam is used to melt the cladding material and a small portion of the underlying substrate to form a coating which is adhered to the substrate. The advantages of laser cladding are the capability to form metallurgical adhesion between coating and the substrate, giving rise to a very fine grain size resulting in high hardness, low dilution of the coating to the substrate, and the production of a small heat affected zone

[59]. However, increasing the laser power can result in an increase of the dilution ratio due to the excessive fusion of the substrate [60]. The dilution ratio might need to be kept as low as possible in order to conserve the initial properties of the coating.

The application of SHS coating combined with laser cladding was found in the fabrication of a hard and nanostructure ceramic composite coating which consists of aluminium oxide, titanium diboride and titanium carbide (Al_2O_3–TiB_2–TiC) obtained from a mixture of aluminium, titanium oxide and boron carbide powder [10]. The powder mixture was blended with the help of a magnetic stirrer to form a slurry. A small quantity of polyurethane based adhesive was added into the mixture in order to produce a sticky liquid suitable for the deposition process. The slurry was then pasted on the steel substrate with hand coater or paint brush to a thickness of about 100 μm. The coated sample was baked in the furnace at 100 °C for 1 hour to vaporize the moisture. A 10 kW transverse flow continuous wave CO_2 laser was used to produce an elliptical shaped laser beam giving a track of 10 mm width. The surface of the coated specimen was scanned with varied scanning speed. The result of the experiment has shown that the laser has been successfully employed to trigger the SHS reaction of the reactant and subsequently applying the synthesized product on the substrate to produce a hard and dense coating. It was reported that the grain size of synthesized product can be very fine depending on the laser scanning speed. Table 2.3 shows the effect of laser scanning speed on the hardness. The laser scanning speed determines the interaction time of the laser beam with the material. Faster laser scanning speeds produce higher cooling rates which result in the increase of coating microhardness. The hardness of the synthesized product developed by laser cladding was identified to be sufficiently high and therefore suitable for wear resistance coating applications.

Table 2.3. The effect of scanning speed on the coating microhardness [10]

Laser scanning speed (mm/s)	Maximum microhardness at the cross-section of the coating ($HV_{0.025}$)
2.5	2246
5	2432
10	2507

In the coating processing route which combines SHS with laser surface alloying (LSA), the SHS process of the reactant mixture is initiated by the strike of the laser beam on the surface of preplaced powder. When the laser is acting on the reactant mixture, its temperature rises. SHS reaction is initiated when the precursor temperature has achieved its ignition. The synthesized product formed by the SHS process is then subsequently laser alloyed onto the substrate to form an alloy. In LSA, the formation of the coating is characterized by some degree of dilution of an added constituent from the substrate [61]. The formation of alloy in the combined SHS and LSA process has been reported to be advantageous to reduce the porosity which is generally apparent on the synthesized product produced by SHS reaction. It has been thought that LSA has a function similar to laser post treatment which is used to remelt the coating. In LSA, the synthesized product of the SHS process is mixed together to produce an alloy with the surface part of the substrate [62]. In laser surface remelting, a high power scanning laser beam is used to melt the top layer of a surface, followed by rapid cooling and resolidification. This process can be used to tailor surface properties without substantial changes in material composition. Laser surface remelting is popularly referred to as laser glazing [63].

The technique which combined SHS and LSA has been utilized to fabricate nanostructured Al_2O_3–TiB_2–TiN based coatings [61]. The reactant powder mixture underwent the SHS process due to the high temperatures induced by 4 kW continues wave (CW) CO_2 laser. The products of SHS were subsequently laser alloyed onto the substrate to produce a coating. The result has shown that the microhardness of the coating was identified to be significantly higher when compared to that of the low carbon steel substrate. The high hardness of the coating was attributed to the formation of a fine grain structure as a result of the rapid cooling and the formation of a hard phase during the SHS process.

Amongst the laser processing techniques such as CO_2 laser, high power diode laser (HPDL), and Nd:YAG laser, the HPDL process has a number of specific features which are suitable for surface modification. The intensity distribution of HPDL can be shaped with almost complete uniformity. In addition, by using simple optics the spot shape can be extended to create a wider scanning track [9]. To the

contrary, CO_2 and Nd:YAG require complex and expensive focusing techniques to tailor the spot size of the laser in order to obtain uniform intensity distribution. Multi-phase ceramic composite coatings of TiB_2–TiC–Al_2O_3 with $TiAl_3$ matrix have been fabricated by combining self-propagating high temperature synthesis assisted by a high power diode laser (HPDL) subsequently applied on the steel substrate. In this case, the laser was used to trigger the SHS reaction to produce a composite system. The laser then melted the cladding of the synthesized product into the substrate. The result has shown that a fully dense, hard and wear-resistant ceramic matrix composite (CMC) could be successfully developed using combined SHS and HPDL on a steel substrate.

2.2.3.3. SHS assisted with Concentrated Solar Energy

Concentrated Solar Energy (CSE) has been used as a power source for surface treatment. This method is carried out by concentrating the solar irradiation through a convergence lens to produce a focused solar spot on the sample surface. The installation of the lens is designed so that the position of lens surface is normal to solar radiation which is then focused on the surface of the material. Since the source of heat comes from the sun which moves from east to west, the installation of the lens has to be adjusted to follow the solar tracking which can be controlled by computer. The solar spot produced by CSE can be set either fixed on the sample surface or moved for scanning across the sample surface such as found in laser processing technique. Meanwhile, the sample material can be fixed or moved towards the solar spot [64].

An important feature of the CSE is that the power density obtained in the solar spot mainly depends on the concentrator device. Low concentration devices such as in a Fresnel lens can achieve power densities up to 2.5 MW/m^2 in a solar spot of 5 mm in diameter, while high concentration devices such as a solar furnace can achieve up to 100 MW/m^2. Low concentration devices only produce low power and a small focusing area, while high concentration devices can produce a higher power density allowing them to be used in the processing of larger areas and in shorter periods of time [65]. A study has shown that a variety of solar spots can

provide the heat necessary to generate a high temperature on a sample surface in order to initiate the synthesis reaction since the energy developed from CSE can be sufficiently high to achieve the melting temperature at the surface of metallic materials [66]. In addition, the solar spot can also be used to maintain the combustion propagation of the SHS process [64].

The use of CSE for SHS coating can be found in the fabrication of NiAl coating carried out by C. Sierra et al. [55]. Concentrated solar energy converged by a Fresnel lens was used as a power source to initiate the SHS process of NiAl and to subsequently deposit the synthesized product on the steel substrate. When the sample is passed under the solar spot, it is progressively heated until reaching its ignition temperature. The result has shown that a solar spot was able to produce a high temperature in the sample to initiate the synthesis reaction of Ni/Al. The exothermic reaction between nickel and aluminium as the reactant produced a high heat release which can achieve the molten phase of nickel aluminide. The molten phase is then cooled down and solidified after the combustion process is completed. Solidification of this phase then creates adhesion between the coating and the substrate. The study has identified the influence of the reactant mass on the adhesion strength and the porosity of coating. The sample was prepared using different mass of Ni/Al reactants with 0.3, 0.6, and 1.7 grams, whilst the substrate was a cylindrical shape with a diameter of 16 mm and thickness of 5 mm. To accommodate the reactant, a cavity was built in the surface of the substrate with 14 mm diameter and 3 mm depth. Subsequently, the reactant was placed in the cavity of steel substrate and compressed by 300 MPa. The SHS process of the reactant was then initiated using the solar energy. The result of the study showed that the porosity and adherence between the coating and substrate depend on the mass of Ni/Al. A higher mass of reactant has produced better adherence, but contains more pores. It may be thought that increasing the content of NiAl will generate more heat which then permits high diffusion and better bond strength. Higher heat release by SHS reaction will provide more energy for atoms in the substrate surface to diffuse into coating and form a thicker interphase at the interface between coating and the substrate. A thicker interphase will result in

better metallurgical bonding. On the contrary, higher mass of NiAl will produce a thicker coating layer which results in an increase in the amount of gas entrapped in the coating. In thick coating layer, the void inside the coating will require a longer distance to escape from the coating layer. Since the SHS reaction occurs in a very short time, some voids will be entrapped inside the coating as pores.

An advantage of concentrated solar energy is its applicability to act as a substitute for the laser beam. In general, laser beams can produce high flux density. However, CSE is also capable of generating sufficiently high flux density to quickly reach the ignition temperature of a metallic surface. This is due to the absorption factor of metals in the wavelength of the solar radiation which is higher than that of the CO_2 laser [65]. A study has been carried out to fabricate NiAl coating via the CSE technique using different heating fluxes; 1640, 1550, and 1265 W/cm^2 [64]. The result showed that a higher flux density accelerated the SHS process, but it was accompanied by the melting of the substrate. Meanwhile, using a lower flux density it was difficult to initiate SHS process and a low scanning speed had to be used. By using a scanning speed of 1 mm/s, the SHS process could be initiated but there was overheating which resulted in the melting of some parts of the substrate.

Another advantage of CSE is its capability for scanning. The scanning process in CSE can be performed by moving the specimen under the CSE beam. When CSE is used to initiate the SHS process on a localized area, the propagation of wave front might be slowed down or even stopped because the substrate and the boundary behave as a heat sink. CSE can be used to continuously supply additional energy in order to maintain the heat propagation to ensure the completion of the SHS reaction. In this case, scanning speed has to be adjusted in order to avoid insufficient heating or overheating. Too high scanning speed might not be able to produce sufficient energy to ignite the SHS process, while too low scanning speed might result in overheating and result in the melting of the substrate. An investigation has observed the effect of different scanning speeds of CSE in the fabrication of stainless steel coating by using 0.8 mm/s, 1.6 mm/s and 1.8 mm/s scanning speeds [66]. The result has shown that a lower scanning speed has produced vaporization of the reactant resulting in the loss of the alloying element.

Increasing scanning speed has reduced the loss of alloying element and produced quick solidification. However, a too high scanning speed has resulted in a too short heating time which produced low adhesion between the coating and the substrate.

As with a laser, CSE can also be used for post treatment of coatings. CSE has also been used for cladding process. A study has been carried out to use CSE for cladding of stainless steel on a steel substrate [66]. Cladding is carried out by melting the powder coating raw material and applying it on the substrate. The important parameter in the cladding process is to control the dilution of the coating in the substrate as finely as possible. The control of the scanning speed and flux density is necessary to avoid vaporization of the reactant and overheating on the substrate. Determining the optimum value of these processing parameters is required to produce low dilution.

2.2.3.4. Combined SHS with microwave

In recent years, microwaves have been effectively used to assist the ignition of combustion synthesis. Microwaves are oscillating electromagnetic field having a frequency in the range of 300 MHz to 300 GHz, but the effective range for dielectric heating lies between 0.915 and 2.45 GHz [67]. Microwaves are produced by microwave source called an applicator. The most commonly used microwave source is a magnetron. When microwaves interact with matter, power density is generated in the material depending on the frequency of the incident microwave, the dielectric and magnetic properties of the material, including its electrical conductivity losses. The electromagnetic field energy from the microwaves is converted into heat in the material which occurs in a very thin layer. The thickness of the layer being heated is described by the skin depth [68].

The advantage of using microwaves for heating process is their capability to synthesize material in a shorter time compared to a conventional electric furnace, due to the heat from the microwave source being generated internally within the synthesized material [69]. Other advantages of microwave heating over conventional systems are that the equipment is compact and the use of

microwaves produces a clean environment at the point of use [67]. However, there is limitation of using microwave to ignite combustion synthesis which lies in its non-uniform heating and inherently low reproducibility due to the dependence of temperature distribution on the dielectric and magnetic properties of the material during heating [70]. During microwave heating, the load properties such as the dielectric properties, magnetic permittivity, and electrical conductivity of the material are rapidly changed as a consequence of temperature variation. The change in load properties affects the electromagnetic distribution in the material which in turn influences the heat generation pattern, and finally changes the temperature distribution [68]. Owing to the dependence of microwave on the dielectric and magnetic properties of the material, the microwave heating can be expressed as a selective, volumetric, and localized heating process [67].

The microwave heating technique has been applied to activate the combustion synthesis of several materials such as intermetallic Al–Cr [71], Ti–Al [72], and Al–TiO_2–H_3BO_3 system [69]. Microwave was also used to ignite the SHS reaction combined with coating deposition in the synthesis of NiAl powder which was subsequently applied as a coating on the Ti substrate in one step [11][12]. Due to the heat generated by microwave, the powder reactant underwent SHS reaction and produced highly exothermic energy to form the liquid phase of NiAl. The energy supplied by microwave was also used to maintain and prolong the existence of the liquid phase allowing the liquid phase to react with the underlying Ti substrate to form an interface layer of Ni–Al–Ti system. The presence of the interface Ni–Al–Ti layer has been claimed to become a supplementary layer which increased adhesion strength.

2.2.3.5. Combined SHS with induction furnace

Induction heating has been applied to produce required the heat generation and successfully used to initiate the SHS process [19][18][17]. The induction heating process is fast, efficient, and environmentally friendly compared to other conventional heating processes. Induction heating equipment is basically composed by two components, a high frequency generator used as the power supply and an

induction coil as the inductor. The power supply sends an alternating electric current through an induction coil to produce an electromagnetic field. When the part to be heated is placed inside the coil, circulating eddy currents are induced inside the part. These currents are short-circuited and generate precisely localized heat, depending on the operating frequency, electrical conductivity and magnetic permeability of the material. Due to the magnetic effect, however, there is a hysteresis loss as a result of the molecular vibration in the frequency of the electromagnetic field. The heat penetration in the heated part depends on the penetration depth of magnetic field which is influenced by the frequency of power supply. A low frequency of the power supply leads to a high penetration depth while a high frequency of the power supply produces a low penetration depth [73].

The principle of induction heating has been applied in an induction furnace to initiate the SHS reaction combined with the fabrication of coating by H.Y. Lee et al. to produce NiAl coating [74][75]. The mixtures of Ni and Al powders have been reacted by using varied heating rates in order to obtain the intermetallic compound coating layer of NiAl on a substrate of ductile cast iron. This investigation has been carried out to explore the effect of heating rate on the combustion behaviour, temperature, product microstructure and properties of the synthesized product NiAl. Different heating rates were controlled by changing the applied current and voltage of induction. The result of studies has shown that heating rate has significantly influenced the combustion behaviour. It was indicated that increasing the heating rate can increase the ignition temperature and the maximum temperature of the combustion process. It has also been identified that increasing the heating rate can reduce the required time to achieve the ignition temperature of combustion reaction, called the ignition time. This means that increasing the heating rate results in a faster process to achieve the ignition temperature of combustion. This result is in line with that observed in other investigations [17][18][19]. To the contrary, a reduction in heating rate would lengthen the synthesis process. By conducting experiments it has been found that if the heating rate is too low, the synthesis reaction could not occur. There is critical value of heating rate below which the combustion synthesis cannot start [17][18][19][75]. A

low heating rate means that the heat supplied by the external heat source is too low or might be insufficient to provide the required energy for ignition due to the heat losses in the substrate and environment.

The effect of heating rate on the microstructure of products has also been studied. Since there is a minimum heating rate to guarantee that combustion synthesis can be initiated, then there is a critical value of heating rate above which the combustion can be completed to produce synthesized product. It also means that heating rate influences the completion of the reaction. An example was given in the study carried out by H.Y. Lee et al. [75]. It has been shown in their studies that in the synthesis reaction of Ni and Al, a medium heating rate has proven to produce multi phase structure of the product composed by Ni_2Al_3, Ni_3Al and NiAl respectively rather than an individual product. Only at a higher heating rate can the reaction produce single product of NiAl. Increasing the heating rate has been shown to affect the microstructure of the synthesized product creating a single phase corresponding to the initial reactant which is composed of mixed powders.

H.Y. Lee et al. [75] have also studied the dependency of product properties on the heating rate. The effect of heating rate on the hardness of product has shown that variation of the heating rate has produced varied hardness. However, it was difficult to draw a general trend from the study of the effect of heating rate on the hardness of the synthesized product. Supporting result obtained from other investigations might be necessary to describe the effect of heating rate on product properties. Recently, Zhu et al. [17] have shown the tendency of increasing the heating rate could increase the hardness of synthesized product. In their experiments, the variation of heating rate was carried out by changing the current of the power supply, while the reactant was obtained from elemental powders of Ni and Al. When the current was increased from 200 to 300 A, the hardness of NiAl was increased from 297 to 331 HV. The authors found that the increase of hardness was attributed to the reduction of grain size as the heating rate was increased. This can be explained by the fact that the higher supply current increases the heating rate and supports the fast completion of combustion synthesis. Faster completion of the combustion synthesis can inhibit the grain growth.

2.2.3.6. Combined SHS with thermal spraying

Thermal spraying techniques have also been combined with the SHS technique to produce coatings. Several thermal spraying techniques have been used to produced coating from SHS product such as flame spraying [76], atmospheric plasma spraying (APS) [77], high velocity oxygen fuel (HVOF) spraying [78][79], cold spraying [80], arch spraying (AS) [81], and vacuum plasma spraying [56]. Basically, the thermal spraying technique consists of two steps. The first step is to synthesize the SHS product from the powder mixture through SHS reaction which is then followed by crushing and sieving of the SHS product to obtain fine powders as feedstock for coating. The second step is to deposit the powders produced by SHS onto a substrate using thermal spraying. During spraying, the powder will melt and accelerate towards the substrate surface to produce a coating.

Plasma spraying has been studied to fabricate a ceramic metal composite of TiC–Fe [76]. There were different approaches to spray this system. The first approach was by spraying the ceramic and metal powder directly. TiC particles produced by SHS were directly added into a metallic binder of Fe and sprayed onto the substrate followed by sintering. Since the TiC particle is produced prior to the spraying or referred to as an *ex situ* process, the particles of TiC were often polluted. As a result, the interface between reinforcing phase TiC and matrix Fe was not clean which then became the source of a weak point in the adhesion. The hard phase TiC in the cermet coating produced by this method is also relatively large (more than 1 μm) and unevenly distributed which might affect the hardness of the cermet coating. Since TiC is already formed by SHS before spraying, the spraying process requires strict spraying conditions such as high temperature and high velocity to ensure that the TiC can be embedded in the melted matrix phase and deposited on the substrate. Another approach was undertaken by simultaneous synthesis and deposition in one step by plasma spraying, which is known as reactive plasma spraying (RPS) [82]. In this approach, spraying was carried out to the granular powder composed by Fe–Ti–C. The formation of TiC occurs during the spraying process or called an *in situ* process. Since TiC is formed during the spraying

process, TiC has a clean interfacial structure with the matrix Fe, which results in a stronger bond strength.

TiC/Fe cermet coating produced by combined in situ SHS synthesis and plasma deposition seems to give good bond strength. However, there are limitations on the homogeneity of the product which is affected by the reactivity of the powders. When the granular powders are prepared by mechanical blending, the formation of the cermet coating is often inhomogeneous. This is due to the agglomeration of the granular powders and the loss of carbon during spraying. As a result, some unreacted materials are still left in the product. In order to produce a homogenous product, it is therefore necessary to use reactive materials in the spraying. A study was carried out to produce TiC/Fe coating by plasma spraying Fe–Ti–C powder obtained from carbonization of sucrose [82]. In this method, reactive elemental powder Fe–Ti–C was prepared by heating a mixture of ferrotitanium and carbon which was obtained through the carbonization of sucrose. It was shown that the carbonization of sucrose could be easily completed in low temperature without impurity. It was also reported that carbon produced by the carbonization process is a reactive constituent as well as binder for the ferrotitanium which results in a tight structure of the compound powder. The tight structure during spraying is very important to avoid the separation of reactive elements during spraying which can result in the incomplete reaction and residual raw materials of FeTi or carbon. The ferrotitanium particles have a large interface with carbon since ferrotitanium can be easily milled into small particles, which is an advantage for the synthesis reaction between Ti and C. Having a very tight structure of FeTi and reactive carbon, the in situ synthesis using plasma spraying has produced TiC–Fe with the reinforcing phase TiC and the matrix Fe which have a clean interfacial and homogeneous structure.

2.2.3.7. Combined SHS with magnetron sputtering

Magnetron sputtering is the most widely used physical vapour deposition (PVD) coating technique as it can be used to coat any material. Sputtering is basically the removal of the atomized material layer by the bombardment of ion or

neutral particles. Sputtered atoms ejected from the target are emitted in the gas phase and deposited on the surface of the substrate in a vacuum chamber. The mechanism of coating deposition using magnetron sputtering is accomplished atom by atom on the surface of the substrate by condensation from the vapour to solid phase [83].

The application of magnetron sputtering combined with SHS has been found in the fabrication of Ti–B–C–N coating deposited from a TiB_2–TiC composite target [84][85]. In this case, the SHS process is only used to produce the composite material of TiB_2-TiC without taking part in the coating deposition. The synthesized material then becomes the raw material, called the target for sputtering, to form the coating layer on the AISI 304 stainless steel substrate after condensation. The sputtering process was carried out in varied argon–nitrogen atmospheres with a total gas pressure of 0.4 Pa, using a RF power density of 11.2 W/cm^2 and a substrate bias of –50 V. Before the deposition of the coating on the substrate bias, the PVD chamber was back-filled with argon gas with specified pressure while the substrate was also set to a defined voltage in order to produce a glow discharge sputter etching. It was reported that a bias applied to the substrate has significant effect on improving the coating property. The results showed that applying a substrate bias of –50 V can significantly improve the performance of the coating. The structure of the coating layer deposited without substrate bias was completely amorphous, while the coating layer deposited with substrate bias of –50 V changed the coating layer from amorphous to very fine crystallites embedded in a quasi-amorphous matrix. As a result, the mechanical properties of the coating are significantly improved. The nanohardness and Young's modulus of the coating deposited with substrate bias of –50 V were higher than that deposited without substrate bias. For instance, when using 20 % of N_2 as the sputtering atmosphere, the nanohardness of coating deposited with –50 V bias was 20 GPa, and without bias it was 16.5 GPa. Meanwhile, the Young's modulus of coating deposited with –50 V bias was 225 GPa, and without bias it was 200 GPa. The adhesion strength and wear resistance of the coating have also been improved by applying a substrate bias. It was reported that the improvement of coating properties using substrate

bias is due to the fact that the bias voltage is able to control the particle energy during deposition. The bias voltage contributes significantly to the acceleration of plasma ions across the plasma sheath and particle bombardment to the substrate which then controls the incident particle energy. The defect, grain growth and crystalline structure of the coating are influenced significantly by the incident particle energy, which in turn, determines the intrinsic stress and the properties of the coating layer [84].

2.2.3.8. SHS and centrifugal casting technology

Self-propagating high-temperature synthesis (SHS) and centrifugal casting technology has been studied to produce ceramic-lined compound copper pipe (CLCCP) [58]. This application was based on the thermite reaction as expressed in equation (2. 2):

$$3CuO + 2Al = Al_2O_3 + 3Cu + 1194.4\ kJ/mol \qquad (2.\ 2)$$

The process is started by mixing the reactant powders and then enclosing the mixture inside the inner surface of the copper pipe. The pipe is then rotated at a controlled speed. Under rotation, centrifugal force acts on the mixture obtains causing outward pressure to form a layer in the inner pipe. The combustion reaction of the samples is initiated using an oxygen-acetylene flame when the specific speed is reached. The SHS reaction as shown in Eq. (2.2) releases high heat energy which may melt the inner surface of the pipe. The molten pipe will form a composite with the reactant. Under the effect of centrifugal force, the molten phases will be separated according to their densities to form multilayers. Since the density of Al_2O_3 is smaller than that of Cu, the ceramic layer will be formed inward while the copper is positioned intermediately between the ceramic and the pipe. The study has shown that the ceramic layer of CLCCP has high hardness, good wear and corrosion resistance, and thermal shock resistance. However, the ceramic coating is still porous. The study has shown that the addition of SiO_2 and CrO_3 can significantly decrease the porosity of the ceramics and improve the coating density.

2.2.4. Post treatment

In some cases, there might be a requirement to modify the performance of coatings, for instance, to produce a tailored surface property without a substantial change in material composition, or to obtain a homogeneous composition. This could be done by post treatment. Research work has been carried out to post treat coatings produced by SHS reaction using remelting and annealing.

2.2.4.1. Remelting

Post treatment might be done by remelting the top layer of the coating surface, followed by rapid cooling. Remelting post treatment can be used to obtain a fine-scale solidified structure on the top surface of the coating. However, it should be mentioned, that in remelting there is a risk of generating a macroscopic crack caused by the mismatch of thermal stresses. This crack might develop to reduce oxidation and corrosion resistance and might produce spallation.

An investigation has been carried out using a laser to post treat Al_2O_3–TiB_2–TiN coating [63]. The reactant powders of Al, TiO_2 and hBN were heated and alloyed on the substrate by laser beam to ignite the SHS reaction and produce the coating in one step. Following this process, post treatment was applied on the coating. A comparison between the original coating and the post treated coating has been reported in Ref. [63]. The results show that there is a very thin layer near the top surface which has been remelted due to the post treatment. The top surface layer exhibited smoother roughness with smaller void. Microstructure observation has also reported that the microstructure of the top layer is dominated by a columnar structure. Evaluation of the micro hardness of the top layer has shown that there is an improvement in this layer, due to the reduction of pore size and the microstructural refinement. As a result, the wear resistance of the post treated coating has been significantly increased.

2.2.4.2. Annealing

Another post treatment for the coating formed by SHS has also been investigated on the Ni–Al–Ti coating fabricated by microwave heating and followed

by annealing [11][12]. High exothermic energy allowed the NiAl formed by SHS reaction to react with Ti substrate at the interface to form an intermediate layer of Ni–Al–Ti. The increase of the thickness of the intermediate layer results in an increase of the bond strength of the coating to the substrate since it is able to reduce the thermal stress in the coating. It is widely accepted that high thermal stress at the interface leads to a reduction of bond strength. The average thickness of the intermediate layer produced by microwave heating before annealing is about 50 μm as shown in Fig. 2.2. Annealing post-treatment applied to the coated substrate was to increase the thickness of underlayer. A thicker intermediate layer is expected to promote stronger chemical bonding and increasing the adhesion strength. Annealing by microwave heating was carried out by extending the heating process for 5–20 minutes after SHS reaction at 950 °C, which is higher than the ternary eutectic temperature of NiAl. During annealing, there is further reaction between NiAl and Ti at the intermediate ternary layer. This annealing process has resulted in an increase of the thickness of intermediate layer by 200 μm after 5 minutes, reaching more than 400 μm after 20 minutes.

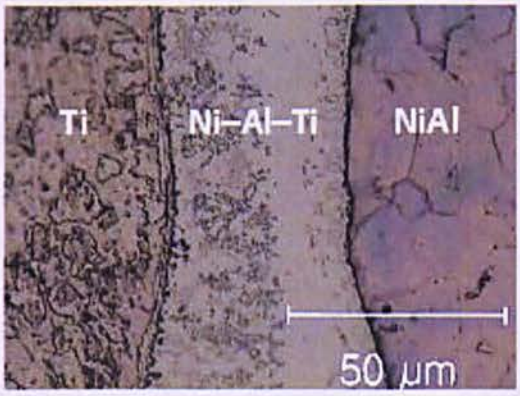

Fig. 2.2. Intermediate layer Ni–Al–Ti between NiAl coating and Ti substrate [11]

2.2.4.3. Densification

SHS reaction has many advantages such as high purity and better homogenization of products, but in most cases the SHS process generates porous products. The application of porous product to the oxidation resistant coating cannot be tolerated since it can permit the infiltration of gas from outside to the

base metal to create an oxidation reaction. The porosity of SHS product has been categorized into two sources: intrinsic and extrinsic [14]. Intrinsic porosity can be in the form of volume shrinkage caused by highly exothermic reaction. Meanwhile, extrinsic porosity can exist in the form of a void formed from entrapped gas during the reaction.

Techniques to produce denser/pores free products have been investigated. Most of the techniques investigated were to combine the combustion synthesis with densification which included: pressureless sintering, hot pressing, shock wave consolidation, hot isostatic pressing and hot rolling. The use of pressure, particularly at the onset of liquid phase formation, has shown to be practical and effective to reduce the porosity of the synthesized product [86]. Qian Dong et al. [47] prepared a nano-composite of Al_2O_3–TiC–ZrO_2 by combustion synthesis followed by hot pressing for densification. The study was carried out using varied content of ZrO_2 addition ranging from 0 to 20 wt. %. Reaction synthesis was prepared using TiO_2–Al–C–ZrO_2 reactant powders and followed by sintering with hot pressing. The result indicated that an optimum amount of ZrO_2 addition was found using 10 wt. % ZrO_2. The density of composite product was successfully improved by more than 94% due to the improved distribution of different phases in the product. Unfortunately, these high temperature densification techniques were too expensive or difficult to be accepted for general applications [87].

With the in situ SHS process, the density of composite product can be improved by generating an excess of liquid metal in the combustion product to infiltrate into the pores in the ceramic matrix product. The in situ reinforcement has many advantages since it is thermodynamically stable in the matrix, produces a clean interface which results in a stronger bonding interface, and forms finer and uniformly distributed particles in the matrix which, in turn, produces better mechanical properties [88]. Azadmehr [89] combined the combustion synthesis with the liquid phase sintering to fabricate TiC–Ni and TiC–WC–Ni composites in a single processing operation. The reactant powders were Ti–W–C, while Ni was used as binder. In the first SHS reaction, the microstructure of the synthesized Ti–C–Ni product was porous and had low strength. The reaction mechanism of the TiC–Ni

formation was achieved through precipitation. The explanation of this mechanism was drawn from the phase diagram of Ti–Ni. When the combustion temperature reaches the eutectic temperature of Ti–Ni, 942°C, TiNi is melted. Carbon particle dissolves into the molten TiNi to form TiC by exothermic reaction. During cooling, TiC precipitates out from the melt. Since the reaction of Ti–C releases a large amount of heat, the temperature increases. This temperature rise increases the amount of liquid and causes further dissolution of Ti and C in the liquid phase. Since TiC is porous, W was added to increase its density. The addition of W using ratio W/Ti = 2 was confirmed to produce dense and high strength product since it has reduced the combustion temperature. The formation of TiC has resulted in high combustion temperature and led to an increase of the amount of liquid. Ti and a part of W will dissolve into the molten phase to produce in situ spherical (Ti,W)C and then precipitates from the melt. A part of W which is not dissolved will form WC.

2.2.5. Bonding to substrate

2.2.5.1. General description

Bonding to substrate is one of the most important factors for the selection of coating material and process. The performance of bonding is often stated in the form of adhesion strength, which illustrates the adherence that occurs at the interface between coating and the substrate. During application, the coating receives an external load and transmits it to the substrate which builds up a stress at interface. The adhesion strength of the coating is the ability of the coating to accept the stress arising from various types of load without adhesive failure. Sufficient adhesion strength is required to assure that the coating does not detach from the substrate.

2.2.5.2. Type of adhesion in coating

The adhesion strength is greatly influenced by the mechanism of how the coating is bonded with the substrate. Generally, there are three types of the adhesion mechanism in the coating and substrate interface, namely, mechanical

interlocking, physical bonding, and chemical bonding [90]. These mechanisms individually or in combination are responsible for the adhesion strength of the coating. In the mechanical interlocking, adhesion is achieved due to the mechanical interlock between the coating and substrate interface. The adhesion strength of this type is dependent of the surface irregularities and size of locking sites such as dovetails and grooves. Grit blasting is often used to make the substrate rougher. Mechanical interlocking is a most effective means to produce strong adhesion. Increasing the adhesion strength is often carried out by increasing the surface roughness which results in the increase of surface contact area at the interface and friction between coating and the substrate. However, thermal stress can arise due to coating shrinkage at high temperature at the interface which causes the separation of the coating. In physical bonding, adhesion occurs due to physical action such as the intermolecular contact between two materials developed from the surface forces at the interface. The most common of the surface forces are the van der Waals forces. However, physical bonding is generally very weak. In chemical bonding, adhesion happens because of the existence of an interphase formed by chemical reaction at the interface. When chemical reaction occurs between the coating and the substrate atoms, the energy of reaction contribute to the diffusion process to form a new interphase. The adhesion strength is then influenced by the interphase property and the solubility of the coating and substrate materials. Because the diffusion process produces an interphase, there is no discontinuity which eliminates the stress concentration at the interface.

2.2.5.3. Factors affecting the adhesion strength

Adhesion strength between the coating and the substrate has become the most challenging issues in the fabrication of protective coatings. There are many factors which affect the adhesion strength such as the wettability of the coating material, mechanism of contact, deposition technique, properties of the interface, processing parameter, and residual stress. Wettability of coating is an important factor affecting the contact and the adhesion between the coating (liquid) and the substrate. If the contact between the liquid coating and substrate is sufficiently intimate, the liquid coating can conform to the surface of substrate due to physical

attraction from the molecular forces. The surface condition of the substrate is also required to be clean and free of contaminant which can interfere with the wetting and spreading of the coating [91].

Of the factors affecting the adhesion strength, the residual stress at the interface between the coating and the substrate often becomes one of the problems which lead to an adhesion failure. This failure problem might come from the mismatch of the thermal expansion coefficient of the coating and the substrate material. It is widely known that high residual stress built in the coating during deposition can result in the detachment of the coating from the substrate. The detachment of the coating then limits the practical application of the coating [92]. The relatively low adhesion strength is the weakness for the coatings fabricated by SHS reaction. The highly exothermic reaction produced by the SHS process leads to the thermal shock caused by the mismatch of thermal expansion coefficient between coating and the substrate. The thermal shock then results in the detachment of coating layer from the substrate.

2.2.5.4. General improvement for adhesion strength

There are a variety of methods which have been extensively used to improve the adhesion between the coating and substrate such as using ion plating prior to the deposition [93], inserting a metal underlayer [94][95], and using multilayer or compositional gradient coatings [92]. The concept of functional gradient material has been applied in thermal barrier coating (TBCs) systems which typically suffered from adhesion failure due to the high residual stress between the metallic bondcoat and the ceramic topcoat [96]. Functional graded material is applied by using underlayer material with continuously changing properties due to the stepwise change in composition from metal to ceramic materials. The objective of using a gradient composition of underlayer was to reduce or redistribute the residual stress within the coating to improve the adhesion.

2.2.5.5. Adhesion Improvement in SHS process

In order to study the adhesion improvement of coatings produced by the SHS process, it is essential to understand the formation of a coating and especially the bonding mechanism at the interface between the coating and substrate [7]. Heat release produced by the exothermic reaction of SHS reaction increases the temperature of the substrate. The increase of temperature may lead to the melting of the substrate at the interface. The melting of coating and substrate surface will then facilitate the diffusion between substrate and coating. Diffusion occurs as a result of concentration difference. This diffusion increases the adhesion of the coating to the base steel substrate. Diffusion continues until the coating solidifies when there is no more energy to melt the substrate surface. Bonding at the interface between the coating and substrate can occur metallurgically.

The diffusion of substrate atoms into the coating forms an interface which is different from the bulk coating and the substrate. The formation of the interface region changes the composition of the coating and substrate. The extent of atomic diffusion determines the thickness of the interface phase. The thickness of the interface phase depends on the time for the composite system to maintain a liquid state. Finally, the time of coating in the liquid state is directly determined by the exothermic energy of the reactants in the combustion process. A study has shown that increasing the amount of powder mixture can produce more heat by the SHS reaction and therefore can create longer heating between the coating and the steel surface [55]. Since the strength of bonding is strongly influenced by the existence of the interphase, many research studies focused on creating an interfacial phase by providing more energy at the interface.

Providing extended energy via the use of microwave for the fabrication of NiAl coating on a titanium substrate has been studied [11]. After the SHS reaction of NiAl, the heat is held for some time to permit the formation of the interphase layer Ni–Al–Ti. With the heat energy supplied to the reacting system during and after SHS ignition, it extends the time that liquid exists at the interface. This method

has improved the adhesion by promoting the formation of a strong metallurgical bonding.

Another method to increase the bond strength was to increase the heat release by second reaction. A study to improve bond strength between a Ni_3Al–TiC coating and steel substrate was carried out by M.X. Wei et al. [97] using the thermal explosion process. The reactant composed of Ti–C–3Ni–Al powders was placed in the bottom of a sand mould. Ignition was initiated using steel melt poured into the mould. Since the temperature of steel melt can reach about 1823 K, which is higher than the ignition temperature of 3Ni/Al system (about 913 K) and Ti/C system (about 1373 K), it is therefore sufficient to simultaneously ignite two synthesis reactions for Ni_3Al and TiC. When the steel melt was poured into the mould, however, its temperature was significantly decreased due to the heat loss to the environment. Ignition therefore could only be initially performed to the 3Ni/Al system which has a lower ignition temperature. Subsequently, the heat produced by Ni_3Al reaction was used to ignite the reaction of Ti/C system. The study on adhesion strength was performed using varied percentage of TiC. It was found that the heat release produced by the second reaction of TiC formation can maintain the molten phase of Ni_3Al for a longer period, which will be able to lengthen the diffusion at the interface. A higher portion of TiC on the Ni_3Al system increased the released heat which then improved the adhesion at the interface.

Multilayer-lined composite pipes composed of Al_2O_3 and TiC were prepared by a SHS centrifugal-thermite process [98]. Under the influence of centrifugal force, the ceramic phase was metallurgically joined with an intermediate layer, situated between the base metal and the ceramic layer. Meanwhile, the use of a supplementary layer was also tried in a SHS–diffusion brazing process. In SHS–diffusion brazing, the heat generated by the SHS reaction is used to melt an underlayer material so that the substrate and the filler are bonded. An example of the application of SHS reaction on diffusion brazing has been studied by C. Pascal et al. [1] who used this method to repair a gas turbine component. The key point of this investigation was that the joining of NiAl layer and a substrate of nickel based superalloys was done by the addition of filler consisting of a small amount of

yttrium to form MCrAlY. Another method used to improve the bond strength was done by adding a fluxing agent from a low melting compound to assist in the joining. Sodium tetra borate ($Na_2B_4O_7$) was added at the interface between the substrate and coating for a ceramic-lined compound copper pipe. The coating was formed by the reaction of CuO and Al powders [58]. At high temperature this compound decomposes into B_2O_3 which reduces the surface tension of the reaction product (Al_2O_3 and Cu). This condition will then improve the wettability resulting in an increase of the bond strength.

2.3. Processing parameters in SHS process

Processing parameters affect the ignition, heat propagation of the SHS process and the property of the synthesized product. Merzhanov [52] has pointed out that in the combustion process that synthesizes materials, the properties of SHS product are strongly dependent on the structure of powder mixture, grain size and density of the green mixture. The grain size and density of reactant also affect the efficiency and completeness of the SHS reaction. Mossino [99] has reported the effects of reaction parameters which affects the SHS process and product properties such as particle size, green density, gas evolution, reactant composition, and heating method for ignition.

A numerical study has reported that the processing parameters can be used to control the ignition of the SHS process [100]. The capability to reach the ignition temperature at a certain time could be affected by the factor which comes from the sample properties (grain size, thermal conductivity, green density) and from external heating sources that influence the heating rate. Meanwhile the reactant compositions also have a significant effect on the ignition of SHS reaction.

2.3.1. Grain size

The grain size has significant effect on the combustion behaviour of the SHS process and product properties since it affects the surface contact area of the reactant. Small grain was claimed to increase the heating rate to achieve ignition temperature. In the reaction synthesis with small grain size, the transition of solid

metal into the molten phase proceeds faster due to the large interface area of the reactants which accelerates the reaction from ignition until completion. An increase in the dissolution process of the solid metal into the molten phase will produce more heat release which subsequently increases the temperature of reaction. An explanation of this phenomenon has been modeled by Gennari et al. [100] who studied the modeling of combustion synthesis of Ni–Al, Co–Al, and TiAl. With smaller particle size, the combustion temperature increases sharply to reach ignition level. Smaller particle size of the Ni, Co, and Ti causes an increase of the number of Ni particles that dissolve into liquid Al after reaching the melting point of Al. The heat produced in every step in the ignition process becomes higher which then accelerates the ignition process.

A study carried out by Ya Feng Yang et al. [101] investigated the effect of C particle size on the ignition time of the SHS reaction of 20 wt% Ni–Ti–C system. The study concluded that the decrease of C particle size has resulted in the increase of the propagation of wave velocity, and the time for ignition becomes shorter. A more detailed study presented by M. Adeli et al. [102] indicated the influence of titanium particle size on combustion synthesis of Ti – 50 at.% Al, having relative density 65% as shown in Table 2.4. A finer particle size of titanium produced a higher propagation of combustion wave velocity due to better interfacial contact between solid titanium which dissolves into molten aluminium. An increase in the wave velocity will accelerate the time to achieve its ignition temperature. It might be thought that the small grain size will give large surface contact area to facilitate combustion reaction and heat transfer between reactant particles.

Table 2.4. The effect of particle size on the SHS process parameters [102]

Titanium particle size (μm)	Combustion temperature (K)	Mean wave velocity (mm/s)	Ignition time (s)
<10	1473	6.06	27
<45	1560.6	1.88	60
90 – 150	1486.35	0.597	90

The relationship between the particle size and wave velocity in the SHS reaction was described by J.J. Moore [49] in Fig. 2.3. The curves illustrate the profile of wave velocity for three different particle sizes of carbon during the formation of TiC. Fig. 2.3 shows that each curve has three regions: region I called the kinetic region where the diffusion mode is dominant and the wave velocity is independent of the particle size, region II called the transition region where wave velocity decreases dramatically with the increase of particle size, and region III called the capillary region where the wave velocity is relatively independent with particle size.

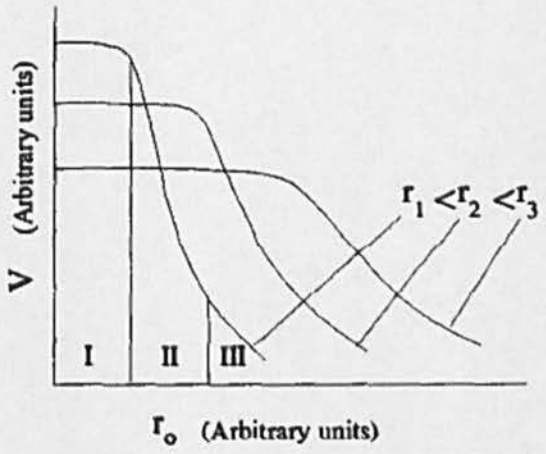

Fig. 2.3. The effect of particle size (r_o) on wave velocity (V) [49]

From Fig. 2.3, it can be observed that the particle size of reactant affects the combustion mode which is through the diffusion or capillary mode [49]. The particle size takes control of the combustion process either through diffusion between the reactant particles or by the rate of capillary spreading during the molten phase. For instance, in the case of the reaction between Ti and C to form TiC, observation has shown that the SHS reaction was initiated by the melting of Ti. The molten phase then spreads to the C particles. The velocity of spreading determines the mode of combustion until completion. Both of these schemes depend significantly on the size of the carbon particle. When the carbon particle size is small, the combustion process is carried out through the diffusion process in which the carbon particles diffuse into the molten liquid of Ti to form TiC.

Recent investigation carried out by Binglin et al. [103] has also shown that in the synthesis reactions of Al–Ti–B_4C and Al–TiO_2–B_4C systems, the reaction behaviour depends on the particle size of B_4C. Increasing the particle size of B_4C resulted in a difficulty to ignite the combustion reaction and to continue the wave propagation. The reason for this has been linked to the inverse relationship between wave velocity (v) and radius (r) of solid reactant particle as formulated by Mossino [99] as follows:

$$v^2 = \frac{k}{Q\rho}\frac{RT_c^2}{E}\frac{K_o \exp(-E/RT_c)}{f(\eta)}A \qquad (2.3)$$

with

$$A = \frac{3C}{a\rho r} \qquad (2.4)$$

for surface-reaction-controlled kinetics, and

$$A = \frac{3C}{a\rho r^2} \qquad (2.5)$$

for diffusion-controlled kinetics. Where k is the thermal conductivity, ρ is the density of compacted reactant, Q is the heat of reaction, R is the gas constant, T_c is combustion temperature, E is the activation energy, K_o is a constant, $f(\eta)$ is kinetic function, C is the initial mass fraction of the reactant in the mixture, and a is the stoichiometric ratio.

Particle size can also affect the green density. Smaller particles increase density and reduce porosity. Feng Yang et al. [101] investigated the effect of carbon particle size on the porous formation of TiC particulate using the SHS reaction of Ni–Ti–C system for casting. It was found that the increase of C particle size significantly increased the porosities of the composites. Particle size of C was also confirmed to affect the properties of the product. It was observed that the hardness and wear resistance of the composites increased as C particle size decreased.

2.3.2. Thermal conductivity

Thermal conductivity is an important parameter affecting the ignition and propagation of the SHS process. Thermal conductivity is a physical property of the sample which controls the transfer of energy and the heating process. Thermal conductivity of a mixture describes the ability of the sample to conduct heat between the particles. However, the effect of thermal conductivity on the SHS process is considered to be inherently complicated due to the difficulty to control thermal conductivity of a sample in a real experiment [100]. It was reported that thermal conductivity of a sample changed during reaction synthesis due to many factors such as the formation of low thermal conductivity during intermediate phases [104]. Z. Huque and G.M.S. Azad [105] described that thermal conductivity was dependent on the initial density of the compacted pellet, mixture ratio, and particle size of the reactant components. Meanwhile, Silvia Gennari et al. [100] suggested that porosity is a more dominant parameter to control the thermal conductivity of a sample. The thermal conductivity of a sample increased as porosity decreased. However, variation of porosity became more complex since it also changed the transferred energy from the synthesis reaction. It was reported that thermal conductivities affected the required energy supplied for the ignition process. This effect has been demonstrated with computer simulation. The effect of effective thermal conductivity (k/k_{bulk}) and porosity of Ni–Al compacted mixture on the ignition energy (E_{ig}) are shown in Fig. 2.4(a) and (b). In Fig. 2.4(a), the thermal conductivity from a fully dense sample (starting from right to left of the graph) is initially reduced and followed by a sharp increase after reaching a minimum value. This indicates that with the reduction of thermal conductivity, the sample required less energy to achieve its ignition until achieving a minimum value of ignition energy. However, approaching zero thermal conductivity results in a large energy required for ignition. This may explain that at high thermal conductivity, some portions of heat supplied for ignition from an external source was lost to the cold particles which resulted in the need significant energy for ignition. The reduction of thermal conductivity then decreased the heat lost, and consequently, decreased the required energy for ignition. However, when thermal conductivity was too low,

the heat transferred from the supplied energy to the sample was insufficient to ignite the reactant constituents which then required high energy for ignition. Fig. 2.4(b) shows the effect of porosity on the ignition energy which produces a fairly similar trend to that seen in Fig. 2.4(a). Increasing porosity initially resulted in the decrease of ignition energy. Further increase of porosity led to an increase in the energy required for ignition. This may be due to the fact that the heat supplied from the external source for ignition could not be transferred directly to the porous pellet since there was no contact amongst the particles in the pellet due to their inability to hold together [105].

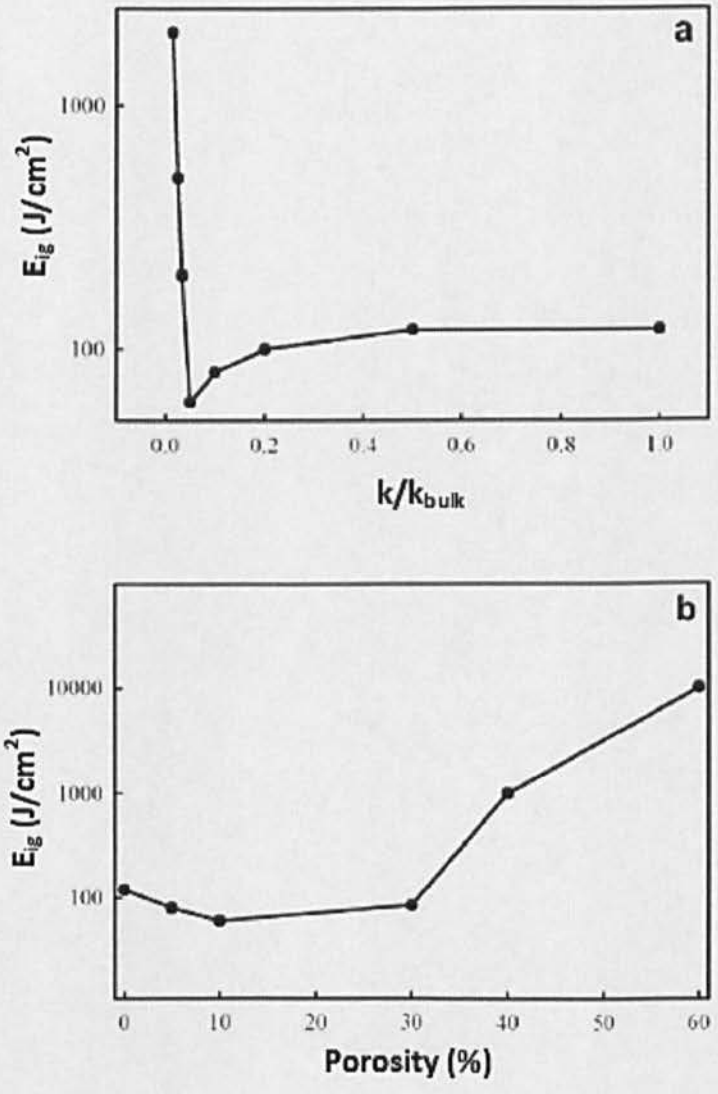

Fig. 2.4. Ignition energy for the SHS of NiAl as a function of (a) effective thermal conductivity; and (b) sample porosity [100]

Thermal conductivity also affects the velocity of wave propagation of the SHS process. Since there is no literature explaining the direct relationship between thermal conductivity and combustion propagation, an indirect relationship obtained from an experiment carried out to study the effect of thermal conductivity of a titanium–carbon mixture on the wave propagation of the SHS process might be useful [105]. In the studies, thermal conductivity of the mixture was varied by modifying the initial density of the mixture. It was found that increasing the density of mixture resulted in the increase of thermal conductivity as shown in Fig. 2.5. However, the results on the effects of density on propagation speed received by experiments and the one derived by theoretical study are different (Fig. 2.6). The experimental results showed that, for low density samples, increasing density of the sample increased the wave propagation at the beginning, but there was an optimum value of density to obtain highest propagation speed, above which, the propagation speed decreases with increasing density. This may be explained when density is low, the process is controlled by heat generation (reaction). High density increases the reaction speed and as a result increases the propagation speed. When the density is high the process is complex since a large amount of liquid will form and in an extreme case, gas may be generated in the sample, heat loss due to conduction will increases as well. These factors affect the propagation of the reaction front as recorded in the experimental measurements. However, these changes were not corroborated in the theoretical study as the result still showed an increase in propagation speed when density increased.

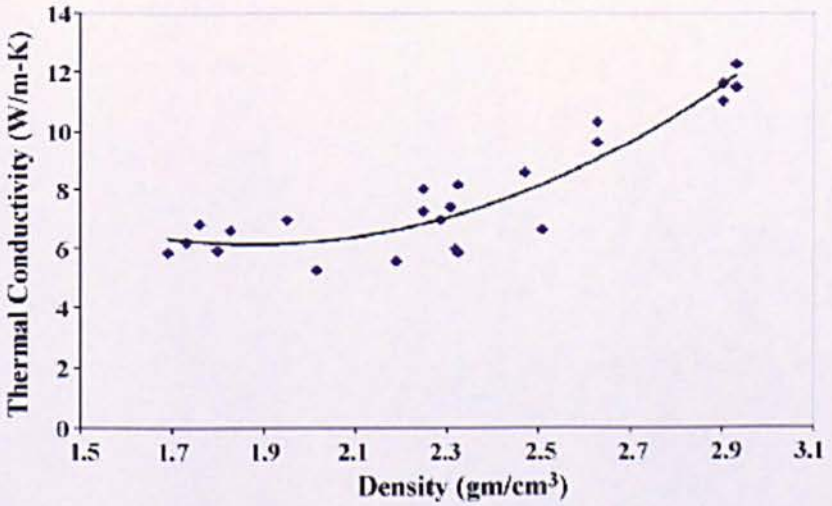

Fig. 2.5. Thermal conduction as a function of green density [105]

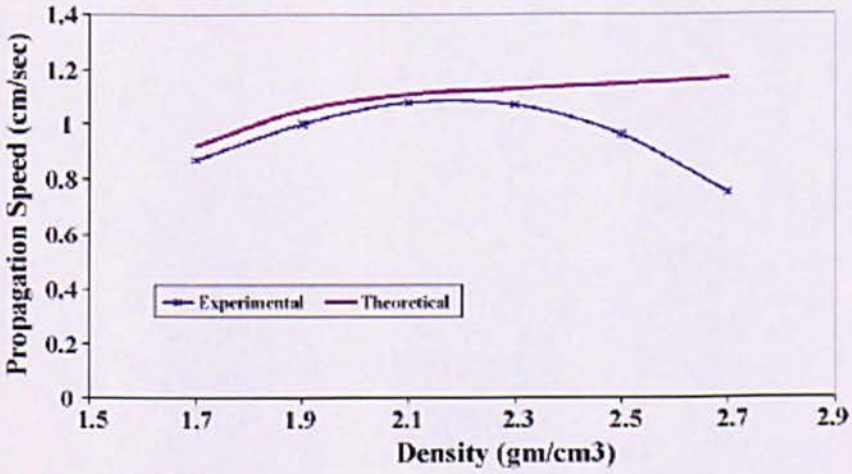

Fig. 2.6. Velocity of combustion propagation as a function of green density [105]

2.3.3. Green density

Green density has played an important role in reaction synthesis. Generally, the powder mixture needs to be compacted to achieve high density. The compaction deals with the balance between the physical contact surface amongst the reactant particles and the heat loss during the reaction [49]. High density will result in high contact surface area which increases the combustion velocity. However, high density will also increase the thermal conductivity which leads to heat loss from the reaction zone. Excessive heat loss may prevent or even stop the SHS process with the decrease of combustion temperature. The optimized green

density of these two opposing effect was reported in a value of 55–60% for the combustion synthesis of TiO_2/Al/C system [106].

An explanation of the effect of green density on the synthesis behaviour in the reaction synthesis has been recently presented by M. Adeli et al. [102] who studied the combustion synthesis of titanium aluminide. It was described that the green density of the sample mixture has a close relationship with the thermal conductivity of green compaction which then facilitates the heat transfer rate between particles. The result of the experiment is shown in Fig. 2.7. It was identified that increasing the green density resulted in the contradictive results for combustion temperature and ignition time. Within the range of 55–65%, the increase of density was shown to increase the combustion temperature and decrease the ignition time. However, further increase of density to more than 65% resulted in the decrease of combustion temperature and increased the ignition time. This finding agreed with previous literature and might be used to predict the optimum value of green density in order to obtain successful combustion synthesis as well as in the design of an efficient tool for green compaction. The best option might be with a density of 65% which produces the highest combustion temperature and shortest ignition time.

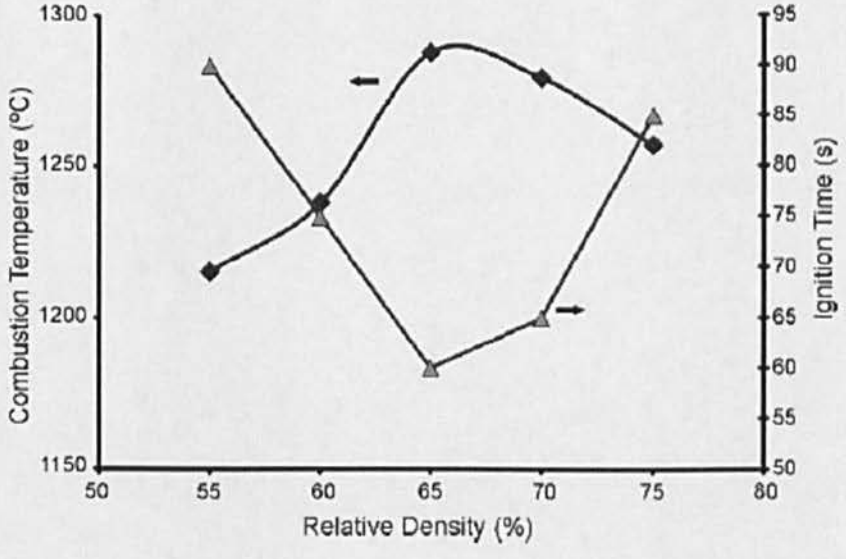

Fig. 2.7. The effect of green density on the combustion behaviour [102]

The effect of green density on the heating rate has also been observed by Zhu et al. [17]. The experimental result given in Fig. 2.8 describes the influence of green density on the heating rate during the combustion synthesis of NiAl which was ignited by induction heating. It was shown that the reduction in the green density resulted in a decrease of the heating rate. It seems that there is no vertical line which shows the ignition point of the combustion synthesis on the green density of 49.4% of the theoretical density, which indicates that the combustion did not occur. The heating energy supplied by induction heating into the green sample with too low green density might be unable to achieve the melting point of aluminium. This opinion is in agreement with the results stated by S. Gennari et al. [100] and C. Zannoti [107].

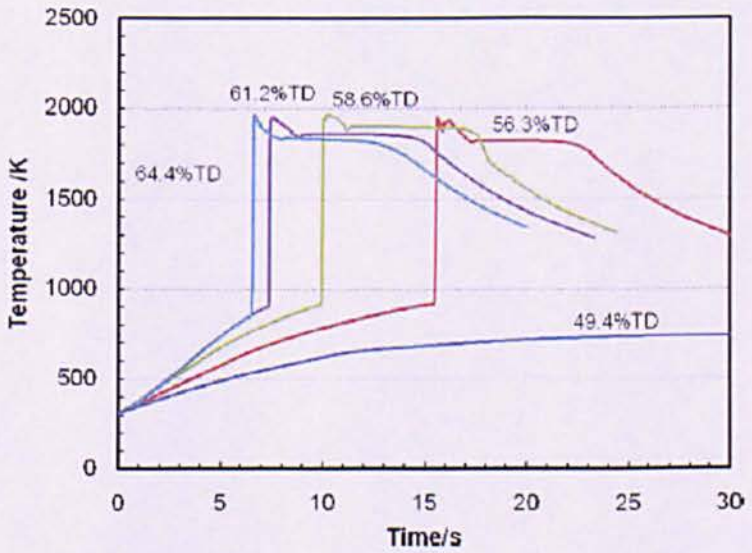

Fig. 2.8. The effect of green density on the heating rate [17]

2.3.4. Heating rate

Heating rate has become the main focus of investigation in reaction synthesis since it has been reported to significantly influence the combustion behaviour and product properties. Heating rate might be defined as the rate of the change in temperature increase of an object or material during a heating process. It can be identified when the sample of material obtains a supplied energy from an external source causing a heating process inside the material. Fig. 2.9 describes an

example of four different heating rates starting from I to IV where the heating rate gets lower [75]. In the figure, the ignition point is indicated by arrow signs. It is possible for different heating rates to occur during the combustion synthesis. This factor might be influenced by many processing parameters; which could come from the physical property of material such as thermal conductivity, green density, porosity, grain size, and from the external energy supplied into the material during the synthesis process [17][100]. The heat capacity of material may also influence the heating rate. When the heat capacity of the material is high, the heating rate will be decreased.

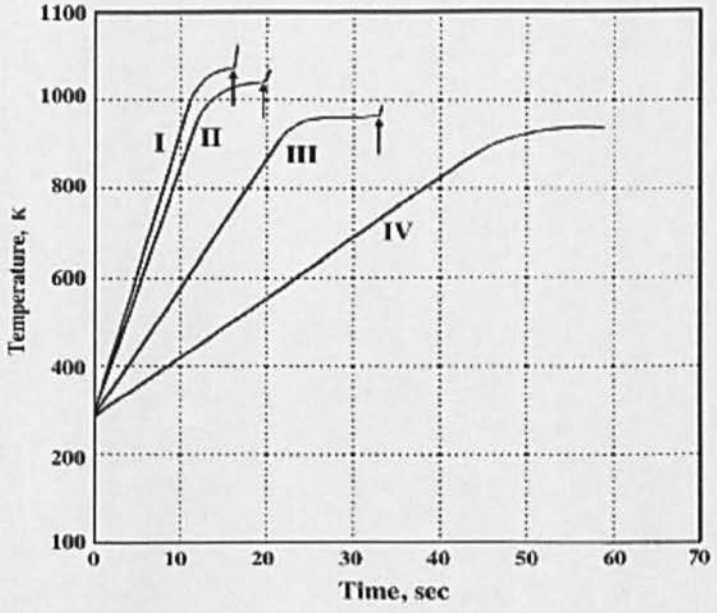

Fig. 2.9. Temperature versus time diagram showing the heating rates [75]

Some investigations have been carried out to explore the effect of heating rate on the behaviour of combustion synthesis [19][18][17][100]. Conclusively, a too low heating rate can slow down the ignition process or may result in the ignition temperature not being achieved. This might be explained by the heat supplied to the material. At a low heating rate, the rate of temperature increase of the heated object is too low due to the low energy supplied to the material which is insufficient to reach the ignition point of the combustion process. This idea is taken from the study for SHS reaction involving metal where the ignition temperature equals the melting point of the component with the lowest melting point [107]. This

means that in the synthesize reaction of NiAl the ignition temperature should be the melting point of Al. When the heating rate is too low and is unable to reach the melting temperature of Al, the combustion cannot be initiated.

2.3.5. Reactant composition

Reactant composition is an important parameter in the SHS process. The composition of reactant is normally combined in a stoichiometric ratio which assumes that the reaction proceeds to completion. The deviation of reactant composition from the stoichiometric ratio will mainly affect the exothermicity of reaction. The modification of reactant composition will also influence ignition time and heating rate [56][108][109]. The reactant composition can be modified, for example, by the addition of metal diluents. M.S. Song et al. [110] conducted a study of TiC formation obtained by self-propagating high-temperature synthesis from Ti–C elemental powders and Al as metal diluents. The result showed that the addition of Al as diluents reduced the combustion temperature. The addition of metal diluents might be needed to make the reaction less violent, or is required as binder, or to increase the density of synthesized product. However, the addition of a compound into the reactant can also increase the adiabatic temperature such as in the addition of TiC into NiAl [5]. In such case, the addition of TiC has increased the exothermic reaction since the combustion of TiC is more exothermic than NiAl. Table 2.5 presents some examples of SHS reaction which shows the effect of reactant composition on the adiabatic temperature. It can be seen that increasing the content of the metal element will reduce the adiabatic temperature.

Table 2.5. The effect of reactant compositions on the adiabatic temperature

Systems	Reactant composition	Adiabatic temperature (T_{ad})/K	[Ref.]
Cr–Ti–C	Cr < 64.7 wt. % Cr > 64.7 wt. %	> 1800 < 1800	[111]
Cu–Ti–B_4C	0 – 6.77 wt. % Cu 13.22 – 40.17 wt. % Cu Cu > 72.22 wt. %	3193 2848 < 1800	[108]
Fe–Ti–B	10 wt.% Fe 30 wt.% Fe	3193 3191	[112]

	50 wt.% Fe 70 wt.% Fe	2586 1813	
Ni–Ti–B_4C	0 – 5 wt. % Ni 5.15 – 17.5 wt. % Ni Ni > 66.4 wt. %	3193 3187 <1800	[113]

The modification of reactant composition can be used to control the SHS process especially to control the combustion temperature. For the SHS reaction with very high exothermic energy such as in the thermite reaction, the synthesis process can be explosive and difficult to control. In this case, the addition of diluents can be used to reduce the combustion temperature [60]. The addition of diluents is generally carried out by metal addition into the system. However, the metal might become involved in the reaction to produce a different product. The addition of diluents using inert material can also be used to reduce the combustion temperature. The advantage of using inert material is that it does not participate in the reaction.

2.3.6. Evolution of gas

The evolution of gas is another parameter which increases the porosity of SHS product. The gas trapped amongst the particles during combustion reaction can cause the occurrence of product imperfection such as void or pores. The occurrence of porous product has been well explained by C. Sierra and A.J. Vazquez [55] in the synthesis of NiAl to produce a coating. When the sample is produced by compression, there are some pores inside the green pellet. During combustion, NiAl melts and the pores need to rise to the surface. The NiAl at the top surface is cooling down and solidifying when the reaction front reaches the steel substrate and all the Ni and Al powders are completely reacted. The cooling rate and solidification depends on the mass of NiAl. The less the mass of NiAl, the faster the cooling rate is. When the cooling rate is too high, the air inside the NiAl system has less time to group and rise to the surface, thus creating a number of small pores inside the product.

2.3.7. Gravity

Gravity is an important parameter in the SHS process since a usual SHS process will result in a melt. Gravity is responsible for the separation between the heavier and lighter phases. Owing to the gravitational effect, the heavier phase tends to precipitates and the lighter phase will rise to the surface to form a multilayer product [114][115].

Gravity is also an important parameter in the development of the microstructure of synthesized product through settling. Gravitational force tends to cause the solid particles suspended in the liquid phase to settle which then generates phase segregation and leads to the formation of a non-uniform microstructure [116][117]. In SHS reaction, settling can take place during melting. It has been observed that during settling, particles might not form dissolution in the liquid phase. The settled medium is the particle having a lower melting point, while settled particle is the other particles that have a higher melting point.

A study was carried out to observe the effect of gravity on the settling of W, Ta, Ni, and Ti in liquid aluminium [116]. In the W–Al system, settling occurred when a portion of reacted W particles settled to the bottom of the sample under terrestrial gravity, while in zero gravity there was no evidence of settling. Fig. 2.10 shows the microstructure of the W–Al sample and the settling phenomenon which reacted at 1600 °C. In that system, settling happened during the melting of aluminium. The liquid phase is aluminium which has melting point of 660 °C, while W (melting point = 3410 °C) becomes the settled particle. The microstructural study revealed that intermetallic phase WAl_4 formed as a result of reaction between W and Al. However, there was evidence of settling of W particles. It can be seen that a part of W particles surrounded by small WAl_4 settled to the bottom of the sample to form a W–rich zone, while in the W–deficient zone, large WAl_4 has precipitated in Al matrix. This means that gravitational force has caused W particles to settle creating sedimentation and therefore an interconnected structure could not form resulting in a non-uniform microstructure.

The effect of gravity has also been linked to the porosity of product in which the pores having lighter phase tends to float to the surface while those with a heavier phase will settle to form phase segregation. An investigation carried out using zero gravity produced samples with uniformly distributed pores [115][118].

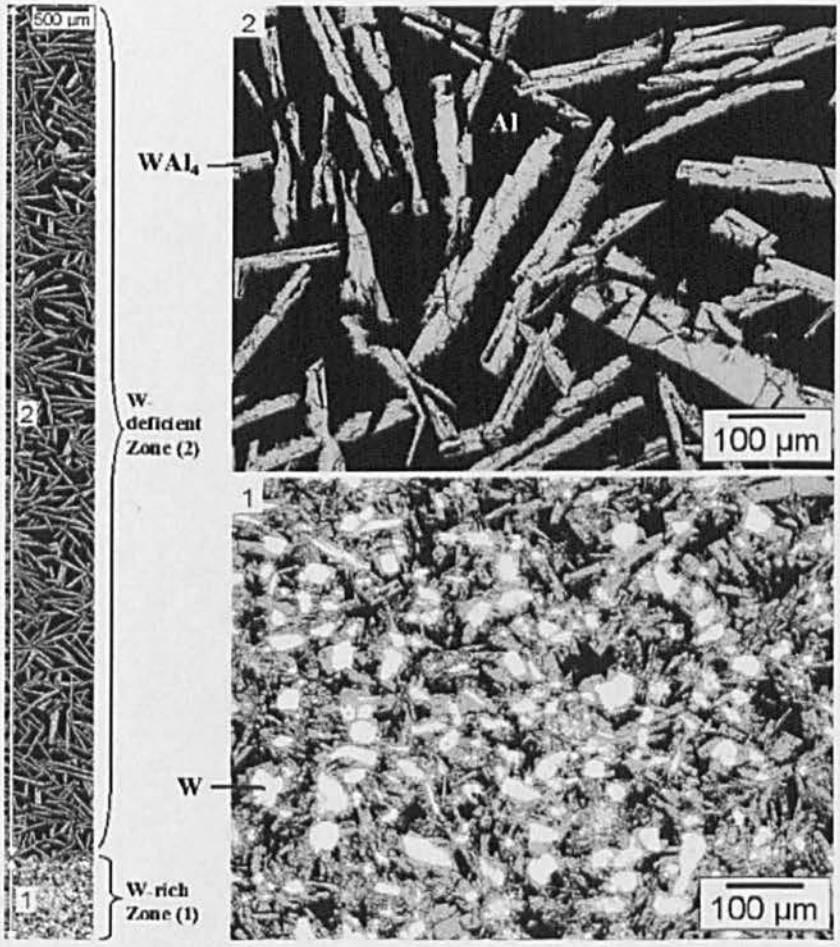

Fig. 2.10. Microstructure of W–Al system described the phenomenon of settling [116]

2.4. Adiabatic combustion temperature

One of the most important parameters in the SHS process is the adiabatic combustion temperature (T_{ad}). The knowledge of the adiabatic temperature is extremely vital in controlling the combustion process since it can influence the property and microstructure of the synthesized product. The term adiabatic temperature refers to the reaction temperature under adiabatic condition. It means

that there is no heat loss and heat gain during the process. In a combustion process which is assumed as being an adiabatic condition, all the heat of formation is used to convert the reactant into product resulting in the increase of temperature from initial condition to a maximum temperature with zero heat losses. Adiabatic temperature then becomes the maximum temperature that can be achieved in a combustion process.

The adiabatic process is an ideal situation which might be difficult to achieve. The actual combustion temperature (T_c) is normally below its adiabatic temperature since there are some heat losses or incomplete reactions which tend to lower the combustion temperature [49]. However, the assumption of an adiabatic condition in combustion synthesis is possible since the combustion process occurs in a very short time so that there is limited time for heat release produced by combustion to escape from the material.

The calculation of adiabatic temperature in combustion synthesis is very important to estimate the maximum temperature of combustion during the synthesis process. It is realized that combustion synthesis can produce very high temperature that might be dangerous for the equipment and environment. After predicting its adiabatic temperature, then the process has an opportunity to be controlled.

To determine the adiabatic temperature of the combustion, the First Law of thermodynamics is applied [119]. The principle of the First Law is the basic of energy conservation in which energy can be neither created nor destroyed. The First Law for a chemical reaction is stated in Eq. (2. 6).

$$Q+W=\sum n_j.\Delta H(P_j)-\sum n_i.\Delta H(R_i) \qquad (2.6)$$

where Q is heat transferred into or out of the system, W is work done by the system, ΔH is the enthalpy of reaction, n_i and n_j is molar number of reactant and product components, and R_i and P_j are identification for reactant and product, respectively. In an adiabatic process, there is no heat transferred into or out of the system ($Q = 0$) and it assumes that no work is done by or on the system ($W = 0$). The

general expression to calculate the adiabatic temperature is then stated in Eq. (2. 7) [49][119][120].

$$\sum n_i.\Delta H(R_i) = \sum n_j.\Delta H(P_j) \qquad (2.7)$$

Eq. (2. 7) means that in the adiabatic temperature, the total enthalpy of reactant equals the total enthalpy of product. The general expression to calculate the adiabatic temperature of combustion synthesis is shown in Eq. (2. 8).

$$\Delta H_{298} + \int_{298}^{Tad} \sum n_j.C_p dT(P_j) + \sum n_j.H_L(P_j) = 0 \qquad (2.8)$$

When the material undergoes melting during the reaction the solid phase of the element changes into the liquid phase. Eq. (2. 8) can then be broken-down into Eq. (2. 9).

$$\Delta H_{298} + \int_{298}^{Tm} \sum n_j.C_p(P_j)dT + \sum n_j.H_L(P_j) + \int_{Tm}^{Tad} \sum n_j.C_p(P_j)dT = 0 \qquad (2.9)$$

where T_m is the melting point of the product constituent. C_p represents the heat capacity of the elements in the solid phase and liquid phase. Table 2.6 shows the calculated adiabatic temperatures for some SHS reactions with varied initial temperature, obtained from many studies.

Table 2.6. The adiabatic temperature of some SHS reactions

Raw materials	Synthesized products	Initial temperature (T_o)/K	Adiabatic temperature (T_{ad})/K	[Ref.]
Ni, Al	NiAl	298 298–835 933 1728	1912 1912 2139 3083	[24]
Ni, Al	Ni_3Al	406–1019 1728	1668 2604	[24]
TiO_2, Al, C	TiC, Al_2O_3	298	2546	[121]
Ti, B_4C	TiB_2, TiC	298	3193	[108]
MoO_3, Al, Si	$MoSi_2$, Al_2O_3	673	3700	[7]
MoO_3, Al, S	MoS_2, Al_2O_3	673	4500	[7]

50 wt.% Cu, Ti, Si	Cu, Ti_5Si_3	298	1641	[122]

2.5. Heat transfer in SHS process

The heat transfer analysis of SHS reaction in an experimental investigation is basically very complicated since the process produces high reaction temperature combined with high propagation of combustion velocity. Many attempts have been tried to model SHS reaction to gain a better understanding of the mechanism of the reaction. Most SHS reaction modeling includes chemical reaction, covering the thermodynamic and kinetics of the reactions which involves the transfer of electrons and the diffusion process at an atomic level. The physical processes associated with ignition, the combustion propagation, the reaction heat released and heat lost and the thermal conductivity of the reactants and products.

Many works developed to model SHS reaction are generally based on the energy and mass balance. A simple model of the governing heat transfer equation for the propagation rate of SHS reaction was proposed based on Fourier's heat conduction equation as below [14]:

$$k\frac{\partial^2 T}{\partial x^2} + Q\Phi = C_p.\rho\frac{\partial T}{\partial t} \qquad (2.10)$$

where C_p and ρ are the heat capacity and density of the product, k is thermal conductivity of system, Q is heat of reaction without phase transformation, x is the coordinate, and T and t refer to as temperature and time, respectively. Φ is the reaction rate, which is defined to have Arrhenius form:

$$\Phi = \rho K_o \exp\left(-\frac{E}{RT}\right) \qquad (2.11)$$

where K_o is constant, R is gas constant (8.314 J/mol.K) and E is activation energy (J/mol).

In Eq. (2. 10), it was assumed that there is no phase change and the chemical reaction before ignition is also ignored. In their development, many works

have been reported to improve the SHS modeling. When the chemical reaction during ignition is taken into account, the chemical reaction rate was assumed as:

$$\Phi = \rho K_o \exp\left(-\frac{E}{RT}\right)(1-\eta)^n \qquad (2.12)$$

where η is the degree of conversion, which has the range of 0 – 1, and n is the order of reaction. Further studies have reported some modifications to the model in Eq. (2. 10) by considering melting of the reactant with addition of latent heat of fusion [14]. By adding the latent heat of fusion, H_L, the heat of reaction becomes $Q + H_L$.

Eq. (2. 10) explains that the first item in the left side is the net heat flux input to the element along the x-axes for case in one dimension modeling. Q is the intensity of the internal heat source which might be caused by many factors such as heat of reaction during phase transformation, electricity currents, and plastic work. While the right side represents the change of heat accumulating in the element per unit time due to the temperature change. To sum up, Eq. (2. 10) shows the sum of heat input and heat generated by the internal heat source is equal to the change in heat accumulating for an element in each time unit.

A more recent approach to SHS modeling was developed based on microscopic reaction mechanism and was used to analyze the temperature profile and wave stability of the reaction of some metal aluminides [123]. The model is basically using Fourier law of heat conduction as used in Eq. (2. 10) with the additional consideration of the heterogeneous aspect of the reaction process as shown in Eq. (2. 13–14). The model was used to model a cylindrical sample with a radius of R and length L.

$$C_p \frac{\partial T}{\partial t} = \frac{\partial}{\partial x}\left(k\frac{\partial T}{\partial x}\right) + \frac{2.\sigma.\varepsilon.\left(T^4 - T_a^4\right)}{R} + \dot{q}_{chem} \qquad (2.13)$$

where $\dot{q}_{chem}$ denotes heat due to chemical process and phase transformation involved in the process, which stated as follows:

$$\dot{q}_{chem} = f(x, y, z, T, t) \tag{2. 14}$$

C_p is heat capacity, and T_a is ambient temperature. Eq. (2. 13) is Fourier law of heat conduction, while Eq. (2. 14) is kinetic equation describing the rate of heat evolution. The initial condition and the boundary condition of the equation are presented as:

Initial condition:

$T(x, t = 0) = T_a$ for $0 \leq x \leq L$ where x is the distance along x-axis.

Boundary condition:

$T(0, t) = f_1(t)$, where f_1 is a function of ignition energy obtained from external heat source.

$$f_1 = T_a + (T_{max} - T_a)\exp\left[-\frac{(t - t_\mu)^2}{2t_\sigma{}^2}\right] \tag{2. 15}$$

where T_a is room temperature, T_{max} is maximum temperature achieved by the external heat source, t_μ is the time lag of ignition, and t_σ is the time range of ignition.

$T(L, t) = f_2(t)$, where f_2 is net heat input and output as a function of conduction, chemical reaction and phase transformation, and radiation.

The model as described in Eq. (2. 13–15) was used to simulate the SHS reaction of Ni–Al, Co–Al, Ti–Al, Nb–Al especially to describe their temperature profiles and the wave velocity. Fig. 2.11 shows the temperature profile for the SHS process of Ni/Al as widely observed by (a) experimental work and (b) simulation result. The temperature profiles are firstly characterized by a sharp increase until achieving a peak. This peak is then decreased and followed by a broader second

peak or a plateau. A comparison of the simulation with experimental results showed fairly good agreement. The only discrepancy of the results lies on the time scale since there is a difference in the thermal conductivity for compacted powders and the simulation data which influences the propagation characteristic of the SHS process. Meanwhile, the effect of porosity on the wave velocity for the SHS process of Ni/Al obtained by simulation and experimental results are presented Fig. 2.12. The continuous line and dotted line represent the simulation and experimental results, respectively. It can be seen that both results are in a good agreement in which the initial reduction of porosity from 60 to 40% (from right to left), the wave velocity is increased. With further reduction of porosity, there is an optimum value of porosity where the wave velocity achieves its maximum value. From the optimum point onward, the reduction of porosity will reduce the wave velocity due to the increase of thermal conductivity of the sample resulting in heat loss.

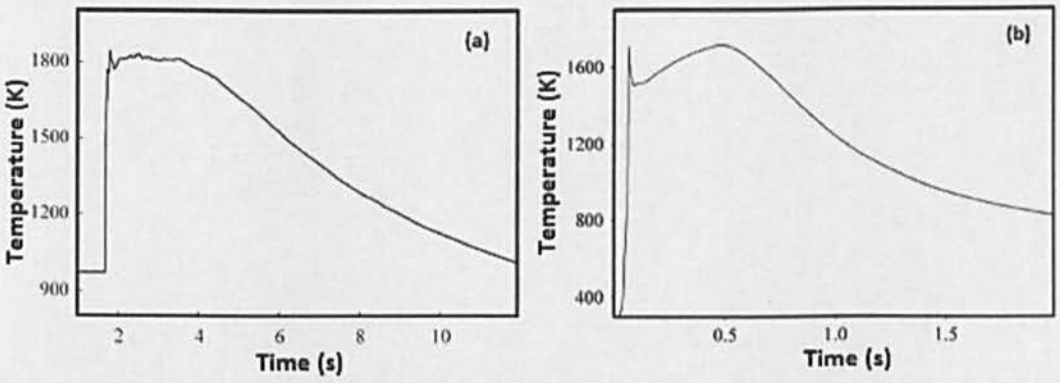

Fig. 2.11. Temperature profile for SHS process of Ni/Al obtained by (a) experiment; and (b) simulation [123]

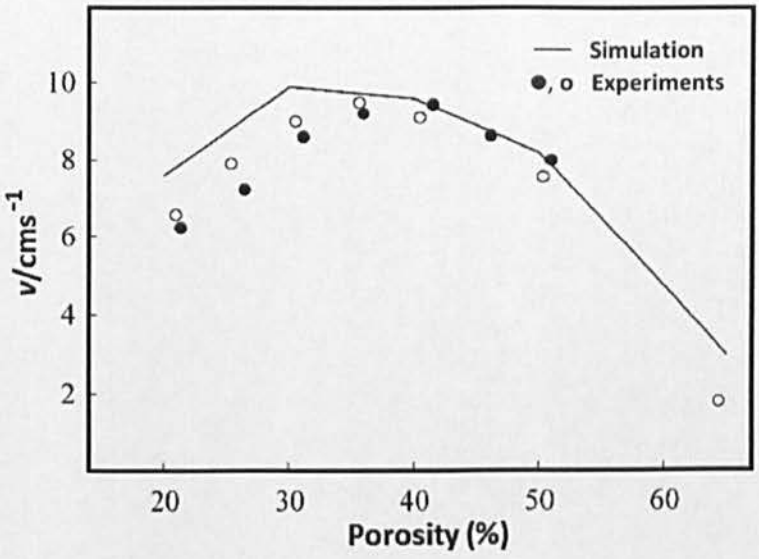

Fig. 2.12. The effect of porosity on wave velocity for the SHS process of Ni/Al with grain size = 50 μm [123]

2.6. Application of SHS products

Materials synthesized by SHS reaction have been widely used in many coating applications such as for oxidation and corrosion resistance, abrasive wear resistance for cutting tools, biomedical applications, protective coating in dangerous environments with high-level radioactive waste which comes from sources such as the nuclear industry, for the fabrication ceramic–lined compound copper pipe, and for repairing gas turbine components.

2.6.1. Oxidation and corrosion resistance coating in high temperature

SHS coatings are used in industrial power plant, aircraft and marine gas turbines, nuclear reactors, aircraft skins and structures, and petrochemical plant for oxidation and corrosion resistances. The tubes, pipes and heaters of the boiler in a thermal power station have to resist oxidation and corrosion which comes from high temperature steam or any other heat transfer medium. For this purpose, the advance coatings such as Al_2O_3, SiO_2, and Cr_2O_3 provide oxidation and hot corrosion protection in high temperature environment [58]. Intermetallic materials also have potential for hot sections of gas turbine engines for aircraft propulsion systems.

Intermetallic Ni_3Al has been produced by SHS–casting routes to provide an oxidation and corrosion resistance coating [13], while NiAl has been produced by pressure-assisted combustion synthesis [86].

2.6.2. Wear resistance for high temperature application

There is a high demand for advance coating having high wear resistance in high temperature applications. Some ceramic metal coatings such as TiC–TiB_2 system which are suitable for wear resistance applications have been produced by SHS combined with high velocity oxygen fuel spray as found in Fe(Cr) matrix reinforced by TiC or TiB_2 [78][80].

2.6.3. Cutting tool and insert coatings

The requirement for a cutting tool is high wear resistance and a low friction coefficient. For this purpose, the complex nitrides of intermetallics such as aluminium, nickel and titanium make very attractive coating materials for cutting tools since they have high hardness, good oxidation resistance and heat insulation. Valery [124] has investigated the fabrication of these compounds by the SHS process. Other material such as $MoSi_2$ provides wear and oxidation/corrosion resistance, and with the addition of MoS_2 in the coating is expected to bring a low friction coefficient to the coating. The composite system of $MoSi_2$–MoS_2 has been produced by SHS combined with casting [7].

2.6.4. Bio medical application

Biomedical materials need some special requirement such as chemical and biological resistance to biological fluids, antibacterial, biocompatibility and must be non-toxic. Advanced coatings with multi-components have been applied to medical application, for example, TiN has good biocompatibility and is suitable for orthopedic implants. Meanwhile, TiC_xN_{1-x} has been widely shown to have high hardness and high corrosion resistance. The addition of TiO_2, ZrO_2, and CaO has increased the performance of the TiC_xN_{1-x} film since they could provide better compatibility with blood; stimulate new bone tissue formation; and eliminate

chemical bond formation with living tissue. The SHS reaction has been used for the fabrication of multi-component thin film on the above mentioned systems [125][126].

Bio material used for medical devices or human implantation has to interact with the biological system. This interaction can become a serious problem when there is mismatch between the properties of the implant and the replaced organ. NiTi shape memory alloy has high potential for bone implantation since its structure is porous which allows the transport of body fluid to facilitate the development of new bone. NiTi alloy implants have also been produced by SHS [35].

2.6.5. Protective coating in polluted environment

Pollution sources such as toxic, radioactive materials and any hazardous air pollutant coming from internal combustion engines, mining, petroleum and chemical industries are dangerous substances for the environment. Since SHS can be operated under atmospheric conditions at room temperature without a furnace, the SHS process can be used to fabricate *in situ* protective coating on any dangerous solid wastes in polluted area [127]. Silicon oxynitride (Si_2N_2O) is a high temperature ceramic material which has a variety of potential applications for high temperature uses such as electric insulators, nuclear-reactor moderator or reflectors and solid electrolyte. This material has been prepared from a compacted mixture of silicon and silica under high nitrogen gas using the high temperature synthesis process [128].

2.6.6. For repairing gas turbine components

SHS reaction of NiAl has been used to provide internal energy as the heat source for melting an underlayer to join a damaged gas turbine component [1]. A deposited underlayer on the substrate surface was melted to fill the gap between the substrate and NiAl. This method has been studied to repair cracks when it is difficult to use welding.

2.6.7. Fabrication ceramic–lined compound copper pipe

SHS reaction has been combined with centrifugal casting technique to fabricate ceramic–lined compound copper pipe (CLCCP). Mixed powder is placed inside the pipe and rotated at a specific speed. When SHS is ignited, the liquid metal will be separated by the density difference due to the influence of the centrifugal force exerted on the pipe. The SHS process combined with the centrifugal technique can be used to produce ceramic-lined composite steel pipes and to produce coatings with excellent wear resistance without cracks and flakes.

2.7. Induction heating

2.7.1. Introduction

Over the past few decades, induction heating has become increasingly attractive due to its ability to generate high heat intensity within a workpiece in a short time with simple equipment. Induction heating equipment is comprised of three main parts: an electrical power source which generates high frequency energy of induction heating, an induction coil which is used to establish suitable electromagnetic flux lines in the material being inducted and a workpiece as the final transfer of the electrical energy into heat. Since the coil works close to the heated material, the coil is cooled by circulating water. The induction heating process is the process of heating a material using the principle of electromagnetic induction. When an electrically and magnetically conductive material enters to the coil inductor, Eddy currents are inducted in the material. This current is short circuited resulting in a heating process in the body of the material.

There are many advantages of induction heating systems. The heating process is non-contact which does not contaminate the material. The process is also clean and fast since the power goes directly to the material being heated. Other features of induction heating are its potential to control the heating time and its applicability to be used for heating a sample in a protective atmospheric such as in a room with an argon atmosphere.

2.7.2. Theoretical considerations

When designing an induction heating system, it is very important to understand the physical properties of the workpiece such as the electric conductivity and magnetic permeability of the material all of which will affect the heating process. In magnetic material, there is also the effect of hysteretic losses caused by molecule vibration which produces additional heat [73]. The penetration of heat in the surface of the material is mainly influenced by the frequency of the electrical generator. A low frequency will produce a high depth of penetration and vice versa. The depth of heat penetration or skin depth and the electrical efficiency of induction heating are expressed in the following equations [129]:

- Skin depth

$$\delta = \sqrt{\frac{2\rho_1}{\mu_o \mu_r \omega}} \tag{2. 16}$$

- Electrical efficiency

$$\eta = \frac{1}{1 + (D_1 / D_2)\sqrt{\frac{\rho_1}{\mu_r \rho_2}}} \tag{2. 17}$$

where ω is the frequency of the electrical generator, D_1 is the diameter of the coil (effective diameter), D_2 is the diameter of the sample, ρ_1 the electrical resistivity of the coil, ρ_2 is the electrical resistivity of the sample, μ_o is the magnetic permeability of free space, and μ_r is the magnetic permeability of the sample relative to free space.

2.7.3. Application of induction heating

Induction heating has been established for different heating applications from surface hardening in sheet metal forming [73], to the high heat volume for melting and heating of bulk metal forming such as forging [130]. In the case of hot stamping, the high heating rate produced by induction heating has avoided the coarsening of grain size during the process. Joining two metals by brazing process

using induction heating has also been studied [131]. Recently, induction heating was used successfully to initiate combustion synthesis [19][18].

2.8. Summary

This chapter has reviewed current progress in the processing routes to fabricate advance protective coating formed by the SHS process, or referred to as the SHS coating. A lot of works have indicated that intermetallics and ceramics have become potential candidates for high temperature applications, particularly as oxidation and corrosion resistance, respectively. The SHS process is suitable to synthesize these materials since it produces high combustion temperature and only takes a short processing time. A number of heat sources such as laser, solar energy, and microwave have been used to ignite the SHS process and subsequently to apply the synthesized product on the substrate in one processing route. This process is often followed by post treatment and densification to improve the coating properties. So far, several attempts have been made to use the synthesized product formed by the SHS process in many coating applications such as for oxidation and corrosion resistance, abrasive wear resistance in cutting tools, and biomedical applications.

Although many studies have been carried out to investigate the processing routes of the SHS coating, there are a number of challenging problems which still need to be addressed dealing with the product property. These problems may be categorized into the following items:

a). Adhesion strength between the coating and substrate

The adhesion strength has become one of the most challenging issues in the coating fabricated by the SHS process since the high combustion temperature of SHS process generates thermal stresses in the coatings due to the mismatch of thermal expansion coefficient between coatings and the substrate. The generated thermal stress in the coating leads to the formation of cracks and may result in the detachment of coating from the substrate. To date, there has

been little agreement on the joining technique for the coatings and the substrate in high temperature applications.

b). Porosity of the synthesized product

It was observed that the synthesized product formed by the SHS process is usually porous. The application of porous product for oxidation protection cannot be tolerated since the pores can permit the infiltration of gas which triggers the oxidation reaction. Although extensive research has been carried out to reduce the porosity in the synthesized product, it is still difficult to prepare densified product.

Among the types of adhesion mechanism, metallurgical bonding may be the best method to improve the adhesion strength by decreasing the stress concentrations at the interface. This is made by the formation of an interphase layer at the interface between the coating and substrate. The interphase layer is formed by the diffusion of atoms in the coating and the substrate facilitated by the melting of the substrate, particularly at the surface of the substrate. To produce a metallurgical bonding, it is necessary for the temperature of the substrate surface to be increased.

Recently, induction heating has become an interesting heat source for the SHS ignition due to its capability of producing high heat intensity on an electrically and magnetically conductive material. In induction heating the material is heated directly resulting in a faster heating process. Hence, the use of induction heating in the coating applications can be expected to increase the temperature of the substrate to assist the formation of an interphase layer. The main purpose of the present study is to use induction heating as a new method to initiate the SHS process of Ni/Al and subsequently to apply the synthesized product onto a steel substrate to produce a coating.

Induction heating used to increase the temperature of the substrate is expected to produce a metallurgical bonding by the formation of an interphase layer. It was observed that the strength of coating adherence is influenced by the

thickness of the interphase layer. The thicker the interphase layer, the stronger the adhesion strength is. This is due to the fact that a thicker interphase layer has the capability to reduce the thermal stress on the coating by providing more gradual change in the thermal expansion coefficient from the coating to the substrate. To produce a thick interphase layer requires more energy supplied by induction heating to maintain the diffusion. However, this method can spoil the substrate. Thus, inserting an underlayer between the coating and the substrate will be undertaken in the present work to produce a thick underlayer instead of generating a thick interphase layer. Part of the aim of the present work is to investigate the role of an underlayer in the improvement of the coating adherence.

During the synthesis process, the underlayer is expected to melt in order to facilitate adhesion between the coating and the substrate. The high heat released by the SHS reaction is responsible for the melting of the underlayer. However, due to the melting of the underlayer, there is a possibility that interfacial diffusion and other chemical reactions between the underlayer and coating may occur. It is also the focus of the present work to study the formation of new phases at the underlayer as a result of interfacial reaction between the underlayer and coating. The effect of interfacial product formation on the mechanical property will also be observed.

Since the NiAl coating fabricated in the present work is designed for high temperature applications, the performance of the coating may be affected in such high temperature situations. Thermal cycling with sudden changes of heating and cooling may be experienced during the coating service. Thermal stresses can be generated due to the sudden change of temperature which can result in the adhesion failure by the formation of cracks at the interface. For that reason, thermal shock tests will be performed to investigate the effect of thermal cycling on the microstructure and the adhesion strength between the coating and the substrate.

The successful investigation on the adhesion improvement of a NiAl coating formed by the SHS process is then expected to encourage its potential application

at elevated temperatures. However, a considerable amount of literatures has reported that the use of single phase NiAl is limited due to its brittleness at room temperature and insufficient creep resistance at elevated temperatures. It is therefore necessary to balance its property by improving its strength at high temperature and its ductility at room temperature. Recent evidence suggests that the formation of a NiAl based composite such as NiAl–Al_2O_3–TiC formed by the SHS process has offered better mechanical properties. However, the synthesized product is still porous. The application of porous product for protective coatings is unacceptable due to the risk of oxidation. Porosity can also ruin the mechanical properties of the synthesized product. To reduce the porosity of synthesized product, the SHS process of ceramics is often followed by densification techniques such as hot isostatic pressure, liquid metal sintering, and hot extrusion. Although the synthesized product can be densified, most densification techniques which involve a high temperature lead to the grain growth which is detrimental to the mechanical properties of the product at room temperature. The present study will further explore the fabrication of NiAl–Al_2O_3–TiC composite formed by the SHS process, with an emphasis on the study of its combustion behaviour, microstructure, and mechanical property. The application of NiAl–TiC composite for coating will also be investigated.

Finally, the successful study on the application of induction heating to fabricate coatings formed by the SHS process is expected to provide a better understanding in the effort to improve the adhesion performance of NiAl coating, to add new information to the debate of porosity in NiAl–Al_2O_3–TiC composite, and to produce a hard coating by a simple processing route with low energy consumption.

Chapter 3

Experimental Procedures

This chapter discusses the preparation and experimental procedures required to perform the SHS process and fabrication of the coating from a powder mixture using induction heating.

3.1. Preparation of starting material and substrate

3.1.1. Material selection

In the present work, powder was used as the reactant based on the consideration that powder metallurgy offers many advantages such as the possibility to produce accurate and complex geometries of product, and provides "near net shape" processing routes which can eliminate machining operations [132]. The use of powder also has economical advantages for large volume production, even though costs of some powder are normally higher than the solid bulk.

The powder materials used in the present work are nickel (Ni), aluminium (Al), titanium (Ti), titanium oxide (TiO_2), carbon black (C), and alumina (Al_2O_3). Data about the materials is given in Table 3.1. SEM micrographs showing the shape and size of particle for each powder are given in Fig. 3.1. It can be seen that the shape of the Al particles is an irregular flake which has a relatively smooth surface with high purity. In this work, Aluminium (Al) was used to produce NiAl since it has low melting temperature. In the synthesis of NiAl, the low melting point of Al is able to initiate the synthesis process by its melt. Meanwhile, the shape of Ni particles is like a cauliflower. The Ni powder is nickel carbonyl type–123 which indicates that the powder is pure and fine. The carbonyl process is a production technique to produce fine metallic powder by thermal decomposition from metal carbonyl such as $Fe(CO)_5$ and $Ni(CO)_4$. Several metals can react with carbon monoxide at a certain condition to form metal carbonyl. Since these compounds have low boiling points,

then they can be easily purified by using a distillation process to yield very pure metal. The remaining impurities are only carbon and oxygen [132]. In the present work, Ni was selected mainly because it is magnetically conductive so that it is capable of being heated through induction heating to produce NiAl.

Titanium (Ti) was mainly used as the material for the underlayer since it has a high melting temperature which can then be used for high temperature applications [133]. Ti was also used to produce titanium carbide by reaction synthesis with carbon black. In this work, titanium dioxide (TiO_2) was used to indirectly obtain titanium and oxide through a thermite reaction to obtain TiC product. For economic reason it is advantageous to use TiO_2 as a reactant to produce titanium carbide compared with elemental Ti powder [134]. In addition, TiO_2 developed by Huntsman has also been designed to contain low volatile organic compounds (VOC) to support worldwide environmental requirement. Meanwhile, Al_2O_3 powder was not used as a reactant but for comparison purpose in the material characterization using laser Raman microspectroscopy.

Table 3.1. Powder materials data

Powder Material	Average particle size/D50 (μm)	Purity (%)	Impurity (%)	Source
Inco Carbonyl Nickel type–123 (Ni)	4.5	99.85	C (0.078) O (0.041) Fe (0.002) S (0.0002)	William Rowland, UK
Aluminium (Al)	45	99.7		William Rowland, UK
Titanium (Ti)	106	99.46	Al (0.01) Fe (0.035)	William Rowland, UK
Low sulphur carbon black (C)	1	99.9	S (max 0.1) Ash (max 0.5)	William Rowland, UK
Titanium dioxide (TiO_2)	0.308	93 – 96		Huntsman Tioxide, UK
Alumina (Al_2O_3)	1	99.8		Alcan Chemical, UK

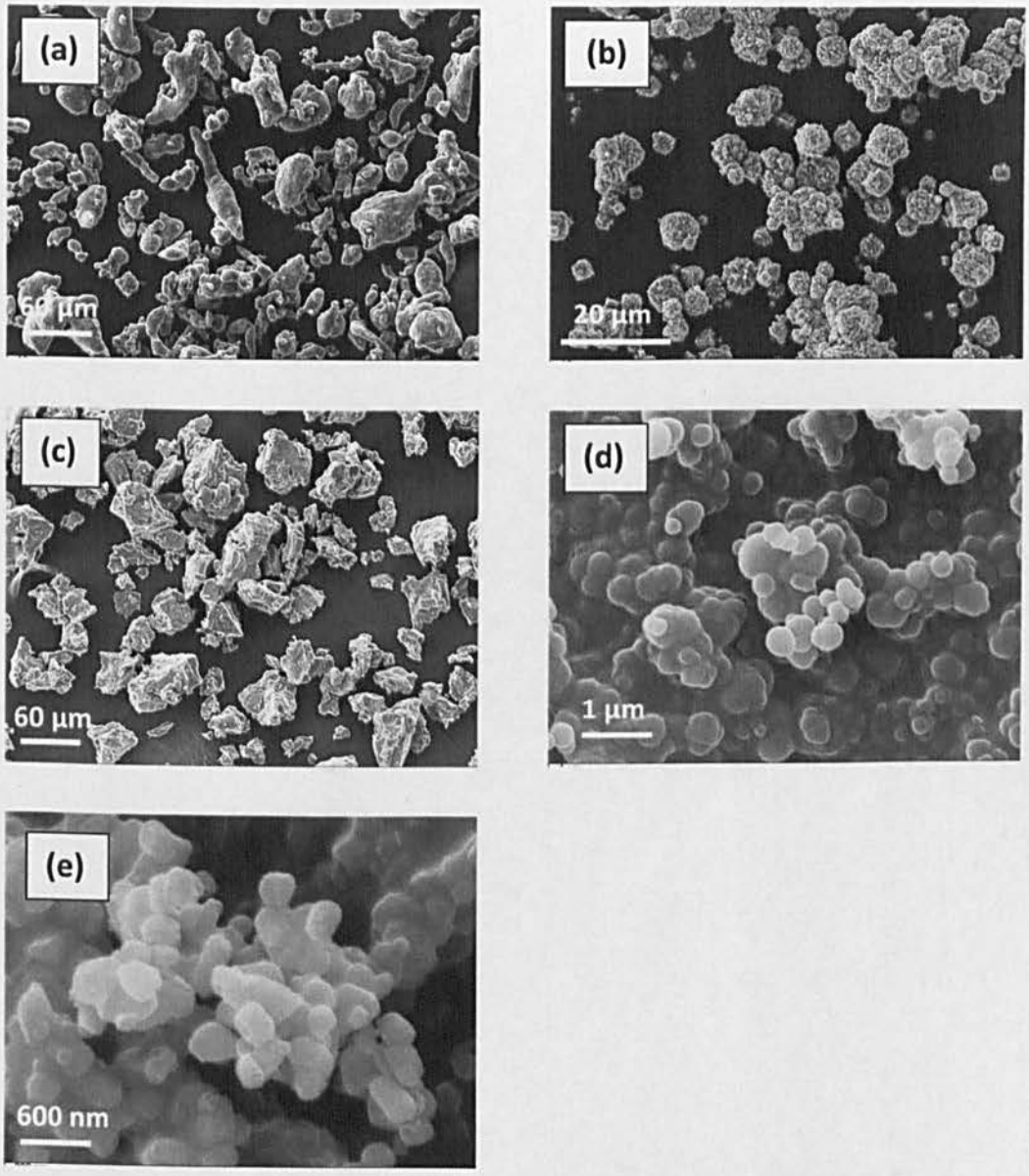

Fig. 3.1. SEM micrographs of reactant powders: (a) Al; (b) Ni; (c) Ti; (d) C; and (e) TiO_2

3.1.2. Sample compositions

The reactant powders used for the synthesis reaction were weighed according to the mass fraction of each element as described in the chemical reaction for each system in Eq. (3.1–3). The mixture of the Ni/Al system with a mole ratio of 1:1 was composed of Ni and Al powders with a composition of 68.51 and 31.49 wt.%, respectively. The same procedure was repeated to produce a TiO_2/Al/C mixture with a mole ratio of 3:4:3 and a Ti/C mixture with a mole ratio of 1:1.

$Ni + Al \rightarrow NiAl$ (3.1)

Powder	Mole ratio	Atomic weight	Mass fraction (wt.%)
Ni	1	58.69	68.51
Al	1	26.98	31.49
Total		85.67	100.00

$3TiO_2 + 4Al + 3C \rightarrow 3TiC + 2Al_2O_3$ (3.2)

Powder	Mole ratio	Atomic weight	Mass fraction (wt.%)
TiO_2	3	79.86	62.47
Al	4	26.98	28.14
C	3	12.01	9.39
Total		383.55	100.00

$Ti + C \rightarrow TiC$ (3.3)

Powder	Mole ratio	Atomic weight	Mass fraction (wt.%)
Ti	1	47.87	79.94
C	1	12.01	20.06
Total		59.88	100.00

3.1.3. Powder mixing

After weighting according to each system as mentioned in reaction (3.1–3), the mixtures were then mixed. The main intention of powder mixing is to achieve a mixture which is as homogenous as possible since the mixture homogeneity significantly affects the microstructure and properties of the product. Generally, powder mixing can be carried out using dry or wet processing techniques [132]. Since powder mixtures obtained by using a dry process may form agglomerates of non uniform particle size which can, in turn, lead to poor mixing and results in a inhomogeneous structure, vibration mixing or a ball mill are often used to achieve thorough mixing. By using the dry process it is difficult to achieve a highly uniform mixture. Meanwhile, the wet process can be used to obtain better mixing since the particles are able to disperse in a liquid and are relatively free to move each other to form a colloidal suspension. This formation is often mixed again using an ultrasonic vibrator. Finally, the powder is dried in an oven to evaporate the

moisture. In the present work, a trial using wet process was carried out by mixing the mixture with acetone in an ultrasonic vibrator (Schlumberger ultrasonic, UK) and stirred for about 15 minutes. However, difficulty was found in removing the liquid from the mixture. The mixing of reactants was then carried out using dry processing. The reactant mixtures of approximately 50 grams were crushed in a ceramic mortar for about 20 minutes. To get better mixing, the reactants were subsequently blended in a grinder (Mini grinder mode Wahl James martin, capacity 70 grams, UK) which has stainless steel inner housing and blade. Finally, the mixture was placed in a carbolite furnace and heated at 100 °C for approximately 1 hour to evaporate the moisture.

3.1.4. Powder compaction

The powder compaction was performed to produce pellets. Compaction is aimed to increase the physical contact between the reactant particles which influences the thermal conductivity of the pellet. The application of compaction for the powder mixture in the present work is advantageous since it can be used to produce a pellet with varied thickness. The density of pellet can also be varied by applying different pressure of compaction. The production of multilayers is also easier when using a compacted pellet. However, it was realised that the pellets could not be made too thin since handling would become difficult. In the present work, the compaction was carried out using a simple package of steel die and punch which was manufactured in accordance with Ref. [132]. The inner diameter of the die was 16.0 mm. The schematic illustration of the powder compaction process using closed die compaction is shown in Fig. 3.2. For compaction, a hydraulic press (Sealy Hydraulic Yankee Floor type YK10F, UK) was used. The ram stroke was 203 mm, whilst the hydraulic oil was Sealey hydraulic jack oil. The maximum pressure of hydraulic compression machine was 1000 kg/cm^2.

The mechanism of powder compaction in the present work was carried out through several steps:

- Filling the powder into the die container.

- Entering the top punch until it touched the powder surface and flattened the top surface of the powder.
- Loading the powder mixture under pressure by single action pressing.
- Ejection of the punch to remove the green sample.

Before the compaction process, the entire wall surfaces of the punch and die were cleaned and free from dust and any grease in order to reduce friction during the compaction. For the production of multilayer pellets, the compaction was basically performed by the same procedure, where the next layer was compacted after the previous layer was formed, without ejecting the first layer.

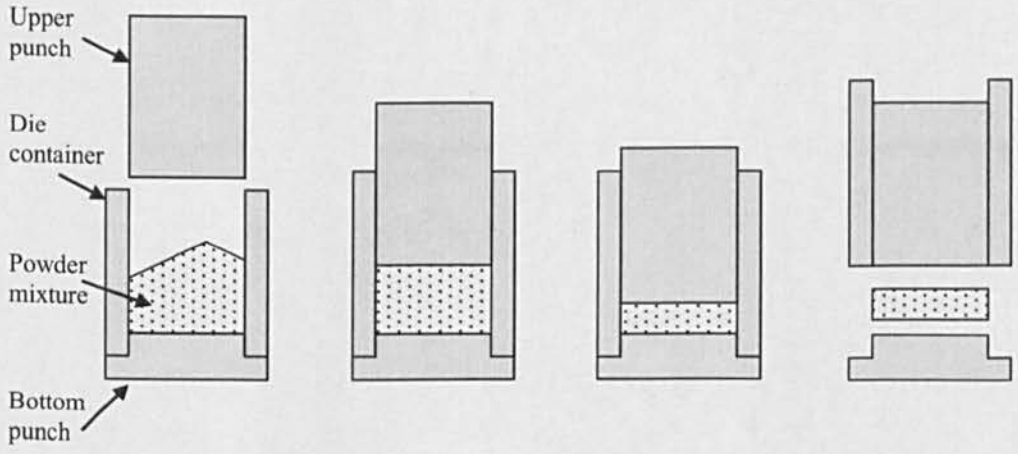

a). Filling b). Flattening c). Loading d). Ejection

Fig. 3.2. Schematic diagram of powder compaction

The compaction pressure used for variation of the reactant in the present work was selected using 100, 150, and 200 MPa as demonstrated in previous study [17]. In order to produce these pressures, the force of the hydraulic machine required for the compaction was calculated based on the required pressure. For instance, to produce a pressure of 100 MPa (100×10^6 N/m^2), the compression force (F) of the hydraulic machine is calculated as follows:

F = (pressure) x (die cross section)

$$F = 100 \times 10^6 \text{ (N/m}^2\text{)} \times \frac{\pi}{4}.\left(16.10^{-3}\right)^2 \text{ (m}^2\text{)}$$

$$F = 20.12 \text{ kN}$$

The pressure of hydraulic press can be calculated by dividing the force with the ram area (Ram diameter = 50 mm^2). For the force of 20.12 kN, the required pressure is 10.24 N/mm^2. Since the pressure gauge unit is stated in kg/cm^2, its conversion is 104.4 kg/cm^2. This means that a compaction pressure of 100 MPa can be obtained by 104.4 kg/cm^2 of the hydraulic pressure. To compact the pellet, the handle of the hydraulic press is pumped slowly until the ram of the press touching the punch. The pressure applied during compaction can be read from the pressure gauge attached on the press tool. The result of calculation for other pressures is presented in the Table 3.2.

Table 3.2. Calculation result of compaction pressure

Compaction pressure (MPa)	Force (kN)	Hydraulic pressure (kg/cm^2)
100	20.12	104.4
150	30.18	156.7
200	40.24	208.9

3.1.5. Preparation of substrate

The substrate acts as a reaction platform to facilitate synthesis reaction and to facilitate the coating. In the present work, carbon steel (Bright mild steel, 16mm in diameter, RS component, UK) was used as substrate since it has wide application. The successful application of a coating in the present work would be expected to extend the application of steel for use in higher temperature environments. To facilitate coating, the substrate should be made free from impurities and be completely dry. In general, the substrate was prepared by the following steps:

- Machining a steel bar to form a flat surface of disc with a finished thickness of 3 mm.

- Grinding one side of the surfaces with silica paper (180 and 600 mesh) to produce a flat surface.
- Cleaning the substrate using acetone in an ultrasonic bath for 15 minutes in order to remove dust, any oil film and grease.
- Drying the substrate in hot air to eliminate moisture on its surface.
- Keeping the substrate in an airtight container to avoid oxidation before use.

3.2. Preparation of tools and equipment

3.2.1. Reaction chamber

The combustion synthesis in the present work was carried out in a reaction chamber made from acrylic. The box was sealed in order to control the atmosphere during combustion synthesis. Generally, combustion synthesis can be conducted in a vacuum, argon, or nitrogen inert gas atmosphere to minimize the oxidation. Pure shield argon was used in this work as it is advantageous to control the high combustion temperature and propagation rate of the SHS process [135], as also demonstrated by previous studies [18]. The samples were held in the reaction chamber through which argon was flowing with a flow rate of 15 litres/min and a pressure of 13.79 MPa (2000 psi). A granite block supported by an adjustable stall was used as a platform to place the samples. An induction heating coil installed in the reaction chamber was placed over the sample. The distance between the bottom of coil and the top surface of the sample was approximately 3 mm. To monitor the combustion temperature, a pyrometer was located vertically at about 0.4 m above the sample, on the outside of the box. Fig. 3.3 shows the schematic diagram of the experiment set up.

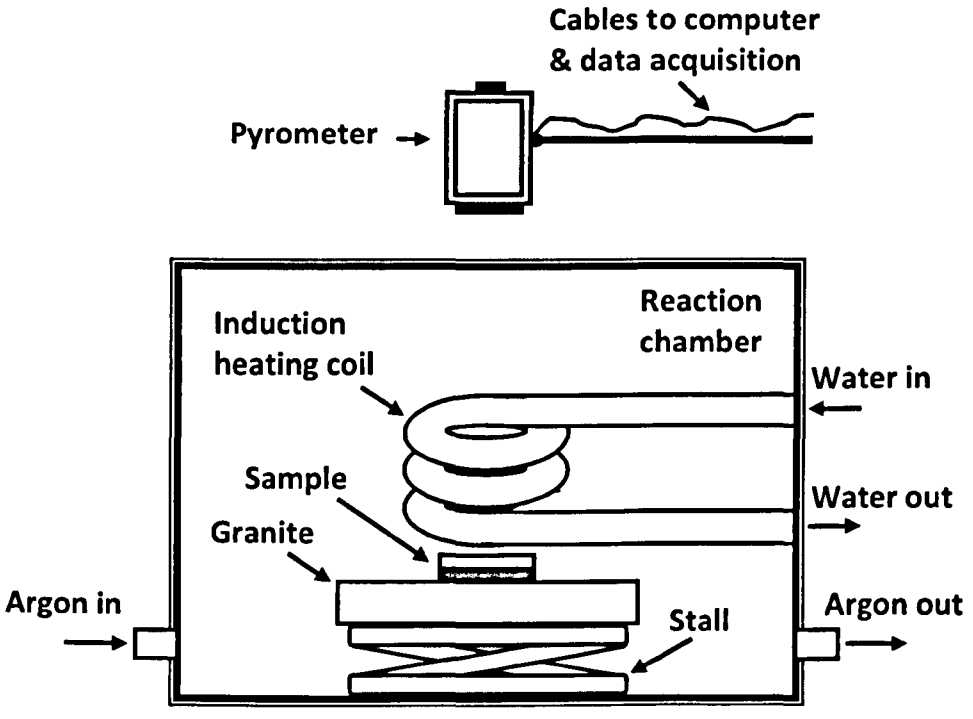

Fig. 3.3. Schematic diagram of the experimental set up

3.2.2. Induction heating

In the present work, induction heating equipment (model Easy Heat, manufactured by Cheltenham Induction Heating Limited, UK) with a maximum power of 2 kW and voltage range of 200–250 V was used as a heat source for ignition of the combustion synthesis. In the coating fabrication experiment, induction heating also has the function to preheat the substrate. The induction heating equipment was fitted with a front mounted control panel used to program the current requirement and heating time. The selection of coil shape and heating parameters are considered as follows:

3.2.2.1. Coil selections

The selection of the induction coil is very important since it affects the heating pattern and determines the production rate which can maximize the efficiency of the power supply. Induction coils are generally made from copper tube since it has very high thermal and electrical conductivities. The selection of

induction coil is basically directed to the design of coil shape, which usually can have single or multiple turns of helical, round or square shape. A classical cylindrical induction coil design includes the number of turns, its length, and inner diameter. In the present work, there was no desire to design a new coil but simply to choose an appropriate one from commercially available coils with different shapes and frequencies. A helical coil with a maximum frequency 387 kHz was chosen as it was a suitable match with the shape and size of the heated object, in this case, a package of the sample and the cylindrical substrate.

3.2.2.2. Selection of heating parameters

The main goal of using induction heating in the present work was to obtain fast heating in the sample to initiate the ignition of combustion synthesis. However, it was realized that the heating rate in the heated body is also important since it can influence the microstructure and mechanical property of the synthesized product. In the present work, different heating rates of the heated sample were obtained by changing the current and heating time. The selection of parameters in the induction heating was mainly based on the requirement of the skin depth and processing time of the heating process. The selection of heating parameter is also important for process optimization.

3.2.3. Temperature monitoring and emissivity calibration

Monitoring the temperature of the combustion process is extremely vital to study the reaction mechanism. In the present work, the measurement of the combustion temperature was carried by using a combination of thermocouple and non contact infrared pyrometer. A type–K thermocouple which has a temperature range of -50 – 1100 °C was used to measure the low combustion temperature range, whilst a pyrometer type Marathon MM (manufactured by Raytek®, UK) which has a capability to measure high temperature in the range of 540–3000 °C was applied to measure the high combustion temperature range. The temperature data measured by the pyrometer was recorded using Raytek Data Temp Multidrop software which was installed on an attached computer. Temperature measurement

using a pyrometer is more accurate compared with other non-contact tools such as an infrared thermometer since the focus diameter is sufficiently small, which is less than 2 mm. The response time is also very small since the measurement is taken in millisecond. It is realized that the shorter the response time, the more measured temperature data will be taken to achieve the real value. Since the temperature change in SHS process is very rapid, the shorter response time is required [136].

Using a pyrometer is an indirect method to measure the temperature of a sample through the radiation emitted from its surface. The use of a pyrometer requires the knowledge of emissivity (ε) to obtain the true temperature of the sample. Emissivity is a property which reveals the amount of emitted radiation energy of a given body as compared to a blackbody. It is realized that emissivity of surface is hard to establish since it can be influenced by wavelength, surface roughness and geometry, melting and surface pollution [137][138][24]. For instance, the emissivity of a clean and polished surface is low, whilst the emissivity of a roughened surface is high. In accordance with the limitation of the equipment provided by manufacturer, however, the emissivity in the pyrometer was set to be fixed during the measurement. To minimize uncertainty in the measurement of combustion temperature, the emissivity set up in the pyrometer was calibrated using other measuring tools. In the present work, emissivity calibration was carried out by comparing the result of measurement obtained by pyrometer and thermocouple. Thermocouple was embedded in a shallow groove of approximately 1 mm depth cut into the surface. For the steel sample, thermocouple was kept using a spot welding whereas for the compacted powder, the thermocouple was claimed using a cylindrical bar from granite. The hot spot of the thermocouple was placed in the centre of sample, whilst the focus of the measurement which used a pyrometer was located adjacent to the centre of the sample. The emissivity calibration of NiAl, titanium, and steel substrate is presented below.

3.2.3.1. Emissivity of NiAl

To select the emissivity of NiAl, the profile of the combustion temperature for the SHS reaction of Ni/Al was measured. Two compacted layers of Ni/Al and Ti

underlayer with a thickness of approximately 0.5 mm for each layer were placed on the steel substrate. Compaction on the sample was carried out using a pressure of 200 MPa. A thermocouple was embedded in a shallow groove on the surface of Ni/Al pellet, where the junction of thermocouple was located in the centre of the surface of Ni/Al. A pyrometer was located at about 0.4 m perpendicular to the sample pellet with a focus adjacent to the centre of the pellet surface. There are many variables on the pyrometer which can be adjusted such as response time, focus, and the emissivity. The response time was set to 1 millisecond, while the focus was modified to find the best view. Different values of emissivity were used to obtain different profiles of combustion temperature. The combustion process was carried out inside the reaction chamber with an atmosphere of argon gas flowing at a rate of 15 l/min.

Two groups of experiments were carried out to investigate the matching line of the temperature profile of Ni/Al reaction obtained by thermocouple and pyrometer measurements, and to investigate the temperature profile of Ni/Al reaction using different values of emissivity. In the first experiment, the current and time of induction heating were set to preheat the sample and ignite the SHS process of Ni/Al, whilst the second experiment was focused on monitoring the temperature profile of Ni/Al reaction which used different values of emissivity. Fig. 3.4 shows the temperature profile of Ni/Al reaction obtained by thermocouple and pyrometer. It can be seen that in the initial heating as obtained by thermocouple, the temperature of the sample increases from its initial condition at room temperature to a temperature at 400 K, where the temperature then levels off for about 9 s. This shows that induction heating can be adjusted to maintain the sample temperature for a period of time during heating. The temperature of Ni/Al reaction then increases slightly but suddenly drops during its increase after 16 seconds due to the loss of contact between the thermocouple and the sample as a result of overheating. The continued measurement of the combustion temperature of the sample is then obtained from data provided by the pyrometer. As measured by pyrometer, the temperature of the sample increases from 813 K to achieve its ignition temperature where it then rises dramatically until a maximum value. Since

the temperature measurement using a pyrometer needs a value of emissivity, a number of experiments were then carried out to investigate the temperature profile of Ni/Al reaction using different values of emissivity. Fig. 3.5 shows a part of temperature profile for the SHS process of Ni/Al which used different values of emissivity. The graph only describes the top part of the temperature profile in order to show the temperature difference between the maximum combustion temperatures of Ni/Al reaction. It can be seen that four values of emissivity produce a similar trend. However, different values of emissivity significantly affect the combustion temperature. The use of low emissivity results in the increase of the combustion temperature. As a consequence, the maximum combustion temperature is also affected. It is obvious that the maximum combustion temperature of Ni/Al reaction using $\varepsilon = 0.82$ is 1907 K. This temperature is the closest value with the adiabatic temperature of Ni/Al reaction which is 1911 K. Thus, based on the matched line of the temperature profiles obtained by the pyrometer and thermocouple, including the consideration of NiAl melting point (1911 K), the emissivity of 0.82 is estimated as appropriate to obtain the true combustion temperature of Ni/Al reaction. A small difference below the adiabatic temperature is acceptable due to the heat loss to the environment. In addition, the present selection of NiAl emissivity is also consistent with that obtained by previous studies [139].

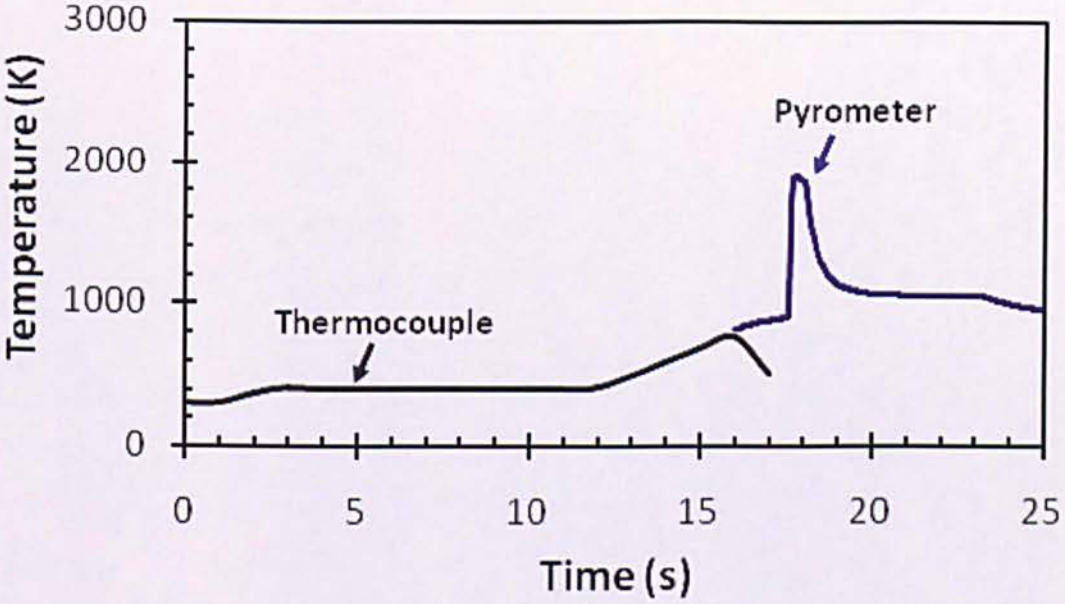

Fig. 3.4. Temperature profile of the Ni/Al reaction

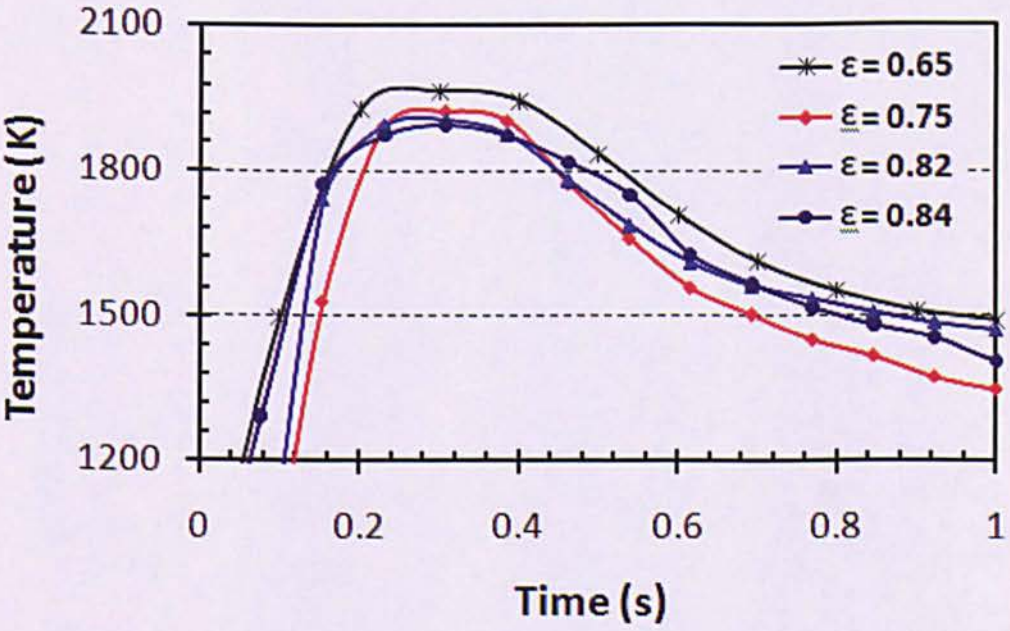

Fig. 3.5. Temperature profile of the Ni/Al reaction using various emissivities

3.2.3.2. Emissivity of titanium

The emissivity of titanium was investigated to obtain its temperature profile during its application as an underlayer in the fabrication of NiAl/Ti coating formed by the SHS process. Since the main concern is to monitor the temperature increase

of Ti, a substrate was not used. The sample was made using two layers only, which composed of compacted pellets of Ni/Al mixture and Ti. To facilitate the temperature measurement which was conducted using a pyrometer, the titanium pellet was placed on the top of the Ni/Al. The sample was heated by induction heating using a current of 300 A, and a heating time of 7 s. Fig. 3.6 shows the temperature profile of titanium obtained using several values of emissivity. It can be seen that all samples produces the same temperature trend profile. The temperature of titanium increases sharply from its initial temperature to achieve its maximum value, and followed by a slow decrease and the formation of a plateau. The detailed temperature profile of titanium using some selected values of emissivity is illustrated in Fig. 3.7. It can be seen that the emissivity value of 0.95 has produced the maximum temperature of 1940 K which is just slightly below the melting temperature of Ti (1941 K). Thus, the value of 0.95 was selected as the emissivity of titanium with the assumption that the Ti underlayer has achieved its melting point during the combustion synthesis of NiAl/Ti.

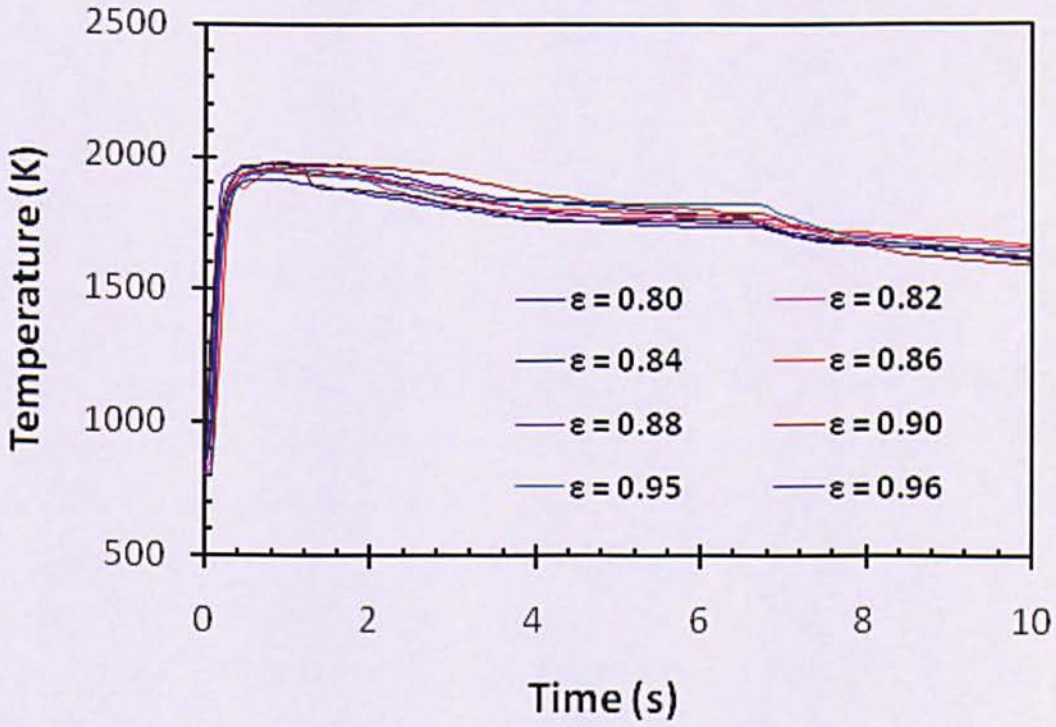

Fig. 3.6. Temperature profile of Ti using various emissivities

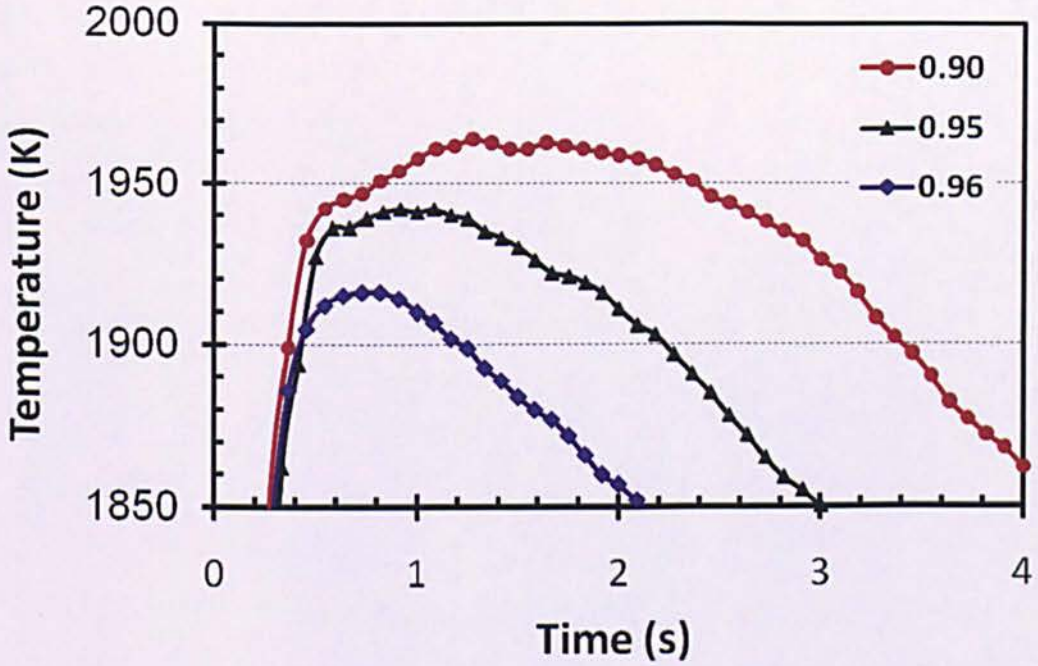

Fig. 3.7. Enlarged temperature profile of Ti using selected emissivity

3.2.3.3. Emissivity of the steel substrate

The emissivity of the steel substrate was measured to study its temperature increase during the fabrication of the NiAl coating using induction heating. Since the steel substrate is magnetically conductive and its position is separated from the NiAl pellet during the synthesis reaction, the investigation on the emissivity of the steel substrate was carried out without the presence of Ni/Al or Ti. The steel disc of 16 mm diameter and thickness of 3 mm was heated using induction heating with a current of 300 A for 3 s, and then maintained at approximately 1173 K (900 °C) for 30 s. The measurement of the heating temperature was performed using a pyrometer and a thermocouple, the latter was spot welded onto the steel surface. The value of emissivity was changed several times to obtain matched lines between the measured temperatures obtained from the pyrometer and thermocouple. After several trials using different value of emissivities, the value of 0.8 was finally taken as the emissivity of steel since the measured temperatures obtained by the thermocouple and pyrometer were, as shown in Fig. 3.8, a sufficiently good fit. To validate the correctness of the result, the temperature profile obtained by both instruments was checked by comparison with the thermal property of steel. Both

graphs show that there is a deflection in the Curie temperature at about 1023 K (750 °C) which confirms that both results have a good approximation for the selection of emissivity value.

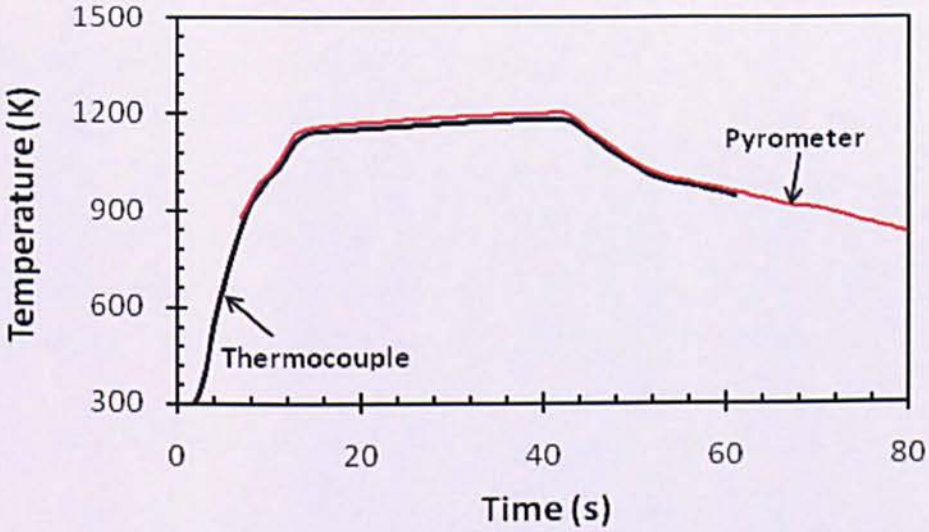

Fig. 3.8. Temperature profile of the steel substrate using ε = 0.8

3.3. Preparation of SHS process

The section deals with the selection of the sample used for the reactant and the processing parameters of the process. Based on these factors, the present work divided the experiment into three sections, namely the fabrication of the NiAl coating, the synthesis of NiAl–TiC–Al_2O_3 composite, and the fabrication of a TiC intermetallic composite coating.

3.3.1. Fabrication of NiAl coatings

The initial part of the experiment in the present work was conducted to fabricate a NiAl coating on the steel substrate using induction heating. The focus of this part was to improve the adhesion between the coating and substrate. It took a significantly long time to solve the difficulty experienced during the work. Many methods have been tried to generate adhesion between the coating and the substrate such as by densification using mechanical pressure during the synthesis and the application of adhesive material such as standard glue and polyurethane based adhesive. But the adhesive could not be used for the SHS process. In this

work, an underlayer was studied to improve the adhesion between the coating and substrate. The samples were then constructed using two layer structures of compacted pellets which comprised of Ni/Al mixture and underlayer.

Since the underlayer plays an important part in the preparation of the coating, it is vital to select a suitable material for use as the underlayer and to study the role of the underlayer on the microstructure and mechanical properties of the products. After the underlayer was selected, further works were then carried out to observe the effect of the thickness of the underlayer, the compaction pressure of the reactant pellet, and the melting point of the underlayer. The effect of current variation on the heating behaviour was also investigated.

3.3.1.1. Variation of underlayer thickness

The thickness of the underlayer was studied based on the expectation that a thick underlayer may increase the adhesion strength by reducing higher residual stress. However, some limitations were observed when using a thick underlayer. Under the high temperature of the SHS reaction, the metal underlayer was melted and sucked away from its place to leave some voids at the interface which can decrease the coating adherence. The use of a thin layer showed a better result in avoiding excessive liquid from the underlayer melt. However, a thin underlayer was difficult to compact. Three different thicknesses of underlayer were investigated in this work (thin, medium and thick) represented by group A, B, and C. The Ti underlayers were prepared using mass of 0.2, 0.3 and 0.5 grams and compacted using a pressure of 200 MPa. After compaction, the thickness of underlayer was measured and the result is given in Table 3.3.

Table 3.3. Thickness variations of underlayer

	Thickness of sample group A (mm)	Thickness of sample group B (mm)	Thickness of sample group C (mm)
Sample 1	0.34	0.61	0.75
Sample 2	0.36	0.51	0.93
Sample 3	0.24	0.47	0.80
Average	0.31 ± 0.04	0.53 ± 0.04	0.83 ± 0.05

3.3.1.2. Variation of compaction pressure

The density of the compacted powder influences the thermal conductivity of the sample which, in turn, affects the completeness of the underlayer melting. The present study investigated the effect of underlayer density using compaction pressures of 100, 150, and 200 MPa obtained from 0.3 gram of Ti. Since the pellets were compressed with different pressures, the thickness of pellet was varied. Table 3.4 shows the thickness of compacted pellets after compacted by different pressures. The SHS process of the reactant was initiated using induction heating with 300 A for 11 s.

Table 3.4. Thickness of underlayer with varied compaction pressure

	Thickness of Ti compressed by 100 MPa (mm)	Thickness of Ti compressed by 150 MPa (mm)	Thickness of Ti compressed by 200 MPa (mm)
Sample 1	0.67	0.46	0.61
Sample 2	0.82	0.62	0.51
Sample 3	0.64	0.63	0.47
Average	0.71 ± 0.06	0.57 ± 0.06	0.53 ± 0.04

Since the weight of Ti was identified as 0.3 gram, the density of the underlayer after compaction can be calculated using the weight of the sample divided by the volume of the pellet, the latter being obtained by multiplying the surface area of the sample (diameter = 16.0 mm) with the thickness after compaction. The density of the underlayer obtained by different compaction pressures is given in Table 3.5. It can be seen that an increase in the compaction pressure increases the density of the compacted samples. However, all of the results are less than the theoretical density of Ti (4507 kg/m^3) due to the presence of air gaps between the particles.

Table 3.5. Density of Ti underlayer after compaction

	Density of Ti compressed by 100 MPa (kg/m^3)	Density of Ti compressed by 150 MPa (kg/m^3)	Density of Ti compressed by 200 MPa (kg/m^3)
Sample 1	2226.69	3243.23	2445.71
Sample 2	1819.37	2406.26	2925.26
Sample 3	2331.07	2368.07	3174.22
Average	2125.71 ± 156.11	2672.52 ± 285.57	2848.39 ± 213.79

3.3.1.3. Variation of melting temperature of the underlayer

In the selection of the underlayer, the melting point of the material is an important factor since it has a close relationship with the adhesion between the coating and the substrate. During coating production, the underlayer has to melt in order to facilitate adhesion between coating and the substrate. Thus, the exothermic energy released by the synthesis reaction has to provide sufficient energy to increase the temperature of the underlayer to reach its melting point. Low melting point materials are easy to melt. However, when using an underlayer with a low melting point, its application is limited. For high temperature applications, an underlayer with a higher melting point is required. Based on this consideration, Al, Ni, and Ti were studied. Al has a melting point of 930 K which represents a low melting point, Ni (T_m = 1728 K) has a medium melting point, and Ti (T_m = 1941 K) corresponds to a high melting point. This criterion was taken based on the comparison with the melting point of NiAl (T_m = 1911 K).

3.3.1.4. Variation of heating rate

Heating rate has been reported to affect the microstructure of the synthesized product and the behaviour of the combustion synthesis [17]. In combustion synthesis ignited by induction heating, the heating rate is dependent on the heating parameters, particularly the current. The present work has investigated the effect of heating rate using the four different currents of 150 A, 200 A, 250 A and 300 A. The period of induction process time was adjusted so that the induction process was stopped at approximately 1 second after ignition.

3.3.2. SHS Process of NiAl–TiC–Al_2O_3 composite

The second part of the present work was to investigate the SHS process of composite material (NiAl–TiC–Al_2O_3 system) obtained from low cost precursor (TiO_2 powder). The objective of this part was to investigate the effect of reactant composition on the combustion behaviour, microstructure, and mechanical properties of the synthesized product. The reactants were composed using (1–x)Ni/Al + (x)3TiO_2/4Al/3C, where x is varied by 10, 20, 30, and 40 wt.%. Since the

mixture of TiO_2/Al/C powders is magnetically non-conductive, then the ignition using induction heating becomes very important. The ignition of the Ni/Al + TiO_2/Al/C system was initially observed using induction heating. In this configuration, the combustion synthesis of the sample was only initiated using induction heating without the application of steel substrate to assist the ignition. Fig. 3.9 shows the configuration of the sample for the ignition study using induction heating without substrate.

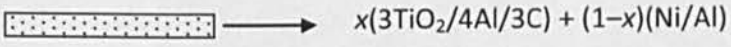

Fig. 3.9. Schematic picture of the Ni/Al + TiO_2/Al/C without substrate

In this composite system, Ni/Al reaction was expected to occur first before the occurrence of further reactions. The high exothermic temperature of the Ni/Al reaction then becomes the ignition source for the second reaction. However, it was indicated that this method was very limited in terms of reactant composition. A higher percentage of TiO_2/Al/C mixture accompanied by a reduction of Ni/Al composition affected the ignition process. It was observed that the maximum percentage of TiO_2/Al/C addition which could still be ignited was 9%. Thus, the use of steel to help the ignition was taken. The configuration of the samples is described in Fig. 3.10.

Fig. 3.10. Schematic picture of the Ni/Al + TiO_2/Al/C with substrate

3.3.3. Fabrication of TiC intermetallic matrix composite coating

This part was focused on the study of the fabrication of a TiC coating on the steel substrate. TiC was synthesized from elemental powders using Ti and C, while Ni/Al was used to generate ignition and to produce an intermetallic matrix. In this work, the sample was configured using multilayer structures, where TiC is placed on the top of the Ni/Al. By considering the result of the preliminary study on the

coating fabrication of NiAl, Ti was used as the underlayer to increase the adhesion with the substrate. Preliminary studies in the present work have shown that the thickness of all layers has a significant effect on the formation of the coating. Since thick coatings were not able to maintain their shapes, the production of coating was then performed using a thin layer to produce a better coating system. In the present work, the thickness of Ti/C, Ni/Al, and Ti layers were 0.40, 0.54 and 0.31 mm, respectively. Compaction of the layers was carried out using a pressure of 200 MPa.

3.4. Microstructure characterizations

The microstructure of synthesized product is greatly affected by its processing route. Microstructure characterization is mainly used to identify the phase constituents and morphology of the product. Identification of product composition can also be used to indicate whether or not the combustion reaction is complete. Meanwhile, the study of product morphology can be used to observe the grain growth and homogeneity of synthesized product. In the present work, microstructure characterization was carried out using a combination of different techniques: light microscopy, X-ray diffraction (XRD), scanning electron microscopy (SEM) equipped with an Energy Dispersive detector (EDS), and laser Raman microspectroscopy.

The observations of the product surface, such as porosity and cracking was done using an optical microscope (FX-35WA Epiphot Nikon, Japan) using Leica DFC295 software, and connected to a monitor screen with a high definition multimedia interface. Scanning electron microscopy (Zeiss EVO50, Germany) was utilized to investigate the microstructure of product focusing on the phase composition and element distribution. SEM was used to obtain two kinds of image, namely backscattered electron mode and secondary electron mode. XRD spectra were recorded using RINT2000 vertical Goniometer which operated at a voltage of 40 kV and a current of 200mA with CuKα radiation (λ = 1.5405 Å), using a continuous scanning mode (2θ/θ), a fixed-angle monochromator with divergence slit of 1 deg., a scatter slit of 1 deg., a receiving slit of 0.3 mm, a scanning step of

0.02 deg. and a scanning rate of 4 deg./min. The analysis data for XRD spectra was executed using MDI Jade 5 software. To study the microstructure of product using SEM and XRD, the samples are required to be polished and etched. Investigation of the microstructure of the samples was initially carried out by cutting the samples about their cross sectional area and mounted with epoxy resin. The surface of the samples was then ground using silica papers with 180 and 600 grits, polished with a sequence of abracloth, nylap, trunoire papers with diamond paste down from 9, 3, to 1 micron, and etched with a mixture of methanol and nitrite acid with volume ratio of 98% : 2% as mentioned by ASTM E407. In particular for the NiAl coating, XRD was used to observe the phases formed in the coating and underlayer. To study the formation of synthesized product in the coating and underlayer, the sample was cut layer by layer. Observation on the formed phases in the coating was conducted by removing a certain layer with the depth of 40 and 70 microns from the coating surface. Meanwhile, the phase formed in the underlayer was observed by cutting the samples with the depth of approximately 400, 500 and 600 microns from the coating surface. The XRD observation was then performed in the solid-flat surface of each layer. To cut the layers, the sample was machined using a CNC milling machine.

In the present work, laser Raman microspectroscopy was also used as tool for microstructure characterization to identify the phases of the synthesized product prepared by Ni/Al and $3TiO_2/4Al/3C$ mixture. The use of laser Raman microspectroscopy was performed to support the chemical analysis of the formed phases completed using SEM and XRD. A laser Raman microspectroscopy test is advantageous since it requires no complex preparation, is rapid and non-destructive. The equipment used was a Renishaw RM1000 Raman spectrometer (Renishaw inVia Raman Microscope, UK) using WiRe 3.3 software and coupled to a Leica DM 2500M optical microscope, and the laser beam focal point being 5–7 μm. The Raman spectra were taken using He–Ne lasers with a maximum power of 500 mW over the wave number in the range of 100–1800 cm^{-1} with an interval of 0.86 cm^{-1}. The samples used for Raman testing obtained from powders and synthesized products were directly tested without polishing and etching. However, the samples

obtained from coatings were mounted in an epoxy resin such that their cross sections could be observed. The samples were mechanically ground and etched using the same procedures as previously described to prepare the samples for the SEM and XRD tests.

Raman spectroscopy has become significantly more important in material characterization since it can be used to identify phase and element distribution of specific molecules in a sample, similar to that of element analysis in X-rays diffraction and electron microscopy techniques. Raman spectroscopy is generally attractive to assess the element composition of ceramic and polymeric materials by simply illuminating their surfaces regardless of their thicknesses and shape. Laser Raman microspectroscopy is the most common spectroscopic technique to assess the molecular motion of a material based on inelastic scattering of a monochromatic light obtained from an excitation source. Different type of lasers can be used as an excitation source such as diode laser, Nd:YAG, He:Ne, krypton ion, and argon ion. When the photon of the laser interacts with a material, it can be absorbed and reemitted. The frequency of the reemitted photon in monochromatic light is shifted up or down compared to its original frequency. Inelastic scattering means that the frequency of the reemitted photon is changed from the original frequency. Raman spectroscopy utilizes the signal of the shifted frequency to provide information about the vibration level of the atomic bond in a molecule. Thus, the signal in Raman spectroscopy in general refers to the vibration band of the photon with a certain wavenumber expressed in cm^{-1}. The peak intensity of the signal is affected by the atomic bond, where the more covalent the bond the higher the Raman peak intensity since there is a higher number of electrons involved [140].

The application of Raman spectroscopy for microstructure characterization can be found in many studies. Raman spectroscopy was used to identify phase composition of coatings composed by different C:N ratios in the TiC, TiN, and $TiC_{1-x}N_x$ systems [141]. Using a Nd-YAG laser, it was shown that laser Raman spectroscopy was very sensitive to a composition difference. As shown in Fig. 3.11, the Raman spectra of the different compositions of $TiC_{1-x}N_x$ were compared with

TiC and TiN. With composition variation of $TiC_{1-x}N_x$, the peak intensity was continuously shifted, where the peaks of intensity increased with an increase in the carbon content, and the content of nitride decreased when the peaks got lower. This indicated that even with a small change in the element composition, the different peaks of band intensities were clearly visible. Additionally, there was band shifting of approximately 10 cm^{-1} as described in TA (transversal acoustic) and LA (longitudinal acoustic) which was thought to be through the effect of laser power, when its increase was observed to produce local heating.

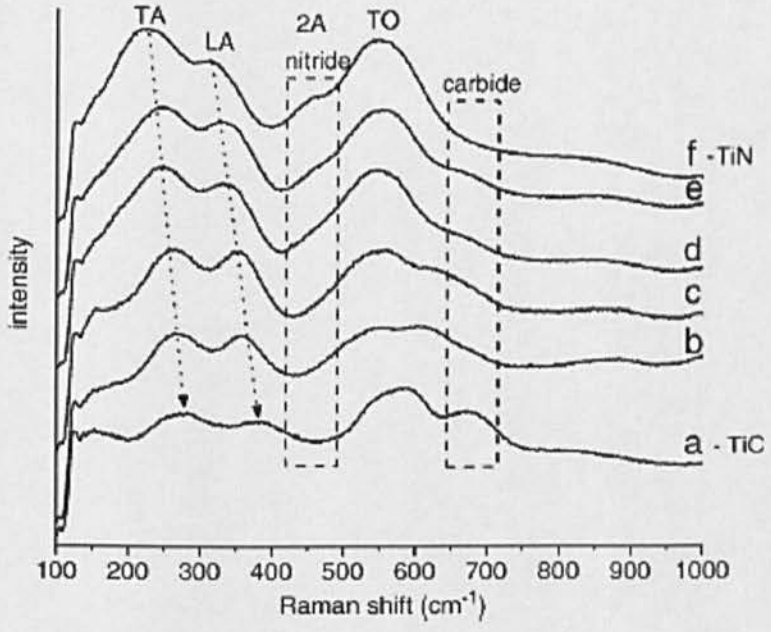

Fig. 3.11. Raman spectra for TiN, TiC, and $TiC_{1-x}N_x$ [141]

3.5. Properties evaluation

Property evaluation in the present work was carried out to investigate the microhardness and adhesion strength. In addition, thermal shock tests were performed to study the adhesion performance of the coating at high temperature.

3.5.1. Hardness test

For the evaluation of mechanical properties, a Vickers microhardness tester (Model Duramin-1/DURA1, Struers) with an objective lens of x40 and an eyepiece

of x10 was used to investigate the microhardness of the synthesized products, which realized using a load of 0.098 N for 15 seconds. The load was selected to produce an impression diagonal of sufficient dimension without producing cracks. At the coating side, the centre of the load was spread wide enough to ensure that there was no influence of the edge and the accommodation of the indentation diagonals [142]. For the measurement of hardness distribution, indents were made along the cross section of the coating, underlayer, and substrate with distances of approximately 30–50 micrometers.

3.5.2. Adhesion strength

Adhesion strength is the property which determines the bonding performance of the coating to the substrate. Some methods which can be used to measure the adhesion strength are a pull-off test, shear test, scratch test and indentation test. In the present work, a Vickers indentation test was used to measure the quality of adhesion at the interface between coating and underlayer. The measurements of adhesion strength were carried out using a Vickers indentation test as demonstrated by Ref. [143] since the measuring technique and sample preparation are relatively simple, and are suitable for small specimens such as thin coatings. The positioning of the top of the punch at the interface region is also possible. In addition, this method did not require adhesive glue such as used in the tensile tests. Indentations were directed to the exact interface between the two layers. Some preliminary trials were required since some indentations were not located in the best position due to the different properties of the materials. Adhesion strength was evaluated using different loads of indenter, and the length of the generated crack was observed.

3.5.3. Thermal shock test

One of the properties affecting the quality and performance of a protective coating is the adhesion strength. Since the NiAl coatings developed in the present work were designed to be resistant in high temperature applications, an awareness of how their performance might be affected in such service conditions is necessary.

In high temperature applications, thermal cycling with sudden changes of heating and cooling might be experienced during coating operation. In this work, thermal shock tests were carried out to investigate the quality of coating adherence after experienced thermal cycling. The test was conducted by repeated thermal shock in a Carbolite furnace with water quenching technique, as demonstrated by J. Lesage et al. [143]. The sample was heated inside the furnace at a temperature of 900 °C (1173 K), and held for 10 minutes to allow the samples to reach temperature equilibrium. The hot sample was then quickly removed from the furnace and dropped into a water bath at room temperature. The thermal shock test was repeated after the specimen had cooled in the water for 5 minutes. The heating cycles were stopped when cracks became visible in the surface of the sample.

Temperature calibration was carried out to control the temperature of the furnace for the thermal shock test. A sample was put in the furnace and heated from room temperature to achieve the temperature required for the thermal shock test at 900 °C (1173 K). The temperature of furnace was monitored using a type–K thermocouple located inside the furnace. The temperature of the sample was observed using another thermocouple which was spot welded to the surface of the sample. The temperature profile of the furnace and the sample are presented in Fig. 3.12. It can be seen that there is no significant difference between the temperature of the furnace and the sample surface. The furnace was able to achieve the temperature required for the thermal shock test at 1173 K after 45 minutes.

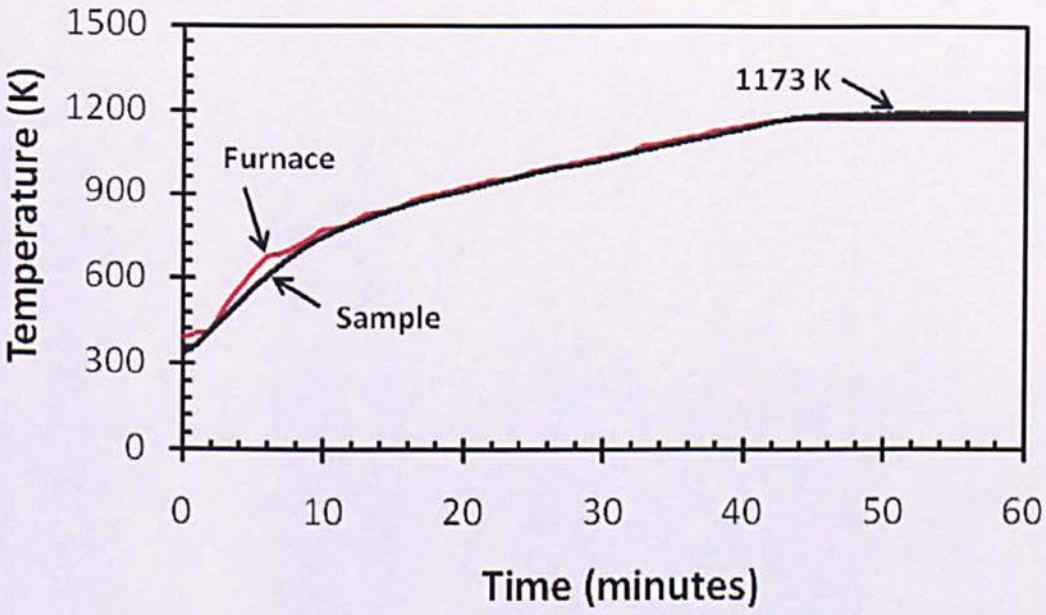

Fig. 3.12. Temperature calibration of furnace

3.6. Summary

This chapter has described the steps used for the preparation of the materials and experimental procedures used for the research, commencing with the preparation of the raw materials, a thorough description of the tools and equipment used for combustion process and their preparation and concluding with microstructure characterization and properties evaluation. The detail of the results and their discussions will be given in the next chapters.

Chapter 4

Combustion Behaviour and Microstructure Characterization of NiAl Coating

This chapter reports a study in the development of a new technique to fabricate NiAl coatings formed by the SHS process on a steel substrate. Induction heating was used to ignite and preheat the substrate and underlayers were used to enhance the adhesion between the coating and substrate. The effect of heating parameters on the combustion synthesis process and microstructure of synthesized product was investigated. The role of underlayer on the microstructure of the product was studied. The formation mechanism of the synthesized products is discussed in this chapter.

4.1. Introduction

NiAl is one of the intermetallics which has shown promising as a candidate of protective coatings for high temperature applications since it offers several advantages, such as high melting point (1911 K), relatively low density (5.86 g/cm^3), high hardness, and good oxidation resistance at elevated temperature [21][64]. The SHS process has been considered as an attractive method to synthesize NiAl and other intermetallics since it produces high heat formations and takes a short processing time [2]. Recent study showed that the fabrication of coating in one step with its synthesis offers an effective process [13]. Researchers have carried out the combination of the SHS ignition and coating fabrication of NiAl in one processing route using different heat sources such as concentrated solar energy [55][64], microwave [11][12], and induction furnace [74][75].

The fabrication of coating combined with the SHS process, however, has a problem in the adhesion between the coating and substrate. The high combustion temperature of the SHS process releases a thermal shock during the synthesis

resulting in the detachment of the coatings from the substrate. In addition, the temperature changes during cooling from a high combustion temperature of the SHS process can generate thermal stresses in the coatings due to the mismatch of coefficient of thermal expansion (CTE) [92]. The thermal stresses will lead to the formation of thermal cracks resulting in poor adhesion strength. Reducing the thermal stresses is therefore required to build strong adhesion.

In the present work, an approach to decrease the thermal stresses in the fabrication of NiAl coating was carried out by a combination of induction heating and underlayer. Induction heating was simultaneously used to ignite the SHS process of Ni/Al system and to increase the temperature of the steel substrate. Meanwhile, an underlayer was applied to reduce the thermal stresses built up at the coatings by decreasing the CTE mismatches. Since the urgency of underlayer was mainly to facilitate adhesion, the underlayer is required to have a mutual diffusion at the interface between the coating and the steel substrate [16]. The material used as underlayer is therefore required to melt during the synthesis process. A high melting temperature of underlayer materials was considered to minimize the CTE difference and to take advantage of its benefit for high temperature applications. The objective of this work, in particular, was to investigate the effect of induction heating parameters on the combustion behaviour of Ni/Al and to study the role of underlayer on the microstructure of synthesized product and the improvement of the coating adherence. Based on the microstructure analysis, the formation mechanism of the synthesized product is discussed.

4.2. Experimental procedures

Commercial carbon steels with a diameter of 16 mm and a thickness of 3 mm was used as the substrate. The surface of substrate was ground and polished to produce a flat and rough surface. Cleaning was accomplished with acetone in an ultrasonic bath for 15 minutes to remove dust, any oil film, and grease from the surface. The moisture contained in the surface was then evaporated by drying with hot air.

Nickel (Ni) carbonyl type–123 and aluminium (Al) and titanium (Ti) were used as material for the reactant and underlayer. The specification of the reactants is given in Table 3.1 (Chapter 3). Ni and Al powders were weighed with an atomic ratio of 1:1, and subsequently mixed and crushed using a ceramic mortar to achieve a mixture which is as homogenous as possible. The mixture was placed in a furnace at 100 °C for 1 hour to evaporate its moisture content. The mixture was cold compacted using a steel die package to form green pellets. The Ti powder which used as underlayer was poured into the die container, above the compacted Ni/Al pellet, and compressed to form two layers. The schematic diagram of the sample is described in Fig. 4.1. The finished thickness of Ni/Al was 0.54 ± 0.01 mm, while the thickness of underlayer was varied with 0.31 mm, 0.53 mm and 0.83 mm. Finally, the compacted pellets were placed on the substrate to prepare for the synthesis reaction. The schematic diagram of the experimental set up is given in Fig. 3.3 (Chapter 3).

Fig. 4.1. Schematic configuration of the coating, underlayer and substrate

The tests were started by programming the current and time of induction heating according to the heating requirement. Water circulation was turned on prior to the induction process to avoid coil overheating. When the SHS process of the sample had been initiated, induction heating was turned off about one second after ignition. The different processing parameters observed in the present work consist of the variation of currents (150 A, 200 A, 250 A and 300 A), the variation of underlayer thickness (0.31 mm, 0.53 mm and 0.83 mm), the variation of compaction pressures (100 MPa, 150 MPa, and 200 MPa), and the variation of underlayer materials with different melting points (Al, Ni, and Ti).

The measurement of the combustion temperature was carried using a combination of type–K thermocouple which has a temperature range of -50 – 1100 °C and non contact infrared pyrometer type Marathon MM which has capability to measure high temperatures in the range of 540 – 3000 °C. The microstructure

characterization of the product was carried out using SEM (Zeiss EVO50, Germany) and XRD (RINT2000 vertical Goniometer) using a scanning rate of 4 deg./min. The samples used for the microstructure characterization were polished and etched using standard procedures as described in Chapter 3.

4.3. Results and discussion

4.3.1. Calculation of the adiabatic temperature

The adiabatic temperature of combustion synthesis was calculated to predict the maximum combustion temperature without the heat loss during the process. The calculation of adiabatic temperature in reaction (4.1) is accomplished using the principle of the first law of thermodynamics [119] as given in Eq. (4.2). In the calculation of adiabatic temperature, three assumptions are made [139]. Firstly, it is assumed that the reaction occurs in adiabatic condition since the reaction occurs in a fast heating rate indicating that there is no heat loss and heat gain during the process. Secondly, all the reactants are consumed and the reaction proceeds to complete by producing NiAl without any intermediate phases. Thirdly, the reactants are heated to a uniform temperature.

Since the reaction is assumed to produce a single phase NiAl, the combustion synthesis of Ni/Al prepared from elemental powders can be expressed according to Eq. (4.1).

$$Ni + Al \rightarrow NiAl + 118.4\ kJ/mol \qquad (4.1)$$

In adiabatic condition, all the heat of formation is used to convert the reactants into product without heat losses. As a consequence, the adiabatic temperature then becomes the maximum temperature of the reaction that can be achieved. The calculation of the adiabatic temperature of NiAl reaction can be determined using Eq. (4.2).

$$\Delta H_{298,NiAl} + \int_{298}^{1911} C_{p,NiAl}\,dT + H_{L,NiAl} + \int_{1911}^{Tad} C_{p,NiAl}\,dT = 0 \qquad (4.2)$$

where ΔH_{298} is the enthalpy of reaction at 298 K, C_p is the heat capacity of element, H_L is the latent heat of phase transformation, and T_m is the melting temperature. The heat capacity of element is influenced by temperature as formulated by Eq. (4.3) as follows:

$$C_p = A + BT + CT^{-2} + DT^2 \tag{4.3}$$

where *A*, *B*, *C*, and *D* are the constants, and *T* is the variable of temperature. The thermodynamic data of the materials including the specific heat (C_p) and temperature transition (T_{trans}) are taken from Kubaschewsky's book as given in Table 4.1 [120]. Enthalpy of the reactants and product is obtained by integrating the specific heat of each material. The equations used to calculate the enthalpy are given in Table 4.2, where the melting heat of Al, Ni and NiAl is given in parenthesis in order to distinguish between the latent heat and the heat obtained from the specific heat. The result of enthalpy calculation obtained from Eq. (4.2) is presented in Fig. 4.2.

Table 4.1. Thermodynamic properties of Al, Ni, and NiAl [120]

Sub-stance	Phase	T_{trans} (K)	H_{298} (kJ/mol)	$C_p = A + BT + CT^{-2} + DT^2$ J/deg. mol				H_L (kJ/mol)
				A	B	C	D	
Al	fcc	298	0	31.38	-1.64E-02	-3.60E+05	2.07E-05	
	liquid	934		31.76				10.7
Ni	fcc	298	0	11.17	3.78E-02	3.18E+05		
	fcc	631		20.54	1.01E-02	1.54E+06		
	liquid	1728		38.91				17.2
NiAl	cubic	298	-118.4	41.84	1.38E-02			
	liquid	1911		71.13				57.6

Table 4.2. Equations used for enthalpy calculations

Enthalpy (J/mol)	Temperature (K)	Equations
H_{Al}	298 - 933	$-10014.14 + 31.38T - 3.6 \times 10^5 T^{-1} - 8.2 \times 10^{-3} T^2 + 6.92 \times 10^{-6} T^{-3}$
	934	-11487.8 + 31.76T + (10700)
H_{Ni}	298 – 631	$-3939.94 + -3.18 \times 10^5 T^{-1} + 1.89 \times 10^{-2} T^2$

	631 – 1728	$-2401.27 + 20.54T - 1.54 \times 10^{6}T^{-1} + 5.05 \times 10^{-3}T^{2}$
	1728	-19956.61 + 38.91T + (17200)
H_{NiAl}	298 – 1911	$-131481.07 + 41.84T + 6.9 \times 10^{-3}T^{2}$
	1911	-162258.91 + 71.13T + (57600)

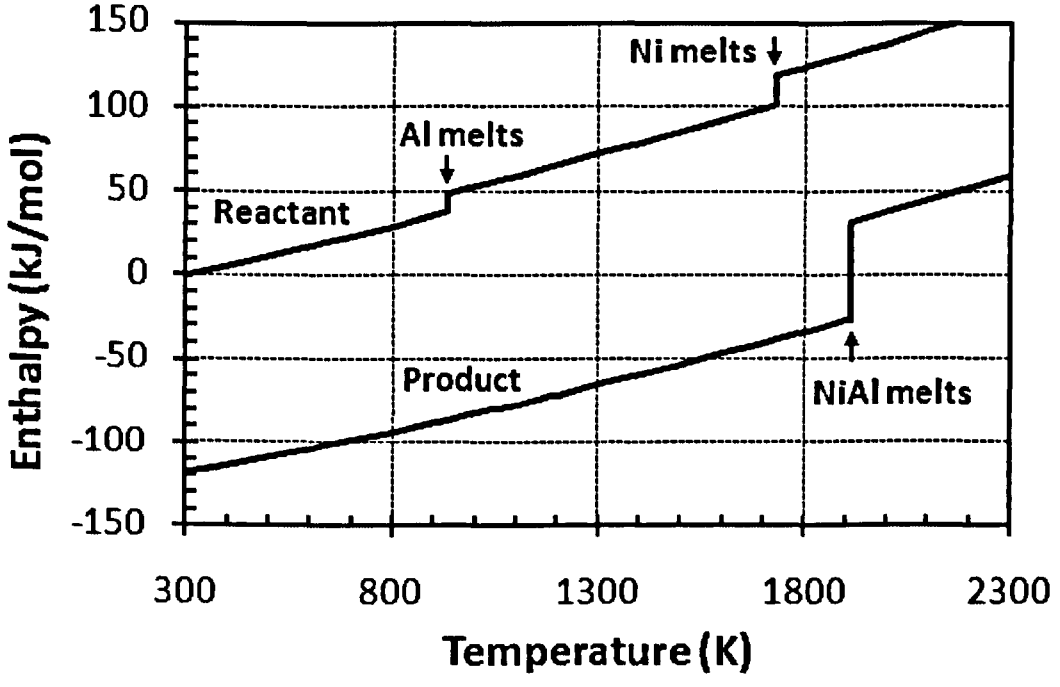

Fig. 4.2. The enthalpy versus temperature diagram of Ni/Al

Fig. 4.2 shows the enthalpy versus temperature diagram of Ni/Al. The result of this calculation is in well agreement with that obtained by Ping Zhu [24], although the data for the melting heat are different. According to the present result, when the Ni/Al reaction is initiated at room temperature, the adiabatic temperature of Ni/Al reaction in Eq. (4.1) is 1911 K, which is the same as the melting temperature of NiAl. This indicates that a part of the synthesized product is in the liquid phase before it solidifies. To expect the synthesized product is fully melted during the reaction, it is required to preheat the reactants to produce the adiabatic temperature above the melting point of the product. The effect of preheating temperature (T_{pre}) on the adiabatic temperature (T_{ad}) for the SHS process of Ni/Al can be calculated using Eq. (4.4). The result of calculation is presented in Fig. 4.3.

$$\left[\Delta H_{298,Ni} + \Delta H_{298,Al}\right] + \int_{298}^{T_{pre}} \left[C_{p,Ni} + C_{p,Al}\right] dT -$$

$$\left[\Delta H_{298,NiAl} + \int_{298}^{1911} C_{p,NiAl}\, dT + H_{L,NiAl} + \int_{1911}^{Tad} C_{p,NiAl}\, dT\right] = 0 \qquad (4.4)$$

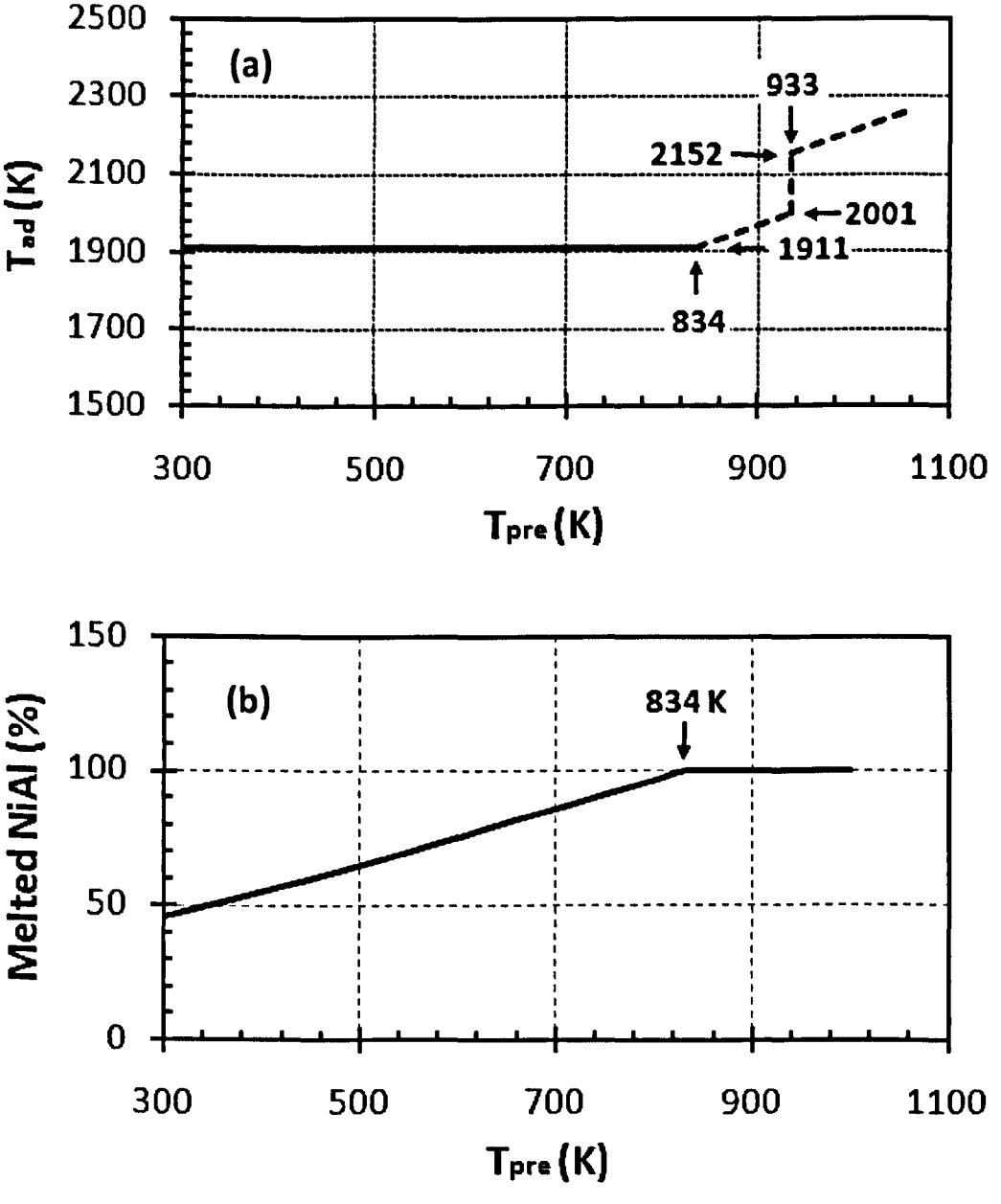

Fig. 4.3. The effect of preheating temperature on: (a) adiabatic temperature of NiAl; (b) fraction of melted NiAl

Fig. 4.3 shows the effect of preheating temperature on the adiabatic temperature for Ni/Al reaction and the fraction of melted NiAl. It can be seen in Fig. 4.3(a) that the adiabatic temperature of Ni/Al reaction is remained the same at 1911 K when the preheating temperature is increased from 298 to 834 K. This shows that the adiabatic temperature is equal to the melting point of NiAl. When the reaction is initiated below 834 K, the synthesized product is a mixture of solid and liquid. The fraction of melted NiAl as a function of preheating temperature is shown in Fig. 4.3(b). This graph is obtained using Eq. (4.2), while the fraction of melted NiAl is determined by dividing the heat of product at T_{pre} with the latent heat of fusion of NiAl (57.6 kJ/mol). The result shows that when the reaction is initiated at room temperature without preheating, the amount of melted NiAl is 45.6%. Increasing the preheating temperature above 834 K will increase the adiabatic temperature to above the melting point of NiAl and the amount of the melted NiAl becomes 100%. This indicates that the synthesized product is fully melted. The adiabatic temperature above the melting point of Al is illustrated in a dotted line for a prediction since there is no exact temperature range for the specific heat of Al, Ni and NiAl after melting. The result of calculation indicates that increasing the preheating temperature to the melting point of Al at 933 K will increase the adiabatic temperature from 2001.6 K to 2152.04 K, where its increase is dependent on the fraction of melted Al.

4.3.2. Measurement of temperature profile

The temperature profile of combustion synthesis was measured to describe the thermal history of the process. In the fabrication of NiAl coating conducted in the present work, there are three components in which their temperatures have been affected, namely Ni/Al system, titanium underlayer, and the steel substrate.

4.3.2.1. Temperature profile of Ni/Al reaction

The combustion temperature of Ni/Al systems was investigated to show their combustion behaviours during the SHS process and coating fabrication. Fig. 4.4 shows the combustion temperature of Ni/Al system ignited by varied currents

of induction heating from 150, 200, 250, to 300 A. When using 150 A, there is no sharp increase of the temperature indicating that the heat supplied by induction heating was insufficient to initiate the combustion synthesis. Thus, only the currents of 200 A, 250 A and 300 A which produce a sharp increase of combustion temperature showed that Ni/Al reaction was complete. It can be seen that the SHS process using 200–300 A produces a temperature profile with a similar trend. The combustion temperature increases from its initial conditions at room temperature to achieve an ignition point in which the combustion temperature then rises sharply to reach a maximum point. When the combustion was completed, the temperature quickly decreases to a temperature which then forms a plateau for a period of time and is followed by a decrease to room temperature. At approximately 813 K, there is a sharp rise of temperature under all the heating rates which indicates that the ignition point of Ni/Al reaction is independent of the variation of current. In most Ni/Al reaction, the ignition point occurs at the melting point of Al (933 K). However, a lower ignition temperature in the present work show a similar result as obtained in Ref. [17]. A lower ignition point may be related to the particle size of the reactants which affects the heat transfer during heating. From the initial temperature to the ignition point, the combustion temperature increases with different heating rates depending on the currents. An increase in the current of induction heating results in the increase in the heating rate. As a consequence, it shortens the ignition time, which is referred to as the time required by the sample to achieve an ignition point from an initial condition. The average heating rate of the heating using currents of 300, 250, 200, and 150 A is 85.5, 57.0, 46.6, and 15.9 K/s, respectively. The maximum combustion temperature of all reactions shows the same temperature at approximately 1911 K, which can be associated with the melting temperature of NiAl. The combustion temperature decreases from its maximum value to a certain temperature where it then becomes steady forming a plateau at a temperature in the range of 1095–1291 K for different currents. It can be seen that the temperature level of the plateau is reduced with a decrease in the current. The average temperature of the plateau is approximately 1291, 1211.3, and 1185.6 K for the currents of 300, 250, and 200 A, respectively. The formation of plateau after reaching a maximum value was previously observed in the SHS

process of Ni/Al, which describes the phase transformation of NiAl at about 1911 K [17]. However, the present finding is somewhat surprising that the temperature of plateau was varied with the variation of currents. Further investigation is required to determine exactly on how the current affects the formation of the plateaus.

The present temperature profiles as shown in Fig. 4.4 shows that the chronology of combustion synthesis for Ni/Al system consists of four stages: initial heating, combined ignition and combustion, plateau, and cooling. This trend is generally consistent with that obtained by the previous investigation reported by Zhu et al. [17]. However, the present result shows that after reaching a maximum point, the combustion temperature decreases immediately. This can be attributed to the existence of titanium underlayer and the steel substrate used in the present work which has become a heat sink which quickly absorbed the heat released by the Ni/Al reaction and resulted in the sharp fall of the combustion temperature.

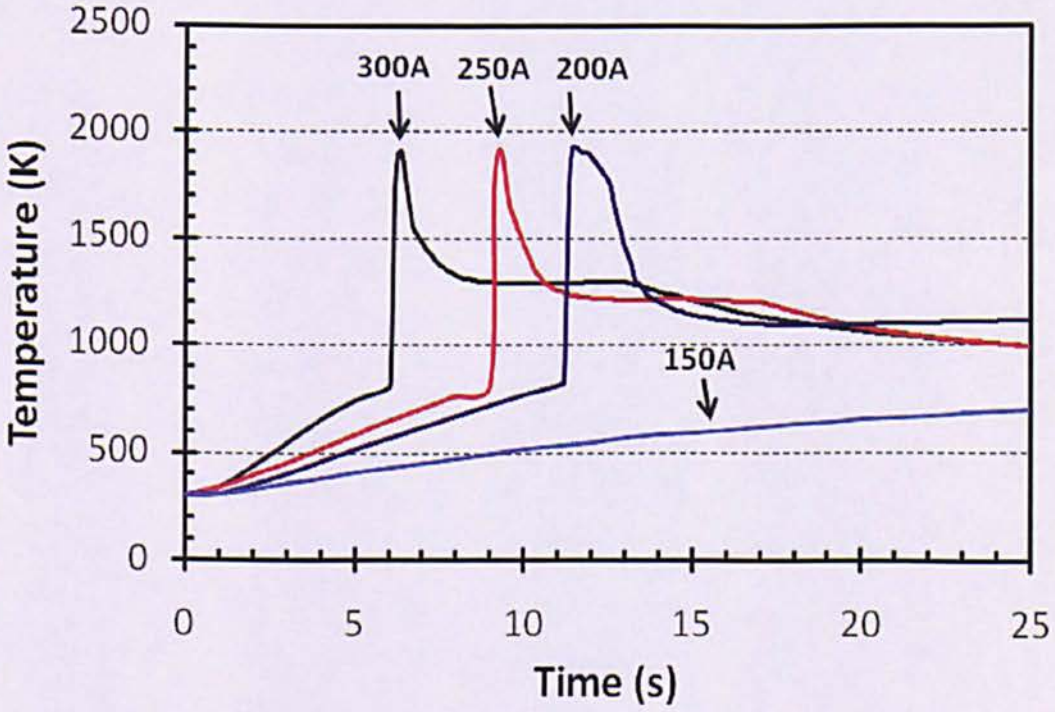

Fig. 4.4. Temperature profile of NiAl/Ti using varied currents of induction heating

4.3.2.2. Temperature profile of Ti

In the fabrication of NiAl coating using titanium as underlayer, titanium was required to melt in order to facilitate adhesion between the coating and the substrate. Since the heat supplied by induction heating was insufficient to melt Ti due to the heat loss, its melting was mainly achieved by the heat released by Ni/Al reaction. To investigate the temperature profile of titanium during the SHS process of Ni/Al system, a sample composed of compacted Ti and Ni/Al mixture was heated by induction heating with a current of 300 A for 9 s. No substrate was used in this test in order to facilitate the temperature measurement on the surface of Ti. Fig. 4.5 shows the schematic configuration of Ti/NiAl where Ti was compacted in the top of the Ni/Al mixture. The thickness of the Ni/Al and Ti is 0.54 mm and 0.53 mm, respectively. The measurement of Ti during heating was carried out using a pyrometer using $\varepsilon = 0.95$ as described in Chapter 3. Fig. 4.6 shows the temperature profile of titanium in the Ti/NiAl system after heated by induction heating. It can be seen that the temperature of Ti increases from its initial condition at room temperature to a maximum value at 1941 K. The maximum temperature of Ti which achieves 1941 K indicates that titanium has melted during the synthesis reaction of Ni/Al system. The result in this study indicates that the heat released by Ni/Al reaction was sufficient to melt Ti for the specific ratio between the two. When the melting of Ti was completed, the temperature is decreased slightly and followed by the formation of a plateau for a period of time. The formation of plateau after melting is surprising since the temperature of Ti should be decreased to room temperature instead of producing a high temperature plateau. This result then suggests that after the Ti was melted, there were mixing and further reactions between the molten Ti and the liquid Ni/Al. Further data collection obtained by the microstructure characterization will be presented to confirm the products in the reaction of the molten Ti and liquid Ni/Al.

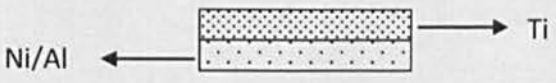

Fig. 4.5. Schematic configuration of Ti/NiAl

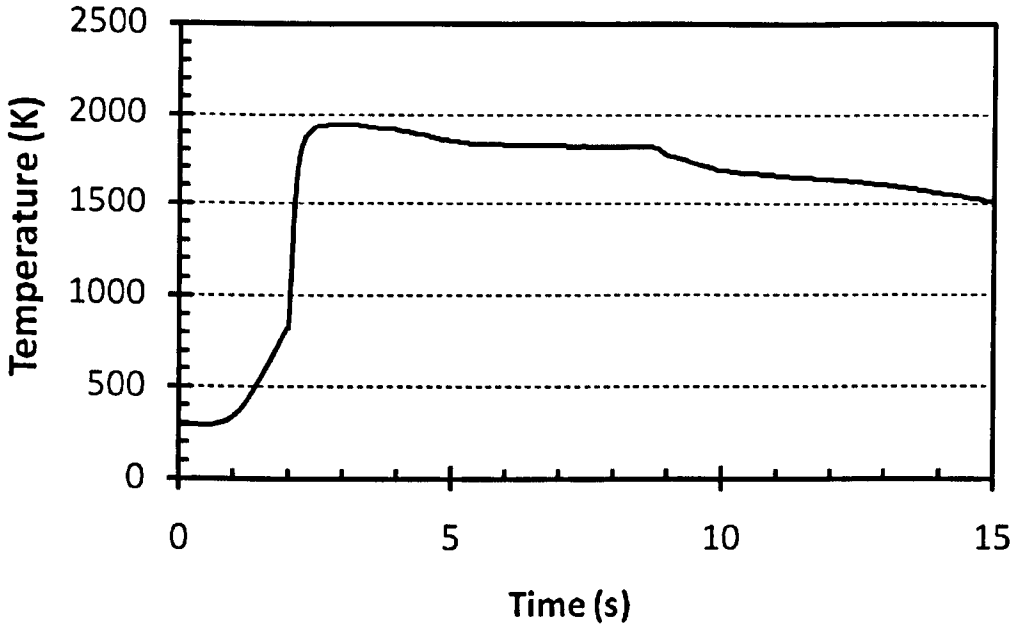

Fig. 4.6. Temperature profile of Ti underlayer heated by Ni/Al reaction

4.3.2.3. Temperature profile of steel substrate

The use of induction heating in the present work was not only to ignite the SHS process of Ni/Al system, but also to increase the temperature of substrate. The temperature of the steel substrate was measured to observe its response during the fabrication of NiAl coating using induction heating. The temperature increase of the steel substrate can be caused by the heat conducted by titanium and induction heating. The investigation on the temperature increase of the steel substrate was conducted without the presence of Ni/Al or Ti. The steel disc with a diameter of 16 mm and a thickness of 3 mm was heated by induction heating with the currents of 300, 250, 200, and 150 A. The temperature monitoring was carried out using thermocouple embedded in a shallow groove with the depth of approximately 1 mm which spot welded on the centre of the surface. Induction heating to the steel substrates was stopped when their temperatures have achieved about 1000–1200 K to avoid their melting. Fig. 4.7 shows the temperature profile of the steel substrate heated by different currents of induction heating. It can be seen that the temperature of steel substrate increases depending on the current of induction heating. An increase in the current leads to an increase in the heating rates.

Although the temperature profile of the steel substrate was obtained without the presence of Ni/Al and Ti, it can be used to estimate the substrate temperature during the combustion synthesis and coating fabrication of NiAl on the steel substrate. For instance, in the Ni/Al reaction using a current of 300 A shown in Fig. 4.4, the ignition occurred at about 6 s from its initial heating. This indicates that after 6 s the steel has achieved a temperature of about 928.1 K, as shown in Fig. 4.7. Using the same procedure, the temperature of steel substrate for the SHS of Ni/Al using 250 and 200 A is 953.3 and 927.7 K, respectively. This shows that the temperature of steel substrate at the ignition point of Ni/Al is almost the same for all reactions. However, it is worth noting that the temperature increase of the steel substrate in this study was used only for estimation purpose since its actual temperature may also be affected by the heat obtained by titanium through conduction mechanism.

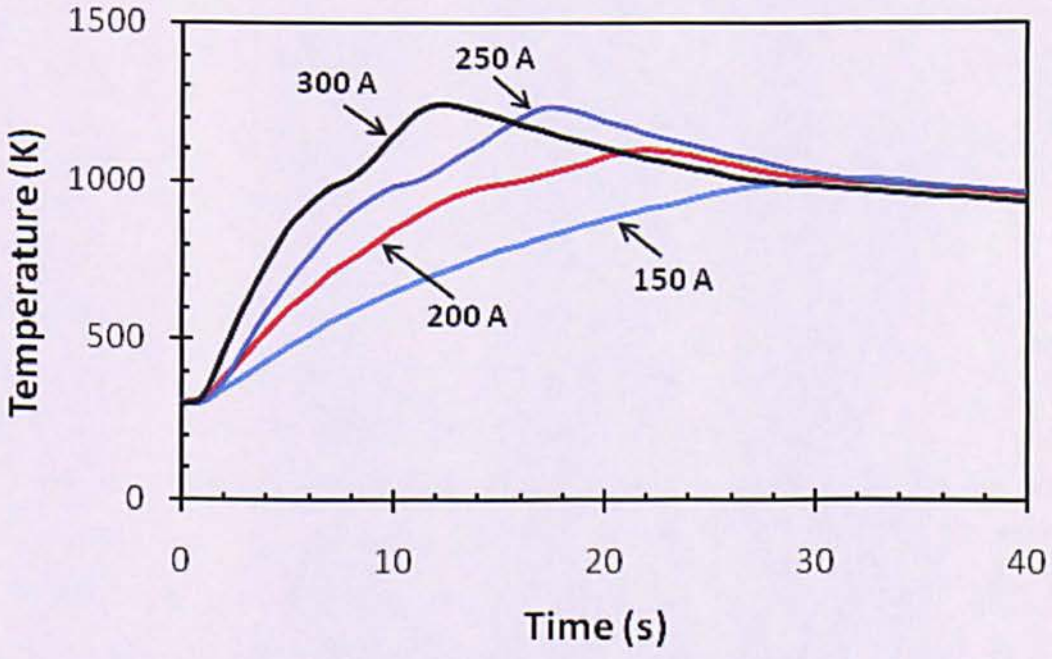

Fig. 4.7. Temperature profile of the steel substrate heated by induction heating with various currents

4.3.3. Microstructure characterizations

4.3.3.1. Phase identification

The phase identification of the synthesized products was mainly carried out using XRD technique. The reactant mixtures were prepared using Ni/Al mixtures and Ti as underlayer which compacted using a pressure of 200 MPa, and heated by induction heating with a current of 300 A. The thickness of Ni/Al mixtures was 0.54 mm, while the thickness of underlayer was 0.31 mm, 0.53 mm and 0.83 mm. Fig. 4.8–10 show the XRD spectra of the synthesized products obtained from the samples with the underlayer thickness of 0.31 mm, 0.53 mm and 0.83 mm. The XRD spectra of the samples were observed at different depths below the coating surface. To show the location of the observation in the coating and underlayer, the related SEM micrographs taken on the cross sectional area of the products are given in section 4.3.3.2.

a) Sample with underlayer thickness of 0.31 mm

Fig. 4.8(a) and (b) show the XRD spectra of the sample with underlayer thickness of 0.31 mm which were observed in the depth of 40 μm and 70 μm below the coating surface, respectively. All spectra were taken in the coating zone which therefore describe the phases existed in the coating. It can be seen that the XRD spectra in the coating zone show the formation of NiAl, $Ni_{0.58}Al_{0.42}$, and $Ni_{1.04}Al_{0.96}$ phase. The presence of these phases indicates that the combustion synthesis of Ni/Al has proceeded to complete and formed a stoichiometric and substoichiometric phases of NiAl. In particular, the presence of $Ni_{0.58}Al_{0.42}$ and $Ni_{1.04}Al_{0.96}$ suggests the formation of NiAl with Ni–rich. A possible explanation for the formation of Ni–rich of NiAl might be due to the melting of Al (T_{melt} = 933 K) which occurred first before Ni (T_{melt} = 1728 K) during the Ni/Al reaction resulting in the amount of Al which spread into Ti underlayer is higher than that of Ni. The existence of Ni_xAl_y is generally dependent on the chemical composition of the raw material, particularly on the ratio of Ni and Al. However, the present work implies

that the deviation from the nominal formula of NiAl is attributed to the diffusion of liquid Al and Ni, as also suggested by Ref. [144] and [145].

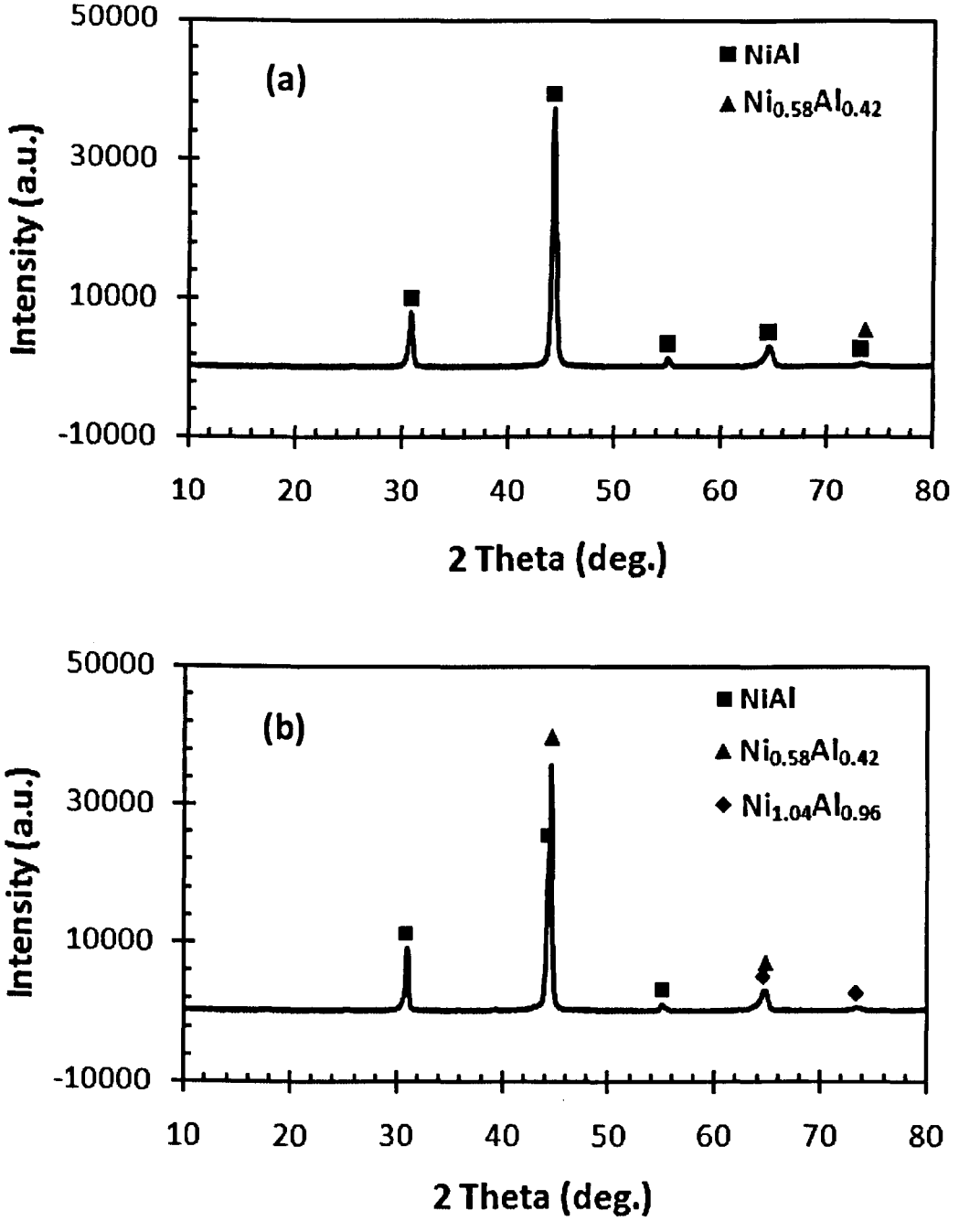

Fig. 4.8. XRD spectra of the sample with underlayer thickness of 0.31 mm observed at: (a) 40 μm; and (b) 70 μm below the surface

b) Sample with underlayer thickness of 0.53 mm

Fig. 4.9(a) and (b) show the XRD spectra of the sample with underlayer thickness of 0.53 mm which were observed in the depth of 40 μm and 600 μm below the coating surface, respectively. The first spectra were taken in the coating zone; while the second spectra were taken in the underlayer zone. It can be seen that the XRD spectra of the coating in Fig. 4.9(a) show the formation of NiAl, $Ni_{0.58}Al_{0.42}$, $Ni_{0.9}Al_{1.1}$ and Ni_2Al_3. It is apparent that the majority of the phase in the coating is NiAl with Ni–rich. As explained before that this is due to the melting of Al resulting in a decrease of Al content in the coating adjacent to underlayer. The presence of a small amount of $Ni_{0.9}Al_{1.1}$ shows the formation of Al–rich of NiAl indicating a higher content of Al in that phase, while Ni_2Al_3 indicates the existence of the intermediate phase of NiAl due to an uncompleted Ni/Al reaction. This result suggests that an increase in the underlayer thickness produced an incomplete reaction of Ni/Al which resulted in the formation of intermediate phase of NiAl. A possible explanation for this might be that an amount of the heat released by Ni/Al reaction was absorbed by the underlayer leading to an insufficient energy to finish the SHS process of Ni/Al.

Fig. 4.9(b) shows the XRD spectra in the underlayer of the sample using underlayer thickness of 0.53 mm. It is evident from this result that Ti_2Ni, Ti_3Al, $AlNi_2Ti$ and Ti were formed in the underlayer. Ti_2Ni has the strongest peak compared with that of other phases which should be attributed to the largest amount of the Ti_2Ni. The XRD spectra also detect the formation of Ti_3Al in the underlayer. The formation of Ti_2Ni and Ti_3Al shows the reaction product of Ti–Ni and Ti–Al systems, respectively. A small amount $AlNi_2Ti$ was also observed in the underlayer which indicates the reaction of Ni–Al–Ti system. Meanwhile, the presence of Ti in the underlayer can be attributed to the existence of unreacted Ti. An unexpected appearance of Fe_2Ti_4O occurs in the underlayer which might be due to the presence of Fe melts and oxygen resulting in the formation of oxides.

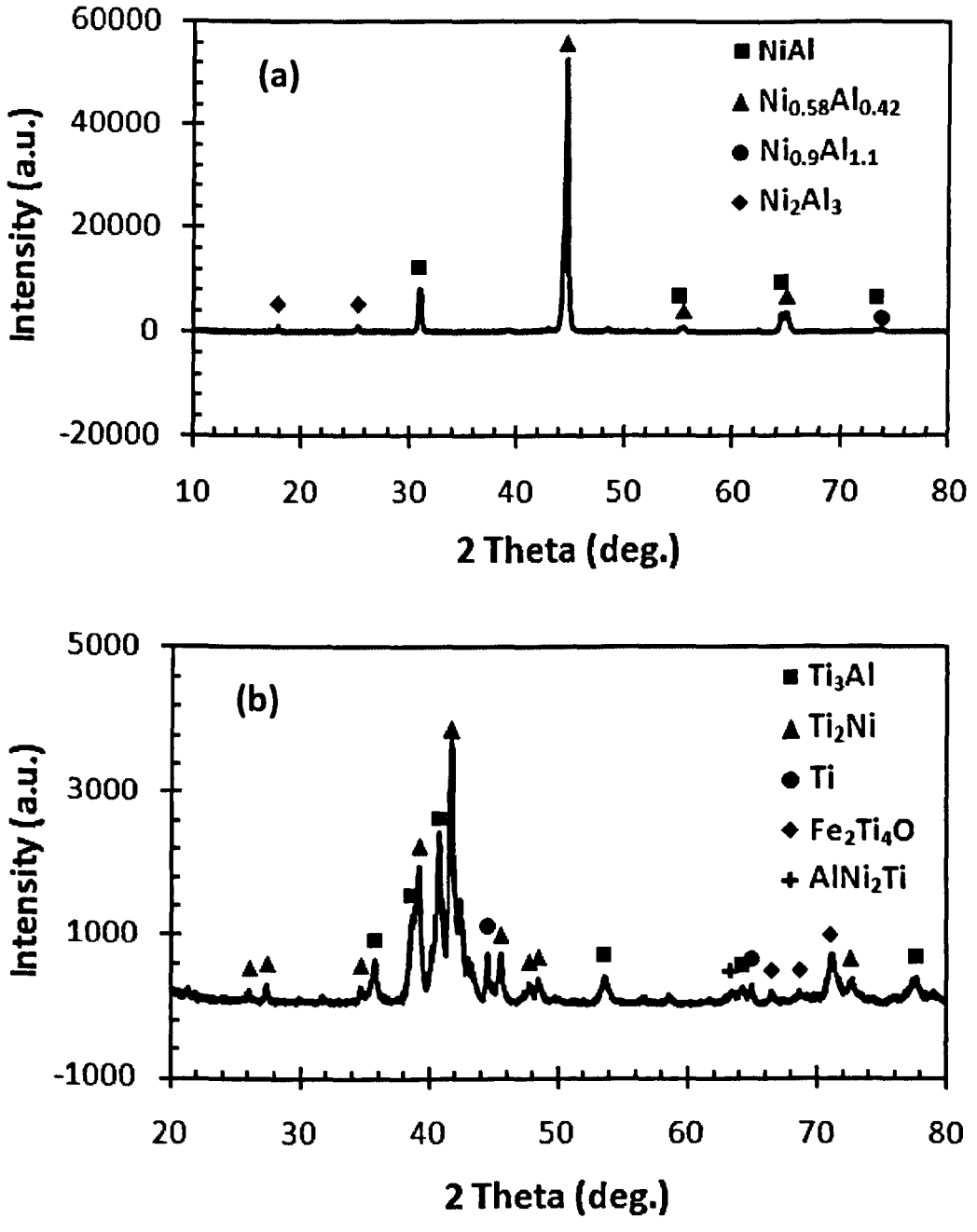

Fig. 4.9. XRD spectra of the sample with underlayer thickness of 0.53 mm observed at: (a) 40 μm; and (b) 600 μm below the surface

c) Sample with underlayer thickness of 0.83 mm

Fig. 4.10(a), (b) and (c) show the XRD spectra of the sample with underlayer thickness of 0.83 mm. Fig. 4.10(a) shows the XRD spectra which were observed in the coating area with the depth of 40 μm; while Fig. 4.10(b) and (c) show the XRD

spectra which were taken in the underlayer zone with the depth of 400 μm and 500 μm. In the coating zone as shown in Fig. 4.10(a), the spectra show the phase of NiAl and $Ni_{1.04}Al_{0.96}$ which indicate the formation of Ni–rich of NiAl. In Fig. 4.10(b), the XRD spectra show a significant amount of Ti_2Ni, Ti_3Al and Ti, and a small amount of Ti_6O. The existence of Ti_2Ni and Ti_3Al and Ti indicates the main phases observed in the underlayer. Meanwhile, the presence of Ti_6O in the underlayer indicates the formation of titanium oxide which can be categorized as non-stoichiometric oxides deficient oxygen. By referring to the phase diagram of Ti–O system, it can be confirmed that when titanium is heated to 400–600 °C, the oxidation state of titanium can be formed. Their existences are caused by the diffusion of oxygen through the melted surface into the bulk titanium due to the fast heating and cooling [146]. The different sources of oxygen can exist during the SHS process such as from the pores formation. In Fig. 4.10(c), the XRD spectra show the presence of Ti_2Ni, Ti and Ti_6O. However, it can be seen that the dominant phase of the scanned area is Ti. The spectra of Ti have peaks at (100), (002), (101), (102), (110), (103), and (201). These peaks are consistent with α–Ti peaks as also confirmed by Ref. [146]. This result suggests that the majority of phase observed in the underlayer with a thickness of 0.83 is unreacted Ti.

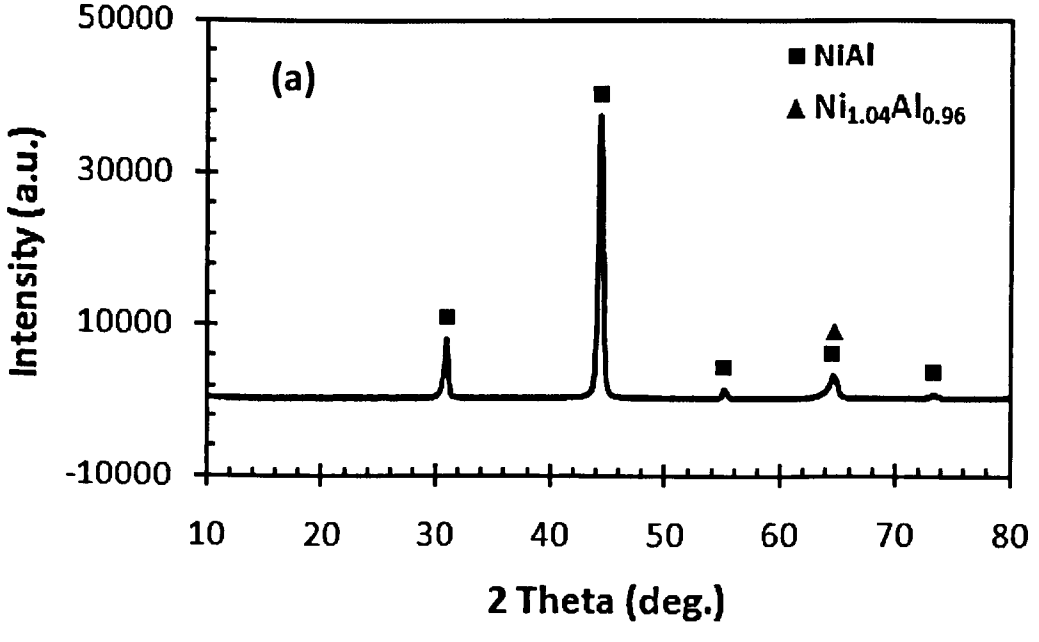

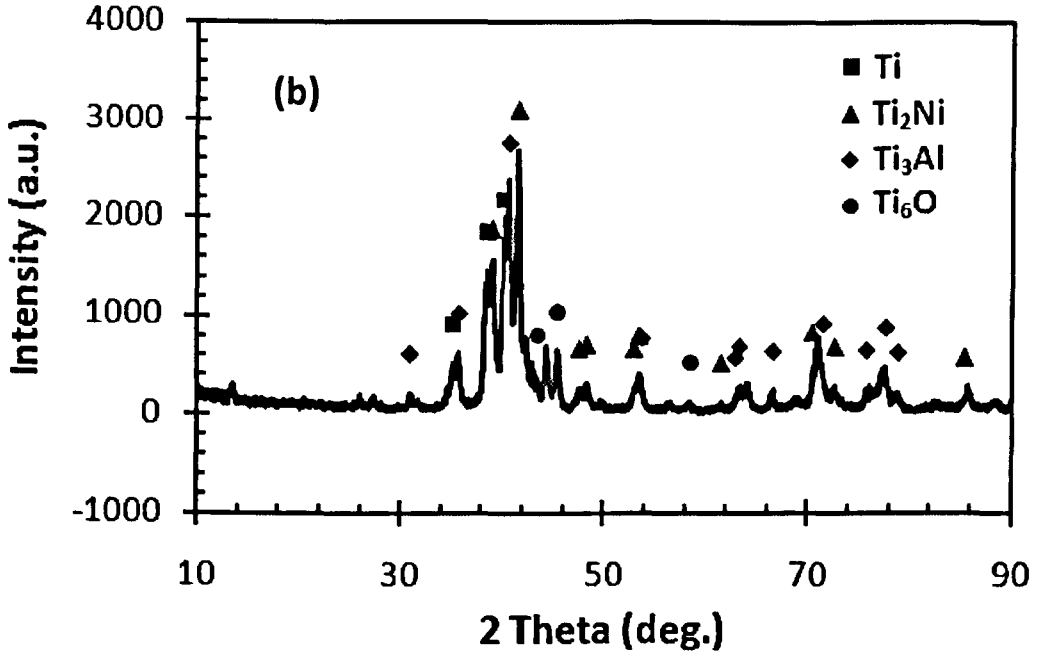

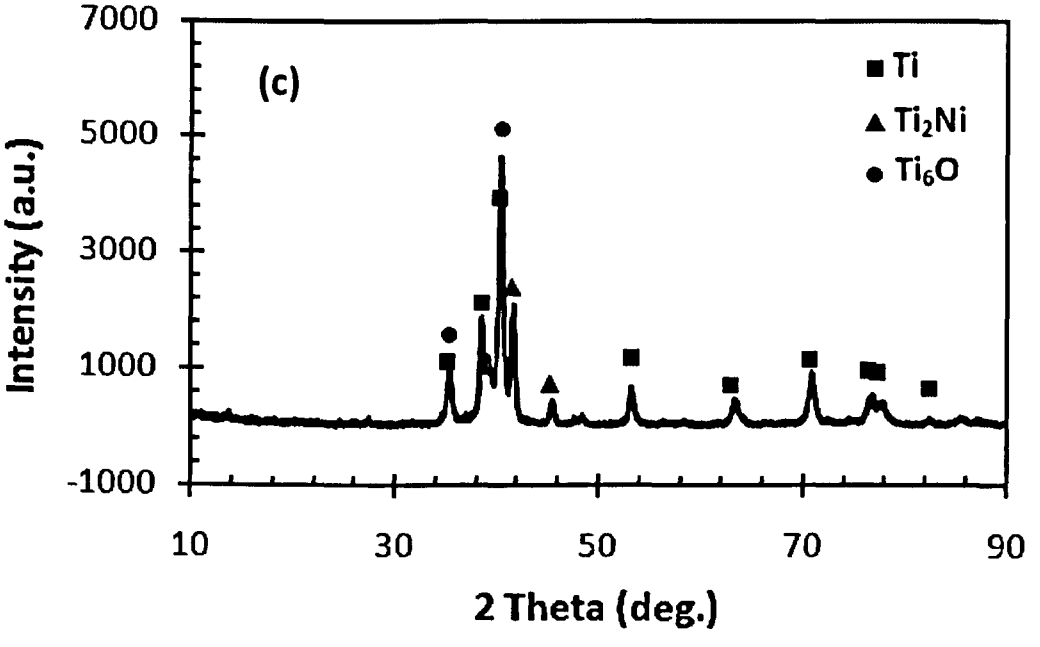

Fig. 4.10. XRD spectra of the sample with underlayer thickness of 0.83 mm observed at: (a) 40 μm; (b) 400 μm; and (c) 500 μm below the surface

4.3.3.2. SEM micrographs

Fig. 4.11, Fig. 4.12 and Fig. 4.13 show the cross sectional SEM micrographs of the synthesized products with underlayer thicknesses of 0.31 mm, 0.53 mm and 0.83 mm. The samples were compacted using a pressure of 200 MPa and synthesized using induction heating with a current of 300 A. The figures show that the structural morphology from the coating to the substrate can still be divided into two distinct layers, namely the coating and the underlayer. It is observed that the coating surface is flat which indicates that the coating could maintain its shape during the exothermic reaction of the SHS process. Meanwhile, the interface between the coating and underlayer is a bit wavy but is still relatively parallel to the substrate surface, which demonstrates a planar growth of the formed phases. Although the coatings were prepared with a thickness of 0.54 mm, the thickness of coatings becomes much reduced to about 200 μm which indicates that a part of the NiAl coating has diffused into the underlayer and formed different phases. In the underlayer, the appeared mixed phases indicate that the titanium underlayer has been transformed into new phases in the underlayer. It is also shown that the presence of underlayer has facilitated good adhesion between the coating and the substrate. A fully fused interface between the underlayer and substrate is clearly evident. The bond line between the underlayer and substrate is free from discontinuities or cracks. The back scattered mode as illustrated in the SEM result also shows that the NiAl coating is relatively dense, which can be thought as the formation of liquid phase during the combustion synthesis. A small amount of pores appears in the coating and underlayer which can be attributed to the entrapped gas evolved during the SHS reaction. The gases may come from the low boiling point of impurities in the reactant or the absorbed gas from the surface. Due to a short time of the SHS reaction, the entrapped gases could not rise to the surface resulting in the porosity [49].

(a). Description of the phase in the Fe substrate

In Fig. 4.11, the back scattered electron micrograph indicates that the substrate contains a homogeneous phase. The chemical composition of Fe atoms

obtained by semi quantitative EDS analysis as given in Table 4.3 shows that the substrate which marked by the spot A is mainly composed of Fe atoms with some impurities of Mn and S. The substrate surface located near the underlayer tends to become brighter since the grain size of the substrate in the surface appears to grow bigger than that in other locations. The grain coarsening in the substrate surface indicates that the surface of Fe substrate has melted and cooled down which might be due to the combination of the heat released by Ni/Al reaction and the heat generated by induction heating.

(b). Description of the phases in the coating

The SEM micrograph of the coating zone as shown in Fig. 4.11 indicates that the coating contains grey and bright phases marked by the spot B and C. The analysis of chemical composition as given in Table 4.4 shows that the phase B is composed of Ni and Al that have an atomic percentages of 0.58 and 0.42, respectively, while phase C is composed of Ni and Al with an atomic percentage of 0.45 and 0.54, which is close to 1: 1. By referring to XRD result shown in Fig. 4.8, the phase B indicates the formation of NiAl phase with Ni–rich, whilst the phase C corresponds to NiAl. The formation of NiAl with Ni–rich composition in the coating area shows that an amount of Al was firstly melted during the Ni/Al reaction causing an amount of Al to spread into Ti underlayer.

(c). Description of the phase in the underlayer

In the underlayer as shown in Fig. 4.11, the visible phases are complex and heterogeneous. It can be clearly seen that there are several available phases which compose the synthesized product in the underlayer. The heterogeneous phase appeared in the underlayer suggests that there were reactions and interdiffusion between Ti and NiAl which formed new interfacial products during the synthesis reaction.

Fig. 4.12 shows the back scattered SEM micrograph of the sample with underlayer thickness of 0.53 mm. It is obvious in the underlayer that there is a dark zone shaped like an island marked by the spot D which shows a homogeneous

phase. The element composition of the spot D given in Table 4.6 indicates that the homogeneous phase contains a large amount of Ti with concentration of 84.8 at.% and a small amount of Ni and Al with concentration of 8.6 and 6.5 at.%, respectively. The existence of the dark phase can also be clearly observed in the underlayer of the sample with underlayer thickness of 0.83 as shown in Fig. 4. 13. By referring to XRD result in Fig. 10(c), it can be confirmed that the dark phase corresponds to unreacted Ti which formed an alloy with Ni/Al. The existence of Ti alloy can be attributed to the extremely rapid SHS process and relatively low thermal conductivity of titanium which was unable to conduct the heat from the Ni/Al reaction to promote further reactions between Ti and NiAl [11]. Comparing the microstructure of the samples with different underlayer thicknesses, it can be seen that the amount of Ti alloy is increased with an increase in the thickness of Ti underlayer. This result can be explained by the fact that the heat released by Ni/Al reaction was insufficient to promote a higher content of Ti with an increase in the underlayer thickness.

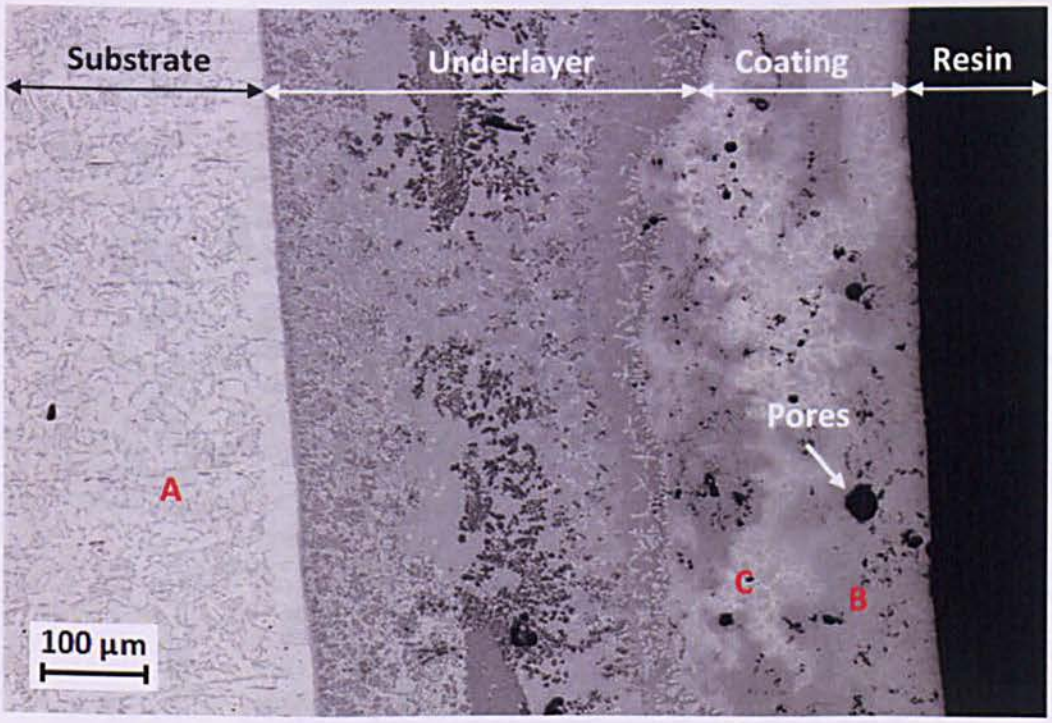

Fig. 4.11. Back scattered SEM micrograph of the sample with underlayer thickness of 0.31 mm

Table 4.3. Chemical composition (in wt.%) of the phases in Fig. 4.11

Spectrum	Al	S	Ti	Mn	Fe	Ni
A		0.47		0.97	98.56	
B	25.34					74.66
C	35.64					64.34

Table 4.4. Chemical composition (in at.%) of the phases in Fig. 4.11

Spectrum	Al	S	Ti	Mn	Fe	Ni
A		0.82		0.98	98.20	
B	42.47					57.53
C	54.65					45.35

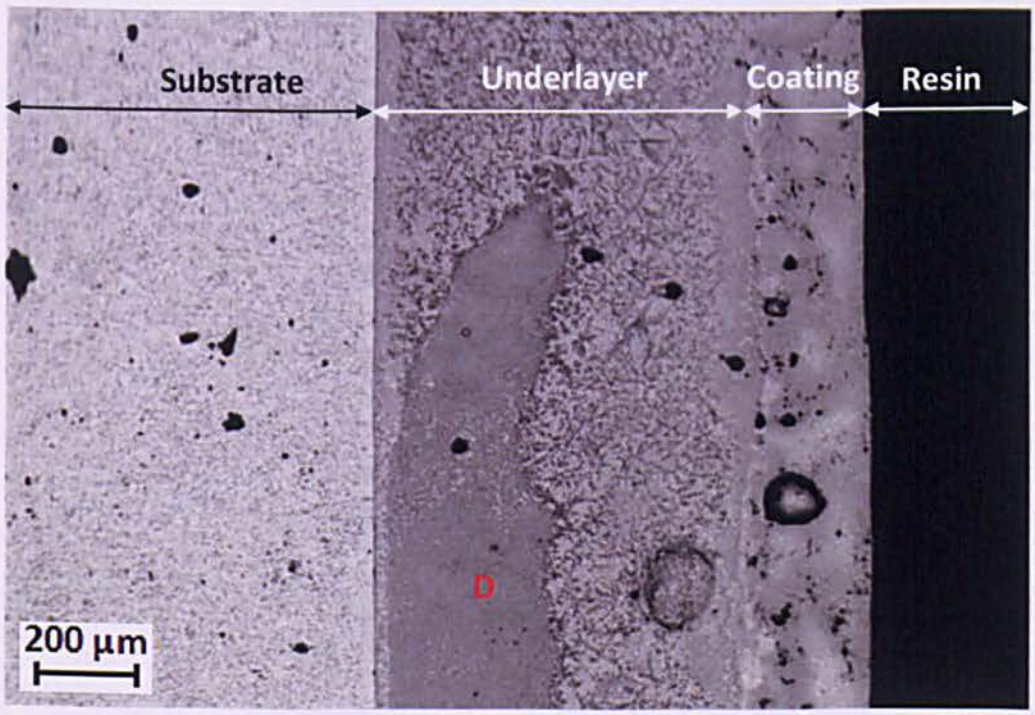

Fig. 4.12. Back scattered SEM micrograph of the sample with underlayer thickness of 0.53 mm

Table 4.5. Chemical composition (in wt.%) of the phases in Fig. 4.12

Spectrum	Al	S	Ti	Mn	Fe	Ni
D	4.99		86.77			8.23

Table 4.6. Chemical composition (in at.%) of the phases in Fig. 4.12

Spectrum	Al	S	Ti	Mn	Fe	Ni
D	8.65		84.79			6.56

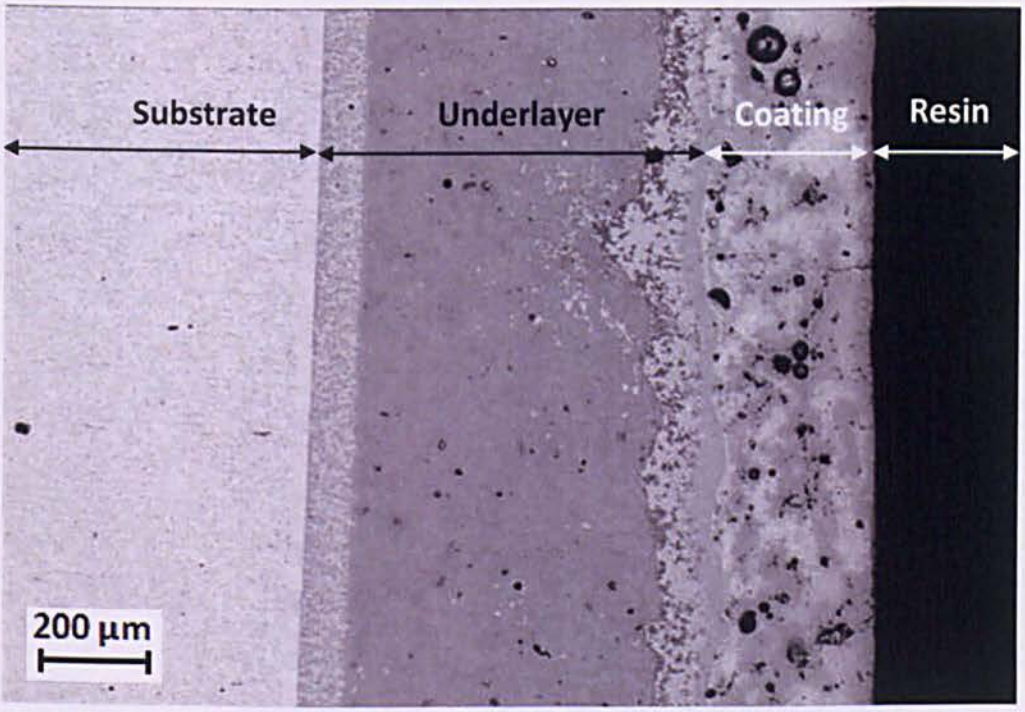

Fig. 4.13. Back scattered SEM micrograph of the sample with underlayer thickness of 0.83 mm

In order to get more detailed information about the heterogeneous phases comprising the underlayer, further SEM observations with higher magnifications were taken as shown in Fig. 4.14(a) and (b). It can be seen that the black phase formed a dendrite structure is dominant. An EDS semi quantitative analysis as given in Table 4.8 shows that the black phase as marked by the spot E reveals atomic contents of Ti and Al with the proximate proportion of 3 to 1, with a minor concentration of Ni. As observed by XRD in Fig. 4.9(b), this phase indicates the formation of Ti_3Al intermetallic, with a little content of Ni for about 1 percent which could appear at the boundary during observation. Surrounding the black phase, there is a grayish phase which becomes the matrix for the black phase. The chemical analysis of the grayish phase marked by the spot F indicates that the

atomic concentration of Ti to Ni is about 2 to 1 with a low concentration of Al. As indicated by XRD in Fig. 4.9(b), this composition suggests the formation of Ti_2Ni with a small diffusion of Al.

Considering that there are many phases existed in the underlayer, it is evident that this finding supports the previous result which obtained by the temperature profile of Ti during the SHS process of Ni/Al. As described in Fig. 4.6, the temperature of Ti is still high after melting. The formation of Ti_2Ni and Ti_3Al suggests that there were further reactions in the underlayer due to the mixing of the liquid Ni/Al from the coating to the Ti underlayer which kept a high temperature of Ti underlayer after melting. The heat released by Ni/Al reaction is responsible for the initiation of further reactions between the liquid Ni/Al and Ti to form Ti_2Ni and Ti_3Al.

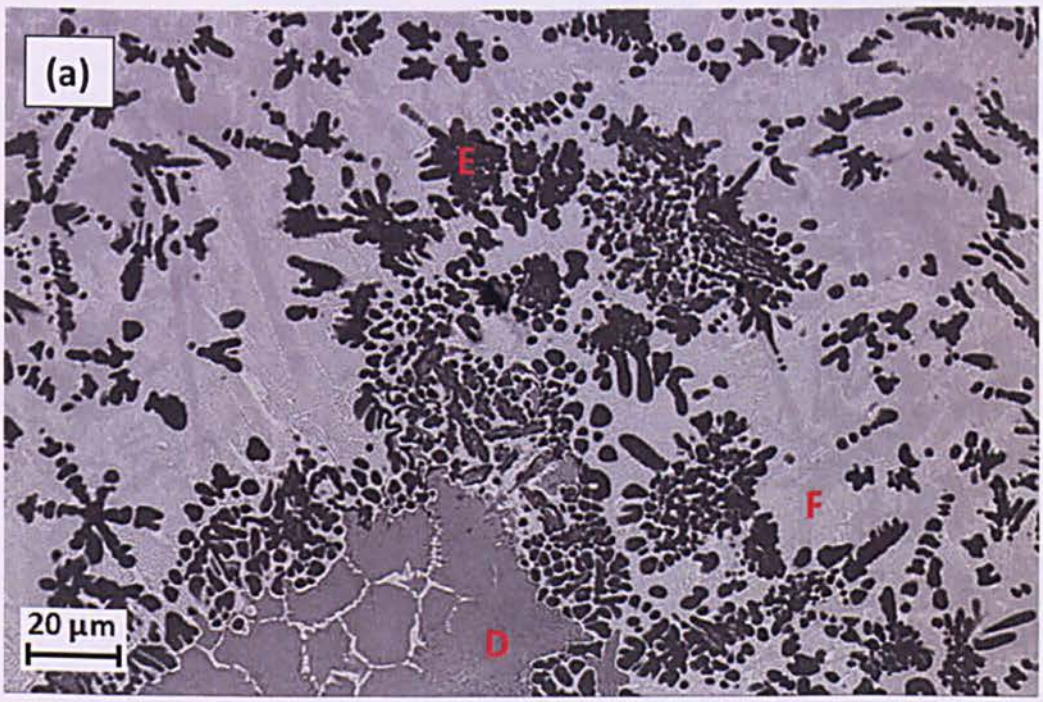

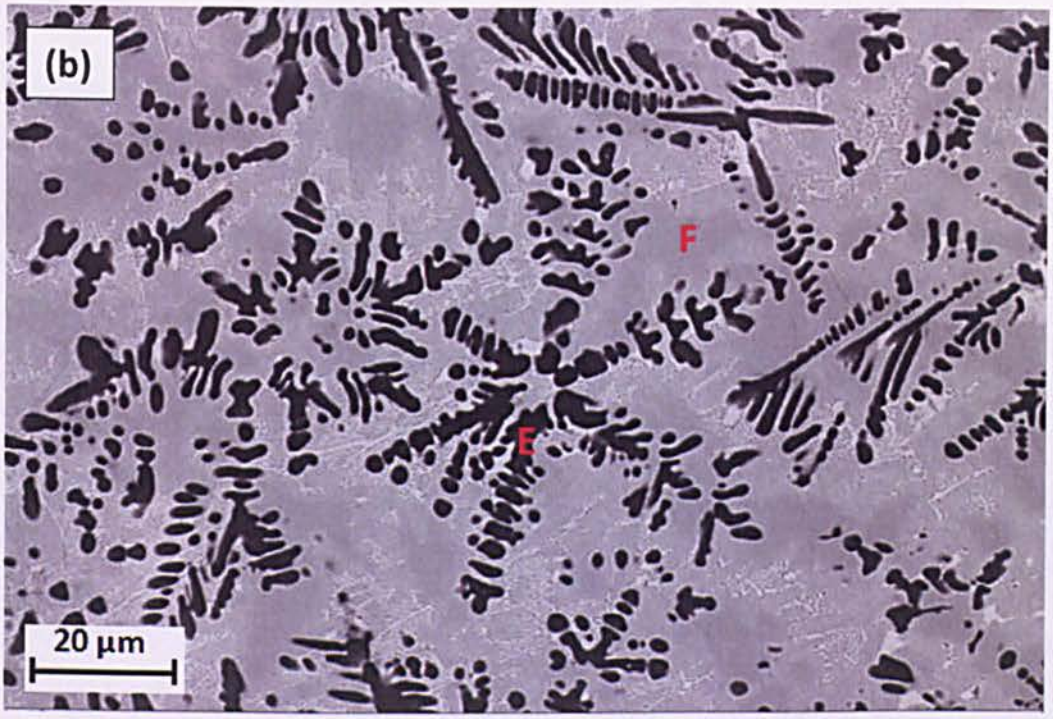

Fig. 4.14. Back scattered SEM micrograph of microstructure in the underlayer of the sample with underlayer thickness of: (a) 0.53 mm; and (b) 0.31 mm

Table 4.7. Chemical composition (in wt. %) of the phases in Fig. 4.14

Spectrum	Al	Ti	Ni
D	5.79	82.77	11.43
E	14.15	84.41	1.43
F	7.88	60.37	31.27

Table 4.8. Chemical composition (in at. %) of the phases in Fig. 4.14

Spectrum	Al	Ti	Ni	Possible phase
D	10.04	80.86	9.11	Ti alloy, NiAl
E	22.68	76.27	1.06	Ti_3Al, Ni
F	14.01	60.45	25.54	Ti_2Ni, Al

Further SEM analysis was carried out to study the microstructure at the interface between the underlayer and coating, as shown in Fig. 4.15. The semi quantitative EDS analysis of the phase composition appeared in Fig. 4.15 is given in Table 4.9 and Table 4.10. The EDS analysis of the spot L observed in the coating indicates the formation of NiAl. The examination of the microstructure in the

underlayer shows that there are a number of phases in the interface between the coating and the underlayer which can be defined using a phase contrasts. It can be seen that in the middle of underlayer, there is a black phase denoted by the spot H as also previously indicated in Fig. 4.14. According to Table 4.10, the atomic percentage of the black phase shows the formation of Ti_3Al phase. Around the black phase, there are mixed phases composed of various layers with different grey phases as identified by the spot G, I, and K. The mixed phases which appeared around the black phase are shown by the different grey tones in the backscattered image which can be identified as a number of intermetallic phases of Ni–Al–Ti system. The element concentration of the spot G and K indicates the formation of Ti alloyed with Ni/Al, while the spot I points to the formation of Ti_2Ni which mixed with Al. Meanwhile, at the interface between the underlayer and coating, a brighter phase as marked by the spot J was observed. The chemical analysis of the spot J shows that the atomic proportion of Al, Ni, and Ti is 1, 2, and 1. Thus, the bright phase can be indicated as the formation of $AlNi_2Ti$ phase.

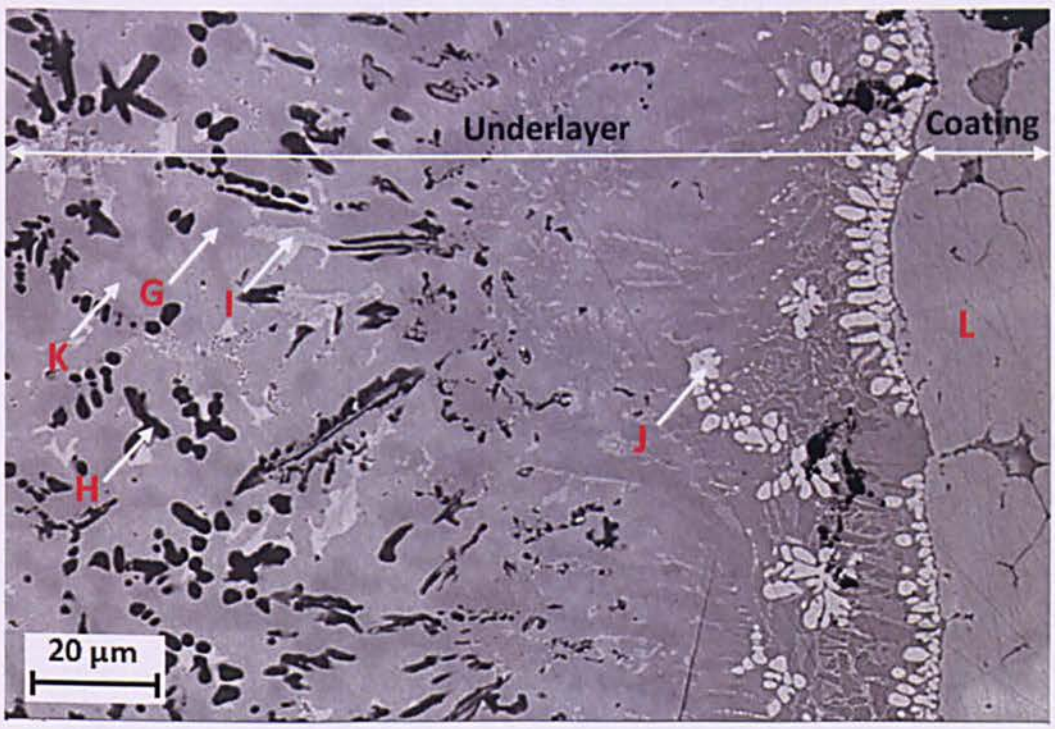

Fig. 4.15. Back scattered SEM micrograph of the microstructure across the interface between underlayer and coating in the sample with underlayer thickness of 0.31 mm

Table 4.9. Chemical composition (in wt.%) of the phases in Fig. 4.15

Spectrum	Al	Ti	Ni
G	17.40	46.58	36.02
H	16.06	82.25	1.69
I	8.89	53.39	37.72
J	15.01	25.51	59.48
K	13.07	52.17	34.76
L	33.18		66.81

Table 4.10. Chemical composition (in at.%) of the phases in Fig. 4.15

Spectrum	Al	Ti	Ni	Possible phase
G	28.90	43.60	27.50	Ti alloy, NiAl
H	25.41	73.36	1.23	Ti_3Al
I	15.78	53.43	30.79	Ti_2Ni, Al
J	26.46	25.34	48.20	$AlNi_2Ti$
K	22.36	50.30	27.34	Ti alloy, NiAl
L	51.93		48.07	NiAl

Fig. 4.16(a) shows the typical microstructure at the interface between the underlayer and substrate. It can be seen that there is an intermediate layer with a total thickness of 40–60 μm. The phases which compose the intermediate layer were labeled by the spot A, B and C. The atomic composition of the spot A, B and C is given in Table 4.12. The dark phase marked by the spot A represents a major concentration of a phase composed of Ti and Al atoms with an atomic proportion close to 3 and 1, and a minor concentration of a phase composed of Fe and Ni atoms with the proximate proportion to 1 and 3. This phase may indicate the formation of Ti_3Al with a small concentration of $FeNi_3$. Using the same procedure, the chemical analysis of the grey phase (marked by the spot B) may indicate the formation of Ti alloyed with NiAl, whilst the bright phase (marked by the spot C) may indicate the formation of Ti_2Ni with a small concentration of Fe_2Al_5. The formation of Ti_2Ni and Ti_3Al, as already explained, is due to the reactions between the liquid Ni/Al and molten Ti which were promoted by the heat released by the Ni/Al reaction. Meanwhile, the presence of $FeNi_3$ and Fe_2Al_5 can be attributed to the diffusion of the Fe melts from the steel substrate to the underlayer. The

diffusion of Fe is possible due to the heat generated by induction heating and the heat released by Ni/Al reaction. The presence of $FeNi_3$ and Fe_2Al_5 in a small concentration indicates the limited amount of Fe melt which diffused into the underlayer. Previous studies reported the formation of $FeNi_3$ and Fe_2Al_5 in the Fe–Al system [30] and Fe–Ni system [147].

The result of this study also suggests that the adhesion between the underlayer and the steel substrate was achieved by metallurgical bonding which formed a solid interface. The existence of metallurgical bonding is indicated by the presence of an intermediate layer as a product of the interfacial reactions between the elements at the interface of underlayer/substrate. The joint of the interface is confirmed by a secondary image shown in Fig. 4.16(b) which indicates that the interface between the underlayer and substrate is solid and no cracks can be observed. The secondary image also shows that the intermediate layer is dense.

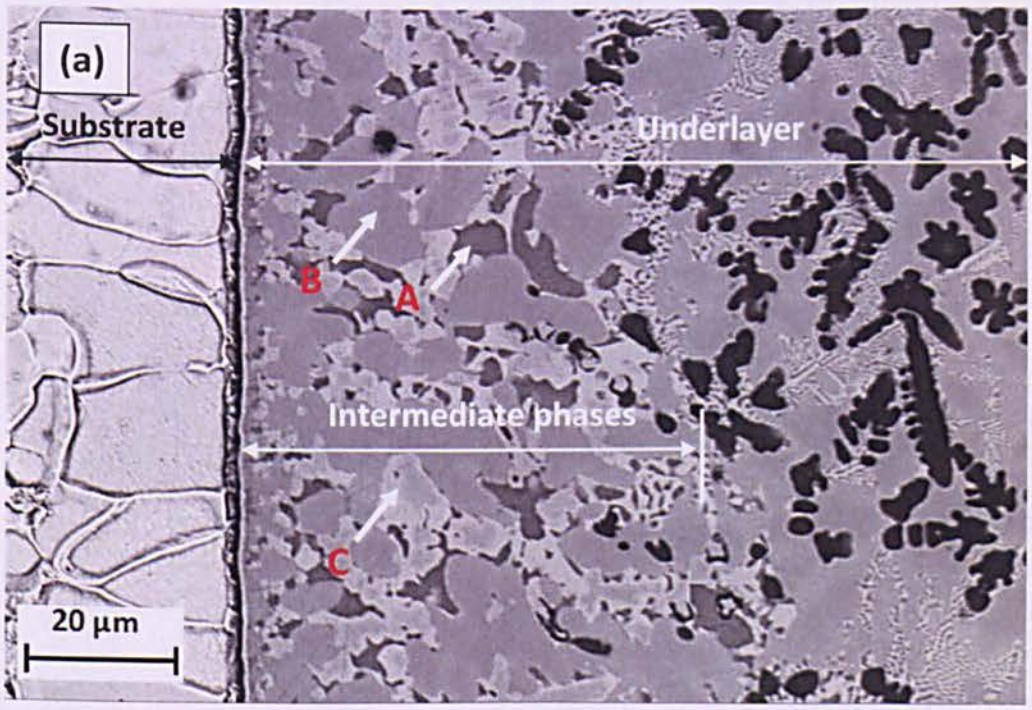

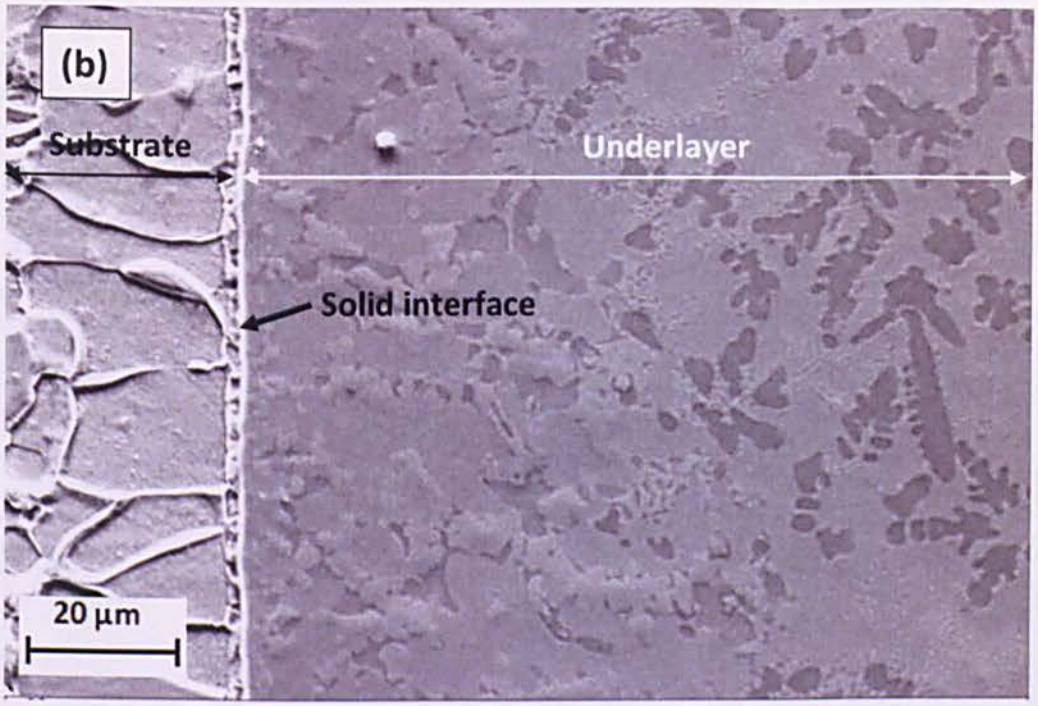

Fig. 4.16. Microstructure at the interface between underlayer and substrate obtained by: (a) Back scattered images; (b) secondary images of the sample with underlayer thickness of 0.31 mm

Table 4.11. Chemical composition (wt.%) of the phases in Fig. 4.16

Spectrum	F	Al	Ti	Fe	Ni
A		12.48	71.65	4.08	11.79
B	3.07	14.46	47.26	5.09	30.12
C		7.22	53.99	5.86	32.93

Table 4.12. Chemical composition (at.%) of the phases in Fig. 4.16

Spectrum	F	Al	Ti	Fe	Ni	Possible phase
A		20.72	67.02	3.27	8.99	Ti_3Al, $FeNi_3$
B	7.06	23.41	43.13	3.98	22.42	Ti alloy, NiAl
C		12.99	54.71	5.09	27.22	Ti_2Ni, Fe_2Al_5

4.3.3.3. Element distribution across the interfaces

The element distribution across the interface is important to give information about the diffusion of atoms through the interface which finally can be useful to identify the phase evolution across the interface region. The element

distribution across the interface is also related to the interfacial bonding of the two connected layers. Fig. 4.17(a) and (b) describe the distribution of elements obtained by a line scan analysis of SEM across the interface between the coating and underlayer, and between the underlayer and substrate, respectively.

Fig. 4.17(a) illustrates the element distribution of Ni, Al, and Ti across the interface between the coating and underlayer. The atomic concentration of Ni and Al shows a moderate decrease of Ni and Al from the coating to the underlayer. This indicates that there was an intense diffusion of Ni and Al from the coating to the underlayer. A large amount of Ni and Al diffusions into the underlayer was responsible for the generation of other reactions with Ti to form new products in the underlayer. Meanwhile, the evolution of Ti indicates that the concentration of Ti is sharply decreasing from the underlayer to the coating. The rapid fall of Ti concentration from the underlayer to the coating and the nearly absence of Ti in the coating indicate that Ti diffusion into NiAl coating did not occur at all or it occurred in very little amount. A small amount of Ti appeared in the coating layer may be caused by powder contaminations during preparation.

Fig. 4.17(b) shows the distribution of Ti, Ni, and Al across the interface between the underlayer and substrate. The evolution of Ti concentration shows that the content of Ti is significantly high and fluctuating at the middle of underlayer. However, the concentration of Ti then dramatically goes down when it is adjacent to the substrate. The irregular profile of Ti in the underlayer indicates that there were formations of mixed phases in the underlayer. It has been indicated by EDS analysis that Ti reacted with Ni/Al to produce Ti_2Ni and Ti_3Al compounds in the underlayer. In addition, the dramatic fall of Ti near the substrate is also indication that Ti did not diffuse into the steel substrate which may be due to the limited solubility of Ti into the solid state of the steel substrate. Meanwhile, the distribution of Fe reveals that a small content of Fe can be seen in the underlayer indicating that there was a slight diffusion of Fe from the substrate into the underlayer. It should be noted that the continuity of Fe concentration from the substrate to the underlayer demonstrates that there was metallurgical bonding between the substrate and the underlayer which can improve the adhesion

strength. It is obvious that the extent of Fe diffusion in the Ti underlayer is about 40–60 µm. The diffusion distance of Fe in Ti is generally higher than that of Ti in Fe due to the high degree packing fcc structure of Fe compared with open bcc structure of Ti [148][149].

As also shown in Fig. 4.17(b), there is an existence of Ni and Al in a small concentration which goes through the underlayer and achieves the substrate. This shows that Ni and Al have diffused throughout the underlayer. The effect of capillary action which governs the liquid against the solid surface is responsible for the infiltration of Ni and Al liquid through the porous Ti particles in the underlayer.

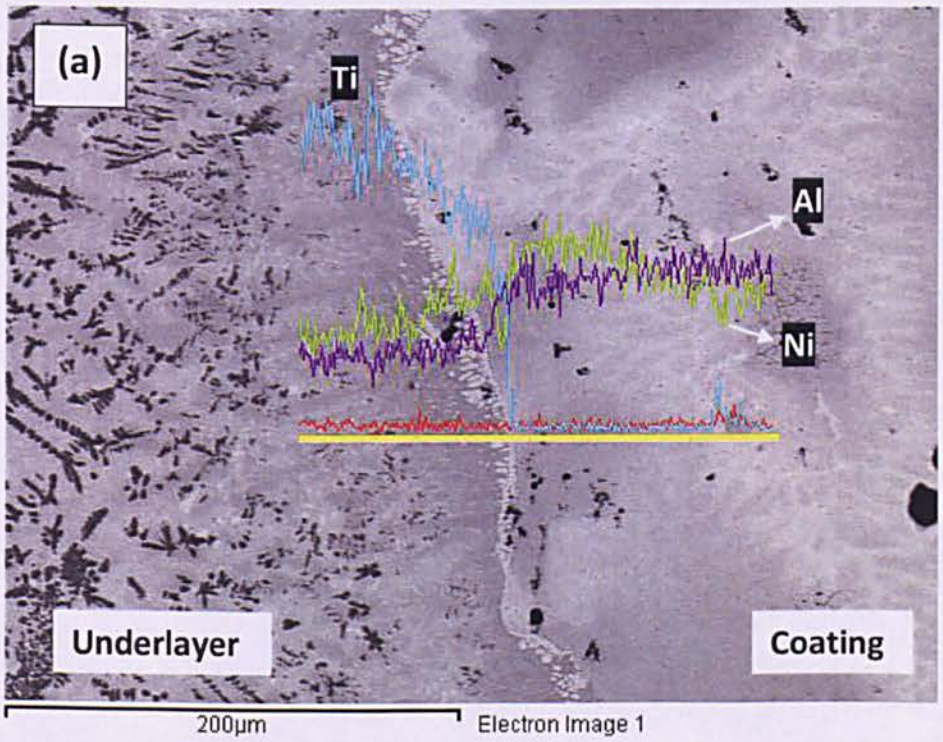

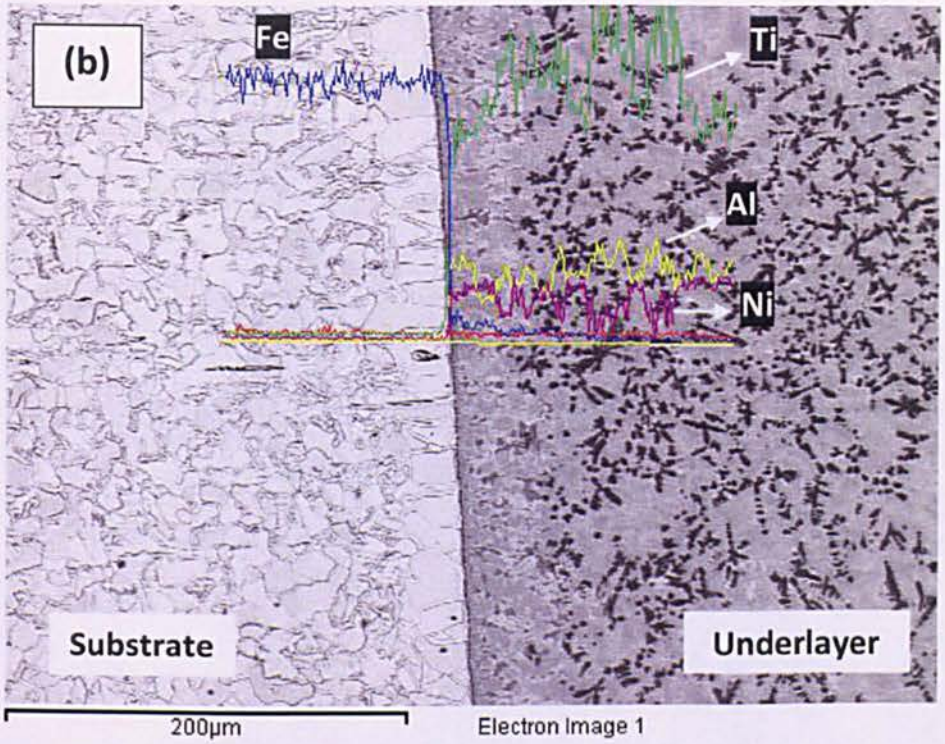

Fig. 4.17. Element distribution across the interfaces; (a) between underlayer and coating; (b) between substrate and underlayer, in the sample with underlayer thickness of 0.31 mm

4.3.3.4. Formation mechanism of the synthesized products

According to the analysis of preceding results regarding the identification and distribution of the phases and the distribution of element in the synthesized product, the microstructure of the coating is mainly composed of NiAl phase, while the underlayer mainly consists of Ti_3Al and Ti_2Ni phases. The formation mechanism of each phase can be described as follows:

(a). Formation of NiAl

The mechanism in the SHS process of NiAl coating was initiated by the generation of heat in the Ni/Al mixture using induction heating resulting in the temperature increase of Ni/Al from its initial condition to an ignition point. After reaching the ignition point, the combustion synthesis of Ni/Al was initiated and the combustion temperature increased sharply to reach its maximum value. The

temperature profile of Ni/Al has shown that the maximum temperature of SHS process achieves a temperature of approximately 1911 K. This indicates that the synthesized product, which confirmed as the NiAl phase, was in the form of a liquid phase before full solidification. Due to the effect of capillary action, an amount of the liquid phase of NiAl which positioned near the underlayer spread and dispersed through the sideline of underlying Ti and begun to wet the surface of Ti particles. Due to the lower melting point, Al was melted and spread first before Ni resulting in the formation of NiAl with Ni–rich in a significant quantity. A small amount of NiAl with Al rich was also found in the coating. The formation of substoichiometric NiAl is possible in the reaction between Ni and Al as described in the binary phase diagram of Ni–Al as shown in Fig. 4.18. According to the phase diagram of NiAl, there are some possibilities of metastable phases, such as Al_3Ni, Al_3Ni_5 and Al_3Ni_2, which can be formed in the initial stage of the reaction process of Ni/Al. These phases then change into a single stable phase, which is NiAl or Ni_3Al, depending on the initial composition of Al and Ni. Several processing parameters of the combustion synthesis have been identified to have a significant role in determining whether or not the metastables will be formed [150]. In the present work, a small amount of Ni_2Al_3 was also observed in the coating, particularly in the sample with underlayer thickness of 0.53. As has been shown, the SHS process of Ni/Al in that sample was unable to complete since an amount of the heat was absorbed by the Ti underlayer.

As confirmed by the temperature of Ti, the heat released by Ni/Al reaction caused the solid Ti which covered by the liquid Ni/Al to melt and, consequently, produced a new liquid system composed of Ti and NiAl liquids. The primary elements of the molten underlayer were then composed of Ti, Ni, and Al. This ternary system led to generate further reactions between Ti–Ni, Ti–Al, and Ni–Al–Ti. The microstructure analysis revealed that new binary and ternary phases were formed in the underlayer.

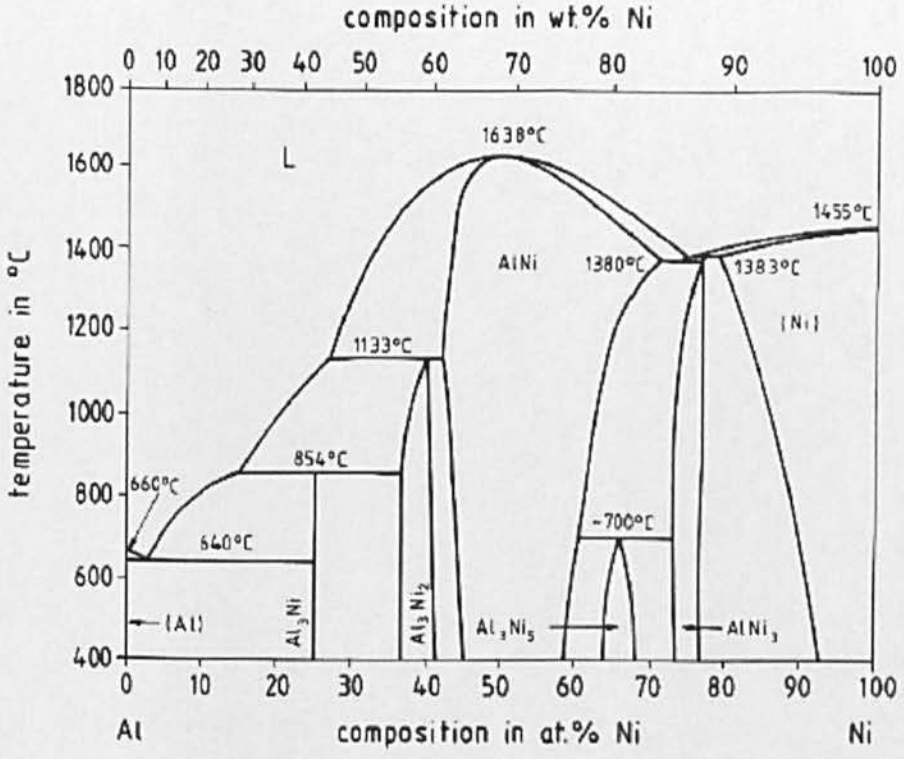

Fig. 4.18. Phase diagram of Ni–Al binary systems [2]

(b). Formation of Ti_2Ni

The present work has shown that the formation of Ti_2Ni matrix was widely observed in the underlayer. Since the underlayer was initially composed of Ti powders, the formation of Ti_2Ni was attributed to the one of the synthesized products formed by the reaction between the liquid Ni/Al and Ti. According to the phase diagram of binary Ti–Ni system as shown in Fig. 4.19, nickel–titanium system contains the stable TiNi, $TiNi_3$, and Ti_2Ni phases. Ti_2Ni can be formed in the liquid phase at 942 °C (1215 K) by eutectic reaction or at 984 °C (1257 K) by peritectic reaction [151]. In the high content of Ti, the final microstructure is Ti_2Ni phase and αTi due to the eutectoidic transformation of βTi–Ni solid solution at 765 °C [11]. A study carried out by Li Hai-Xin et al. [152] reported that during isothermal solidification of the molten underlayer of Ni–Al–Ti system (*L*), TiNi was formed first. Peritectic reaction then occurred at 984 °C to produce Ti_2Ni and $AlNi_2Ti$ using reaction in Eq. (4.5).

$$L + TiNi \rightarrow Ti_2Ni + AlNi_2Ti \quad (4.5)$$

In this work, Ti_2Ni reaction occurred in the underlayer after obtaining a sufficient energy from the heat released by the synthesis reaction of Ni/Al. This energy was used to ignite the reaction of Ti–Ni to form a Ti_2Ni phase. This assumption is corroborated by the result reported by N. Bertolino et al. [8] who investigated the ignition behaviour in the combustion synthesis of Ti_2Ni reaction obtained from elemental powders of Ti and Ni. It was observed that the ignition point of Ti_2Ni reaction was 930 ± 30 °C, which is close to the lowest melting eutectic temperature and presents the maximum solubility of Ni in βTi. The formation Ti_2Ni in the present work is also in good agreement with the result obtained by G.P. Cammarota et al. [11] who have studied the formation of Ti_2Ni in the microwave assisted SHS reaction of Ni–Al–Ti system. It was reported that during the combustion synthesis of Ni and Al which placed on Ti substrate, the heat exothermic reaction of Ni/Al was transferred to the Ti surface to promote the formation of an intermediate layer composed of α-Ti and Ti_2Ni phases with a variable content of Al.

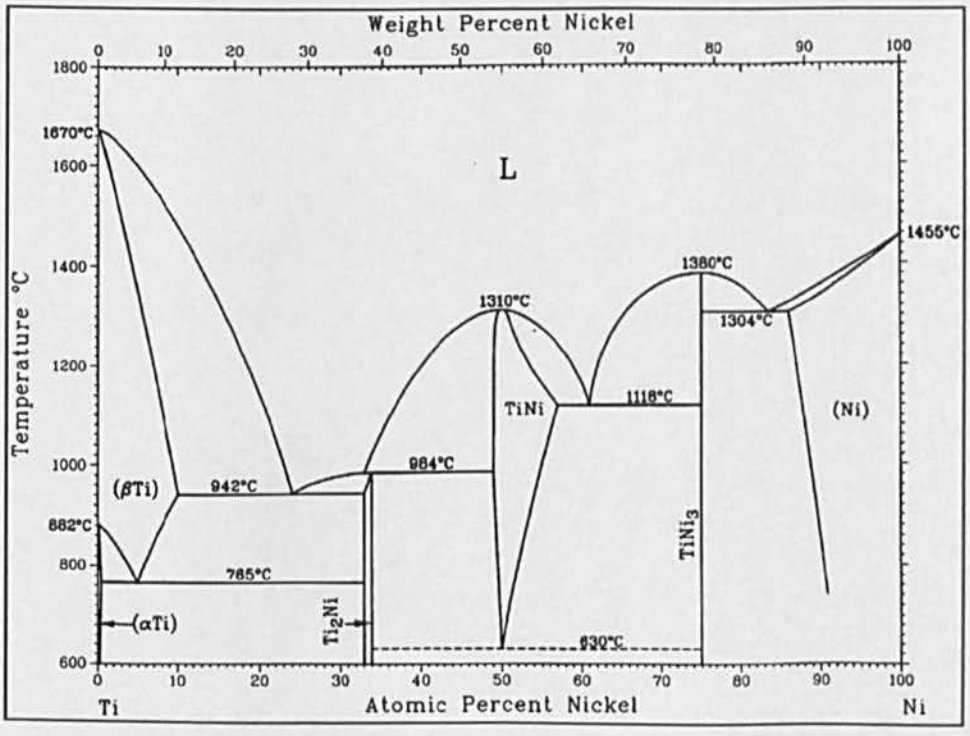

Fig. 4.19. Phase diagram of Ti–Ni binary system [33]

(c). Formation of Ti_3Al

The semi quantitative EDS analysis of the black phase in the underlayer has described the formation of Ti_3Al intermetallic which forms a dendrite structure in the Ti_2Ni matrix. The formation of Ti_3Al in the underlayer can be occurred by the diffusion of liquid Al into Ti–rich area in the underlayer. In this work, the ignition of Ti–Al reaction was not identified. However, Bertolino N. et al. [153] reported that in the combustion synthesis of Ti–Al system using CO_2 laser, the ignition of Ti_3Al synthesis can take place at 645 ± 50 °C, with the maximum combustion temperature of 1200 ± 50 °C. In addition, according to the binary phase diagram of Ti–Al system as shown in Fig. 4.20, the formation of Ti_3Al was possible to be detected at an equilibrium condition [27]. The family of titanium aluminide is mainly composed of three compounds: $TiAl_3$, Ti_3Al and TiAl. However, according to the Ti–Al binary system, there are six kinds of phases which can appear in the reaction between Ti and Al, which consist of α Ti, Ti_3Al (α_2), TiAl (γ), $TiAl_2$, $TiAl_3$ (η) and Al, depending on the composition of Ti–Al and temperature. Ti_3Al and TiAl have a larger homogeneity range, but cannot be used in a single state because they have low ductility at room temperature. Alloying is one of methods to improve their mechanical properties [27].

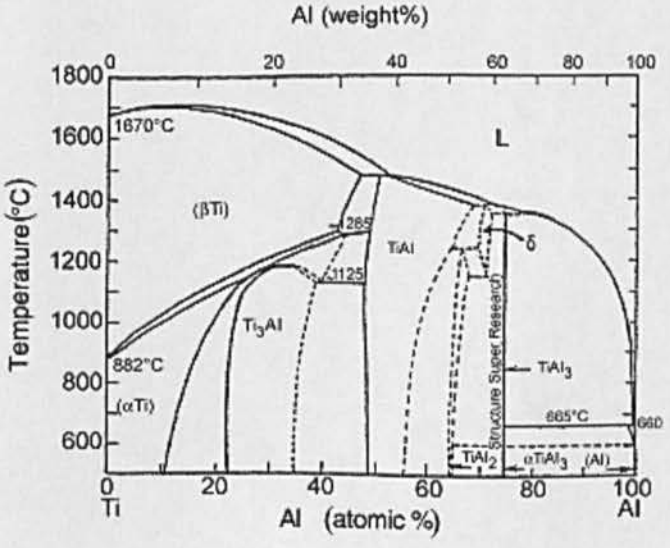

Fig. 4.20. Phase diagram of Ti–Al binary system [27]

Several studies showed an evidence that Ti_3Al can be formed at the final stage of the combustion synthesis between Ti and Al based on the reaction in Eq. (4.6) [3][28][72][154]. It was reported that the formation of Ti_3Al is started by the reaction of Ti particles with liquid Al to form $TiAl_3$. A study carried out by Shant Prakash Gupta [155] demonstrated that at this stage the liquid Al was observed to spread over the surface of Ti particles and formed a layer which covered Ti in the core. The next stage was the reaction between $TiAl_3$ and the core Ti to produce TiAl. In the final stage, Ti was reduced and TiAl changed to form Ti_3Al [28].

$$Ti + Al_{(liquid)} \rightarrow Ti + TiAl_3 \rightarrow Ti + TiAl_3 + TiAl \rightarrow Ti_3Al \qquad (4.6)$$

Considering the reaction sequence in Eq. (4.6), Ti_3Al can be formed after Al liquid covers the Ti solid particle and followed by the formation of $TiAl_3$ and TiAl. However, the microstructure analysis in the present investigation has shown that there are no $TiAl_3$ and TiAl phases which can be detected. This is due to Ti was already in the liquid phase before the solidification of Ti_3Al. The reaction of the molten Al and Ti can then be said to accelerate the formation of Ti_3Al [37]. The factor of time and heating rate can also influence the completeness of Ti_3Al reaction. A sufficient time and heating rate are required to completely form Ti_3Al without producing intermediate products [3]. Although the formation of Ti_3Al by reaction synthesis is very short, the high heat release produced by the reaction can increase the heating rate in the Ti–Al reaction [153]. A study also observed that the reaction of Ti–Al cannot proceed to complete without the assist of an exothermic agent obtained from the high heat release produced by previous reaction [156]. In the present work, the exothermic agent was obtained from the heat released by Ni/Al reaction. Thus, it can be confirmed that the heat released by Ni/Al reaction has promoted the completion of Ti–Al reaction to form Ti_3Al.

The present result has also observed that a high volume fraction of the black phase Ti_3Al is established near the Ti alloy. According to previous study [154], this phenomenon is normal as a consequence of the increase of Ti content. M. Nassik et al. [157] reported that a high content of Ti can contribute to maintain the reaction

of Ti–Al by providing a relatively high amount of additional heat. The heat absorbed by Ti can be maintained in a longer time due to its low thermal conductivity.

(d). Formation of $AlNi_2Ti$

In the underlayer near the interface of NiAl, the analysis of element concentration of the bright phase has shown the formation of $AlNi_2Ti$ phase. This phase formed as a result of peritectic reaction during the solidification of the molten underlayer of Ti–Ni–Al system, as described in Eq. (4.5) above. The formation of $AlNi_2Ti$ at the interface between NiAl and Ti in the present work is consistent with the result of previous study conducted by Sonia Simoes et al. [11]. They reported the formation of several AlNiTi intermetallic compounds including $AlNi_2Ti$ at the interface between NiAl and Ti/Ni foils during the diffusion bonding performed at 800 and 900 °C. In the present work, the microstructure examination of $AlNi_2Ti$ has also shown that the bright phases were developed to form a columnar crystal along the interface path and grow perpendicularly to the interface, from the coating layer to the underlayer. This exhibits that the development of the bright phase of $AlNi_2Ti$ is in line with the direction of the heat flow which comes from the exothermic reaction of NiAl [12].

(e). Formation of oxides (Fe_2Ti_4O and Ti_6O)

The existence of a small amount of Fe_2Ti_4O and Ti_6O in the underlayer has been confirmed by XRD observation. The formation of Fe_2Ti_4O can be associated with the presence of dissolved oxygen in titanium and Fe diffusion from the substrate which led to the formation of this oxide, while Ti_6O was due to the presence of oxygen in the Ti underlayer. The dissolved oxygen may be acquired from different sources such as the hot air as a result of the high exothermic SHS process, the absorbed oxygen from the free surface during preparation, and the oxygen impurity from the argon atmosphere. The formation of oxide compounds at the interface can become a trouble for the generation of a complete bond. The brittle oxide is responsible for a decrease in the adhesion strength since it can produce the initiation and propagation of cracks through the interface [158].

4.3.3.5. Effect of underlayer thickness on the microstructure of synthesized products

The effect of underlayer thickness on the microstructure of synthesized product was observed using underlayer thicknesses of 0.31 mm, 0.53 mm and 0.83 mm as described in Fig. 4.11, Fig. 4.12, and Fig. 4.13 above. The result shows that an increase in the thickness of underlayer has increased the amount of Ti alloy in the underlayer. It can be seen that the dark grey zones which show Ti alloyed with NiAl are more dominant compared with the bright and black regions which show the formation of new phases (Ti_2Ni–Ti_3Al) in the underlayer. This is due to the heat released by Ni/Al reaction transferred to the underlayer was insufficient to promote further reactions to consume all titanium content. Thus, the large amount of Ti alloy formation can be attributed to the lack of prolonged second reactions between the liquid Ni/Al and Ti. As shown in Fig. 4.11, the underlayer with a thickness of 0.31 mm showed that the most amount of titanium can be transformed into new formed phases. This shows that the use of a thin underlayer is favoured to produce an underlayer which contains new formed phases of Ti–Al and Ti–Ni systems.

4.3.3.6. Effect of heating rates on the microstructure of synthesized products

Different heating rates were produced by applying different currents of induction heating. As described in the temperature profile of Ni/Al reaction, the variation of currents using 200 A, 250 A and 300 A has generated the SHS of Ni/Al with heating rates of 46.6 K/s, 57.0 K/s, and 85.5 K/s, respectively. In this work, the effect of current on the microstructure of synthesized products was studied using a Ni/Al mixture and Ti underlayer with thicknesses of 0.54 mm and 0.53 mm, respectively, and a compaction pressure of 200 MPa.

Fig. 4.21 shows the typical microstructure of the synthesized products obtained by different heating rates. When the heating rate is slow (46.6 K/s), as shown in Fig. 4.21(a), a high amount of Ti alloy as shown by the dark grey phase is observed. Comparing Fig. 4.21(b) to Fig. 4.21(c), it indicates that an increase in the

heating rate reduces the amount of Ti alloy and promotes a higher portion of Ti_2Ni–Ti_3Al phases in the underlayer. A possible explanation for this result might be that when the heating rate is slow, the time needed to melt Ti and initiate the reaction between the liquid Ni/Al and Ti is longer which results in a high heat loss. As a consequence, the reaction between the liquid Ni/Al and molten Ti in the underlayer was incomplete. On the contrary, increasing the heating rate has produced a higher amount of the Ti_2Ni–Ti_3Al phases in the underlayer. This indicates that an increase in the heating rate produces a high amount of the liquid Ni/Al which reacts with Ti in the underlayer. This can be attributed to the higher heat released by Ni/Al reaction which transferred into Ti compared with the heat which lost into the surrounding.

The result in this study also indicates that the difference of heating rates produce different movements of the interface between the coating and underlayer. The result shows that the heating rates of 46.6 K/s, 57.0 K/s, and 85.5 K/s produce the average thickness of coating by 200 mm, 300 mm and 400 mm, respectively. This indicates that the coating thickness in the slower heating rate is smaller than that in the faster heating rate. This result suggests that the amount of liquid Ni/Al consumed into Ti_2Ni–Ti_3Al phases in the slower heating rate is higher than that in the faster hating rate. By relating to the temperature profile for the SHS of Ni/Al with different currents as previously described in Fig. 4.4, a possible reason for this might be that the time for diffusion of the liquid Ni/Al into Ti underlayer is longer than that in the faster heating rate resulting in the higher amount of consumed Ni/Al.

The different heating rates have also affected the porosity of synthesized product. It can be seen that a large amount of pores was formed in the synthesized product with a heating rate of 85.5 K/s. The result shows that the amount of pores in the synthesized product with a faster heating rate (85.5 K/s) is higher than that in the slower heating rate (46.6 and 57.0 K/s). The source of porosity in the synthesized products is mainly due to the existing pores in the compacted pellet [159]. The other factors which involves in the pores formation are the reduction in the specific volume from the reactant to product, the difference of diffusion rates

during solid state sintering which known as the Kirkendall effect, and the gas evolutions during the phase transformation in the SHS reaction [160]. The result in this study indicates that a high porosity observed in the faster heating rate was due to the short time of the reaction causing the pores not to have sufficient time to rise to the surface. On the contrary, a longer time of reaction in the slower heating rate led to a decreased amount of the residual porosity. Based on this result, a slow heating rate has shown to be more effective to eliminate porosity and promote the densification compared to a fast heating rate.

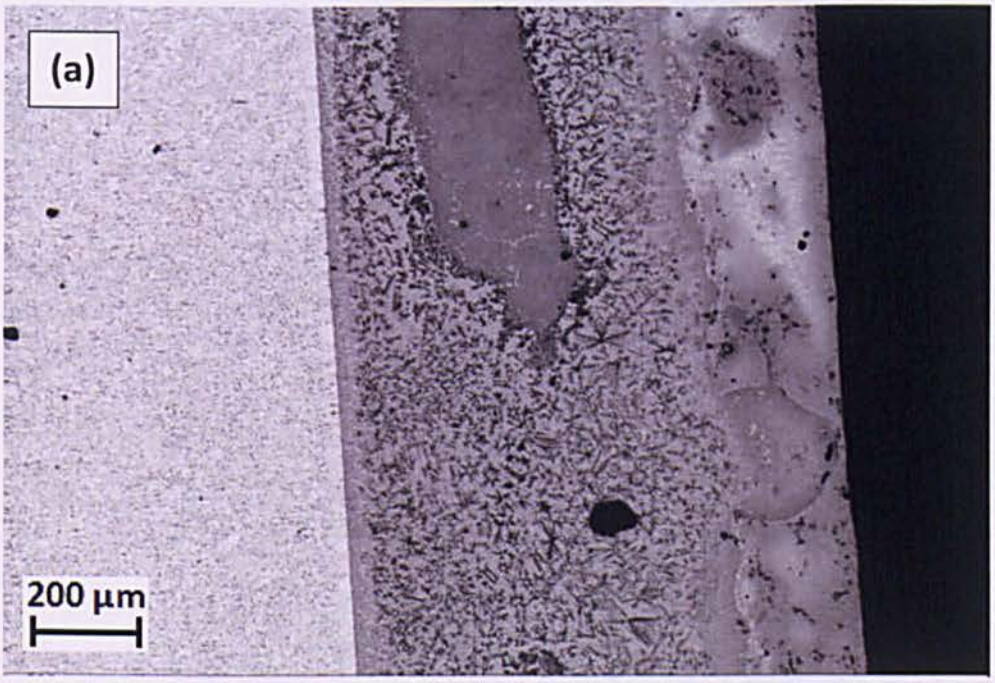

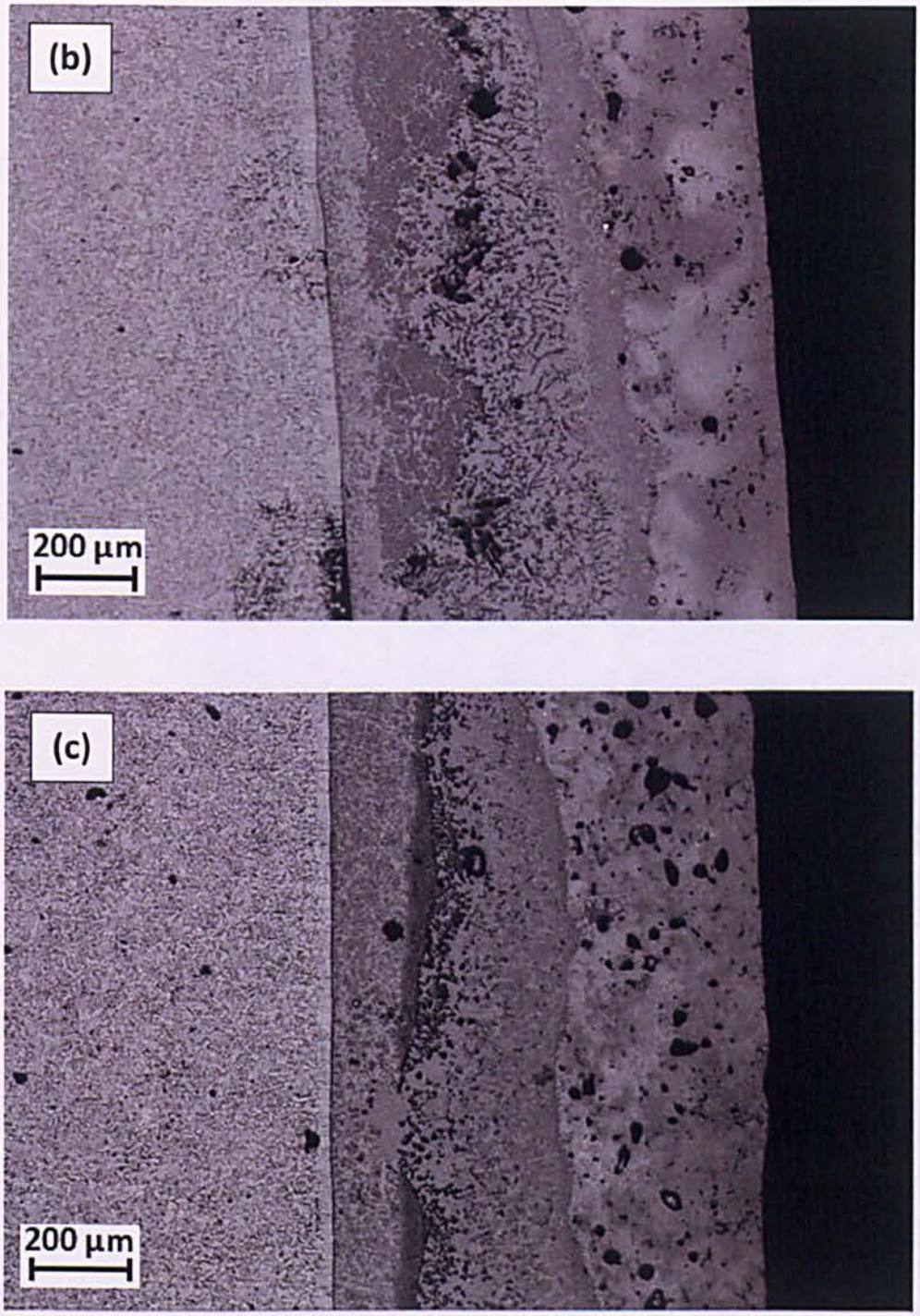

Fig. 4.21. Back scattered SEM micrograph of synthesized using heating rates of: (a) 46.6 K/s; (b) 57.0 K/s; and (c) 85.5 K/s

4.3.3.7. Effect of compaction pressures on the microstructure of synthesized products

The effect of compaction pressure was investigated using 100 MPa, 150 MPa and 200 MPa on the compacts which composed of Ni/Al mixture and Ti layers. In general, compaction is related to the contact between the surface areas of particles which affect the thermal conductivity of the sample. In the SHS process, the thermal conductivity of reactant significantly affects the heat propagation and heat loss which establish the ignition and wave propagation of the reaction [49]. In the present work, the green density of underlayer after compacted using 100 MPa, 150 MPa and 200 MPa was 2125.71 ± 156.11 kg/m^3, 2672.52 ± 285.57 kg/m^3 and 2848.39 ± 213.79 kg/m^3, respectively. The calculation of the green density after compaction is given in Chapter 3. Other parameters were kept the same using 0.5 gram of Ni/Al mixture and heated by induction heating with a current of 300 A. Preliminary observations on the SHS process of all samples showed that all compaction pressures have resulted in the completeness of the SHS process. This indicates that all compaction pressures have produced a sufficient density to cause the ignition and propagation of the SHS process. Previous investigation on the Ni/Al system carried out by Zhu et al. [17] reported that too low compaction pressure (35 MPa) was unable to initiate the reaction.

The typical microstructure of the synthesized products obtained by compaction pressure of 100 MPa and 150 MPa are shown in Fig. 4.22(a) and (b). The microstructure of the product compacted using 200 MPa is previously described in Fig. 4.21(c). The result shows that the variation of compaction pressure has significantly affected the microstructure of synthesized product, particularly, on the amount of Ti alloy and the product porosity. The result in this study shows that the different amount of Ti alloy can be observed in all products. The appearance of Ti alloy in all samples indicates that the heat produced by the Ni/Al reaction was insufficient to promote further reactions between the liquid Ni/Al and all amount of titanium underlayer. However, a comparison of the result shows that the amount of Ti alloy in the compaction pressure of 150 MPa is higher than that in the samples compacted by 100 and 200 MPa. In other words, an increase of compaction

pressure initially increased the amount of Ti alloy, and further increase of the compaction pressure resulted in a reversed trend by producing a smaller amount of the Ti alloy. This trend may occur as a result of the thermal conductivity of the samples which generated two opposing effects simultaneously between the amount of the heat transferred to the underlayer and the heat lost to the environment. The heat released by Ni/Al reaction which transferred into underlayer was dependent on the thermal conductivity of the compact. An increase in the compaction pressure led to an improvement in the particle contacts which hence increased the thermal conductivity [102]. A high amount of Ti alloy in the sample with a compaction pressure of 150 MPa may be due to the amount of heat lost to the surrounding was higher than the heat conducted to the underlayer, which in turn, became a barrier to the reaction of the liquid Ni/Al and Ti. Further increase in the compaction pressure (200 MPa) resulted in an increase in the thermal conductivity which was favoured to the heat transfer and consequently promoted the reaction between the liquid NiAl and Ti.

The result in this study shows that an increase in the compaction pressure led to an increase in the formation of pores in the synthesized product. As mentioned in the previous section, there are a number of sources leading to the formation of porosity [159][160]. In SHS product, the porosity is generally formed due to the existing pores in the compacted reactant. An increase in the compaction pressure should therefore decrease the porosity since it decreases the distance between particles resulting in the reduction of the inter–particle pores. The present work, however, produces a contradictive result. The result indicates that the porosity of synthesized product increases with an increase in the compaction pressure (see Fig. 4.21(c)). This may be due to an increase of the compaction pressure produced a high thermal conductivity which resulted in a high heating rate and a short time of the reaction. Due to insufficient time, the formed pores could not rise to the surface and resulted in the formation of porous product. The effect of varied compaction pressure on the porosity, therefore, showed a similar response to the variation of heating rates.

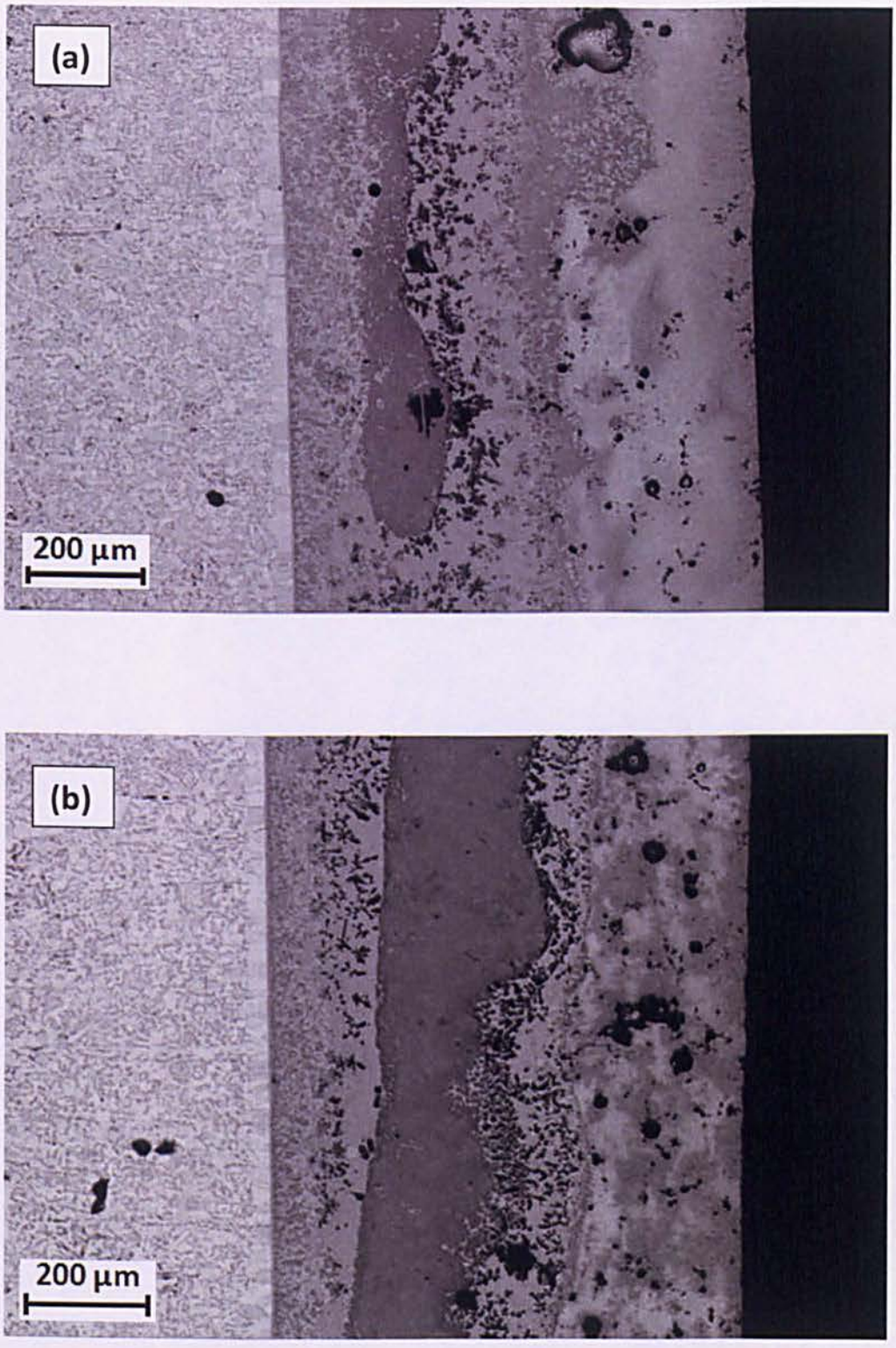

Fig. 4.22. Back scattered SEM micrograph of synthesized product prepared by compaction pressure of: (a) 100 MPa; and (b) 150 MPa

4.3.3.8. Effect of the melting points of underlayer material on the microstructure of synthesized products

The main concern in the application of different underlayers is the adhesion between the coating and the substrate after synthesis. The adhesion strength can be determined from the morphology at the interface between the underlayer and the substrate which shows their interactions. In this work, the effect of the melting point of underlayer on the microstructure was investigated using aluminium (T_m = 933 K) and nickel (T_m = 1728 K), as a comparison for titanium (T_m = 1941 K). The compacts were prepared using Ni/Al mixture with Al and Ni as underlayer, compacted using a pressure of 200 MPa, and heated by induction heating with a current of 300 A. Fig. 4.23 and Fig. 4.24 show the microstructure of synthesized products which use Al and Ni as underlayer, respectively. The element distributions of Al, Ni, and Fe are described in the figures in order to help the identification of the formed phases.

a). Sample with Al as underlayer

Fig. 4.23(a) and (b) show the microstructure of synthesized product which used Al as underlayer. It can be seen that an interfacial layer was formed at the interface between Al underlayer and substrate. This indicates that metallurgical bonding was generated at the interface. The element distribution of Fe atom shows that Fe atoms decreases gradually across the interface between the substrate and Al underlayer. This indicates that a significant amount of Fe atoms have diffused from the substrate to the Al underlayer. The existence of Fe atoms in the interface is required to form interfacial products after the reaction with Al atoms. Meanwhile, the element distribution of Ni shows that the content of Ni, which seems to level off from the coating to the underlayer, falls sharply prior to the interface of the substrate. This indicates that Ni has only diffused into Al underlayer, but could not reach the interface of the substrate. Thus, the possible phase of interfacial products at the interface between Al underlayer and the substrate is the intermetallic system of Fe–Al.

The present result indicates that the SHS of Ni/Al has affected the microstructure of underlayer. It can be seen in Fig. 4.23(a) that Al underlayer is composed of a heterogeneous structure. The element distribution of Al and Ni shows that a high content of Al and Ni elements has diffused from the coating to the Al underlayer. The line scan of Al atoms shows that the atomic concentration of Al increases at the interface between the coating and Al underlayer which indicates that Al also diffused from the underlayer to the coating, in the opposite direction with the diffusion of Al from the coating to the underlayer. Meanwhile, the line scan of Ni shows that its concentration is relatively flat indicating that the amount of Ni which diffused into the underlayer is as high as the quantity of Ni which remained in the coating. The formation of a multiphase existed in the Al underlayer can be attributed to the further reactions between Al and Ni, in which Al were obtained from the coating and underlayer, while Ni was diffused from the coating. The heat released by Ni/Al reaction has melted the Al underlayer and promoted further reactions between the liquid NiAl and molten Al in the underlayer. According to the binary phase diagram of Ni–Al, a high content of Al in the underlayer can promote the formation of intermetallic phases of NiAl with Al–rich such as $NiAl_3$ and Ni_2Al_3. The atomic composition of the phase in the coating and underlayer of the sample with Al underlayer is given in Table 4.14. The dominant phase in the coating marked by the spot A indicates the formation of NiAl. A small fraction in the coating shown by the spot E indicates a formation of intermediate phase of Ni–Al system. An enlarged SEM picture of the microstructure in the underlayer in Fig. 4.23(b) shows more detailed information of the formed phases in the underlayer. According to Table 4.14, the atomic composition of the spot B, C and D as shown in the underlayer indicates the formation of $NiAl_3$, Ni_2Al_3 and $NiAl_3$. The formation of these phases indicates that the underlayer was composed of intermediate phase of Ni–Al system with Al rich due to the reaction between Al underlayer and Ni diffused from coating. Meanwhile, the spot F indicates the formation of Al–Fe–Ni system which becomes an intermediate layer between underlayer and the substrate.

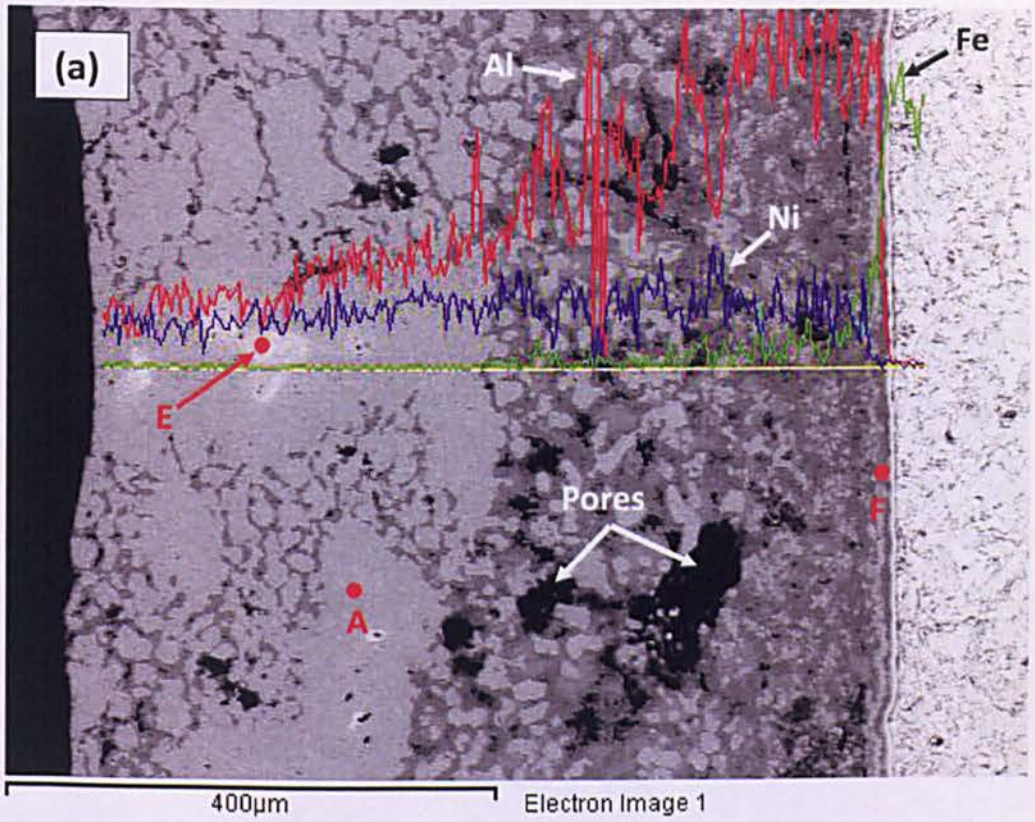

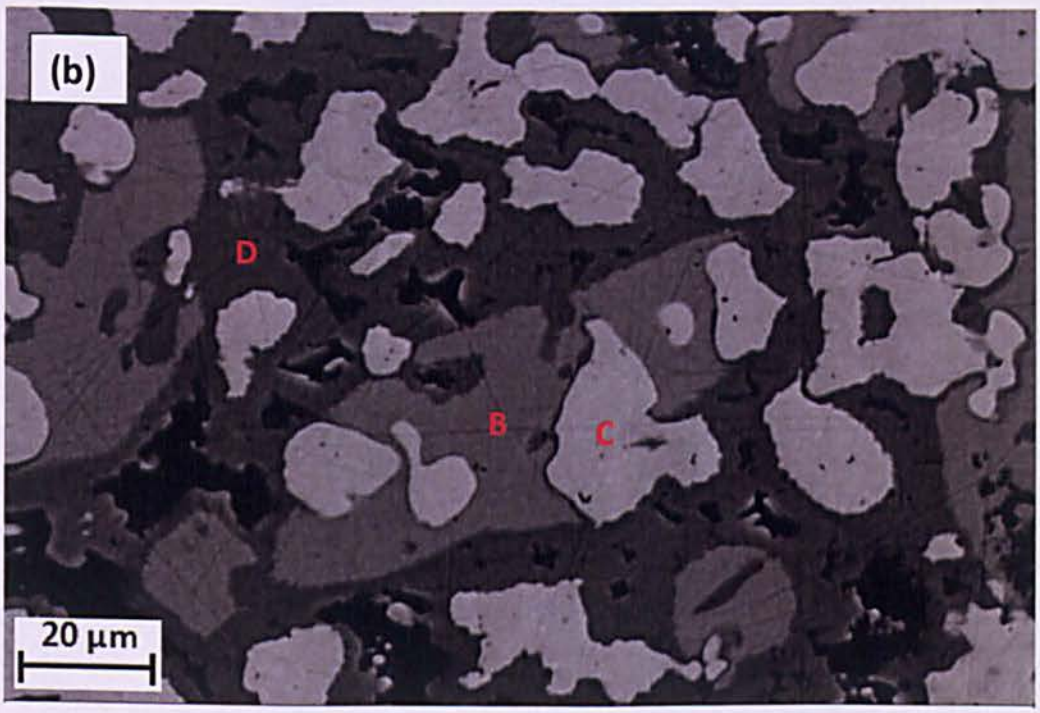

Fig. 4.23. Back scattered SEM micrograph of synthesized product using Al as underlayer: (a) image across the coating, underlayer and the substrate; (b) high magnification image at the underlayer

Table 4.13. Chemical composition (in wt.%) of the phases in Fig. 4.23(a) and (b)

Spectrum	O	Al	Fe	Ni	Total
A		37.80		59.21	97.01
B	1.65	49.94	7.84	38.92	98.35
C	0.39	37.26	0.49	59.85	97.99
D	0.67	55.67	0.54	42.93	99.80
E		23.61		75.46	99.07
F		34.77	17.94	44.79	97.49

Table 4.14. Chemical composition (in at.%) of the phases in Fig. 4.23(a) and (b)

Spectrum	O	Al	Fe	Ni	Possible phase
A		58.14		41.86	NiAl
B	3.75	67.13	5.09	24.04	$NiAl_3$
C	0.99	56.76	0.36	41.89	Ni_2Al_3
D	1.48	72.49	0.34	25.69	$NiAl_3$
E		40.49		59.50	Ni_5Al_3
F		54.31	13.54	32.15	Al–Fe–Ni

b). Sample with Ni as underlayer

Fig. 4.24 shows the microstructure of synthesized product which used Ni as underlayer. It can be seen that the interfacial layer between Ni underlayer and the substrate is absent. The element distribution of Fe atom shows that the content of Fe drops sharply from the substrate to the Ni underlayer. The atomic composition observed by EDS analysis also shows that the spot F located near the substrate contains a very small amount of Fe which is about 1 at.%. This indicates that the diffusion of Fe atoms from the substrate to the Ni underlayer did not occur. The lack of Fe diffusion in the interface of substrate suggests that metallurgical adhesion was not formed. The interface structure shows that the adhesion between underlayer and the substrate was formed by a mechanical interlocking through the anchors generated by the melted Ni which dispersed into the substrate.

The microstructure of synthesized sample in Fig. 4.24 shows that three distinct layers exist in the product which composed of coating and two homogeneous-dense structures in the underlayer marked by zone A and B. In the

coating, the atomic composition of the spot A and B indicates the formation of NiAl. The spot A located near the underlayer shows the formation of NiAl with Ni-rich composition due to the diffusion of Ni from underlayer. In the underlayer, the zone A shows the formation of dense and homogeneous phase. The element distribution in this region shows that the content of Ni atom is high, while Fe and Al atoms are almost absent. The atomic composition obtained by EDS analysis in Table 4.16 shows that the spot E in the underlayer was composed of approximately 96 at.% Ni and 4 at.% Al. This indicates that this region is mainly composed of unreacted Ni which formed an alloy with Al. This is due to the heat released by Ni/Al reaction was insufficient to promote further reactions in the underlayer. The dense structure of the underlayer illustrates that the Ni underlayer has melted. The heat released by Ni/Al reaction was responsible for the melting of the Ni underlayer. In the second homogeneous region marked by the zone B, the line scan shows that the element distribution of Ni is decreased. Two phases can be identified in this region; spot C and D. The atomic compositions of the spot C and D given in Table 4.14 by EDS analysis indicate the formation of Ni_3Al and Ni_5Al_3. The formation of these phases shows that intermediate phases of Ni–Al system with Ni-rich composition were formed between Ni underlayer and NiAl coating.

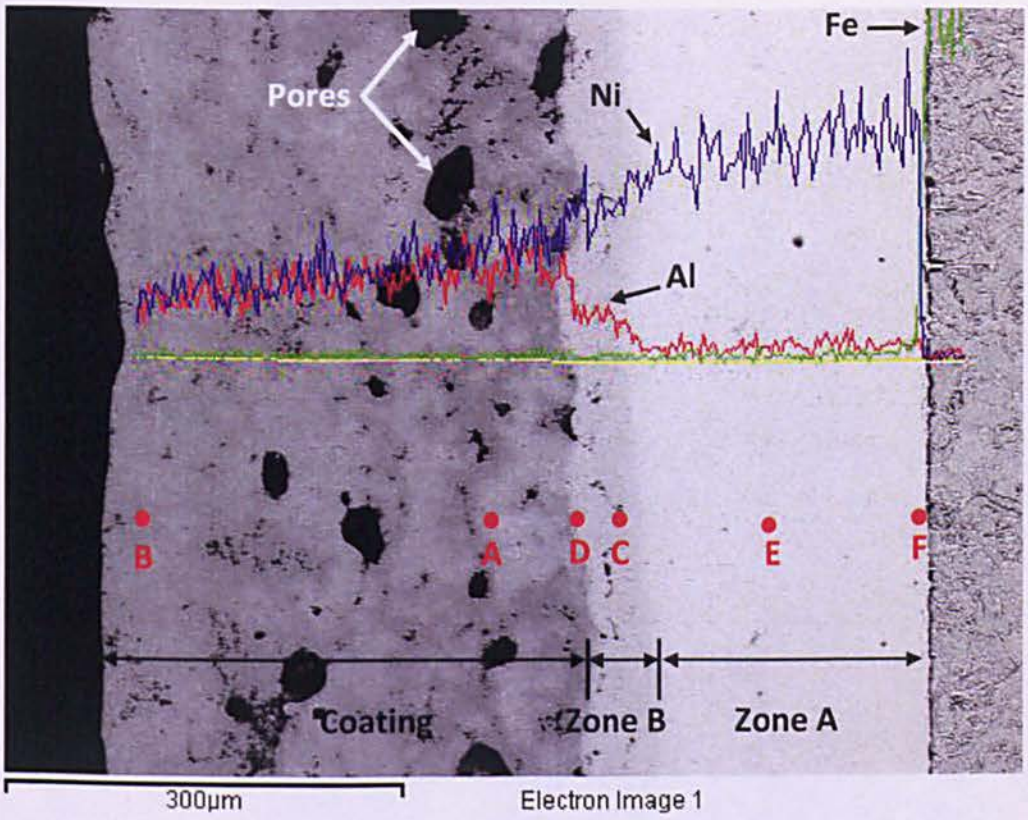

Fig. 4.24. Back scattered SEM micrograph of synthesized product using Ni as underlayer

Table 4.15. Chemical composition (in wt.%) of the phases in Fig. 4.24

Spectrum	Al	Fe	Ni	Total
A	28.38		70.16	98.54
B	32.08		65.39	97.46
C	11.95		88.31	100.26
D	21.33		80.57	101.89
E	2.04		98.28	100.32
F	2.36	1.02	97.40	100.78

Table 4.16. Chemical composition (in at.%) of the phases in Fig. 4.24

Spectrum	Al	Fe	Ni	Possible phase
A	46.81		53.19	NiAl
B	51.63		48.37	NiAl
C	22.75		77.25	Ni_3Al
D	36.55		63.45	Ni_5Al_3
E	4.33		95.67	Ni, Al
F	4.96	1.04	94.00	Ni, Fe

c). Porosity in the sample with Al and Ni as underlayer

The microstructure of synthesized product as shown in Fig. 4.23(a) and Fig. 4.24 illustrates that the application of Al and Ni as underlayer has produced porous products. The porosity of sample with Al underlayer indicates that a significant amount of open pores was formed in the underlayer region. Meanwhile, the porosity in the sample with Ni underlayer in Fig. 4.24 shows that a considerable amount of closed pores was appeared in the coating near the underlayer. This indicates that the porosity was mainly due to the gas evolved from the Ni/Al reaction. The dense structure of Ni underlayer indicates that Ni has melted and no reaction occurred in the underlayer.

In general, the formation of pores can be attributed to the different sources. During powder preparation, the pores can be obtained from the green porosity due to the voids generated by the inter-particle distance between the grains of compacted powders. During the SHS reaction, the entrapped gas released by high combustion temperature then produces porous product. The pores can also be obtained from the volatilization of impurities of low melting temperature and the shrinkage of synthesized product due to the different molar volume between the reactant and product [161]. When the mixture is still in the solid state, the pores can occur by the Kirkendall effect [162]. This phenomenon was used to explain that the diffusion of atoms occurs through the vacancy exchange instead of by the direct interchange of atoms during the solid state. The difference of the diffusion rates between atoms resulted in the formation of vacancies which generate voids and pores.

In the sample with Al underlayer, a high amount of pores can be found in the underlayer. The pores were formed, particularly, due to the melting and phase transformation of Al. The high combustion temperature of Ni/Al reaction (1911 K) which is much higher than the melting point of Al (933 K) resulted in the melting of Al in the underlayer and promoted further reactions with Ni which diffused from the coating. This can be indicated by the element evolution of Ni and Al atoms which shows that both atoms have diffused into the Al underlayer. The diffusion of

a significant amount of Ni into the Al underlayer suggests that there were further reactions in the Al underlayer which formed intermetallic phases. Due to the reaction between Ni and Al, an amount of Al underlayers were consumed resulting in the formation vacancies in the site which is initially occupied by Al. These vacancies were then condensed into voids which subsequently connected each others to form the pores. The aggregation and collapse of vacancies led to the formation of open pores. A study showed that an increase in the amount of Al involved in the reaction will produce more vacancies in the reaction product resulting in an increased number of pores [160]. It can also be seen that the size of pores in Ni and Al underlayers is approximately similar to the size of Al powders used for the reactant (45 μm). This result is consistent with a study which reported that the pores size which formed at the sites of Al is dependent on the particle size of Al. In other words, an increase in the particle size of Al will increase the pore size [160].

To sum up, although the synthesized products which used Al and Ni underlayers have shown promising results, both products have shown limitations. Due to the excessive amount in the melt of Al, the product with Al underlayer showed the loss of shape. Meanwhile, using Ni underlayer has produced low adhesion since the interaction between interlayer and substrate only occurs by mechanical bonding through the anchors. Therefore, the use of Ti as underlayer which produced metallurgical bonding is a preference compared to Al and Ni.

4.4. Summary

This chapter has reported the fabrication of NiAl coating formed by the SHS process using induction heating. Titanium was used as underlayer to improve the adhesion between the coating and substrate. The behaviour of Ni/Al reaction and the microstructure of synthesized products were observed. The result showed that that the combustion synthesis of Ni/Al which was ignited by induction heating was complete when using currents of 200–300 A. The formation of NiAl was initiated by the melting of Al and followed by the Ni/Al reaction. Due to the high temperature of Ni/Al reaction, the synthesized product was in the liquid phase during the

synthesis. A part of the liquid Ni/Al then diffused into Ti underlayer and generated the formation of new products in the underlayer. The heat released by Ni/Al reaction was responsible for the melting of Ti underlayer and promoting further reactions between the liquid Ni/Al and Ti in the underlayer. The microstructure analysis showed that the underlayer was composed of Ti_3Al–Ti_2Ni composite and Ti alloy. The effects of heating rates, compaction pressure, underlayer thickness, and melting point of underlayer on the microstructure of synthesized product were observed. It was revealed that these parameters have played an important role in the amount of the formed phases and porosity in the synthesized product.

The developed method in the present work has shown that the adhesion between the underlayer and the substrate was achieved by metallurgical bonding. Interfacial products were formed in the interface between the underlayer and substrate due to the diffusion of Fe melt from the substrate surface to the underlayer. The combination of the heat generated by induction heating and the heat released by Ni/Al reactions were responsible for preheating the substrate and promoting the melting of Fe. The evidence from this study suggests that a solid interface between the underlayer and substrate indicates a good adherence of the coating to the substrate. The present study then makes noteworthy contributions to the adhesion improvement of the NiAl coatings formed by the SHS process.

Chapter 5

Mechanical Properties and Thermal Shock Behaviour of NiAl Coatings

NiAl coatings formed by the SHS process with titanium used as underlayer were successfully fabricated by induction heating. The combustion behaviour of Ni/Al reaction and the microstructure analysis of synthesized products were presented in Chapter 4. In the present chapter, the mechanical properties and thermal shock behaviours of the synthesized products are reported. Vickers indentation was used to investigate the microhardness distribution across the synthesized products and the adhesion between the underlayer and substrate, while the thermal shock tests were performed to examine the thermal shock resistance and to assess the adherence of the produced coatings. The effect of underlayer thickness on the microhardness and thermal shock resistance was studied. The morphology of cracks developed across the samples after thermal shock was observed to analysis the failure mechanism.

5.1. Introduction

Development of new materials with improved properties is the need of the present engineering world, particularly, for high temperature applications such as in aerospace industries. Intermetallics such as NiAl have attracted much interest as a potential candidate for high temperature protective coatings since they have outstanding properties such as high melting point, high oxidation and corrosion resistance, and low density (ρ_{NiAl} = 5.86 g/cm^3) [21][64].

In Chapter 4, a study was carried out to develop a new technique to fabricate NiAl coating using SHS process with titanium as underlayer to improve the adhesion strength. Induction heating was used to initiate the SHS process of NiAl and preheat the substrate. The study in Chapter 4 showed that the synthesized NiAl

was in a liquid phase during the synthesis and partly diffused into underlaying titanium. The heat released by NiAl reaction caused the melting of titanium underlayer and promoted further reactions between the melted Ni–Al–Ti to form the different systems of intermetallics which mostly composed of Ti_3Al–Ti_2Ni composite in the underlayer. The heat generated on the substrate by induction heating has also promoted the formation of interfacial products at the underlayer/substrate interface which produced metallurgical bonding. The formation of Ti_3Al–Ti_2Ni composite in the underlayer was then categorized as an in situ process since these materials were synthesized through the reactions between the liquid NiAl and molten Ti [62]. Many literatures have reported that in situ composites have a number of advantages over conventional composites such as a cost effective process, homogeneous microstructure and excellent mechanical properties [42]. However, the microstructure characterization discussed in the previous chapter has shown that the phase distribution in the underlayer was inhomogeneous. It was observed that processing parameters have an important effect on the formation of the inhomogeneous phases and the porosity of synthesized products. The existence of unreacted Ti in the underlayer, however, must have affected the mechanical properties of product since the metallic Ti, as we realized, has low hardness as compared with the intermetallics. The mechanical properties, particularly, the hardness of synthesized materials is important for high performance protective coatings which have to provide high oxidation, corrosion, and wear resistances. It is therefore very important to investigate the dependence of mechanical properties on the microstructure of the synthesized products in the underlayer.

The adhesion of the coating to the substrate produced by the new method is also a concern for high performance coatings, particularly, for the application of using titanium as underlayer. It was observed that the substrate was preheated during the coating fabrication using induction heating. Microstructure analysis showed that the generated heat on the substrate has allowed the Fe atoms to diffuse into underlayer, and resulted in the formation of interfacial products. A solid interface at the fusion layer indicated that the coating and interlayer had strong

adhesion on the substrate. It is therefore very important to examine the adhesion between the coating and substrate.

Since the developed coating was designed for high temperature applications, it must then be aware that the performance of coatings may be affected in such situation. In high temperature environments, certain thermal cycling with a sudden change of heating and cooling may be experienced during coating operations. Thermal stresses can be generated due to a sudden change of temperature which can result in the adhesion failure in the form of cracks at the interface. Thermal shock test has been widely used as a method to analyze the effect of the sudden change of temperature on the adhesion quality of the coating adherence to the substrate [163]. Thermal shock is referred to as the rapid change of temperature which produces fractures on the material [164]. Thermal shock is often sufficient to induce cracks in the materials which have a high thermal expansion coefficient mismatch [165]. Thermal shock resistance indicates the material ability to withstand the stress generated by sudden changes in temperature. At the interface between the different layers with different compositions such as in the coating/substrate interface, thermal stresses can occur after a high temperature of the synthesis process due to the mismatch of their thermal expansion coefficients. The thermal stress and the existence of interface will contribute to produce cracks affecting the adhesion of coating to the substrate [166]. Coating may be detached from its substrate due to a thermal shock [143]. A coating which is exposed to a thermal shock and shows no cracks or peeling off from the substrate indicates that the coating posses good adhesion.

The adhesion strength of thermal barrier coatings subjected to thermal cycles has been of much interest. Masakazu et al. [167] studied the effect of thermal cycle on the adhesion strength of thermal barrier coating (TBC) using isothermal and cycle thermal shocks. It was found that the adhesion was changed with the application of several cycles of thermal shock tests. The formation of thermally grown oxide was also appeared at the interface. Their works have supported a general understanding that the adhesion between the coating and substrate during thermal shock is significantly influenced by thermal expansion

coefficient mismatches of the component and the formation of thermally grown oxide (TGO) during high temperature exposures.

When a specimen undergoes a thermal shock, thermal stress is developed in the sample due to the mismatch of thermal expansion coefficient between the coating and substrate. The formula of thermal stress can be derived from Hooke's law, and stated in Eq. (5.1) [168].

$$\sigma_c = \frac{E_c.\Delta\alpha.\Delta T}{(1-\nu_c^{\,2})} \tag{5.1}$$

where σ_c is the developed thermal stress in the coating, E_c is the Young's modulus of coating, $\Delta\alpha$ is the mismatch of thermal expansion coefficient between the coating and substrate, ΔT is the difference of temperature during thermal shock, and ν_c is the poison ratio of coating.

During thermal shock test, the failure mode of coating can be different such as surface cracks observed at the coating surface and interface cracks which causes the delamination of the coating to the substrate [169]. The developed thermal stress can lead to the initiation of cracks at the surface of coating as it receives the maximum temperature. Thermal cracks will extend and propagate horizontally with further thermal shock and may link up each other to become crack networks [168].

Improvement efforts on the thermal shock resistance have also been investigated by several studies such as using underlayer. Lijian Gu et al. [170] studied NiCoCrAlY/8YSZ coating deposited by atmospheric plasma spray on an aluminum alloy 5A06 using Ni–P, Ni–W–P and Ni–Cu–P as underlayers. It was found that underlayers were able to produce an improvement of thermal shock resistance. The bonding state has also indicated to improve with the addition of underlayer. Another study also showed that post treatment can improve thermal shock resistance. Raheleh Ahmadi-Pidani et al. [171] reported the improvement of thermal shock resistance of plasma sprayed CYSZ thermal barrier coatings by applying laser surface modification. It was described that there was a failure during thermal shock test in the form of spallation of the topcoat. This failure was mainly

attributed to the thermal stress caused by the mismatch of the coefficient of thermal expansion between the coating and the substrate. Thermal shock resistance of the coating was improved by laser surface modification through the segmented cracks produced by laser glazing.

In this work, the mechanical properties and thermal shock behaviour of NiAl coating which formed by SHS process was systematically investigated. The evaluation of mechanical properties was conducted to study the microhardness and adhesion strength of the synthesized product, while the thermal shock behaviours were used to observe the potential possibility of thermal cracks as one of the forms of reduction in the structural continuity between the coating and the substrate after subjected to thermal shocks. The relationship between the mechanical properties, thermal shock behaviour and microstructure of the synthesized products is discussed.

5.2. Experimental procedures

5.2.1. Combustion synthesis of Ni/Al

Induction heating was used to initiate the SHS process of Ni/Al which subsequently applied as coatings on the steel substrate. The detailed description of the SHS process and coating fabrication was presented in Chapter 3 and 4. Briefly, 0.5 gram of Ni/Al mixtures with an atomic ratio of 1:1 and various weights of titanium used as underlayer were compacted using a pressure of 200 MPa to form two layer pellets. The thickness of Ni/Al after compaction was 0.54 mm, whilst the thickness of titanium was 0.31 mm, 0.53 mm and 0.83 mm. The compacts were then placed on the steel substrate and subsequently heated using induction heating with a current of 300 A in a combustion chamber with an atmosphere of argon gas.

5.2.2. Evaluation of the mechanical properties

The hardness and adhesion strength of the synthesized products were evaluated using indentation with a Vickers microhardness tester (Model Duramin-1/DURA1, Struers). The specimens were cut in their cross sections and mounted in

epoxy resin to form a cylindrical shape, and subsequently ground in both sides to make the two surfaces parallel to the indentation platform. One surface of the samples were polished using abrasive sand papers with 180 and 600 mesh sizes and diamond pasta with the size of 9, 3, and 1 microns. For microhardness evaluation, the indentation was performed using a load of 0.1 N for 15 second. To examine the microhardness distribution across the products, indentations were performed from the coating surface to the substrate with the distance between each indent of about 50 μm. For the sample with underlayer thickness of 0.53 mm, in particular, the microhardness distribution test was also performed in vertical direction for 5 points from the coating to the substrate, in order to reduce the error caused by the hardness evaluation. The observation of the adhesion between the coating and the substrate was also carried out using Vickers indentation since it is relatively simple and does not require adhesive glue as used in the tensile test [143]. Indentations were directed to the exact interface between the two joined layers, which is at the interfaces of substrate/underlayer. Indentations were made using varied loads of 1, 5, 10, and 20 N, in order to observe the resistance of the interface to the crack formation.

5.2.3. Investigation of the thermal shock behaviour

Thermal shock test was carried out to investigate the performance of coatings in high temperature. After the coatings with different underlayer thicknesses were fabricated on the substrate, the products were prepared as the sample for thermal shock test. Thermal shock test was carried out by heating the samples in a carbolite furnace with an atmospheric environment followed by water quenching as demonstrated by Lesage J. et al. [143]. The samples were placed inside the furnace which has achieved a temperature of 1173 K (900 °C), and held for 10 minutes to allow the samples to reach temperature equilibrium. After applying thermal treatment, the hot samples were suddenly taken out from the furnace and dropped into a water bath at room temperature. The volume of water was sufficiently large to make sure that the temperature of water was not significantly affected after quenching. The same procedure for thermal shock test was repeated after the specimen was cooled in the water for about 5 minutes. The

number of heating–cooling cycles in the present work was decided to be 8 times since the thermal crack was visible in the surface of the samples.

After the thermal shock test, the morphology of the surface and cross section of the samples were inspected using optical microscopy (FX-35WA Epiphot Nikon, Japan) which attached with Leica DFC295 software, to assess the damages formation after experiencing a thermal shock test. The surface and cross sections of the samples were observed after mounted with epoxy resin in an automatic mounting press (Metaserv, England) and ground by abrasive papers with 180 and 600 mesh size, and polished with diamond pasta down from 9 to 1 μm using a universal grinder/polisher (Motopol 2000, England). Vickers interfacial indentations were carried out on the heated samples to study the effect of repeated thermal shock on the adhesion between the underlayer and the substrate. Indents were made at the interface between the underlayer and substrate, and the morphology of impressions after indentation test was observed. Laser Raman microspectroscopy operated using HeNe 633nm at a power of 500 mW laser was also used to identify the formation of oxides in the samples after thermal shock test.

5.3. Results and discussion

5.3.1. Microhardness distributions

Fig. 5.1 shows the microhardness distribution which was measured along the cross section of the polished samples with different underlayer thicknesses, whilst Fig. 5.2 illustrates the indentation pictures of the observations. There are three zones in which the hardness becomes a concern: substrate, coating and underlayer zones. In the substrate, the average hardness of steel substrate is 166.15 ± 2.86 HV. In the coating zone, the hardness profile of coatings for different underlayer thicknesses shows a similar trend where the hardness slightly increases from the coating surface to the interface of underlayer. The higher hardness of coating near the interface of underlayer can be attributed to the formation of Ni–rich of NiAl since the liquid Al spread from the coating to the underlayer. The

average hardness of coating for the samples with underlayer thicknesses of 0.31 mm, 0.53 mm and 0.83 mm is 419.4 ± 19.23 HV, 398.4 ± 5.22 HV and 345.2 ± 18.34 HV, respectively. This indicates that an increase in the underlayer thickness has resulted in a decrease in the coating hardness. This fluctuation can be associated with the variation of the formed phases in the coating as a result of the stoichiometric deviation of NiAl, in which an increase in the hardness of coating can be attributed to the higher content of NiAl with Ni–rich composition.

In the underlayer zone, the result shows that the microhardness distribution across the underlayer is varied with the underlayer thickness. It can be seen in Fig. 5.1(a) that the microhardness of underlayer with underlayer thickness of 0.31 mm is high with homogeneous hardness distribution, whilst the microhardness of underlayer with underlayer thickness of 0.83 mm as shown in Fig. 5.1(c) is relatively low with almost homogeneous hardness distributions, and in particular for the sample with underlayer thickness of 0.53 mm as shown in Fig. 5.1(b), the distribution of the microhardness is very inhomogeneous. The result indicates that the average hardness of underlayer with underlayer thicknesses of 0.31 mm, 0.53 mm and 0.83 mm is 978.7 ± 7.62 HV, 772.7 ± 40.04 HV and 680.1 ± 43.42 HV, respectively. The result of this study clearly shows that a decrease in the underlayer thickness produces an increase in the hardness of underlayer. It is encouraging to relate this result to the phase composition of underlayer as obtained by microstructure analysis in Chapter 4. Referring to the microstructure observation as shown in Fig. 4.14, the high hardness (978.7 ± 7.62 HV) of the underlayer with underlayer thickness of 0.31 mm can be associated with the formation of hard intermetallic phases which is mainly composed of Ti_3Al–Ti_2Ni composite, whilst the low hardness in the sample with underlayer thickness of 0.83 mm is attributed to the presence of Ti alloy. The inhomogeneous hardness distribution across the underlayer in the sample with underlayer thickness of 0.53 mm is therefore dependent on the distribution of the formed phases Ti_3Al–Ti_2Ni and Ti alloy. An observation in the middle of underlayer of the sample with underlayer thickness of 0.83 mm shows that there is a high amount of homogen phase which can be attributed to the presence of Ti alloy. The hardness evaluation shows that the

average hardness of this phase is 479.1 ± 7.78 HV. Further analysis in the sample with underlayer thickness of 0.53 mm and 0.83 mm shows that the hardness at the interface between underlayer and coating is higher than that in the midle of underlayer. As observed in the microstructure analysis shown in Fig. 4.15, the highest hardness in the interface of underlayer can be attributed to the the formation of $AlNi_2Ti$.

A comparison of the results reveals that the average hardness of coatings is higher than that of the steel substrate. However, it is somewhat surprising that the hardness of coatings is lower than that of the underlayer. Strong evidence was found in the result which shows that the hardness of Ti_3Al–Ti_2Ni composite and Ti alloy which formed in the underlayer is higher than that of NiAl coating. The hardness distribution in the underlayer with different underlayer thicknesses is affected by the distribution of Ti_3Al–Ti_2Ni composite and Ti alloy which formed in the underlayer. The thickness of underlayer hence has a crucial effect on the hardness distribution in the underlayer. However, it is evident that the sample with the thinnest underlayer (0.31 mm in thickness) exhibits a high hardness with a homogeneous distribution. This result suggests that a thin underlayer in the fabrication of NiAl coating can produce a high strength Ti_3Al–Ti_2Ni composite in the underlayer.

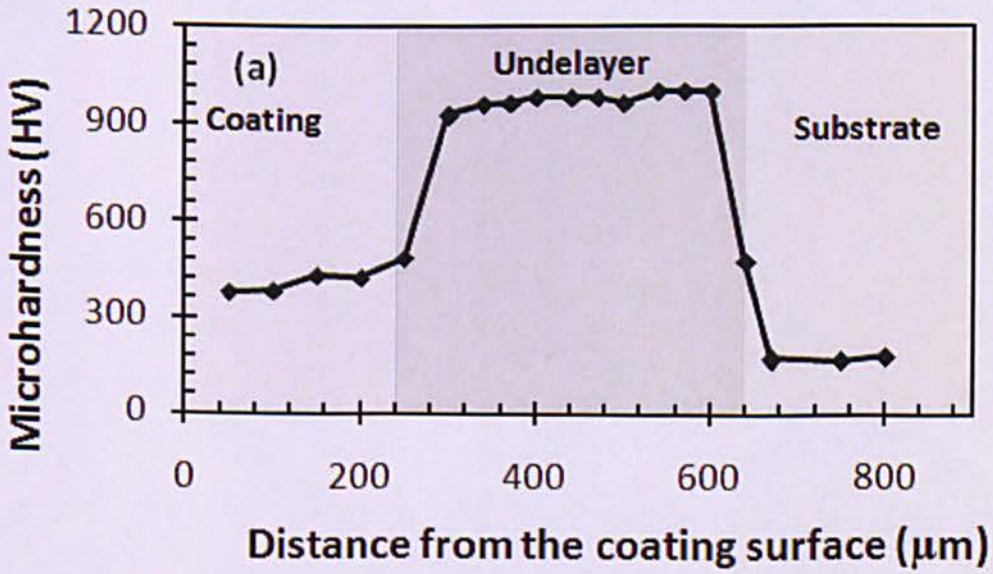

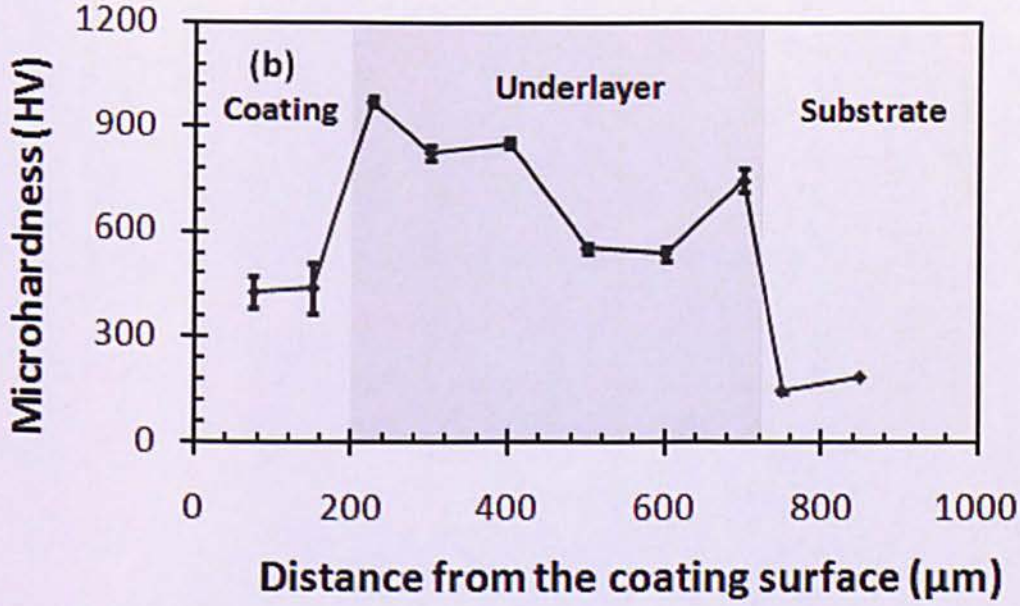

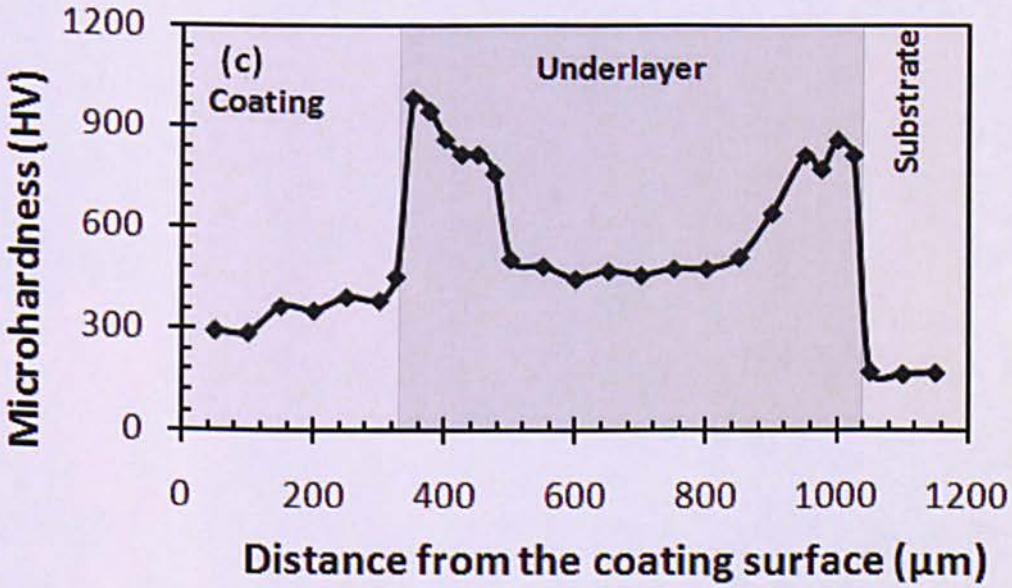

Fig. 5.1. Microhardness distribution across the samples with different underlayer thicknesses: (a) 0.31 mm; (b) 0.53 mm; and (c) 0.83 mm

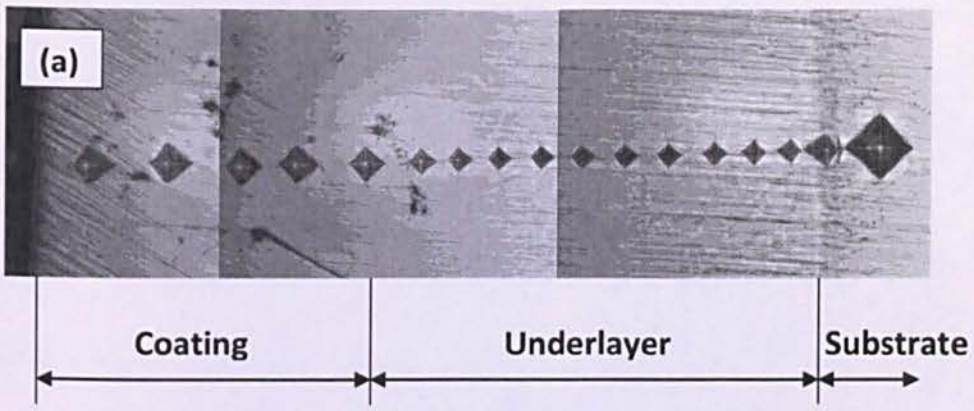
(a)
Coating
Underlayer
Substrate

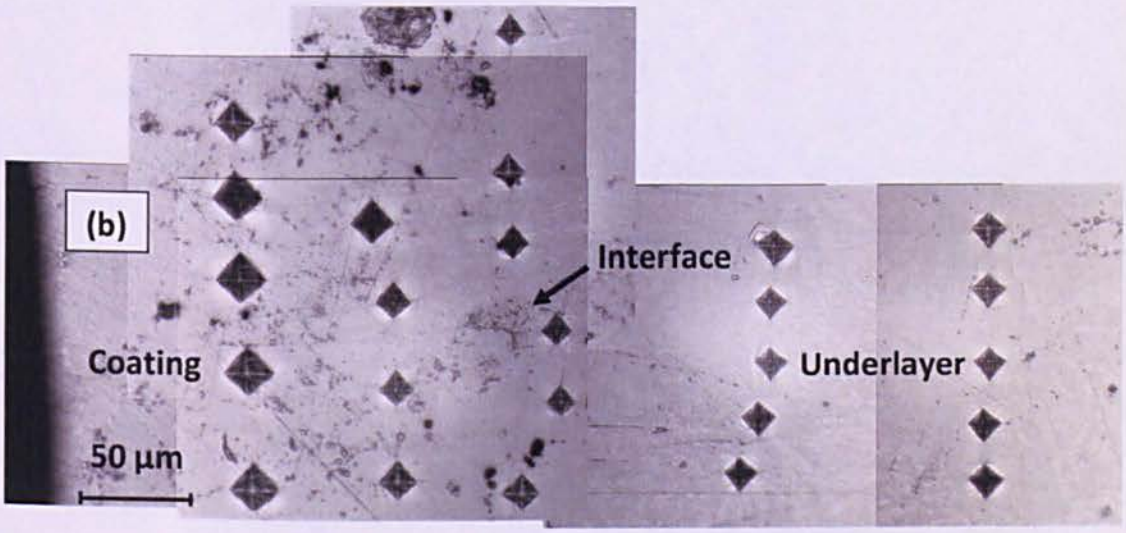
(b)
Interface
Coating
Underlayer
50 µm

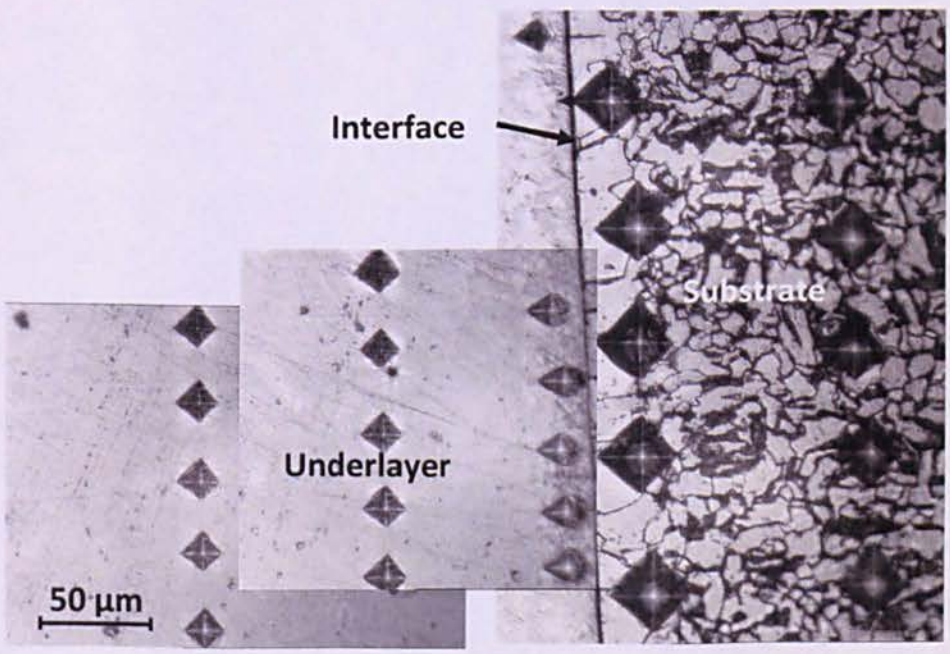
Interface
Substrate
Underlayer
50 µm

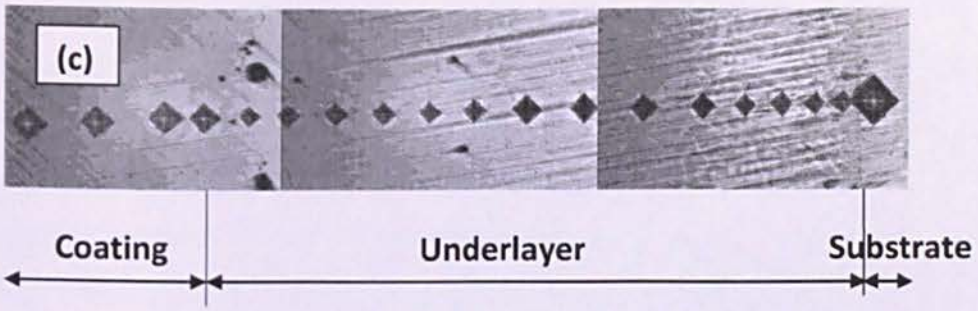

Fig. 5.2. Indentation pictures across the samples with varied underlayer thicknesses: (a) 0.31 mm; (b) 0.53 mm; and (c) 0.83 mm

5.3.2. Adhesion strength

Adhesion strength is one of the most important properties of coating which plays an essential role in the performance and lifetime of the coatings. In the present work, Vickers indentation was used to investigate the adhesion strength of coating, particularly the adhesion between the underlayer and the substrate. Interfacial indentation was chosen since it can be used to evaluate the resistance of coating to the generated cracks at the interface due to indentation. When cracks are developed at the interface, the coating can be delaminated from the substrate.

In this work, indentations were tested using different loads from 1 to 20 N with an expectation that the length of generated cracks could give an indication on the quality of adhesion. The result of indentations using varied loads, however, revealed that no cracks were observed at the interface between underlayer and substrate. The indenter which induced a compressive force in the interface could not provide the driving force for coating delamination. Fig. 5.3 shows the optical micrograph of the indentation using 20 N, which is the maximum load of the indenter, at the interface between substrate and underlayer. Metallographic analysis clearly shows that no cracks could be observed at the indent diagonal directions. The absence of the cracks at the substrate/underlayer interface indicates that the application titanium as underlayer has produced good adhesion on the substrate. The difficulty to generate crack by indentation at the interface can be attributed to the high strength of the adhesion. By considering the result of

microstructure analysis, the generation of good adherence of the coatings can be attributed to the formation of metallurgical bonding at the interface between the substrate and underlayer. As observed by microstructure analysis in Fig. 4.16, Fe has diffused from the substrate to the underlayer and promoted the formation of different phases at the interface between underlayer and substrate. Besides the absence of the cracks, the interfacial structure also shows the absence of porosity. This suggests that the interfacial phases exhibits as a very dense structure.

According to the above analysis, it can be inferred that the coating adherence is mainly attributed to the formation of metallurgical bonding at the interface between substrate and underlayer. The generated heat at the substrate was responsible for the diffusion of Fe from the substrate to the underlayer which subsequently reacted with elements in the underlayer to produce interfacial products. This result suggests that the heat supplied by induction heating and the heat released by Ni/Al reaction were responsible for the temperature increase of the substrate surface, which led to the formation of metallurgical bonding at the interface between underlayer and substrate.

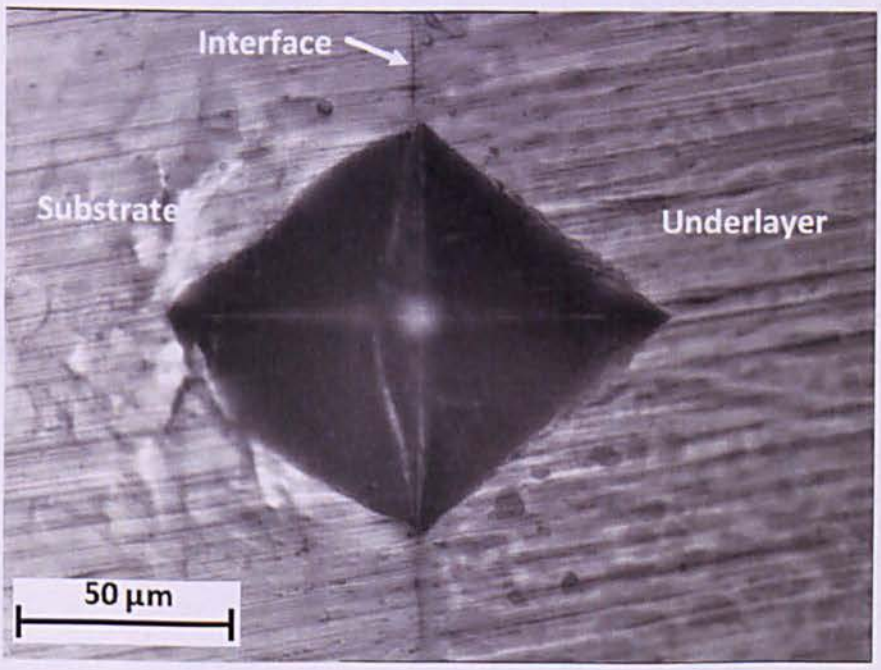

Fig. 5.3. Indentation at the interface between underlayer and the substrate using indenter load of 20 N

5.3.3. Thermal shock behaviours

a). Temperature history

In order to investigate the response of the samples to the thermal shock, the temperature history of the samples experiencing thermal shock was monitored during the testing. The temperature measurement was carried out on the sample surface using type-K thermocouple which was spot welded on the coating surface. A typical temperature history at the surface of coating during thermal shock testing is illustrated in Fig. 5.4. It can be seen that the specimen requires a period at about 2.7 minutes to increase its temperature from 297 K (24 °C) to 1173 K (900 °C). This indicates that the average heating rate of the sample to achieve the thermal shock temperature is approximately 325 K/min. After reaching the thermal shock temperature at 1173 K (900 °C), the temperature of sample levels off indicating that it has achieved equilibrium. During the experiment of thermal shock, the sample was kept in the temperature of 1173 K (900 °C) for about 10 minutes. Since the temperature of the sample remained steady at 1173 K (900 °C), the period of the trial test was stopped before achieved 10 minutes by removing the sample out from the furnace and subsequently dropping it in the water bath for cooling. As shown in the curve during the quenching period, the temperature of sample falls down sharply from 1173 K (900 °C) to room temperature. A rough line appears at the initial of the curve during quenching period is due to the problem occurred during the travelling period of the sample from the inside of the furnace to the bath of water.

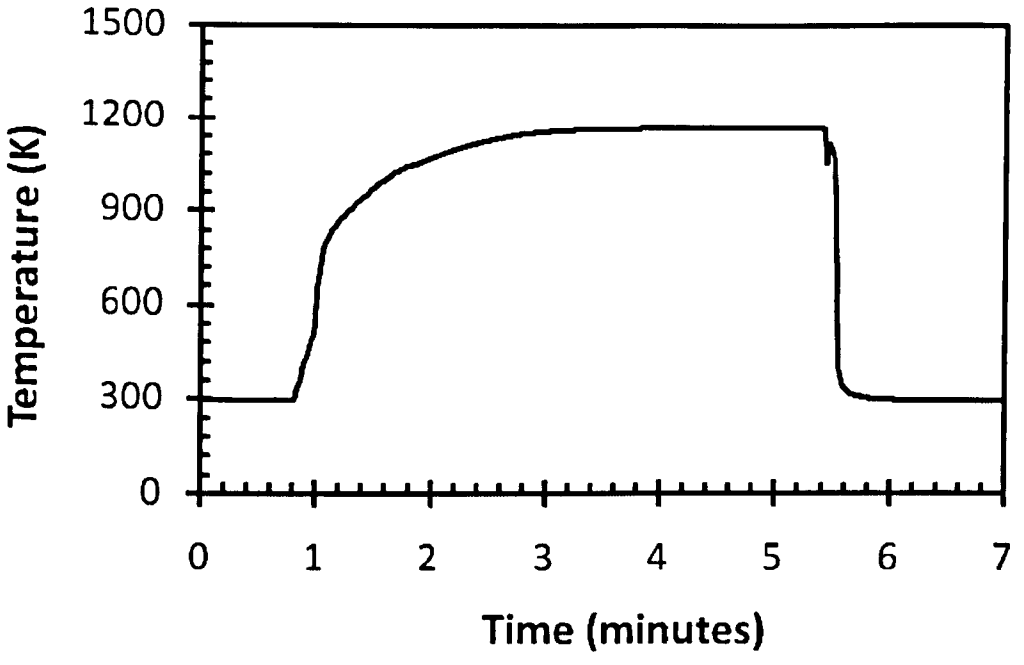

Fig. 5.4. Temperature history of coating surface during thermal shock

b). Morphology of cracks

Fig. 5.5 shows the optical micrograph of the coating surface before and after thermal shock test. It can be seen in Fig. 5.5(a) that the surface morphology of the coating before thermal shock is dense with only small pores. There is no cracks appeared on the surface of the synthesized product. However, after repeated thermal shock test, thermal cracks at the surface become clearly visible. Fig. 5.5(b) describes the formation of horizontal cracks at the coating surface after thermal shock test for 8 times repetition. It can be seen that multiple thermal cracks were linked up each others to form a network of continuous cracks on the coating surface.

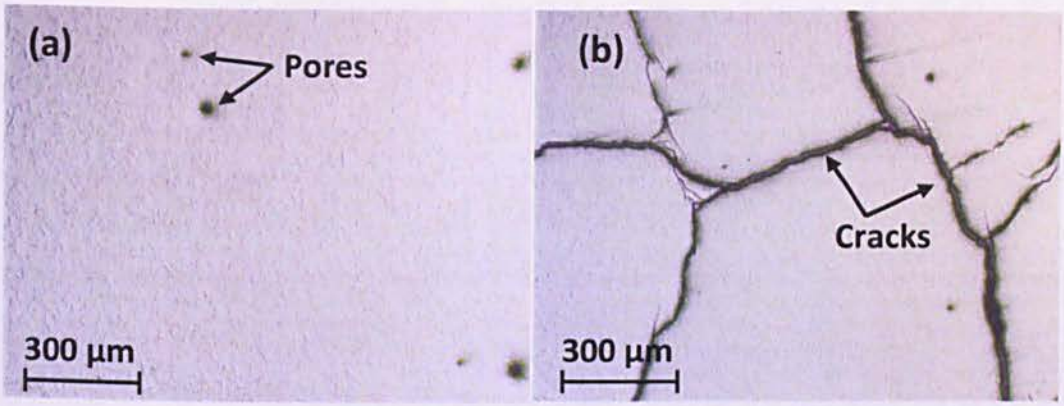

Fig. 5.5. The surface morphology of the coating surface: (a) before; and (b) after thermals shock test with 8 times repetitions

To examine the behaviour of cracks propagation inside the coating and underlayer, the samples were cut and their cross sections were observed. Fig. 5.6 shows the cross sectional morphologies of the samples with underlayer thicknesses of 0.31 mm, 0.53 mm and 0.83, mm after thermal shock test at 1173 K (900 °C) for 8 cycles. Fig. 5.6(a) shows the morphology of thermal cracks in the sample with underlayer thickness of 0.31 mm. It can be seen that cracks develop at the surface of the coating, and propagate perpendicularly to the substrate surface to the underlayer. At the interface between coating and underlayer, the cracks spread out transversely across the underlayer, particularly, along the interface between coating and underlayer, resulting in the coating spallation. The horizontal cracks also appear along the boundary of the different phases of NiAl coatings. As observed by microstructure characterization, the diffusion of Al/Ni from the coating to the underlayer has promoted the formation of several NiAl phases in the coating, where Ni–rich of NiAl formed close to the interface of underlayer due to the initial diffusion of Al liquid into underlayer. Thus, the cracks existed in the coating can be associated with the cracks generated at the boundary between the different phases of the Ni–Al system. It can also be observed that delaminations were developed at the interface between underlayer and substrate. However, the delamination was small and did not produce complete spallations. To describe different types of damage in this study, delamination is used when a portion of coating or underlayer is detached, but still attached to the substrate, while spallation refers to the

detachment of a portion of coating/underlayer from the substrate, which is easy to fall.

The cracks originated at the surface indicate that the coating has experienced extreme heating and cooling conditions producing highest thermal stresses. Such high thermal stresses then led to the formation of cracks in the coating. Previous studies showed that the development of tensile stress is responsible for the initiation of crack on the coating surface when quenched [172]. Due to the repeated thermal shock, the thermal cracks then propagate perpendicularly from the surface to the underlayer. The difference of thermal expansion coefficient between coating and underlayer may promote the propagation of cracks in the vertical direction [173]. However, the horizontal cracks which observed at the interface between coating and underlayer indicates that there were high thermal stresses developed at those regions due to the formations of harder intermetallic phases. The microstructure analysis as discussed in Chapter 4 described that $AlNi_2Ti$ phases were observed in the underlayer near the interface to the NiAl coating. The evaluation of mechanical properties showed that the microhardness of the formed phases at the interface between coating and underlayer is higher than that of the underlayer and coating. Thus, the formation of cracks at the interface between coating and underlayer corresponds to the formation of hard phases $AlNi_2Ti$.

Fig. 5.6(b) shows the morphology of thermal cracks observed in the sample with underlayer thickness of 0.53 mm. It can be seen that a major crack propagates from the coating surface through the underlayer to the substrate. Spallations of fine spots appear at the surface of the coating, but no cracks and delaminations are observed in the interface between underlayer and the substrate which indicates that the coating is still well adhered to the substrate. It can be observed that during the propagation of the major crack through the underlayer, the crack seems to break into some branches to form several micro cracks when it reaches the interface of the substrate. The formation of major cracks propagated from coating to the underlayer can be attributed to the difference of thermal expansion coefficient between coating and underlayer, whilst the formation of micro cracks

may be caused by the brittleness of the formed phases at the underlayer/substrate interface. As described in the microstructure analysis in Fig. 4.16(a) (Chapter 4, section 4.3.3.2), it was shown that a number of intermetallic phases were formed at the substrate/underlayer interface due to the reactions between the diffused Fe from the substrate and the Ni–Al–Ti system in the underlayer.

Fig. 5.6(c) shows the morphology of cracks caused by thermal shock in the sample with underlayer thickness of 0.83 mm, which is the thickest underlayer amongst the investigated samples. It can be seen that only very small number of cracks are existed in the coating, but no cracks can be detected in the underlayer. This indicates that the thick underlayer has a capability for reducing the stress concentration resulted from the mismatch of the thermal expansion coefficient between coating and substrate. A study showed that the application of thick underlayer can improve the thermal shock resistance which tolerates the expansion and contraction of the coating after thermal shock [168]. The microstructure analysis of the thick underlayer as described in Fig. 4.13(c) (Chapter 4, section 4.3.3.2) showed that the composition of underlayer is dominated by Ti alloy since the heat released by NiAl was insufficient to promote further reactions between liquid Ni/Al and Ti. With the formation of a large amount of Ti alloy in the underlayer, the brittleness of underlayer was reduced which restrains the cracks propagation. In addition, the formation of large number of pores in the coating with thick underlayer may contribute to inhibit the cracks propagation [166]. It was shown in Fig. 4.13(c) that the number of pores in the samples with underlayer thickness of 0.83 mm is higher than that in the samples with lower underlayer thickness.

By comparing the cracks observed in the samples with different underlayer thicknesses, it was demonstrated that an increase in the thickness of underlayer has improved the resistance of coating to the thermal shock. This result is consistent with that of previous study which reported that the cracks observed during heating and cooling in thermal shock test were dependent on some factors such as the coefficient of thermal expansion, modulus Young, thermal conductivity, strength, and fracture toughness [166]. An important formula which relates the

thermal stress to other parameters during heating and cooling is given in Eq. (5.1). The present result has shown that the difference of underlayer thicknesses has changed the microstructure and mechanical properties of the underlayer. An increase in the underlayer thickness has resulted in a decrease in the average hardness of underlayer. This result suggests that a decrease in the hardness of the underlayer has increased their fracture toughness. In addition, the cracks observed at the interface between coating and underlayer can also be related to the difference between the hardness of both layers. The result in this study has shown that an increase in the underlayer thickness has reduced the difference between the average hardness of coating and underlayer. As confirmed by previous studies [174], the result in this study has shown that a decrease in the difference between the average hardness of coating and the underlayer has inhibited the formation of cracks at the interface between coating and underlayer.

Another important factor which leads to the formation of cracks after thermal shock is the difference of thermal expansion coefficient. In general, failures in the coating and underlayer during thermal shock test can be associated with the built-in thermal stresses due to the difference of CTE between coating, underlayer, and substrate. When the specimens were taken out from a high temperature furnace and suddenly dropped in cold water during the thermal shock test, thermal stress was developed in the surface and the interfaces of coating/underlayer and underlayer/substrate. As mentioned in Eq. (5.1), the thermal stress has a linear relationship with the difference of CTE and the temperature difference between thermal shock and quenching temperature. The repeated heating and quenching cycles on the sample led to significant temperature change in the material resulting in the high thermal stresses. When the stresses are high enough, microcracks were generated which could propagate in the vertical and horizontal directions resulting in the spallation/delamination of coating/underlayer. For reference purpose, Table 5.1 show the coefficient of thermal expansion (CTE) of several materials obtained from literatures. It is apparent that the CTE of Fe is larger than Ti. This means that the Fe substrate expanded much faster than Ti. In the quenching during thermal shock test, the CTE difference produces thermal stresses at the interface. It is

difficult to compare the CTE difference between Ti alloy and Ti_3Al–Ti_2Ni composite due to the lack of CTE data for Ti_3Al–Ti_2Ni composite. However, the low CTE of Ti can give an indication that a low thermal expansion will increase the thermal shock resistance since it will restrict the amount of strain in the material [166]. The crack formations indicates that the thick underlayer which mainly composed of Ti alloy has a lower CTE mismatch between the underlayer and substrate compared with the thin underlayer which mainly composed of Ti_3Al–Ti_2Ni. The result in this study suggests that the formation of cracks was sensitive to the underlayer thickness since the thermal resistance of thick underlayer is higher than that of thin underlayer. Increasing the thickness of underlayer produced a gradual change of temperature during heating and cooling resulting in the reduction of thermal stress.

Table 5.1. Thermal expansion coefficient (CTE) of several materials

Phase	CTE (x 10^{-6} $^{-}$K)	[Ref]
Fe	11.8	[175]
Ti	8.4	[176]
NiAl	13.22 – 14.67	[177]

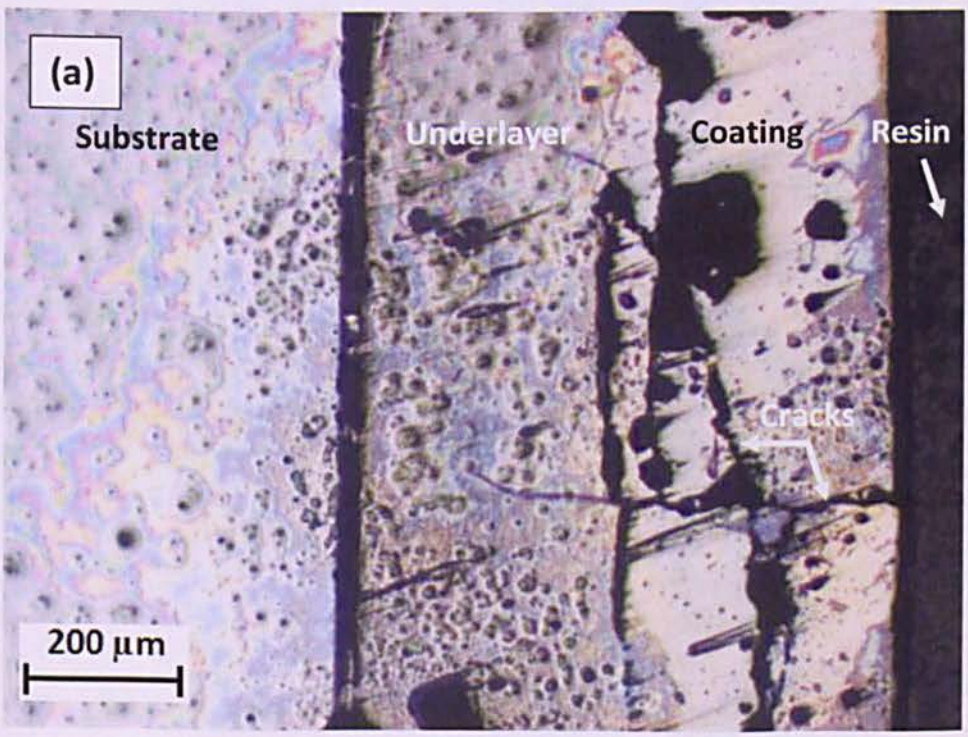

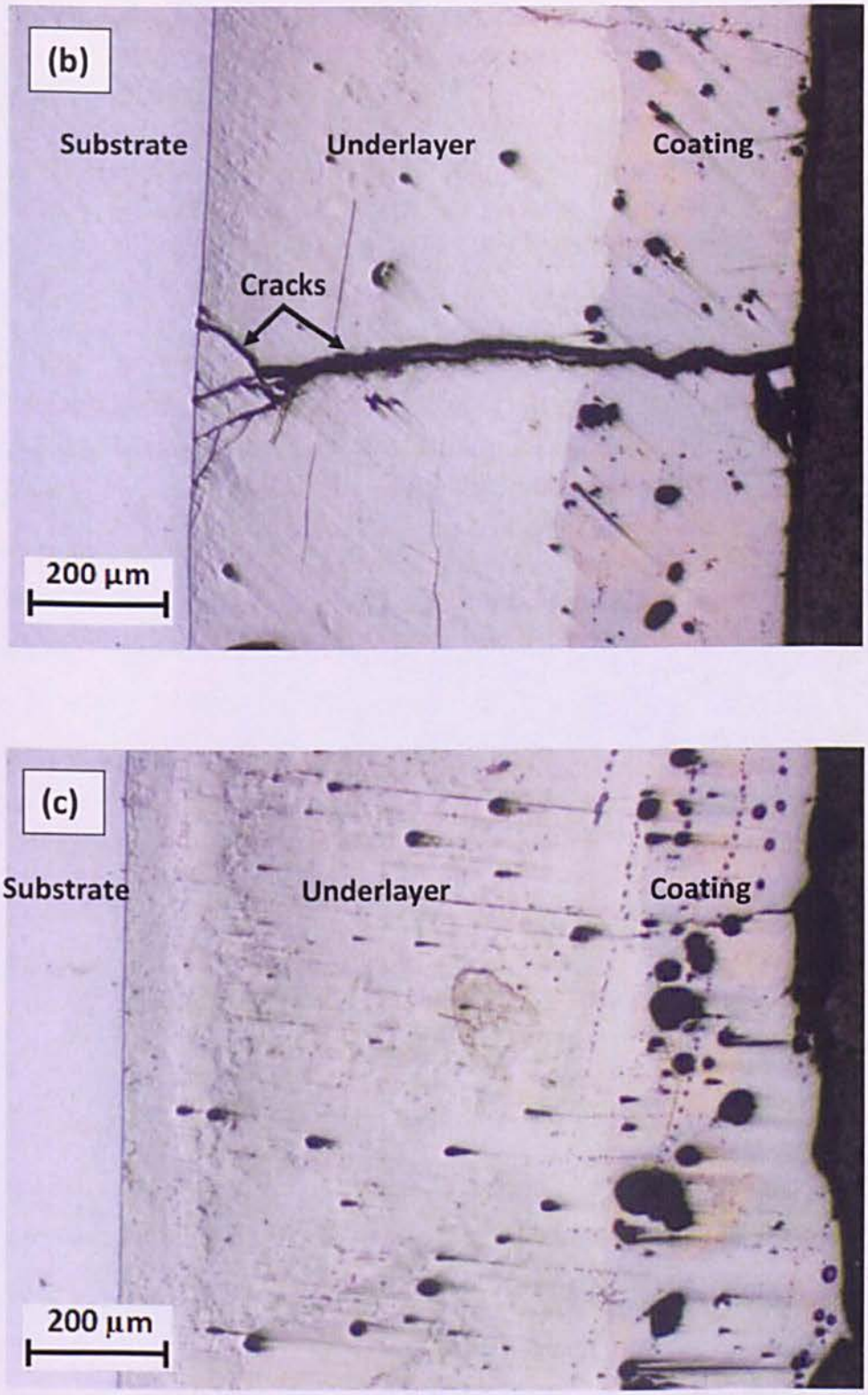

Fig. 5.6. Thermal cracks developed across the samples with underlayer thicknesses of: (a) 0.31 mm; (b) 0.53 mm; and (c) 0.83 mm

c). The adhesion strength after thermal shock

Vickers indenter was also used to investigate the adhesion between underlayer and substrate after thermal shock test. The test was performed using varied loads of 1 N, 5 N, 10 N, and 20 N. 20 N is the maximum load of the equipment. The samples with underlayer thickness of 0.83 mm were used for adhesion test since they still showed good adherence after thermal shock test. The result of the adhesion test at the interface between underlayer and substrate is shown in Fig. 5.7. It can be seen that there is no crack which can be observed at the interface between underlayer and substrate under all the loads tested. The underlayer and coating also show no peeling off from the substrate after indentations. This indicates that coatings have good adhesion on the substrate. The adhesion between underlayer and substrate can be lost when cracks appear at their interfaces. In general cases, the major factor causing the interface degradation can also be attributed to the oxidation when the samples experience a long thermal treatment. However, for the thermal shock test with a short heating length, the degradation is due to the thermal stress [171]. This shows that the samples with thick underlayer have good thermal resistant resulting in the adhesion improvement.

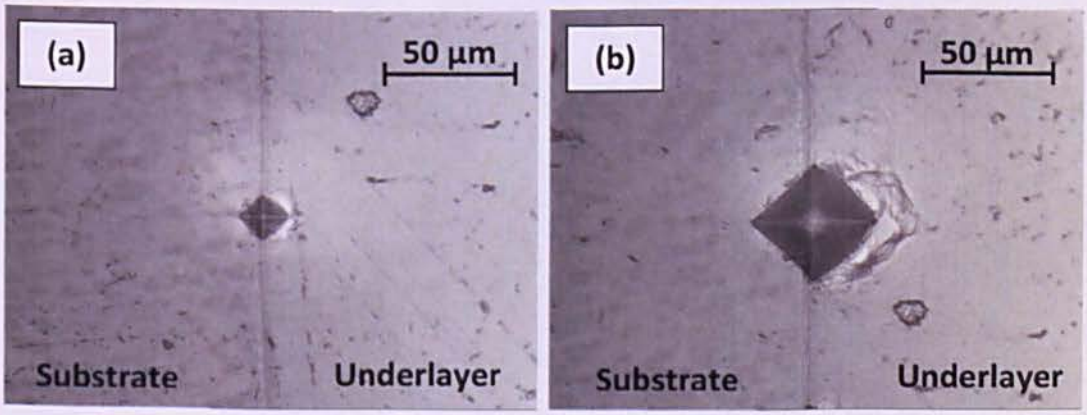

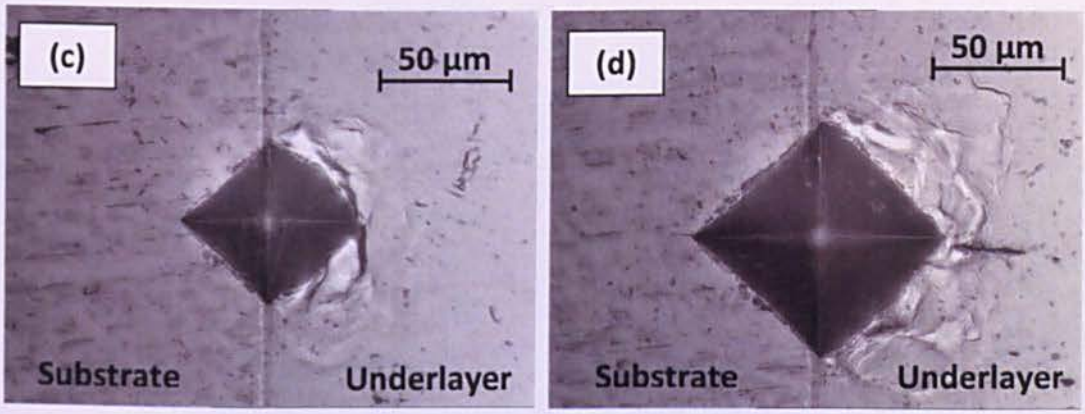

Fig. 5.7. Optical micrograph of the interface between the underlayer and substrate after indentation using loads: (a) 1 N; (b) 5 N; (c) 10 N; and (d) 20 N

d). Formation of oxides

The formation of oxides at the interface between the coating and the substrate when exposed in high temperature can result in the deterioration of adhesion strength which leads to the gradual loss of the bonding [171]. There are some causes of oxides which can lead to spallation during thermal shock such as stress in oxide film growth, thermal strain due to thermal gradient in oxide scale, and coefficient of thermal expansion (CTE) mismatch between oxide and coating [178]. However, for short heating cycle, oxidation does not occur and the degradation of coating is mainly due to the thermal stress [171]. In the present work, the formation possibility of oxides in the coating and substrate was observed using laser Raman microspectroscopy. The cross sections of the samples containing the coating, underlayer and substrate were scanned using Raman shift in the range of 100–1800 cm^{-1}. The result has shown that after thermal shock test no oxides were formed in the coating and the underlayer. However, oxides have been clearly identified in the steel substrate. The Raman spectra of oxides formed in the steel substrate are depicted in Fig. 5.8. In order to identify the type of oxide phase, the Raman peaks of the oxides are compared with previous publications used as references. The result as listed in Table 5.2 shows that all Raman peaks of the oxides appear in the steel are confirmed as Fe_2O_3 [179].

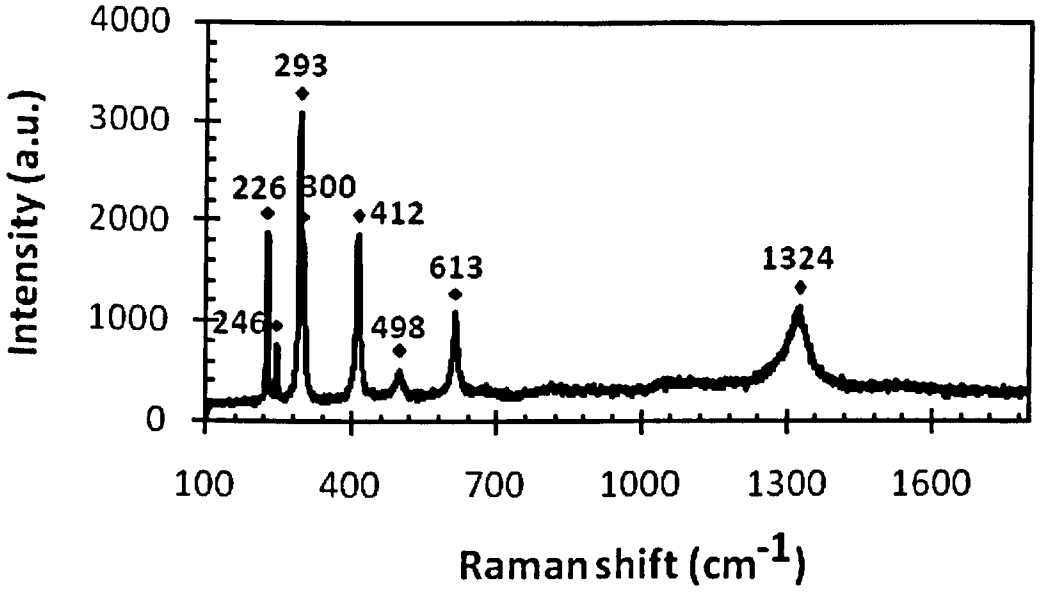

Fig. 5.8. Raman spectra of oxides in the substrate

Table 5.2. Type of oxide in the steel substrate

Peaks	Phase
1324	Fe_2O_3
613	Fe_2O_3
498	Fe_2O_3
412	Fe_2O_3
300	Fe_2O_3
293	Fe_2O_3
246	Fe_2O_3
226	Fe_2O_3

5.4. Summary

This chapter reports the mechanical properties and thermal shock behaviour of NiAl coatings which formed by SHS process. Ti underlayers with thicknesses of 0.31 mm, 0.53 mm and 0.83 mm were used to improve the adhesion between coating and substrate, while induction heating with a current of 300 A was used to initiate the SHS of Ni/Al and preheat the substrate. The result in this study showed that the thickness of underlayer has a crucial effect on the hardness of synthesized products by affecting the distribution of the formed phases. It was shown that the

hardness of steel substrate is 166.15 ± 2.86 HV, while the hardness of coating for the samples with underlayer thicknesses of 0.31 mm, 0.53 mm and 0.83 mm is 345.2 ± 18.34 HV, 419.4 ± 19.23 HV and 398.4 ± 5.22 HV. The hardness of underlayer for different underlayer thicknesses is affected by the formed phases in the underlayer. It was found that an increase in the underlayer thickness has reduced the average hardness of the underlayer. The high hardness of the underlayer was attributed to the formation of Ti_2Ni–Ti_3Al, while the low hardness was attributed to the formation of Ti alloy. A correlation between the hardness and microstructure observations indicates that the hardness of Ti_2Ni–Ti_3Al is 978.7 ± 7.62 HV, while Ti alloy is 479.1 ± 7.78 HV. The average hardness of underlayer with underlayer thicknesses of 0.31 mm, 0.53 mm and 0.83 mm is 978.7 ± 7.62 HV, 772.7 ± 40.04 HV and 680.1 ± 43.42 HV, respectively. The evidence from this study suggests that the hardness of NiAl coating is higher than that of the substrate, but lower than that of the underlayer which is mainly composed of Ti_2Ni–Ti_3Al composite and Ti alloy.

The evaluation of the adhesion strength to the samples as they synthesized showed that coatings have good adhesion to the substrate since no cracks appeared at the diagonal directions of the indent. The improvement of adhesion strength was attributed to the formation of metallurgical bonding at the interface between underlayer and the substrate.

The observation on the thermal shock behaviour showed that during the thermal shock test, failures have occurred in the coating system in the form of cracks. Four types of cracks were observed in the sample with thin underlayer: continuous cracks which developed at the surface, vertical crack which propagated from the surface through the underlayer to the substrate, horizontal cracks which generated along the interface between coating and underlayer, and minor crack which grown in the interface of underlayer/substrate. In some locations on the coating surface, spallations were also created. A possible explanation in the formation of cracks is attributed to the different compositions of phase formed in the underlayer. This difference leads to the variation of hardness and the mismatch between the CTE of the formed phases. In the sample with high thickness of

underlayer, there was no indication of cracks which developed in the interface between underlayer and the substrate after indentation test. This shows that the coating posses a good adherence after thermal shock.

The present work has shown that the application of titanium as underlayer not only has improved the coating adherence, but also was beneficial for high temperature applications. It was observed that the thickness of underlayer has significantly influenced the thermal shock resistance and adhesion strength. It was revealed that a high thickness of underlayer produces the best coating adherence and thermal shock resistance. Considering that the synthesized product are not optimized, the present results are encouraging, with the potential for significant improvement in the thermal resistance of the synthesized products. Further investigation would be put on microstructure to improve the thermal shock performance of NiAl coating.

Chapter 6

SHS Process of NiAl–TiC–Al_2O_3 Composite

This chapter discusses the SHS process of NiAl–TiC–Al_2O_3 composite ignited by induction heating. The reactants were prepared using the stoichiometric mixtures of Ni/Al and $3TiO_2$/4Al/3C with different weight compositions. The effect of reactant compositions on the combustion behaviour, microstructure, and mechanical properties of the synthesized products was investigated. Laser Raman microspectroscopy was also used to confirm the existence of the phases in synthesized products observed by XRD and SEM. The reaction mechanism of the synthesized products is discussed based on the combustion behaviour observation and microstructure characterization. The mechanical properties were also performed to evaluate the microhardness of the synthesized products.

6.1. Introduction

NiAl has been attractive as a potential candidate for high temperature applications due to its advantages such as high strength, low density, high melting temperature, and good oxidation and corrosion resistances. However, the application of single phase NiAl for structural materials is still limited due to its lack of ductility at room temperature and insufficient strength at high temperature. Many efforts have been carried out to balance its properties such as using grain refinement for improving its ductility at room temperature, and alloying or compositing for strengthening at high temperature applications [21].

Recent studies to form NiAl based composites were carried out using the addition of ceramics such as carbide [18], boride [180], nitride [181], and oxide [19]. Among the ceramic materials, TiC has attracted much interest as a reinforcement candidate for NiAl since it offers great advantages such as high hardness, high melting temperature, and high corrosion and wear resistance [40]. A study reported that the combination of high hardness and excellent stability of TiC at high

temperature, together with the strong atomic bonds of NiAl produced composites with an excellent wear resistance at room and high temperature [18]. An alumina ceramic system such as TiC–Al_2O_3 has also been reported to improve the fracture toughness of individual ceramic materials, either TiC or Al_2O_3 [46]. L.Y. Sheng et al. [15] fabricated NiAl–TiC composite with dispersed Al_2O_3 oxides to form NiAl–TiC–Al_2O_3 composite using the SHS and hot extrusion technique. It was reported that NiAl–TiC–Al_2O_3 composite possess better mechanical properties at room temperature due to a fine microstructure and predeformation caused by hot extrusion.

During the past 40 years, the SHS process has attracted a special interest to synthesize intermetallic, ceramic and composite since this process produces high exothermic reaction [99]. Comparing with conventional methods, the SHS process takes a short time and requires a lower energy consumption since the combustion reaction is self propagated using the heat released by an exothermic reaction. The ignition of the SHS process has also developed into many different techniques [49]. Recent studies showed that induction heating offers a great interest for an efficient external heat source in the combustion synthesis considering its capability for a fast heating, clean and efficient process. Induction heating was successfully used to ignite the combustion synthesis of NiAl/Al_2O_3 [19] and NiAl/TiC [18].

Although the SHS process offers significant advantages for synthesis NiAl and NiAl based composites, porosity is still problematic [2]. The material synthesized using the SHS process is often associated with a high level porosity, which can achieve 50% of the theoretical density [14]. The application of porous product to the oxidation resistance of coatings cannot be tolerated since it can permit the infiltration of gas from outside to the base metal to create an oxidation reaction. The porosity, however, is also beneficial for some applications such as biomaterials [34] and a large number of filtration applications [30]. Understanding the pore structure and its formation in synthesized product therefore becomes one of the main challenges to produce a desirable product. It is worth mentioning that few researches on the SHS process of NiAl–TiC–Al_2O_3 composite using induction heating were reported. L.Y. Sheng et al. [15] conducted the investigation of NiAl–

$TiC–Al_2O_3$ composite from Ni, Al, Ti, C and TiO_2 using the SHS process with hot extrusion, where the punch used to extrude the reactant was heated using induction heating. However, the combustion temperature of the SHS process was not monitored due to the limitation of experimental set up. It was realized that the combustion behaviour could provide sufficient information on the reaction mechanism which changes the microstructure and influences the mechanical properties of synthesized product [19].

The objective of this work was to fabricate $NiAl–TiC–Al_2O_3$ composite obtained from a low cost material TiO_2 using the SHS process and induction heating as the ignition source, with an emphasis on investigating the effect of reactant compositions on the combustion behaviour, microstructure, and mechanical properties of the synthesized products. Understanding the relationship between reactant compositions on the combustion behaviour, microstructure, and mechanical properties of the synthesized product, reported herein, is expected to promote the development of dense $NiAl–TiC–Al_2O_3$ composites.

6.2. Experimental procedures

The powders used for the reactants in the SHS process in the present work were Ni carbonyl type–123, Al, C and TiO_2. The specification and morphology of reactants are given in Table 3.1 and Fig. 3.1, respectively. The reactants were prepared by mixing two stoichiometric compositions of (Ni + Al) and ($3TiO_2$ + 4Al + 3C) with different weight percentages as given in Table 6.1. For convenience, the reactants were described as the mixture of Ni/Al and 10, 20, 30 and 40 wt.% TiO_2/Al/C. The reactions were expected to occur according to Eq. (6.1) and Eq. (6.2).

$$Ni + Al \rightarrow NiAl \quad (6.1)$$

$$3TiO_2 + 4Al + 3C \rightarrow 3TiC + 2Al_2O_3 \quad (6.2)$$

Table 6.1. Variation of the weight fractions of reactants

Specimen	Weight percentage of reactants (wt.%)	
	Ni/Al	TiO_2/Al/C
1	100	0
2	90	10
3	80	20
4	70	30
5	60	40

When the reactions are assumed to completely finish without producing any unreacted products or intermediate phases according to the reaction equation in Eq. (6.1) and Eq. (6.2), the theoretical weight fraction of the component in the reaction products is given in Table 6..

Table 6.2. Theoretical weight fraction of the reaction products

Compounds	Weight percentage (wt.%) of products			
	x = 10	x = 20	x = 30	x = 40
NiAl	90	80	70	60
TiC	4.37	9.37	14.05	18.73
Al_2O_3	5.32	10.63	15.95	21.27

The starting materials were dry mixed using a ceramic mortar and dried in a carbolite furnace at about 100 °C for 1 hour to remove any moisture contents. The powder mixture was weighed to produce 2 grams for each reactant and subsequently cold compacted using a pressure of 200 MPa before heating process. Induction heating was used to initiate the SHS process of the reactants which performed inside a glove box with an atmosphere of argon gas flowing with a flow rate of 15 l/min and a pressure of 2000 psi. Since the ignition using induction heating was insufficient to initiate the reaction of the samples with a high content of TiO_2/Al/C, a steel substrate was used to help the heating for ignition. The electric current of induction heating was adjusted to 300 A, while the heating time was turned off at about 1 second after the ignition occurred. The measurement of combustion temperature was carried out using a pyrometer with a temperature range of 540–3000 °C, with a response time of 2 ms, and the data were recorded using Raytek DataTemp Multidrop software. The emissivity of all samples was

assumed to be 0.82, which is similar to the emissivity of NiAl as the major content in the mixture. The schematic diagram of the experiment set up is shown in Fig. 3.3 (Chapter 3).

The microstructure characterization and properties evaluation of the synthesized product were performed using equipments as described in Chapter 3. Scanning electron microscopy and optical microscope were used to observe the microstructure of synthesized products, while the phase identification was carried out using XRD technique with a scanning rate of 4 deg./min, the scanning step at 0.02 deg., and operated with 40 kV/200mA. Prior to the SEM and XRD tests, the samples were polished and etched using a standard procedure as mentioned in Chapter 3. Laser Raman microspectroscopy was used to investigate the Raman spectra of the formed phases. The investigations were conducted at room temperature using He–Ne lasers with a maximum power of 500mW over the wave number range of 100–1800 cm^{-1} at an interval of 0.86 cm^{-1}. The diameter of the laser beam is about 5–7 μm. To evaluate the mechanical properties of synthesized products, Vickers indentation was used to observe the microhardness of the synthesized products, which realized using a load of 0.1 N for 15 second.

6.3. Results and discussion

6.3.1. Combustion behaviours

6.3.1.1. Mechanism of reactions

During the reaction of Ni/Al and TiO_2/Al/C, the chemical reaction of the process is essential to study the reaction mechanism of the system. Although the reactants were prepared with a stoichiometric ratio of Ni/Al and $3TiO_2$/4Al/3C with different weight percentages, they were subsequently mixed together into Ni–Al–TiO_2–C systems. Thus, many possibilities of the reactions can then occur. However, it is reasonable to assume that when the reactions are complete, the synthesized products will be composed of NiAl, TiC, and Al_2O_3 with different volume ratios.

As described in Eq. (6.1) and Eq. (6.2), during the synthesis reaction of Ni–Al–TiO_2–C systems, it is assumed that two reactions will occur: Ni + Al → NiAl and $3TiO_2$ + 4Al + 3C → $2Al_2O_3$ + 3TiC. The reaction in the Ni–Al–TiO_2–C systems may occur firstly by an increase in the temperature of the sample due to the heat supplied by induction heating added by the heat from the steel substrate which used to help ignition. When the temperature of reactant achieves at about the melting point of Al, a part of Al will be melted since it has the lowest melting point [136]. The molten Al then encloses into the sideline of particles Ni, C and TiO_2. Following the melting of aluminium, the exothermic reaction of Ni/Al is more favourable to occur initially. This is due to the ignition of Ni/Al reaction which can be initiated at or below the melting point of Al [136] [182]. In addition, Ni atoms are easier to preheat using induction heating due to its high magnetic permeability compared to C and TiO_2. As suggested by Ping Zhu et al. [136], there are three stages which occur in the combustion reaction of Ni/Al systems. The first stage is initiated after a third of aluminium is melted. The temperature will increase from the melting point of Al to the decomposition of intermediate phase $NiAl_3$ at 854 °C (1127 K). In this period, the reaction mechanism is the dissolution of solid Ni in the liquid Al. Other intermediate phases such as Ni_2Al_3 and Ni_5Al_3 can also be formed at this stage. In the second stage, the reaction is still the dissolution of Ni in the liquid Al which occurs from 854 °C to 1300 °C (1573 K). The third stage is dominated by the exothermic reaction of Ni/Al. In this stage, the reaction rate is very high and the temperature is increased sharply to achieve the maximum value. After the Ni/Al reaction is complete, the heat released by the formation of NiAl becomes the ignition agent to initiate further reactions in the TiO_2/Al/C system to form TiC–Al_2O_3 phases. According to J.J. Moore et al. [14] and Muhammad Sharifi E. et al. [48], the SHS process of TiO_2/Al/C systems involves two reactions: the metallothermic reduction of the oxide (TiO_2) to form an elemental Ti, and the reaction between Ti and C to form TiC. These reactions are described in Eq. (6.3) and (6.4). These reactions are strongly exothermic and spontaneous, and called as a thermite reaction. For the purpose of comparison, the heat of formation (ΔH_f) for different systems is given in Table 6.3, where the negative signs indicate that the reactions are exothermic. Since the combustion temperature of TiO_2/Al/C reaction is

sufficiently high, the heat released by TiC–Al_2O_3 reactions can then maintain the synthesized NiAl in the liquid form causing TiC particles to insert into NiAl melt [18]. The existence of liquid NiAl will also allow the Al_2O_3 to rise to the surface due to its lower density [183].

$$4Al + 3TiO_2 \rightarrow 2Al_2O_3 + 3Ti \quad (6.3)$$

$$Ti + C \rightarrow TiC \quad (6.4)$$

Table 6.3. Heat of formation at 298 K for different systems

Reactions	ΔH_f (kJ/mol)	Ref.
$Ni + Al \rightarrow NiAl$	-118.4	[120]
$4Al + 3TiO_2 \rightarrow 2Al_2O_3 + 3Ti$	-521.2	[48]
$Ti + C \rightarrow TiC$	-184.5	[120]
$3TiO_2 + 4Al + 3C \rightarrow 3TiC + 2Al_2O_3$	-1074.7	[48]

6.3.1.2. Measurement of the combustion temperature

Fig. 6.1 shows the temperature profiles for the SHS reactions of the samples which composed of (1–x)Ni/Al + (x)TiO_2/Al/C with x equals to 10, 20, 30, and 40 wt.%. Since the temperature measurement was only recorded using a pyrometer, the combustion temperature could only be monitored starting from 813 K (540 °C) as the lowest value of the temperature range of the pyrometer. The start point of heating at room temperature was not recorded in this work due to the limitation of the equipment. In addition, the variation before the ignition point in the sample with 30 wt.% TiO_2/Al/C was caused by the movement of the sample during the synthesis reaction resulting in the focus change of the temperature monitoring.

As can be seen in Fig. 6.1, all samples produce a temperature jump which indicates the occurrence of the combustion reactions. The sharp increase of the combustion temperature starts at a point, called as the ignition temperature, and reaches a peak at a maximum point called as the maximum combustion temperature. It can be seen that the ignition temperature and the maximum combustion temperature increase with an increase in the TiO_2/Al/C content. From the maximum point, the combustion temperature decreases and then levels off to form a plateau for a period of time. The length of the plateau is varied depending

on the reactant compositions. An increase in the TiO_2/Al/C content leads to a shorter length of the plateau. Afterwards, the combustion temperature decreases to room temperature which indicates a cooling period. It is also shown that the reactant compositions affect the ignition time, which represents whether or not the reaction is easy to occur. It can be seen that an increase in the content of TiO_2/Al/C increases the ignition time. The ignition time cannot be calculated since the temperature monitoring was not initiated from the start of heating to the occurrence of combustion reaction.

The temperature profile as shown in Fig. 6.1 shows that two temperature stages were observed, where the first stage showing a peak temperature may be attributed to the exothermic reaction of TiC–Al_2O_3, and the second stage showing a plateau may correspond to the solidification of NiAl. This assumption was taken based on the reason mentioned in section 3.1 in which NiAl was synthesized first and the heat released by NiAl was subsequently used to ignite the second reaction of TiO_2/Al/C to form TiC–Al_2O_3 resulting in a simultaneous temperature increase. The high combustion temperature of the second reaction then kept the melting of NiAl for a period of time before cooling down rapidly after full solidification.

It can be observed in Fig. 6.1 that the ignition temperature increases with an increase in the TiO_2/Al/C content. The ignition temperature of the samples with compositions of 10, 20, 30, and 40 wt.% of TiO_2/Al/C can be identified at approximately 852.6 K, 1005.3 K, 1039.6 K and 1133.4 K, respectively. This indicates that the ignition occurred at a temperature below and above the melting point of Al (933 K), as the lowest melting point in the system. It is worth mentioning that in most SHS process for NiAl, the reaction is initiated by the melting of Al which subsequently spreads into the solid element to produce ignition [136]. However, a lower ignition temperature is possible to occur as reported by a recent study carried out by Makino et al. [182] which showed that the ignition of NiAl can be 200 K lower than the melting point of Al depending on the size ratio and the mixture ratio. They reported that the reduction of ignition temperature can be achieved by increasing the particle surface area in the reactant. As found in several literatures, ignition can occur if the heat released by reaction is greater than that which lost to

the ambience. Meanwhile, an increase in the ignition temperature may be explained as follows: (1) Increasing the content of TiO_2/Al/C content will absorb more amount of the heat released by NiAl reaction which results in the increase of the heat required to initiate the exothermic reaction of the system; (2) Increasing the content of TiO_2/Al/C will reduce the thermal conductivity of the sample due to the smaller particle contact, and results in a slower reaction rate of Ni/Al; and (3) Increasing the content of TiO_2/Al/C will reduce the contact between Ni and Al.

As expected, an increase in the TiO_2/Al/C content has increased the maximum temperature of the combustion process. In this investigation, the maximum combustion temperature is referred to the maximum point of the combustion temperature which can be achieved during the first exothermic reaction stage after ignition. The result shows that the maximum combustion temperature of the first reaction stage for the samples with 10, 20, 30 and 40 wt.% of TiO_2/Al/C is approximately 1911, 2093, 2135 and 2208 K, respectively. This result suggests that the maximum combustion temperature for all reactions are below the melting point of TiC (3210 K) [184] and Al_2O_3 (2325 K) [120] which is then responsible for the formation of solid particles of TiC and Al_2O_3. An increase in the combustion temperature can be attributed to the increasing amount of TiO_2/Al/C particles being in contact resulting in the initiation of the TiO_2/Al/C reaction to produce TiC–Al_2O_3 which is more exothermic. An increase in the TiO_2/Al/C content, however, can reduce the thermal conductivity of the reactant which can reduce the degree of completion of the SHS reaction, lengthen the ignition time, or even stop the initiation of the reaction. As can be observed, the ignition time is significantly longer with an increase in the TiO_2/Al/C content. Said another way, the ignition occurs faster in a lower content of TiO_2/Al/C. This is due to the fact that a lower percentage of TiO_2/Al/C had a higher content of the liquid NiAl in the synthesized product which hence increased the thermal conductivity of the reactant. Consequently, the higher thermal conductivity of the reactants will improve the speed of reaction. In the higher content of TiO_2/Al/C, the ignition time is longer due to the lower thermal conductivity. In the sample with 10 wt.% of TiO_2/Al/C, the maximum combustion temperature is approximately 1911 K, which is the same as

the adiabatic temperature or the maximum temperature for the SHS process of Ni/Al. The real temperature may be higher than this value since there were some heat losses to the surrounding. However, the higher amount of Ni/Al (90 wt.%) may result in the large amount of the liquid phase produced by Ni/Al reaction which then absorbs the heat released by TiO_2/Al/C reaction. As a consequence, the combustion temperature was reduced. It can be observed that the subsequent increase in the content of TiO_2/Al/C from 10 to 40 wt.% significantly increases the maximum combustion temperature from 1911K to 2208 K. The reason may be explained as: when the content of TiO_2/Al/C in the preforms is increased, the heat released by the exothermic reactions of TiO_2/Al/C per unit volume of the preforms is also increased. However, increasing the TiO_2/Al/C is accompanied by decreasing the content of the Ni/Al fraction. Thus, the more the TiO_2/Al/C is present in the preforms, the less the heat released by exothermic reactions of TiO_2/Al/C is taken by the melting of NiAl due to the less amount of the molten NiAl. It can be observed that increasing the TiO_2/Al/C content reduces the duration of plateau. This indicates that the reduced content of the liquid NiAl resulted in the shorter period of the NiAl solidifications. It can also be seen that the temperature of the plateau for the different reactant compositions is almost the same at about 1890 K, which corresponds to the phase transformation of NiAl. A little difference from the melting temperature of NiAl at 1911 K is due to the heat loss to the surroundings.

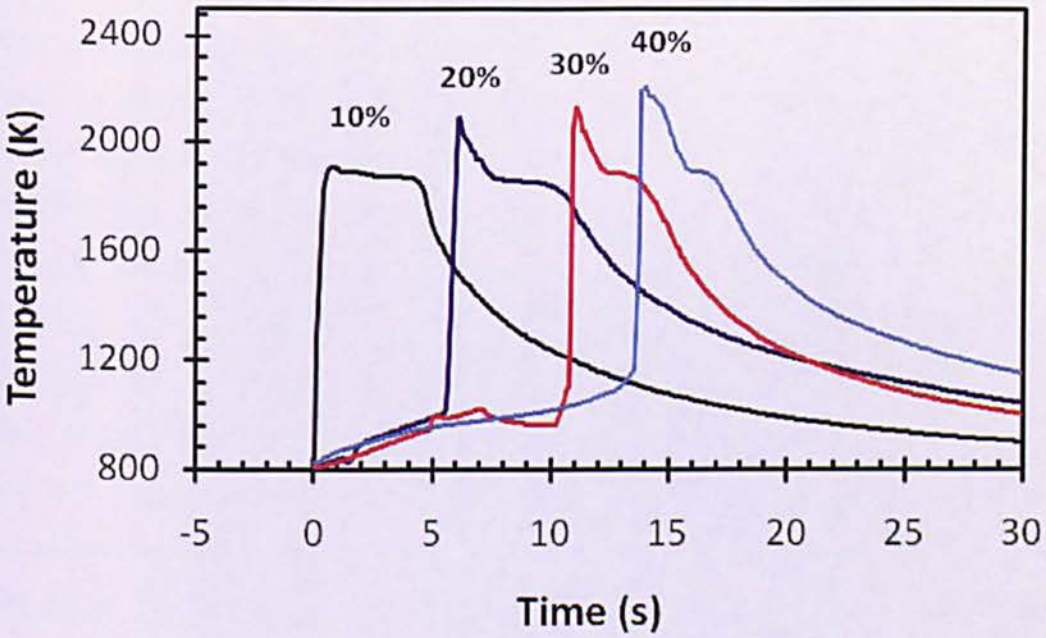

Fig. 6.1. Temperature profiles of the SHS process of Ni/Al with 10, 20, 30, and 40 wt.% TiO_2/Al/C

6.3.2. Microstructure characterizations

Three different techniques consisting of XRD, SEM which equipped with semi quantitative EDS analysis, and laser Raman microspectroscopy were used to investigate the phase characteristics and microstructure of the synthesized products.

6.3.2.1. X-rays diffraction spectra

Fig. 6.2(a–e) show the XRD spectra of the synthesized products prepared by (1–x)Ni/Al + (x)TiO_2/Al/C with x = 0, 10, 20, 30 and 40 wt.%, respectively. Fig. 6.2(a) shows the spectra of pure NiAl, while Fig. 6.2(b-e) show the spectra of NiAl–TiC–Al_2O_3 composites obtained by 10, 20, 30 and 40 wt.% of TiO_2/Al/C. It can be observed in all samples that no spectra of the original reactants can be found which indicates that the SHS processes were completed. The phase composition of the synthesized products in the composite systems mainly contains NiAl, TiC, and Al_2O_3, except in Fig. 6.2(d), where Ni_5Al_3 phase appears. As described in Fig. 6.2(a), the

spectra of pure NiAl have very strong peaks compared with those of TiC and Al_2O_3, where their comparisons can be clearly seen in the sample with 10 wt.% TiO_2/Al/C as shown in Fig. 6.2(b). In Fig. 6.2(b, c, and e), there are only three available phases in the synthesized products which consists of NiAl, TiC, and Al_2O_3. This demonstrates that the initial reactants have been transformed thoroughly to the expected products. The SHS process in these systems can therefore be said as complete. In Fig. 6.2(b) which describes the XRD spectra of NiAl–TiC–Al_2O_3 composite obtained by 10 wt.% TiO_2/Al/C, the peaks of TiC and Al_2O_3 spectra are much weaker than those of NiAl which can be attributed to the small amount of TiC and Al_2O_3 contents in the composite and microstructure of the ceramic phases. By increasing the content of TiO_2/Al/C, the peaks of NiAl spectra are weaker due to decreasing the content of Ni/Al. As can be observed in Fig. 6.2(c-e) which illustrate the spectra of products with 20, 30 and 40 wt.% of TiO_2/Al/C, the peaks of NiAl spectra decrease significantly which can be related to the lower amount of NiAl content in the composite. In the sample with 40 wt.% TiO_2/Al/C, the peaks of NiAl spectra are almost as low as those of TiC and Al_2O_3 spectra which show that the amount of each phase in the composite is nearly similar. In particular for Fig. 6.2(d), a small amount of Ni_5Al_3 phase was found in the final product. According to phase diagram of Ni–Al system [2] as given in Fig. 4.18 Chapter 4, the formation of intermediate phase Ni_5Al_3 can be formed during cooling below ~ 700 °C, when the reaction of Ni–Al is incomplete.

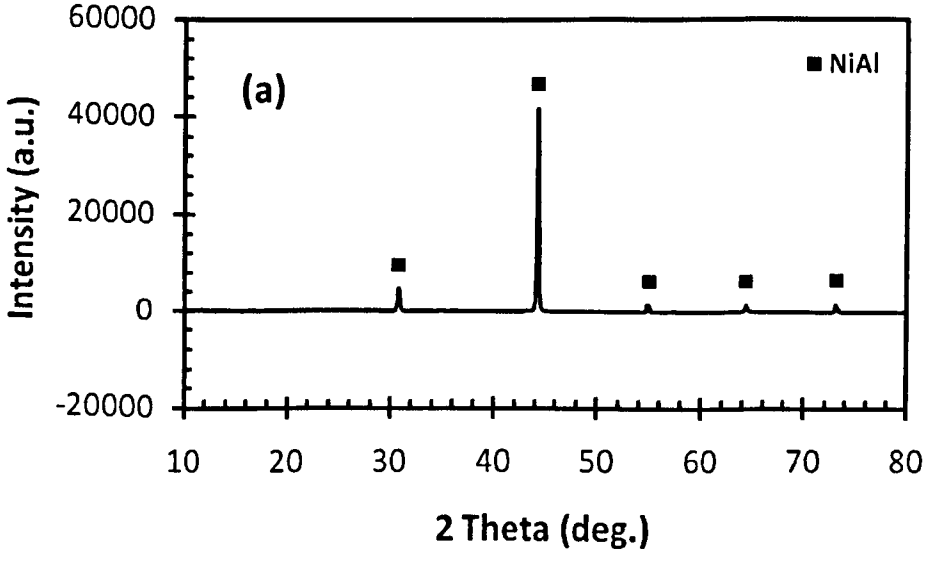

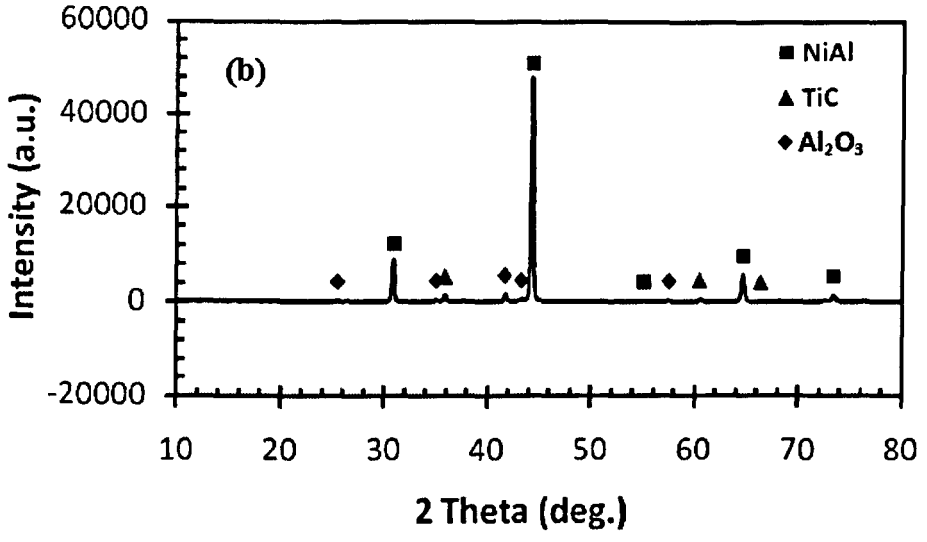
(b)
NiAl
TiC
Al2O3
Intensity (a.u.)
60000
40000
20000
0
-20000
10
20
30
40
50
60
70
80
2 Theta (deg.)

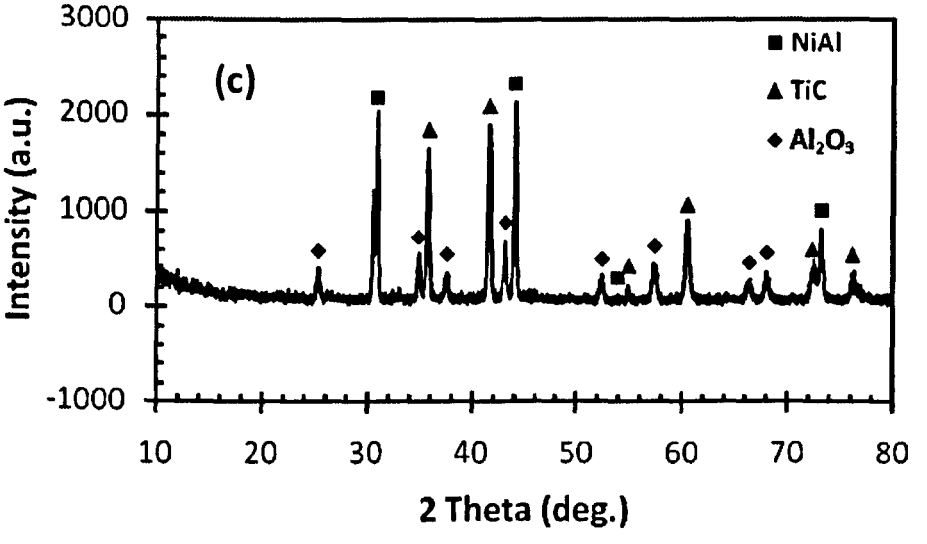
(c)
NiAl
TiC
Al2O3
Intensity (a.u.)
3000
2000
1000
0
-1000
10
20
30
40
50
60
70
80
2 Theta (deg.)

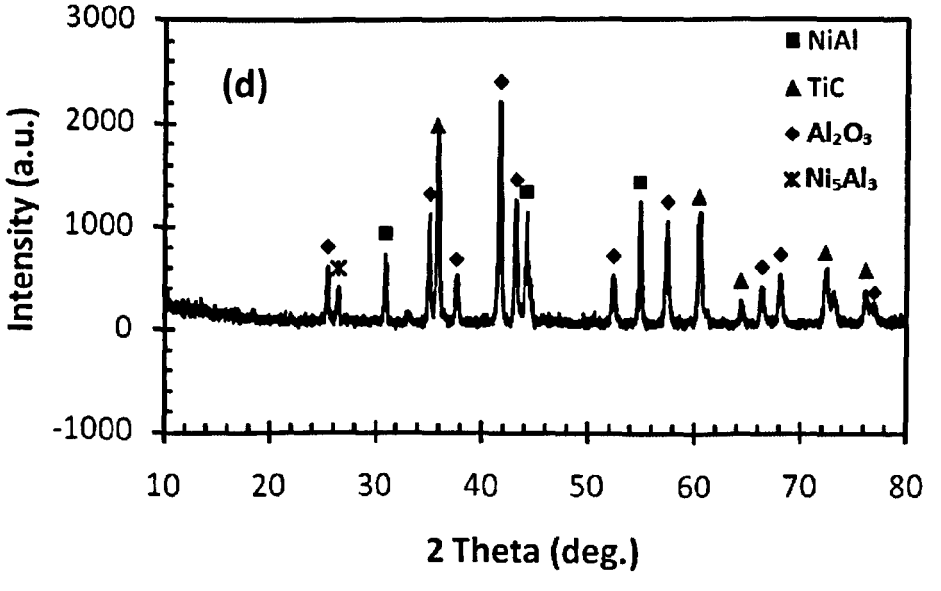
(d)
NiAl
TiC
Al2O3
Ni5Al3
Intensity (a.u.)
3000
2000
1000
0
-1000
10
20
30
40
50
60
70
80
2 Theta (deg.)

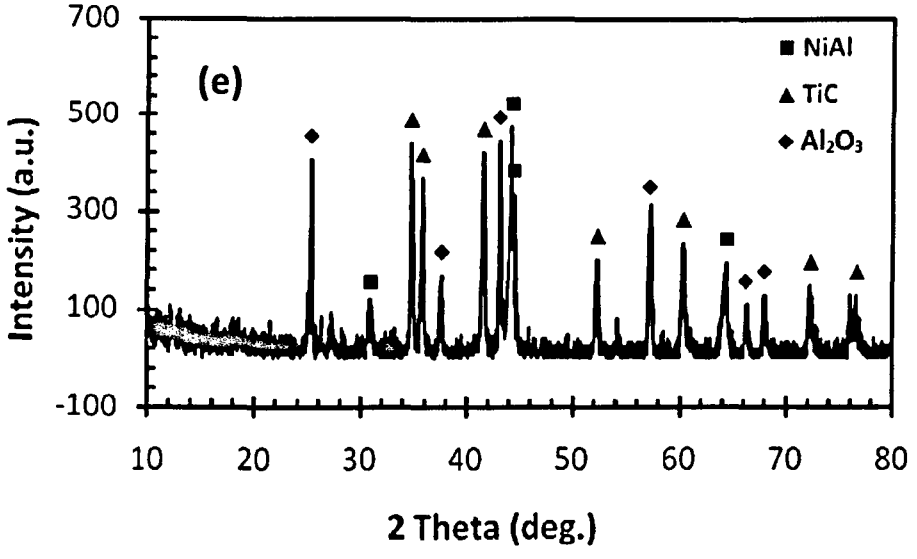

Fig. 6.2. X-ray diffraction spectra of the synthesized products prepared by Ni/Al with: (a) 0; (b) 10; (c) 20; (d) 30; and (e) 40 wt.% of TiO_2/Al/C

6.3.2.2. Scanning Electron Microscopy (SEM)

In order to verify the existence and distribution of the phases in the synthesized products as obtained using XRD methods, the microstructure characterization using SEM techniques was performed. Fig. 6.3 shows the typical SEM micrographs of the synthesized products prepared by Ni/Al with 0, 10, 20, 30 and 40 wt.% of TiO_2/Al/C. Fig. 6.3(a) shows the microstructure of pure Ni/Al, while Fig. 6.3(b–e) show the microstructure of NiAl–TiC–Al_2O_3 composites with 10, 20, 30 and 40 wt.% of TiO_2/Al/C. In Fig. 6.3(a), the microstructure of synthesized product shows a bright and homogeneous phase, while Fig. 6.3(b–e) show that the synthesized products are composed of bright area, dark particles, and grey zones. The element composition of the bright, dark and grey phases was characterized using EDX at positions of A, B, and C, as described in Fig. 6.4.

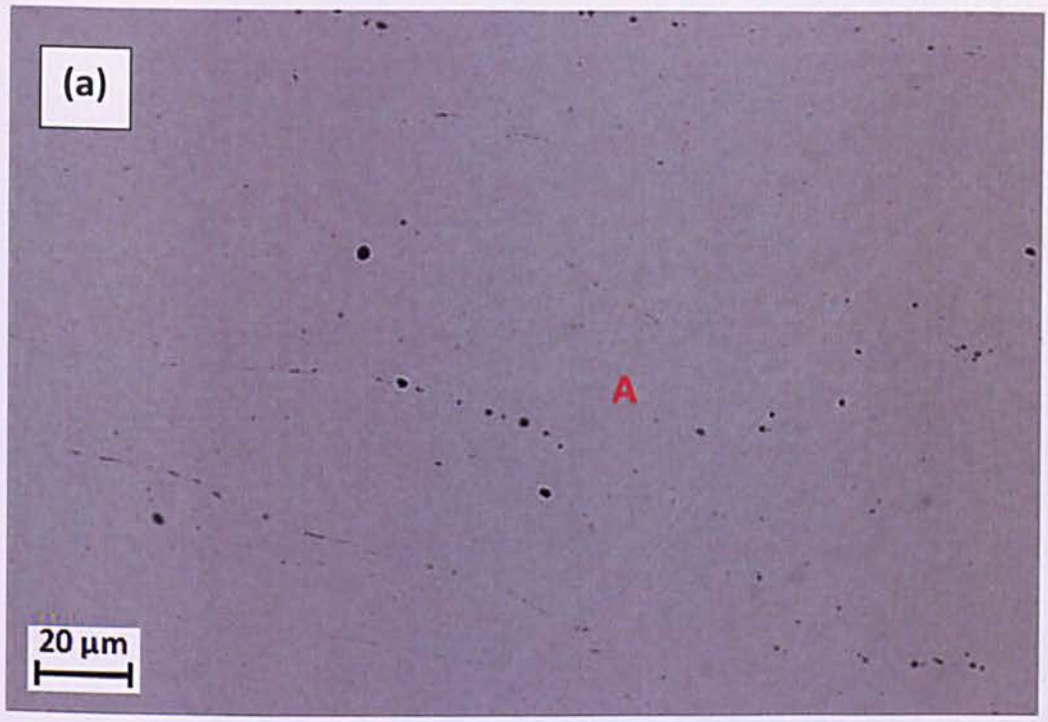
(a)
A
20 µm

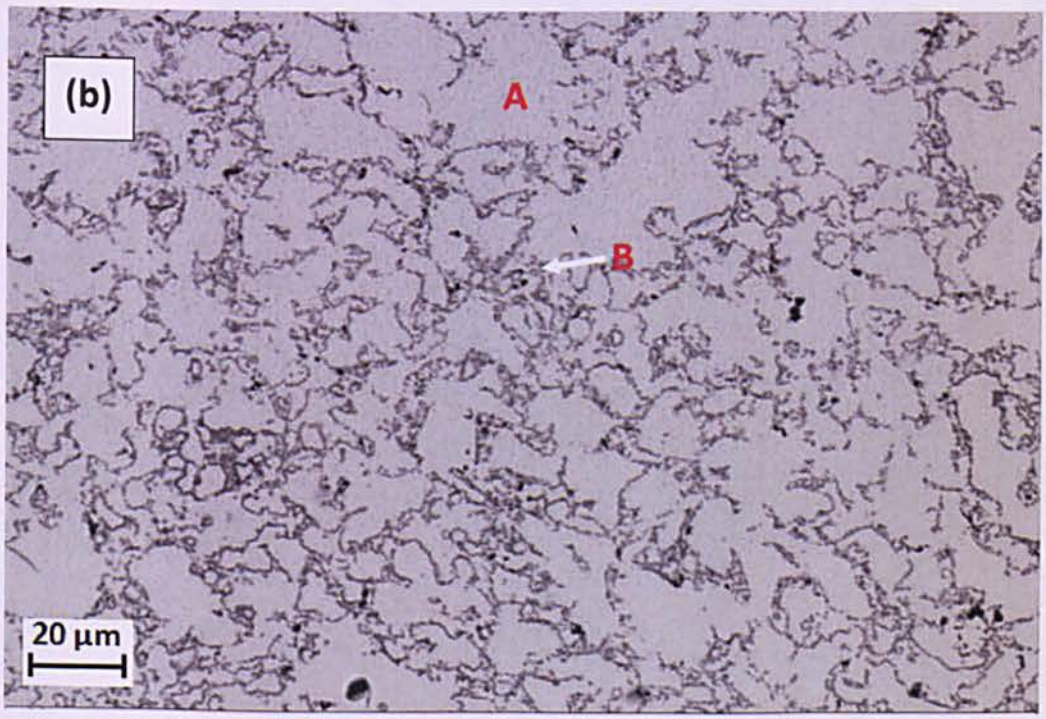
(b)
A
B
20 µm

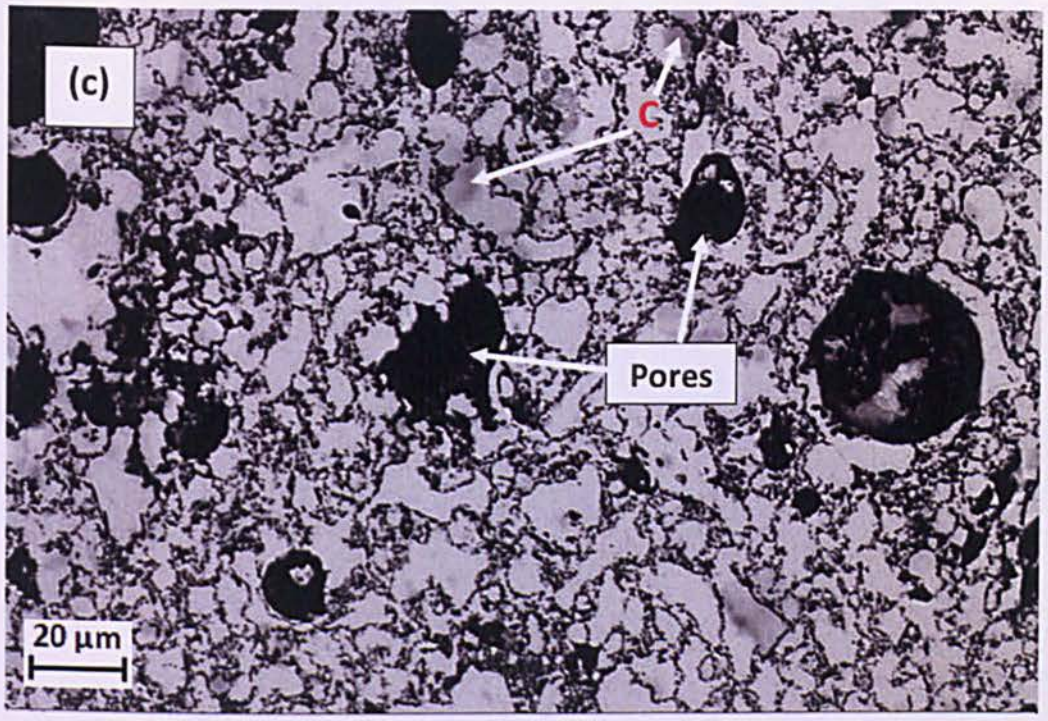
(c)
C
Pores
20 µm

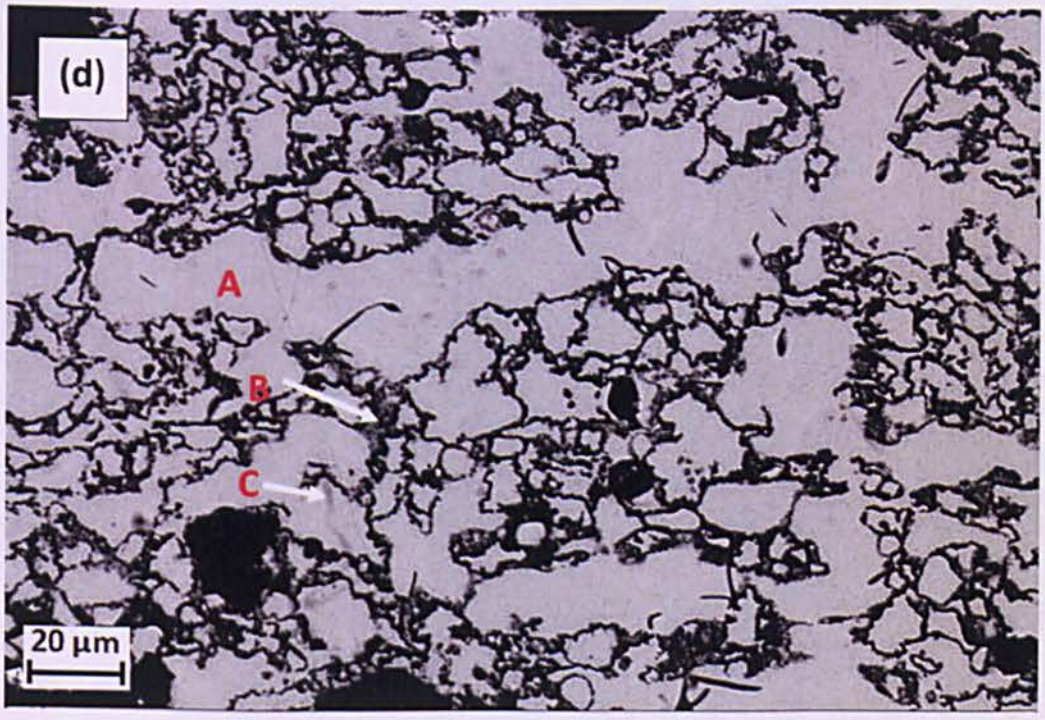
(d)
A
B
C
20 µm

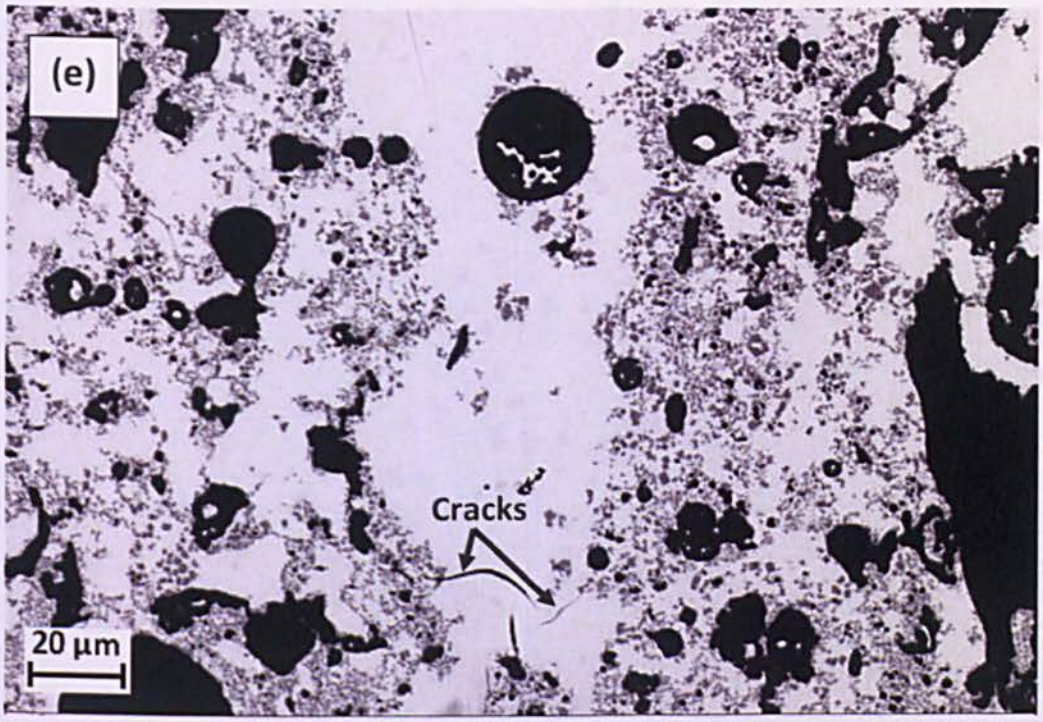

Fig. 6.3. SEM micrograph of NiAl–TiC–Al_2O_3 composites prepared by Ni/Al with: (a) 0; (b) 10; (c) 20; (d) 30; and (e) 40 wt.% of TiO_2/Al/C

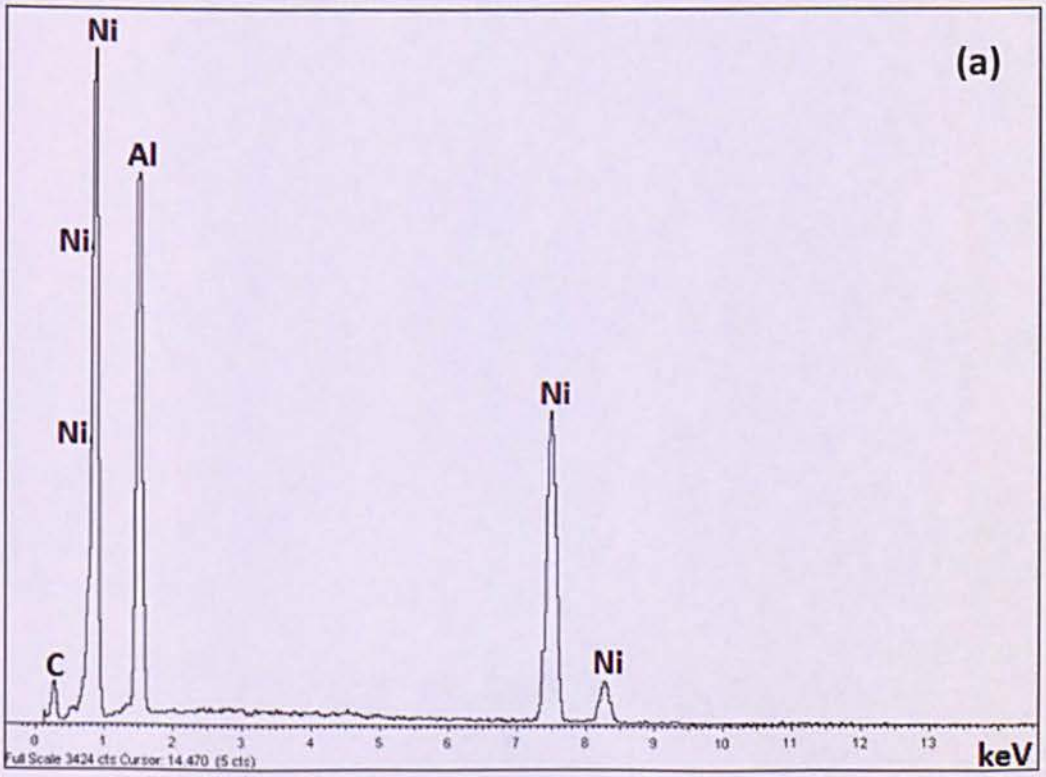

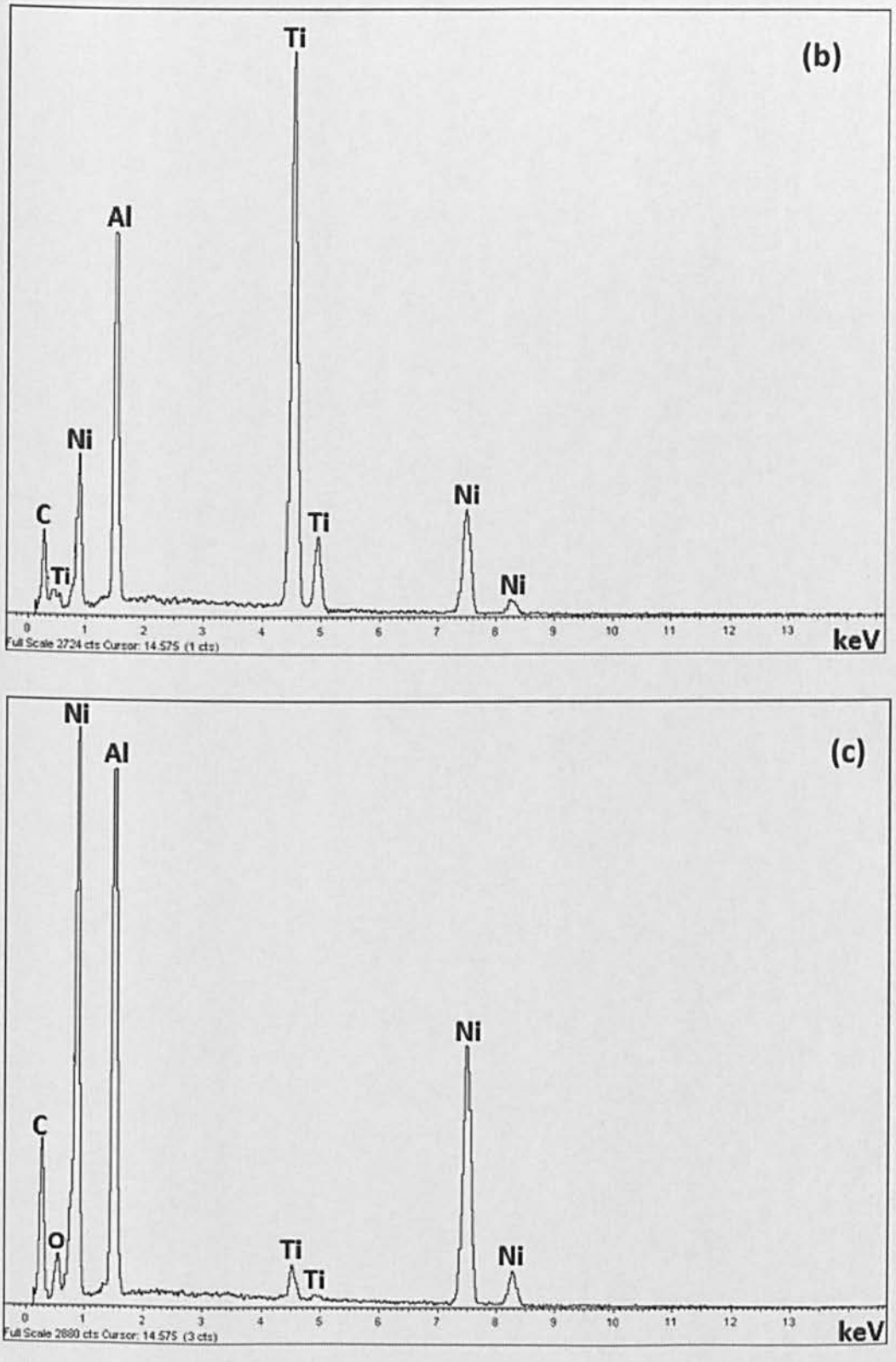

Fig. 6.4. Element composition using EDX of the samples in Fig. 6.3 at positions: (a) spot A; (b) spot B; and (c) spot C

By referring to the XRD results in Fig. 6.2 and EDX in Fig. 6.4, the bright phase shown in Fig. 6.3 can be attributed to the formation of NiAl phase, while the dark and grey phases may correspond to TiC and Al_2O_3 phases. To give more detailed information about the element composition of the phases, semi quantitative EDS analysis was also performed. Fig. 6.5 describes enlarged images of the microstructure of synthesized product with 10 and 30 wt.% TiO_2/Al/C, while the element composition of their phases is given in Table 6.4. The result demonstrates that the bright area is composed of Ni and Al atoms with a weight percentage of 71.37 and 30.92, respectively. The theoretical weight fraction of Ni and Al in the stoichiometric NiAl as determined using calculations in Eq. (6.5) and (6.6) is 68.51 and 31.49, respectively. It is apparent that the weight fraction of Ni and Al obtained by experimental observation is closely similar to that obtained by the theoretical calculation. The atomic percentage of Ni and Al as given in Table 6.5 also indicates a composition of approximately 1 and 1, respectively. This indicates that the bright phase can be attributed to the formation of NiAl.

Theoretical weight fraction of Ni and Al in NiAl:

$$Ni = \frac{58.69}{(58.69 + 26.98)} x100\% = 68.51\% \quad (6.5)$$

$$Al = \frac{26.98}{(58.69 + 26.98)} x100\% = 31.49\% \quad (6.6)$$

The element composition of the spot B as given in Table 6.4 shows that the dark particle is mainly composed of 62.36 wt.% Ti. However, with a total element of 84.23 wt.%, caution must be applied, as the finding might not be transferable to directly identify the formed phase. It should be noted that during the SEM observations using carbon as polishing agents, the information about the atomic compositions of C could not be provided since there is an uncertainty about the source of C whether it comes from the sample or polishing. The theoretical weight fraction of Ti and C in the stoichiometric TiC is given in Eq. (6.7) and (6.8). It is apparent that the difference of Ti content between the result obtained by calculation and observation is significantly large which can be attributed due to the presence of Ni and Al. This is due to the resolution of electron beam, which is 5 μm

x 5 μm x 5 μm, could not precisely detect the element composition in the particle marked by the spot B which has a grain size of approximately 1 micron (shown in Fig. 6.5). By referring to the XRD results in Fig. 6.2, it is likely that a high content of Ti in the spot B indicates the phase of TiC.

Theoretical weight fraction of Ti and C in TiC:

$$Ti = \frac{47.87}{(47.87+12.01)} x100\% = 79.94\% \quad (6.7)$$

$$C = \frac{12.01}{(47.87+12.01)} x100\% = 20.06\% \quad (6.8)$$

The result of this study is supported by a high magnification figure showing the shape and average grain size of TiC particle (1 μm) which is very consistent with the previous result as reported by Zhu et al. [18] who synthesized NiAl–TiC using induction heating. However, the TiC in Ref. [18] was obtained by the reaction between Ti and C as the reactants, while the result in present study reveals that TiC was synthesized from TiO_2 and C. The result in the present study then suggests that TiC can be produced from low cost material (TiO_2). The formation of a fine grain size TiC can be attributed to the fast cooling process during reaction, causing the formed crystals to have insufficient time to grow [183].

The weight fraction of the spot C which represents the grey phase as given in Table 6.4 indicates a high content of Al and O. The atomic fraction of Al and O is given in Table 6.5. By referring to the XRD in Fig. 6.2, the spot C indicates the formation of Al_2O_3. To confirm this conclusion, the theoretical weight fraction of Al and O in Al_2O_3 is given in Eq. (6.9) and (6.10). However, it can be found that the content of Al obtained by observation is slightly higher than that obtained by calculation. This difference can be attributed to the additional mixing of Al from NiAl phase.

Theoretical weight fraction of Al and O in Al_2O_3:

$$Al = \frac{2x26.98}{(2x26.98)+(3x16.00)} x100\% = 52.92\% \quad (6.9)$$

$$O = \frac{3x16.00}{(2x26.98)+(3x16.00)} x100\% = 47.08\% \quad (6.10)$$

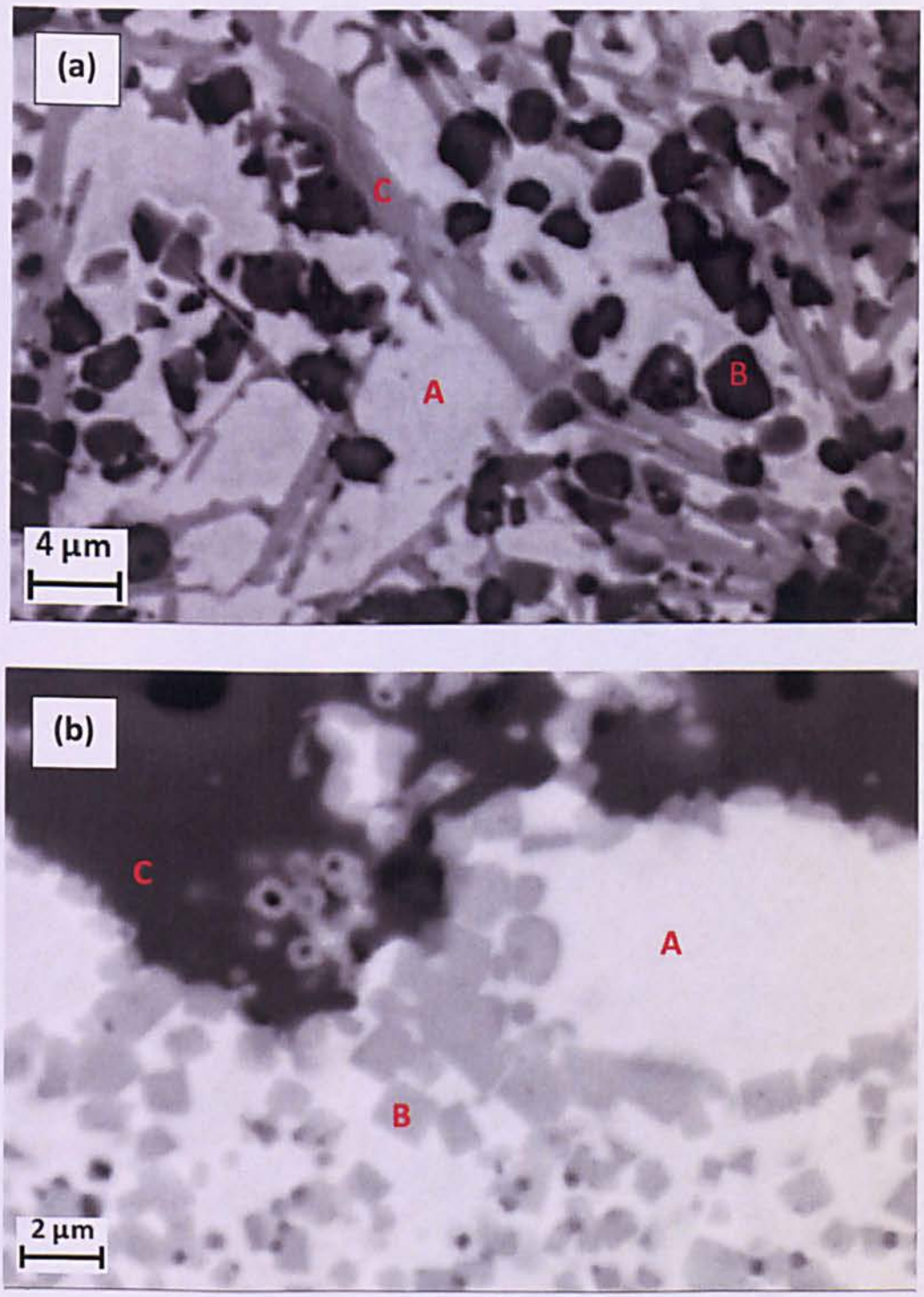

Fig. 6.5. Enlarged SEM micrograph of the sample with (a) 30 wt.%; and (b) 10 wt.% TiO_2/Al/C

Table 6.4. Chemical compositions (in wt.%) of the spot A, B and C in Fig. 6.5

Spectrum	O	Ne	Al	P	Ti	Ni	Total
A			30.92	0.36	0.67	71.37	103.32
B		1.91	5.77		62.36	14.19	84.23
C	65.97		59.67			0.57	126.22

Table 6.5. Chemical compositions (in at.%) of the spot A, B and C in Fig. 6.5

Spectrum	O	Ne	Al	P	Ti	Ni	Total
A			47.99	0.49	0.59	50.93	100
B		5.117	11.53		70.30	13.05	100
C	64.99		34.85			0.15	100

Obviously, the SEM micrograph shown in Fig. 6.3 shows that NiAl phase becomes the matrix of fine TiC particles. However, the distribution of TiC particles is inhomogeneous and concentrated along the NiAl grain boundary. This result agrees with that obtained by Jianting Guo et al. [185]. In addition, Zhu et al. [18] who investigated the combustion synthesis of NiAl–TiC prepared from elemental powders showed that a high concentration of TiC appeared at NiAl grain boundary illustrating that NiAl is synthesized before TiC formation. Further synthesis of TiC then melts NiAl causing some TiC to be embedded in NiAl. In the higher content of ceramic addition, as shown in Fig. 6.3(b-e), TiC and Al_2O_3 particles prefer to be segregated in the shell of pores. This result is consistent with that obtained by L.Y. Sheng et al. [15] who investigated the SHS process of NiAl–TiC–Al_2O_3 composite using hot extrusion. They reported that TiC and Al_2O_3 particles mostly appeared in the surface of formed cavity after SHS process.

It can also be seen in Fig. 6.3(a) that the microstructure of pure NiAl is significantly dense, while an increase in the content of TiO_2/Al/C as shown in Fig. 6.3(b–e) increases the porosity of the synthesized products. The highest density of the composites can be found in the sample with 10 wt.% TiO_2/Al/C, as shown in Fig. 6.3(b), as the sample with the smallest percentage of TiO_2/Al/C or the largest amount of Ni/Al. This result suggests that the presence of the large amount of the intermetallic phase in the composites can be used to densify the product. Increasing the content of TiO_2/Al/C from 20 to 40 wt.% produces unsatisfied results

since the porosity of the synthesized products is increased. A higher fraction of the pores can be found in the higher ceramic content. This indicates that the content of TiC–Al_2O_3 contributes directly to the porosity of synthesized products. The reason for increasing the porosity with an increase in the TiO_2/Al/C content can be related to the temperature profile as shown in Fig. 6.1. It was shown that the maximum combustion temperature for all reactions is below the melting point of TiC and Al_2O_3, which indicates that TiC and Al_2O_3 formed during the reaction are in the solid state. An increase in the TiO_2/Al/C content hence increases the presence of solid phases (TiC and Al_2O_3) in the composite resulting in a higher porosity. Besides pores, microcracks were also observed in the sample with a high TiO_2/Al/C content. The formation of cracks may be attributed to the intrinsic stress generated by the mismatch of thermal expansion coefficient between the different phases during cooling. For reference purpose, Table 6.6 shows the thermal expansion coefficient (α) at 25 °C, thermal conductivity (K) and density (ρ) of NiAl, TiC and Al_2O_3.

Table 6.6. Material properties of NiAl, TiC, and Al_2O_3 [186]

Materials	α (10^{-6}/°C)	K (W/m°C)	ρ (kg/m^3)
NiAl	14.6	5.3	5800
TiC	7.1	27	4900
Al_2O_3	8.1	24	3700

6.3.2.3. Laser Raman microspectroscopy

To support the phase identification of synthesized products which obtained by SEM and XRD techniques, a different method was carried out using laser Raman microspectroscopy. In the present work, laser Raman microspectroscopy was used to identify the phases of synthesized product which composed of NiAl, TiC, and Al_2O_3. To produce the references of the Raman spectra of NiAl, TiC and Al_2O_3, several preliminary investigations were carried out to identify the Raman spectra of TiO_2, Al_2O_3, Ti/C mixture, TiC, Ni/Al mixture, NiAl, and the mixture of Ni/Al with 10 wt.% TiO_2/Al/C.

(a). Raman spectra of TiO_2

In the present work, TiO_2 was used as one of the reactants. Typical Raman spectra of the compressed pellet of titanium dioxide (TiO_2) powders are shown in Fig. 6.6. It can be seen that the Raman peaks of TiO_2 happen at 143, 236, 446, and 610 cm^{-1}. These peaks indicate that the powder is a rutile as confirmed by previous study which reported that rutile has Raman peaks at 144, 238, 447, and 611 cm^{-1} [187]. Other studies also showed that rutile has the peaks at 246, 449, and 611 cm^{-1} [188], and 245, 445, and 610 cm^{-1} [12].

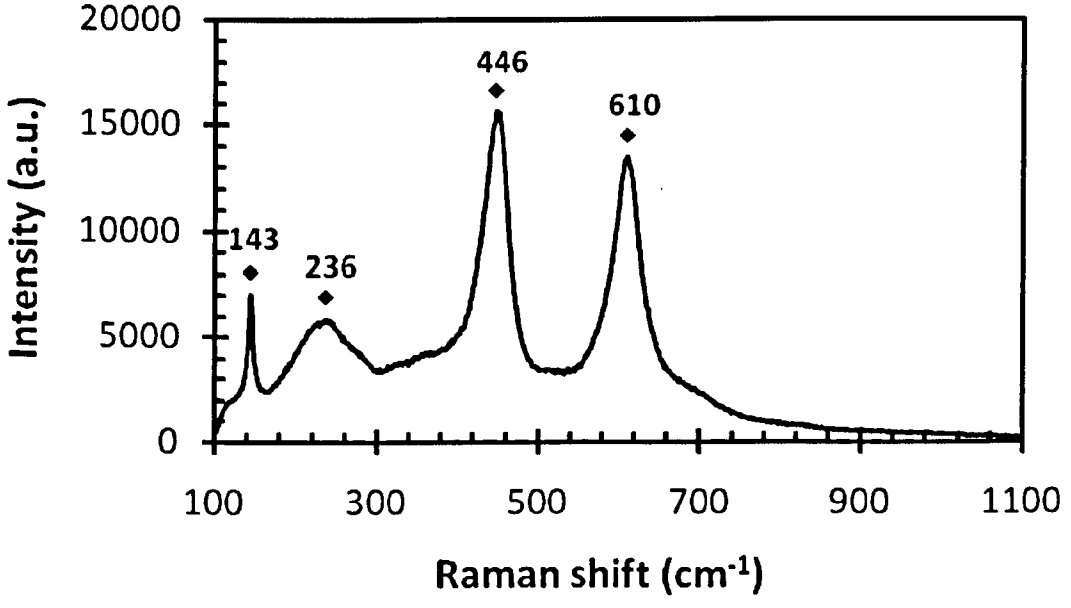

Fig. 6.6. Raman spectra of TiO_2

(b). Raman spectra of Alumina (Al_2O_3)

Al_2O_3 was not used as reactant in the reaction, but the Raman spectra of the compressed alumina powder was identified to become a reference to the Raman spectra of alumina produced by the synthesis reaction of Ni/Al and TiO_2/Al/C. The typical Raman spectra of calcined alumina powder are shown in Fig. 6.7. The Raman spectra of the sample indicate that the peaks of intensity occur at 1371 and 1401 cm^{-1}. These spectra are consistent with the spectra of alumina which is calcined for 5 hours at 1200 °C as described by Sara Boullosa-Eiras [189].

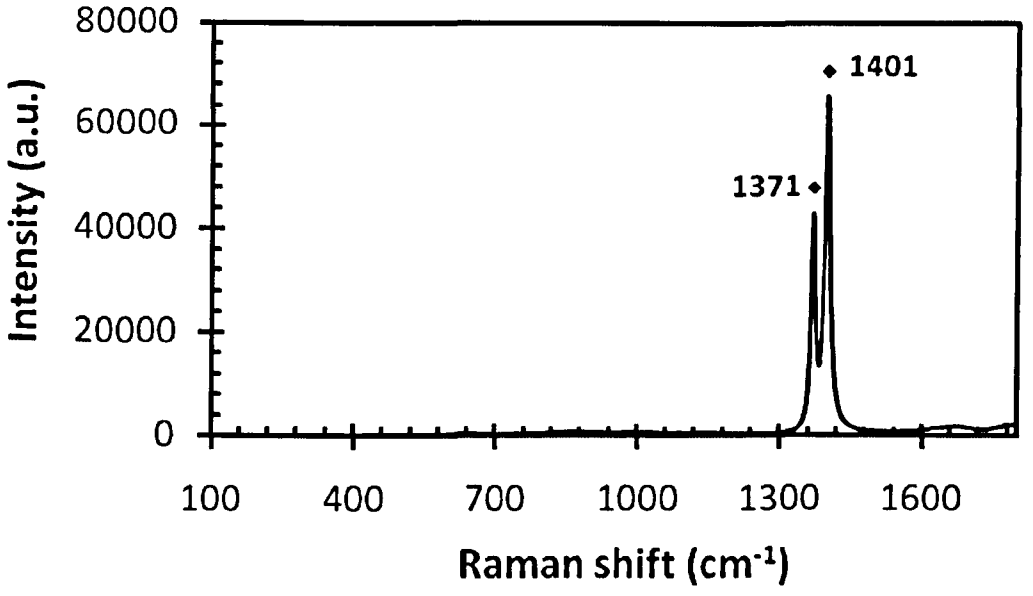

Fig. 6.7. Raman spectra of calcined alumina (Al_2O_3)

(c). Raman spectra of Ti/C mixture

Ti and C powders with an atomic composition of 1:1 were mixed and pressed in a cylindrical die to produce a compressed pellet. The Raman test was then performed on the surface of the pellet. The result of the Raman test, as shown in Fig. 6.8, displays two strong peak intensities at 1322 and 1572 cm^{-1}, which can be associated with vibration modes of graphite [190]. The peak at 1572 cm^{-1} corresponds to a graphitic carbon, while the one at 1322 cm^{-1} shows the existence of amorphous carbon [191]. It is recognized that the Raman spectra of amorphous carbon are composed of D and G bands, in which D band (Disordered carbon) usually appears between 1320 and 1440 cm^{-1}, while G band (Graphitic carbon) occurs between 1480 and 1580 cm^{-1}. Meanwhile, the Raman spectra of Ti are not present in the sample since Ti is not Raman active [190].

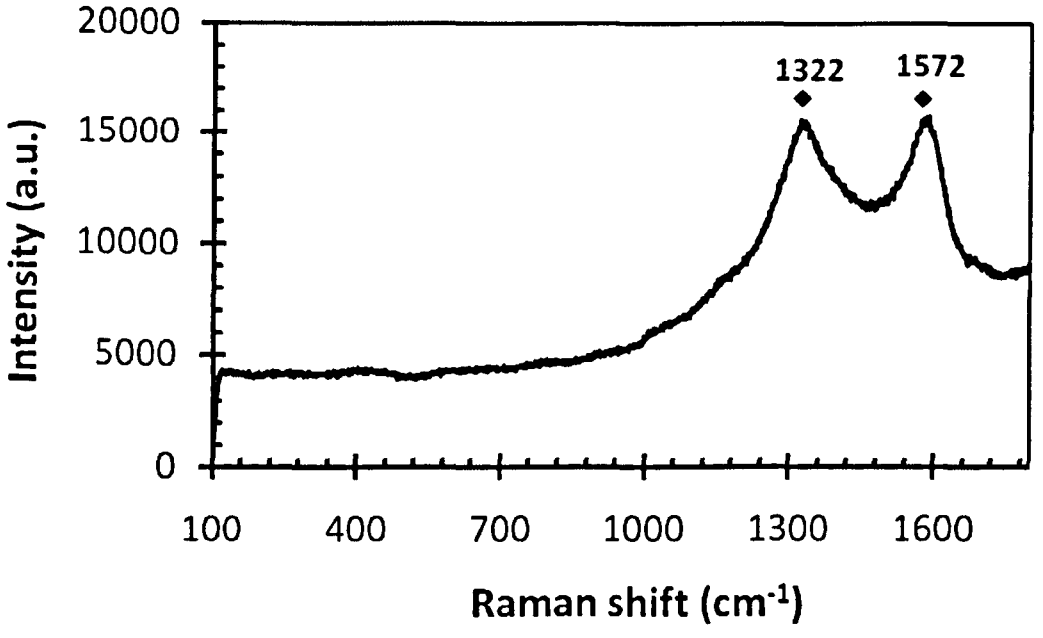

Fig. 6.8. Raman spectra of Ti/C mixture

(d). Raman spectra of synthesized TiC

In order to analyze the Raman spectra of TiC obtained from the SHS process of Ni/Al and TiO_2/Al/C, the Raman spectra of TiC obtained from the synthesis reaction of Ti–C powders were observed. The Raman spectra of TiC produced by the combustion synthesis of Ti–C are shown in Fig. 6.9. The result shows that there are two doublets of the peak spectra; the lower spectra have a centre at 284 and 376 cm^{-1}, while the higher spectra have peaks at 589 and 668 cm^{-1}. This result is in good agreement with a study which reported the Raman signal of TiC which showed that the lower spectra (284 and 377 cm^{-1}) can be assigned to the acoustical bands and the higher one shows the optical bands of the TiC spectra [141]. In the literature, these four peak spectra are usually attributed to a disorder TiC phase. It was reported that stoichiometric TiC is not Raman active [191]. Therefore, the Raman spectra as indicated in Fig. 6.9 may show non-stoichiometric TiC or symbolized with TiC_x. Fig. 6.9 also reveals that the peak spectra of graphite are not clearly displayed which shows that the combustion synthesis in the present work can be said to have proceeded to complete without the presence of raw graphite carbon in the synthesized product.

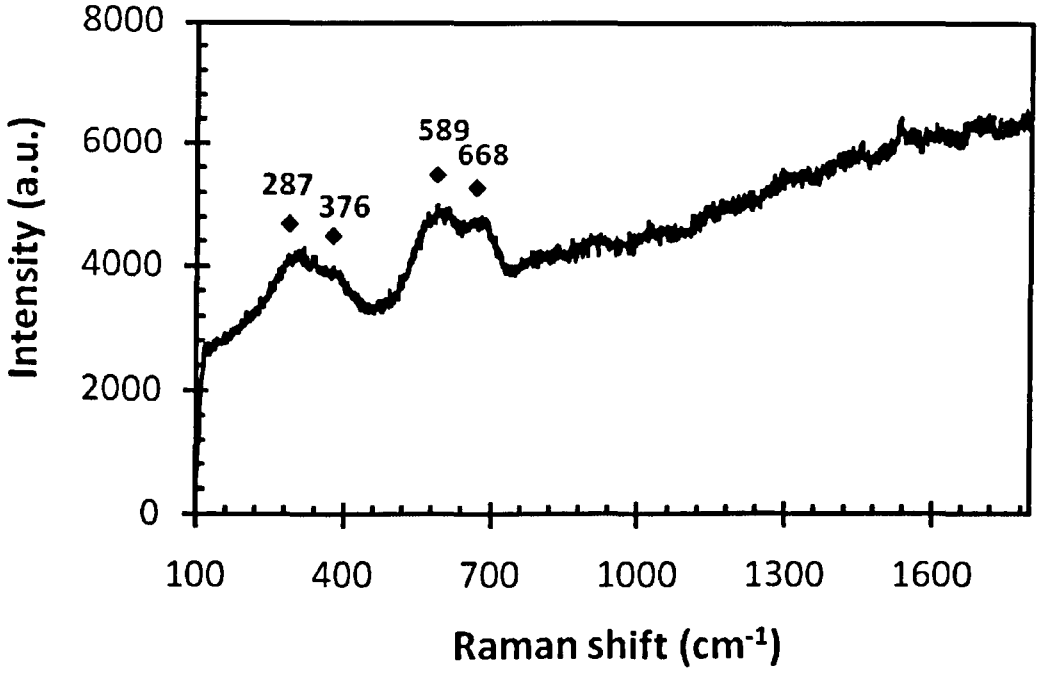

Fig. 6.9. Raman spectra of TiC formed by SHS process

(e). Raman spectra of Ni/Al mixture

Ni/Al mixture was used as the reactant of the composite system. The Raman spectra of the compressed mixture of Ni/Al are described in Fig. 6.10. It can be seen that the peaks of intensity occur at 193, 350, 536, 684, and 1036 cm^{-1}. This result is an initial study for the Raman spectra of Ni/Al mixture since there is no available data for comparison. The aim of the investigation on the Raman spectra of Ni/Al mixture was then used as a comparison for the existence of Ni/Al in the synthesized NiAl.

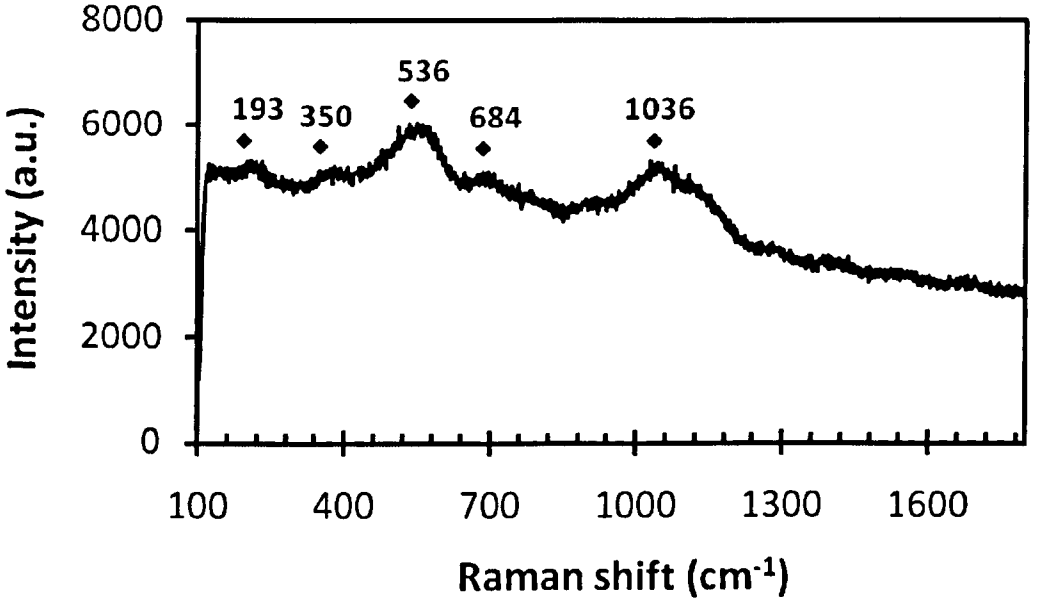

Fig. 6.10. Raman spectra of Ni/Al mixture

(f). Raman spectra of NiAl product

In order to analize the Raman spectra of NiAl obtained from the SHS process of Ni/Al and TiO_2/Al/C, the Raman spectra of NiAl obtained from the synthesis reaction between Ni and Al were observed. The Raman spectra of NiAl produced by the combustion synthesis of Ni and Al powders are shown in Fig. 6.11. It is difficult to identify the Raman spectra of NiAl product since the peaks are weak. In addition, no reference can be found in the literature for the Raman spectra of NiAl. However, Fig. 6.11 shows that no Raman spectra of Ni/Al mixture in Fig. 6.10 can be found. This indicates that the combustion reaction was complete and no reactant was left in the synthesized NiAl. These results, however, would be useful as comparison to the Raman spectra of NiAl in the NiAl–TiC–Al_2O_3 system.

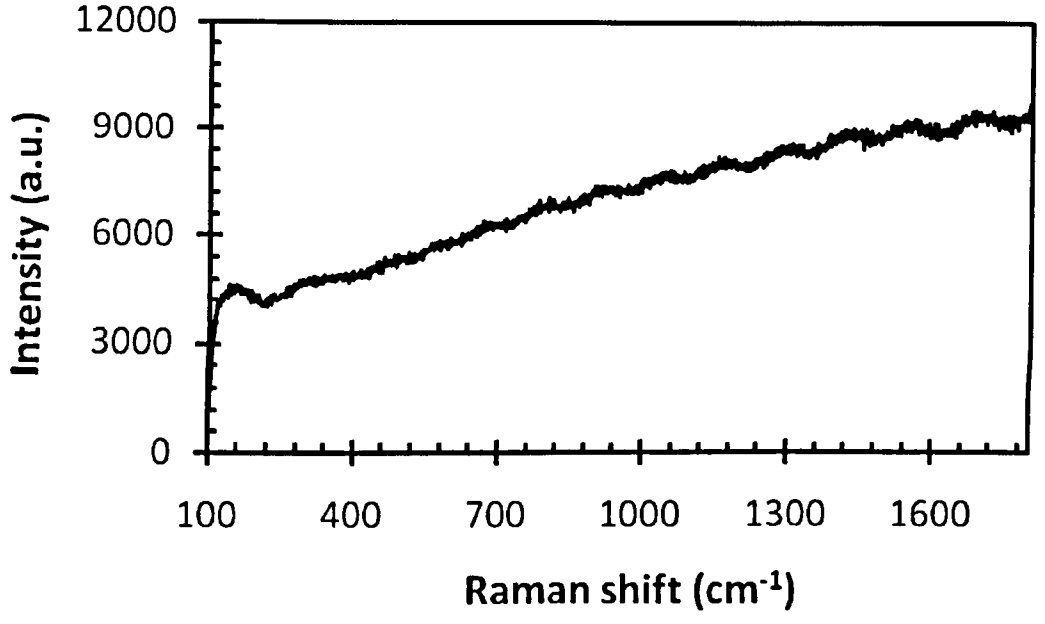

Fig. 6.11. Raman spectra of NiAl product obtained from Ni/Al mixture

(g). Raman spectra of Ni/Al + TiO_2/Al/C mixtures

To check the Raman spectra of the mixture used as the reactant, the Raman spectra of Ni/Al with 20 wt.% TiO_2/Al/C were investigated, and the result is described in Fig. 6.12. By referring to the reference obtained from the former results, it can be seen that there are three groups of the Raman spectra of Ni/Al and TiO_2/Al/C which indicate the presence of titanium oxide, Ni/Al powder and carbon. The first group which shows the peaks at 143, 241, 447, and 614 cm^{-1} indicates the Raman spectra of TiO_2, while the second group showing the peaks at 684 and 1036 cm^{-1} denotes the Raman spectra of Ni/Al mixture, and in particular for the peaks at 1322 and 1570 cm^{-1} represent the Raman spectra of graphite.

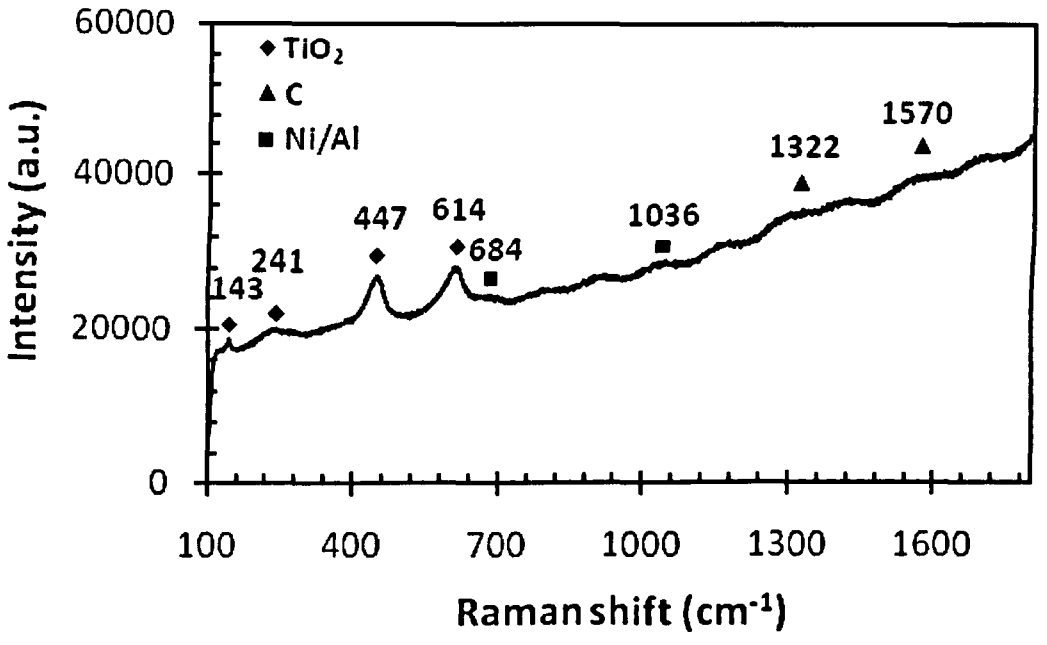

Fig. 6.12. Raman spectra of compressed powder of Ni/Al + $3TiO_2$/A4l/3C mixtures

(h). Raman spectra of NiAl–TiC–Al_2O_3 products

After producing the Raman spectra for references, the Raman spectra of the synthesized product in NiAl–TiC–Al_2O_3 composite were observed. The investigation of the Raman spectra of NiAl–TiC–Al_2O_3 system is supplemented with a micrograph of the objects to show the location and pattern of the observed phases. The study of Raman spectra were carried out in the cross section and the surface of the sample. Fig. 6.13 shows the focused location of the laser Raman in the cross section of the polished sample. It can be seen that there are only two distinct phases marked by point A and B which represent the bright and dark phases. The bright phase indicates a dense phase while the dark one describes the group of small particles. The dark areas have very fine grains; as a result, laser Raman could not be easily focused on a single grain of the particles. The Raman spectra of the location A and B are shown in Fig. 6.14. A comparison of the Raman spectra for the bright and dark area provides a visible difference between the spectra. The Raman spectra of the spot A have no clearly sharp intensity, but their spectra are similar to the Raman spectra of NiAl as described in Fig. 6.11. Meanwhile, the Raman spectra of the dark particles as marked by the spot B illustrates that the Raman spectra of the

spot B are broad, but can be identified to have a peak at 664 cm^{-1}. This spectrum can be characterized as the Raman spectra of titanium carbide (TiC) as previously observed in the reference shown in Fig. 6.9 which have the Raman peaks at 287, 376, 589, and 668 cm^{-1}. The single peak of titanium carbide at 664 cm^{-1} has also been confirmed by a study as shown in Fig. 3.11 (Chapter 3) [141]. A relatively broaden spectra in this study may be attributed to the modification of crystal phase due to the residual stresses in the sample [188]. In addition, it is worth to mention that the scan method for a single particle TiC was difficult due to the small particle size of TiC, as a result, the scan has included some areas of the matrix. For comparison purpose, the spot size of the laser Raman beam is 5 – 7 microns, while the particle size of TiC is about 1 micron.

The presence of NiAl and TiC in the cross section of the synthesized products obtained by Raman spectra is confirmed by the SEM result which showed that these phases can be easily detected in the cross section. During the laser Raman test, it was difficult to find the position of Al_2O_3 along the cross sectional area of the sample. Further test to find Al_2O_3 was performed at the surface of the sample.

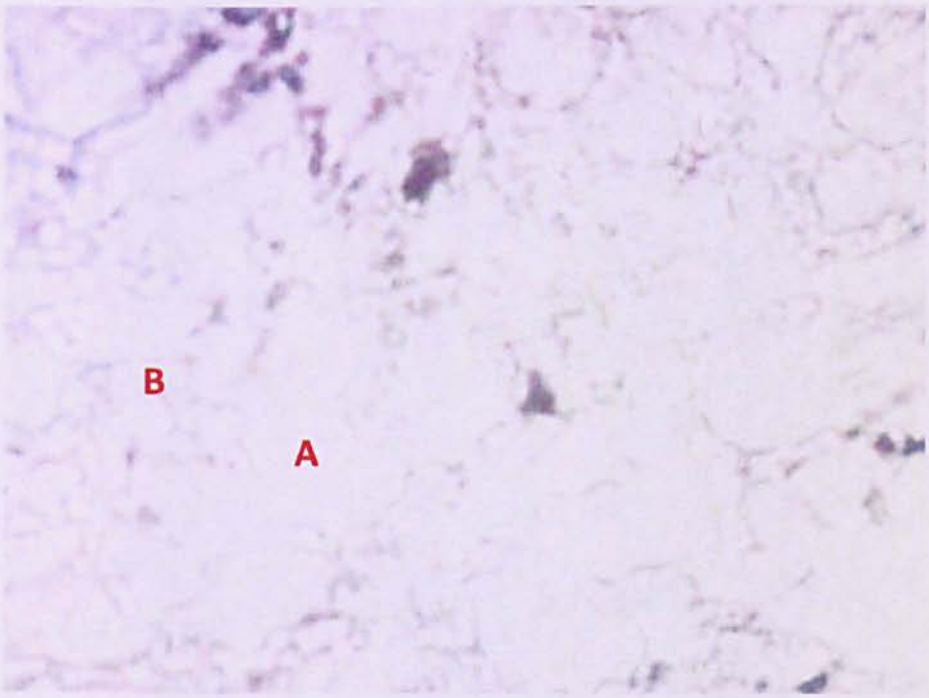

Fig. 6.13. Locations of Raman test on the cross sectional area

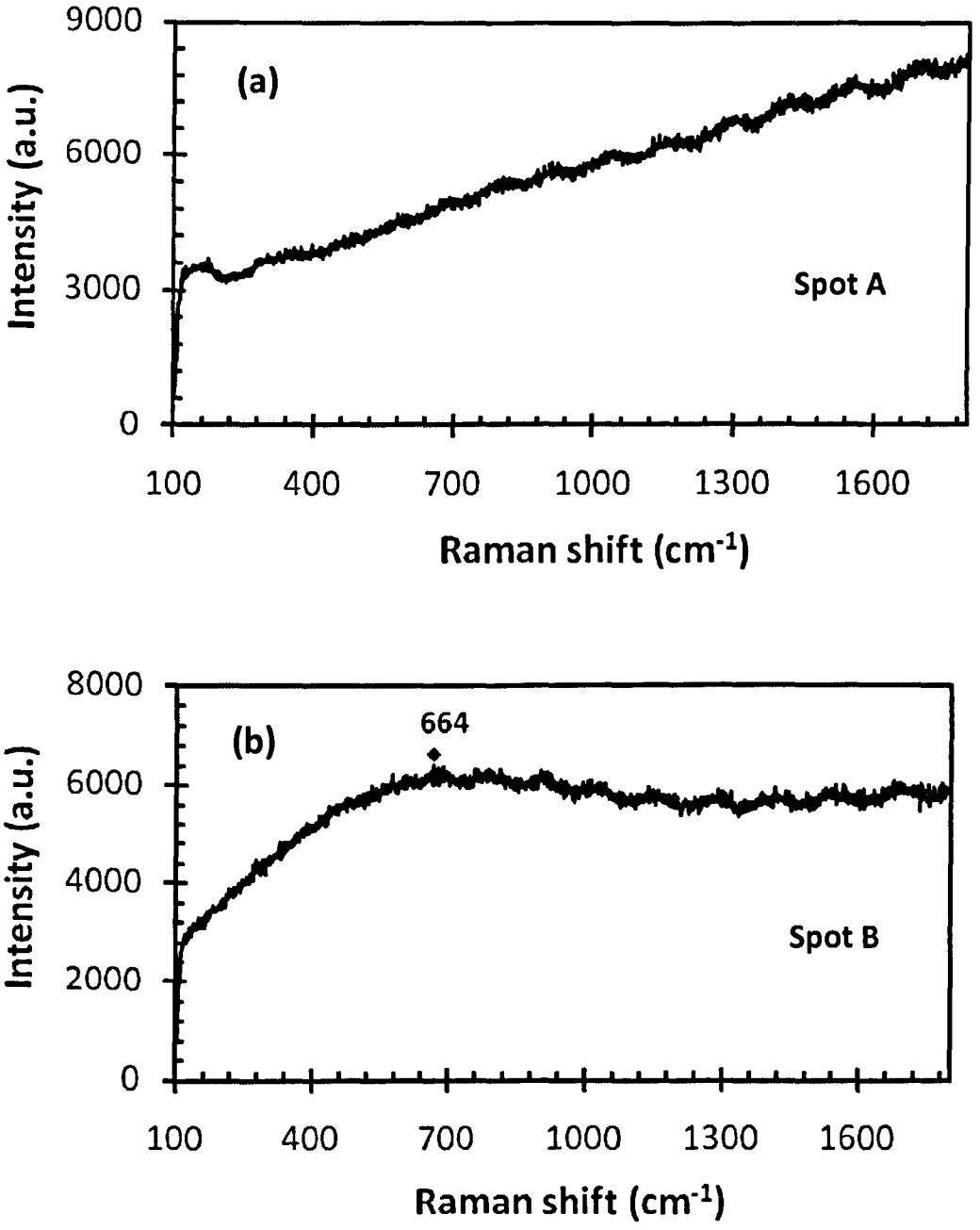

Fig. 6.14. Raman spectra at position: (a) A; and (b) B in Fig. 6.13

Fig. 6.15 shows the location of Raman test at the coating surface. The investigation of the Raman spectra in the surface of coating indicates that there are two different phases which can be distinguished as bright and dark areas. However, the Raman spectra of the dark area are similar to the Raman spectra of NiAl as described in Fig. 6.14(a). The Raman spectra of bright area marked by the spot C is

shown in Fig. 6.16 which shows the Raman spectra of Al_2O_3 as previously observed in Fig. 6.7. Thus, the Raman test at the coating surface has clearly shown that Al_2O_3 was richer on the surface of the synthesized product. The reason of Al_2O_3 appearances on the surface may be related to the difference in density of the synthesized products. The density of Al_2O_3 is lower than that of TiC and NiAl (see Table 6.6). The result in this study has shown that the combustion synthesis of Ni/Al with varied compositions of TiO_2/Al/C was sufficient to generate the liquid phase of NiAl since the combustion temperature achieved or exceeded the melting point of NiAl (1911 K). It was found that increasing the content of TiO_2/Al/C from 10 to 40 wt.% has increased the combustion temperature from 1911 K to 2208 K. This indicates that the formed NiAl was in the liquid state, while TiC and Al_2O_3 were in the solid state during reaction.

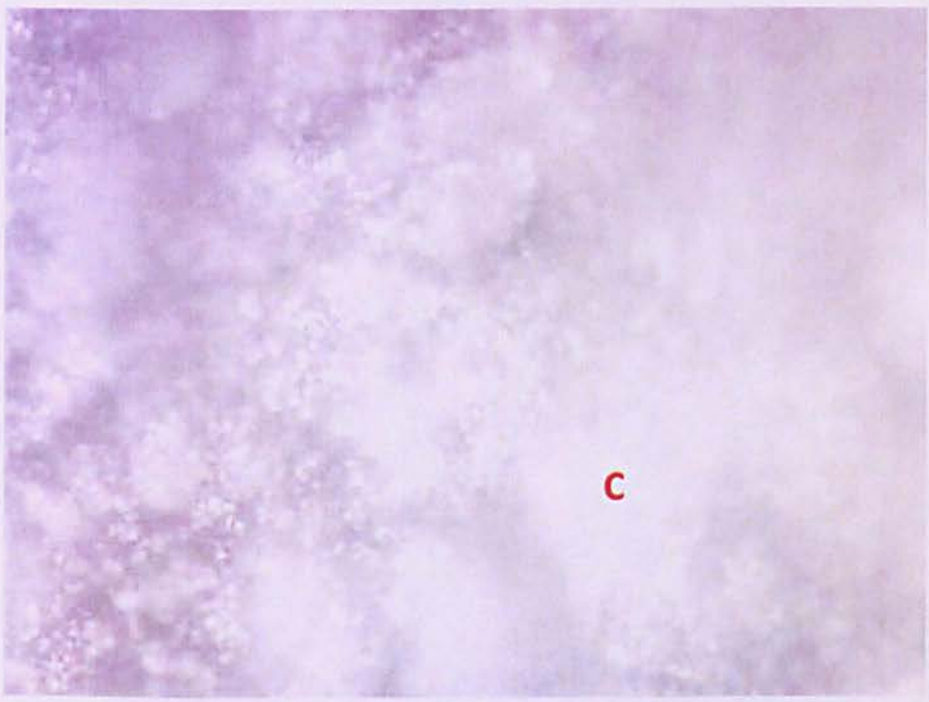

Fig. 6.15. Locations of Raman test on the coating surface

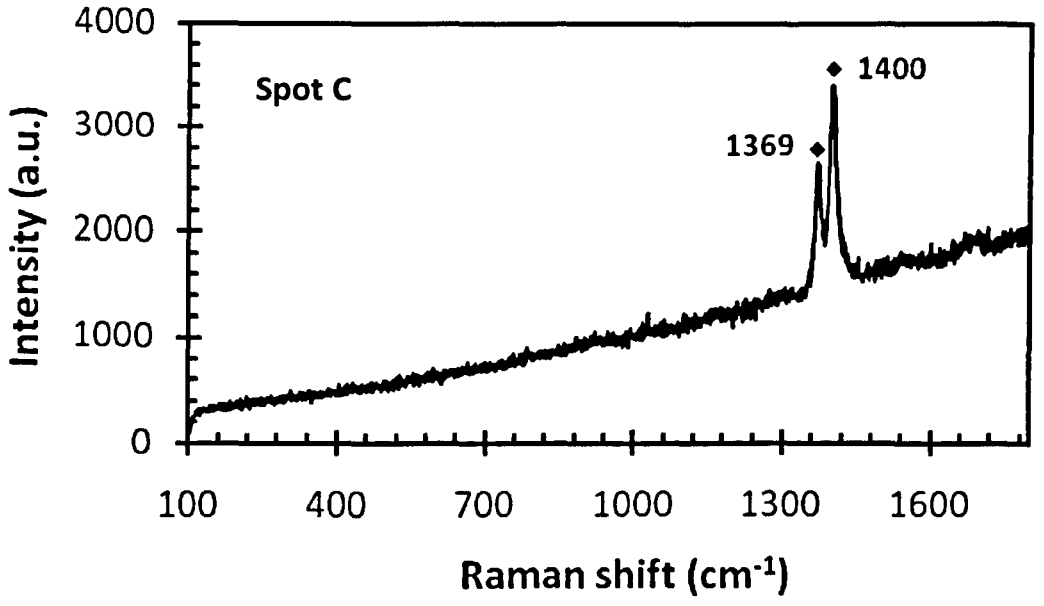

Fig. 6.16. Raman spectra at the coating surface at position C in Fig. 6.15

6.3.3. Evaluation of the mechanical properties

Fig. 6.17 shows the microhardness of the synthesized products prepared by Ni/Al with varied compositions of TiO_2/Al/C as given in Table 6.1, while Fig. 6.18 shows the typical photomicrograph of the Vickers indentation conducted on the synthesized product with 10 wt. % TiO_2/Al/C. In Fig. 6.18, the bright and dark phases represent NiAl and TiC, respectively. The result of microhardness evaluation as shown in Fig. 6.17 shows that the hardness of synthesized product increases with an increase in the TiO_2/Al/C contents. The result shows that the average microhardness of pure NiAl which is 306 HV. Increasing the content of TiO_2/Al/C with 10, 20, 30, and 40 wt.% results in the increase in the microhardness of the synthesized products to 443, 492, 576, and 611 HV, respectively. This result suggests that an increase in the product microhardness is attributed for the higher volume fraction of TiC and Al_2O_3 particles in the products. Indentation in the sample with 10 wt. % TiO_2/Al/C as shown in Fig. 6.18 also shows that no crack was observed, even when the indentation was made at the area with high concentration of ceramic particles. This indicates that a considerable improvement in the strength of the synthesized products with high content of ceramic particles was achieved, without deteriorating their toughness.

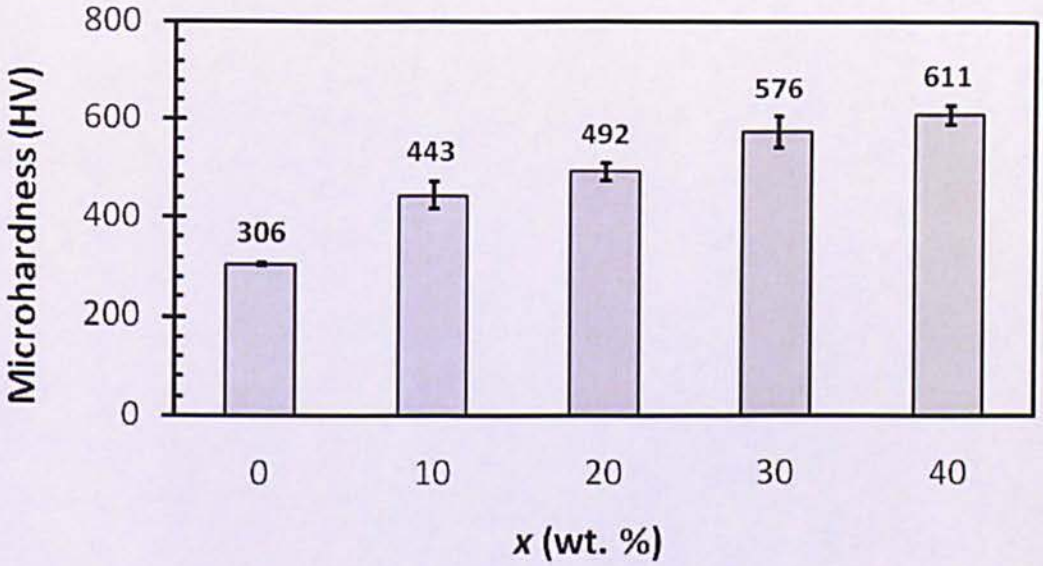

Fig. 6.17. Microhardness of synthesized products prepared by (x) Ni/Al + (1-x) TiO_2/Al/C with x = 0, 10, 20, 30 and 40 wt. %

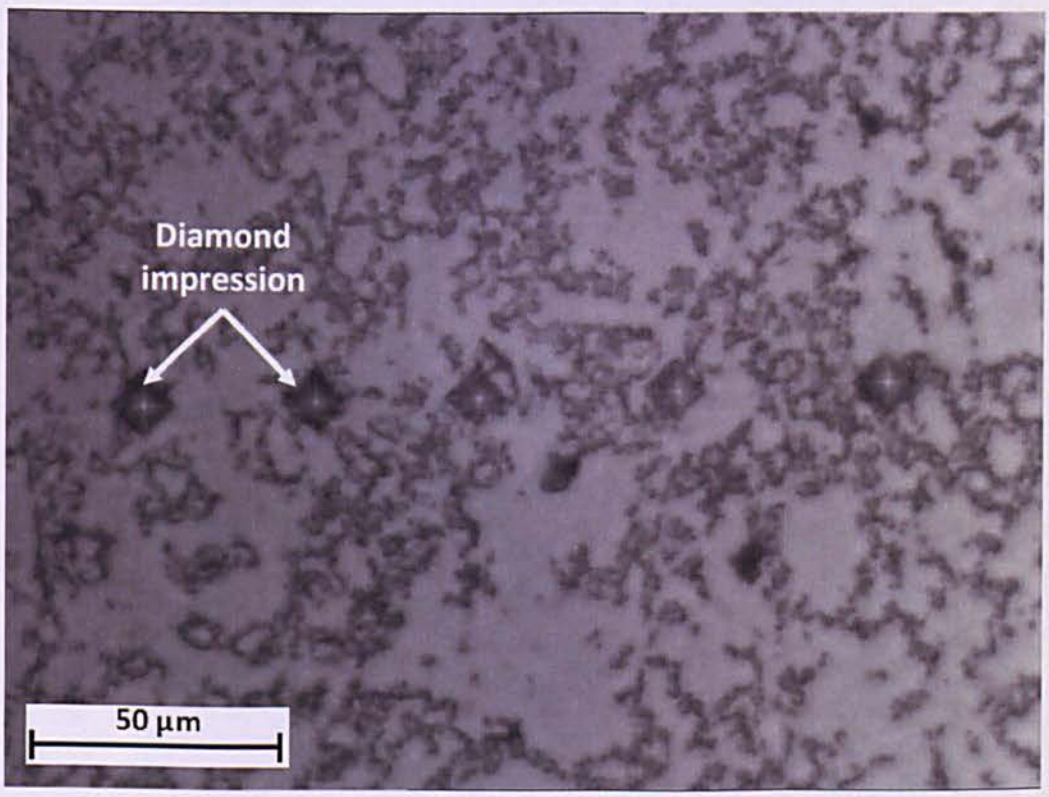

Fig. 6.18. Impressions of Vickers indentation in the samples with 10 wt. % TiO_2/Al/C

6.4. Summary

This chapter reports the SHS process ignited by induction heating to form NiAl–TiC–Al_2O_3 composites prepared using Ni, Al, C and low cost material TiO_2. The objective of the current study was to investigate the effect of reactant compositions on the combustion behaviour, microstructure and the mechanical properties of synthesized products. The reactants were obtained by a composition of (1–x)Ni/Al + (x)TiO_2/Al/C, where x = 0, 10, 20, 30 and 40 wt.%. The measurement of the combustion temperature demonstrated that two stages of reactions were observed, which correspond to the exothermic reaction of TiO_2/Al/C system and the phase transformation of Ni/Al systems respectively. The variation of reactant compositions showed that an increase in the TiO_2/Al/C content increased the maximum combustion temperatures of TiO_2/Al/C reaction which indicates an increase in the TiC–Al_2O_3 and a decrease in the NiAl contained in the product.

The phase identification carried out using XRD and laser Raman microspectroscopy indicated that NiAl, TiC and Al_2O_3 were observed in the synthesized products. This suggests that the SHS process of NiAl–TiC–Al_2O_3 prepared by Ni, Al, C and TiO_2 was completed. Further analysis on the microstructure of synthesized products showed that an increase in the TiO_2/Al/C content increased the porosity of product. The increasing amount of porosity is attributed to the higher content of solid TiC and Al_2O_3 and the lower content of liquid NiAl. As confirmed by the temperature profile, the maximum combustion temperature for all reactant compositions was lower than the melting point of TiC and Al_2O_3 which indicates that TiC and Al_2O_3 was in the solid state during the reaction.

The evaluation on the mechanical properties of synthesized products showed that increasing TiO_2/Al/C content increased the hardness of products. The increase of hardness is attributed to the increased content of TiC and Al_2O_3 and the reduced content of NiAl in the product. Considering that a higher amount of NiAl generated denser products, the existence of NiAl therefore not only became the ignition agent for the SHS reaction of TiC–Al_2O_3 systems, but also served as the

diluents and binder. It was found that 10 wt.% TiO_2/Al/C content produced the highest density of the composite products. The result in this study then provides information for the development of desired product obtained from low cost material (TiO_2) with an efficient process (induction heating).

Chapter 7

Fabrication of TiC Intermetallic Matrix Composite Coating

This chapter describes a process to synthesize a new multiphase TiC/Ti_3Al/Ti_2Ni composite coating prepared with multilayer pellets of Ti/C, Ni/Al, and Ti. Induction heating was used to initiate the SHS process of Ni/Al which produces an exothermic reaction for melting Ti and initiating the subsequent reactions in the Ti–Al, Ti–Ni and Ti–C systems. The microstructure and the mechanical property of synthesized products were investigated. The formation mechanism for synthesized products was analyzed by microstructure analysis.

7.1. Introduction

Titanium carbide (TiC) has become one of the most interesting ceramics since it has high hardness, high melting point, low density and good wear resistance at elevated temperatures [5]. However, the application of monolithic TiC is limited since it is brittle at room temperature [192]. Compared with TiC, intermetallics are more ductile. Intermetallics are also attractive for high temperature applications since they have high melting point, low density, good oxidation and corrosion resistance. Therefore, the combination of TiC and intermetallic is expected to produce unique material properties with significant improvements in strength for wide applications.

SHS process is attractive to synthesize ceramic and intermetallic materials [49]. In the development of ignition techniques for the SHS process, it was reported that induction heating has attracted much attention as an ignition source since this method provides a clean and fast heating [17]. Considering its advantage, induction heating was used as an external heat source to initiate the SHS process of several systems and to fabricate coating in the present works.

In Chapter 4 and 5, the fabrication of NiAl coatings on a steel substrate using induction heating with the application of Ti as underlayer to improve the adhesion between coating and substrate was investigated. The sample was prepared with two layer structures composed of Ni/Al as coating and Ti as underlayer. Induction heating was successfully applied to initiate the SHS process of Ni/Al system and simultaneously preheat the substrate. The combustion behaviour of Ni/Al showed that the synthesized products were in the molten phase during the synthesis. Due to the effect of capillary action, a part of the liquid NiAl infiltrated into the underlayer to produce a Ni–Al–Ti system. It was shown that the heat released by Ni/Al reaction was sufficient to melt Ti and promote the formation of a new intermetallic multiphase of Ti_2Ni–Ti_3Al composite in the underlayer. Interestingly, the hardness of Ti_2Ni–Ti_3Al composite is higher than that of the NiAl coating. Several literatures also reported that Ti_3Al based materials are emerging for revolutionary high temperature applications such as high speed spacecrafts and automotive industries since they have high melting point, high elastic modulus, low density and good oxidation resistance [27][193].

The application of single phase NiAl for structural materials, however, is limited due to its lack of ductility at room temperature and insufficient strength at high temperature. Although much efforts have been carried out to balance NiAl properties by improving its ductility at room temperature and strengthening at high temperature applications, the results are still unsatisfied [21]. The present work was then expanded by investigating the fabrication of NiAl–TiC–Al_2O_3 composite using induction heating. Ceramics TiC–Al_2O_3 were selected as the reinforcing materials for NiAl since these materials have been reported to improve the fracture toughness of the individual ceramic materials, either TiC or Al_2O_3 [46]. The starting materials used to produce NiAl–TiC–Al_2O_3 were Ni, Al, C and TiO_2 as the low cost material. NiAl–TiC–Al_2O_3 composites were successfully synthesized by SHS process using induction heating. The microstructure analysis clearly showed that the synthesized products were composed of NiAl–TiC–Al_2O_3 and no Ni, Al, C and TiO_2 existed in the final product which indicates that the SHS reaction was completed. This work showed that the heat released by NiAl reaction was sufficient to initiate

synthesis reactions of TiO_2/Al/C system to form TiC and Al_2O_3. It was also shown that the presence of ceramic phases has a significant effect on increasing the hardness of monolithic NiAl. However, an increase in the ceramic content in the composite system has reduced the density of materials.

The objective of this part of study was to: (a) further investigate the fabrication of TiC intermetallic matrix composite coating by multilayer configuration of Ti/C, Ni/Al, and Ti pellets, and (b) investigate the microstructure and mechanical properties of the synthesized products. Induction heating was still used as the ignition source, particularly to initiate the reaction of Ni/Al, while the multilayer configuration of the preforms was applied in order to obtain a higher concentration of TiC phase in the coating.

7.2. Experimental procedures

The starting materials used in this work were Ni, Al, Ti and C. The detailed specification and morphology of the materials are described in Chapter 3. The multilayer preforms were prepared using Ni/Al and Ti/C mixtures with a mole ratio of 1:1, respectively, whilst Ti powder was used as underlayer on the steel substrate. The schematic configuration of the system is described in Fig. 7.1. Several preliminary tests were conducted to study the effect of reactant thickness on the SHS occurrence, coating adherence and shape of product. By considering these factors, extensive experimental trials were carried out and the results showed that a successful sample could be produced using a composition of Ti/C, Ni/Al and Ti with thicknesses of 0.40, 0.54 and 0.31 mm, respectively.

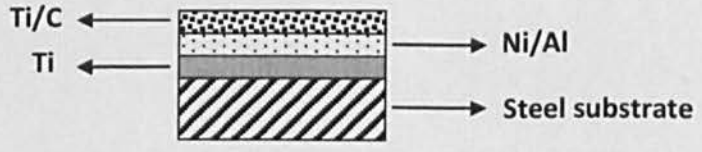

Fig. 7.1. Schematic configuration of the TiC intermetallic coating

In order to produce multilayer pellets, the starting materials were cold compressed in a steel die package with a pressure of 200 MPa. Prior to compaction, the powders were mixed in a ceramic mortar and dried in a carbolite furnace at about 100 °C for 1 hour to remove any moisture contents. Induction heating was used to initiate the SHS process and preheat the substrate. The current of induction heating was set to 300 A, while the heating time was turned off at about 1 second after ignition occurred. The SHS process was performed inside a reaction chamber with an environment of argon gas (purity = 98.5%, mass flow rate = 15 kg/s, and pressure = 2000 psi).

The microstructure characterization of synthesized products was performed using scanning electron microscopy and XRD after the samples were polished and etched using a method as explained in Chapter 3. XRD spectra were operated at a voltage of 40 kV and a current of 200mA with CuKα radiation (λ = 1.5405 Å), and a scanning rate of 4 deg./min. For the evaluation of mechanical properties, a Vickers microhardness tester with an objective lens of x40 and an eyepiece of x10 was used to investigate the microhardness of synthesized products, which realized using a load of 0.098 N for 15 second.

7.3. Results and discussion

7.3.1. Microstructure analysis

Fig. 7.2 shows the X-ray diffraction (XRD) patterns of the synthesized products which observed on the top surface of the samples. It can be seen that the majority of spectra in the synthesized products are TiC. This indicates that TiC coating was successfully fabricated using induction heating. Even though the XRD result indicates that the synthesized products are composed of a large amount of TiC, the products are not in a single phase. A considerable amount of the intermetallic Ti_2Ni and Ti_3Al, as well as a small amount of TiNi, can be observed in the synthesized products. This shows that there was a mixing between Ni/Al and Ti/C which subsequently reacted and formed Ti–Al and Ti–Ni intermetallics systems in the product. Strong peaks of carbon can also be identified in the XRD spectra

which indicate a significant amount of unreacted carbon as the residual phase of synthesized product. During the experiment, some carbon black were found on the surface of synthesized product which may be due to the formation of liquid in the synthesized product during the reaction causing the carbon particles to float. Meanwhile, TiO_2 can also be observed in the XRD spectra which can be identified by XRD spectra as rutile and anatase. The presence of titanium oxides in the synthesized product is due to the existence of oxygen in the high temperature of SHS reaction which subsequently reacted with Ti.

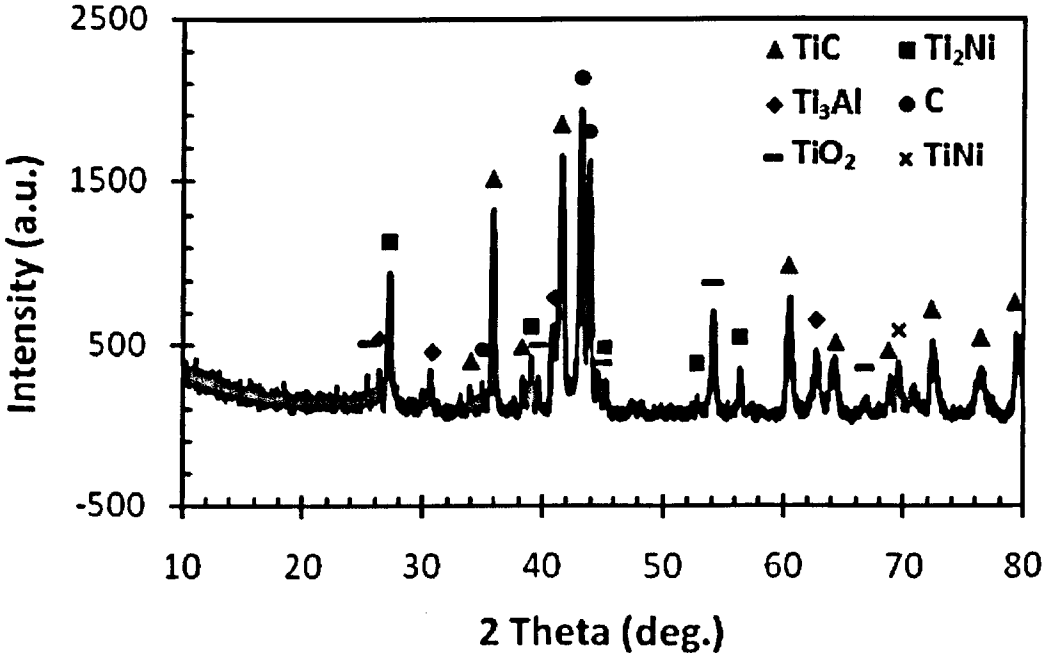

Fig. 7.2. X-ray diffraction spectra of TiC composite system

The appearance of several intermetallic phases of Ti–Al and Ti–Ni systems in the synthesized products as obtained by XRD shows the complexity of process during the reactions. This condition indicates that there was a diffusion and interaction between Ni/Al and Ti/C which then produced a complex Ni–Al–Ti–C system. The microstructure of the synthesized product was identified using SEM which equipped with an EDX/EDS analysis to investigate the distribution of phases across the layers. Fig. 7.3 shows the microstructure across the synthesized product prepared with multilayers of Ti/C, Ni/Al and Ti pellets on a steel substrate. It can be

seen in Fig. 7.3(a) that the coatings have good adherence to the substrate. This indicates that the application of Ti underlayer was successful to produce adhesion between the coating and the substrate. However, the microstructure of the synthesized product is inhomogeneous. The result suggests that there was a mixing between Ti/C, Ni/Al and Ti layers during the synthesis process resulting in the disappearance of the interface between the layers. The synthesized product is significantly dense at the interface to the substrate, but the porosity of product is significantly high at the coating surface. Referring to the initial configuration of the reactant in Fig. 7.1, the high porosity of product particularly at the surface can be attributed to the formation of solid TiC particles concentrated at the surface. Meanwhile, the number of porosity inside the coating is less than that in the surface due to the formation of liquid phase of NiAl and Ti. The pores observed inside the product can be attributed to the entrapped gas during the high temperature of reaction and some other reasons such as the existing pores in the compact, the volume shrinkage, and the diffusion vacancies [49].

Fig. 7.3(b) and (c) show enlarged pictures of the microstructure of the synthesized product in which the different phases can be identified using EDS/EDX analysis. To help the phase identification, the inhomogeneous structure of the synthesized product is divided into coating and underlayer zones. Four different phases were selected; spot A represents the area in the coating which contains a high content of small particles, spot B denotes the dark area in the underlayer which includes a less content of the small particles, spot C describes the grey area around the underlayer zone, and spot D refers to the bright area near the interface to the substrate. The element composition of each phase observed using EDX analysis is described in Fig. 7.4, while semi quantitative EDS analysis is given in Table 7.1 and Fig. 7.2. The atomic composition of the spot A as determined by EDX spectra in Fig. 7.4(a) indicates a high concentration of Ti mixed with a small amount of C, Ni and Al. The atomic composition obtained using semi quantitative EDS analysis shows that the spot A contains a high content of Ti which achieves 57.36 wt.% and a significant amount of Al and Ni with a similar quantity. However, with a total number of the elements which is only 93.63 wt.%, concern must be applied

since the result might not be converted directly to identify the formed phase. As previously explained, the quantity of C could not be provided during the SEM observation because the samples were coated using carbon. With a high content of Ti which contains 58.89 at.%, and with a reference to the XRD result in Fig. 7.2, the spot A can be interpreted as TiC which is mixed with the intermetallic of Ti–Al and Ti–Ni systems, particularly Ti_3Al and Ti_2Ni. A high magnification picture of the microstructure as shown in Fig. 7.3(c) suggests that there are several small particles shaped like a cube with a grain size of about 1 micron, which can be attributed to the formation of TiC. The shape of TiC in this study is closely similar to that obtained from TiO_2/Al/C reaction as described in Fig. 6.5 (Chapter 6). The atomic composition in the present result is also consistent with that in the previous work described in Chapter 6, in which the atomic composition of Ti in the TiC is 58.67 at.%. It should be noted that a precise observation into the TiC particle is difficult due to the limitation of the equipment, in which the resolution of electron beam of the SEM equipment is 5 μm x 5 μm x 5 μm. Due to the inhomogeneous phase of the synthesized product, identification on the single phase of Ti_3Al and Ti_2Ni also could not be performed. However, the SEM micrograph reveals that the upper layer of the synthesized product is dominated by small particles which refer to TiC precipitated in the matrix. A high magnification picture taken at the surface area shown in Fig. 7.3(c) confirms the formation of small particles TiC. The result in this study produces a result which corroborates the finding in the previous work in the formation of TiC obtained from a low cost material (TiO_2).

Turning now to the microstructure in the underlayer zone, the EDX/EDS analysis of the spot B in Fig. 7.4(b) show a similar result to that of the spot A, in which the spot B contains a high amount of Ti and a significant amount of Ni and Al. Similarly, the amount of C could not be provided due to the limitation of the equipment. However, the microstructure of the spot B exhibits a distribution of small-black particles. This result indicates that TiC particles have dispersed inside the matrix in the underlayer. The element composition of the spot B indicates that the matrix of the spot B may be composed of Ni–Al–Ti compounds. Previous studies

described in Chapter 4 have shown that Ni/Al reaction could promote the formation of Ti_3Al–Ti_2Ni composite obtained from Ni–Al–Ti system.

In Fig. 7.4(c), the EDX spectra of the grey phase labelled by the spot C in the underlayer zone indicate a high concentration of Ti with a small content of Fe, Al and Ni. The EDS analysis of the grey phase in Table 7.2 gives the atomic concentration of Ni, Al, Ti and Fe. It can be seen in Table 7.2 that the atomic concentration of Ti, Al and Ni is 50 at.%, 10 at.% and 10 at.%, respectively. This means that the atomic fraction of Ti : Al : Ni has a composition of 5 : 1 : 1. This result indicates that this phase may be composed of Ti_3Al and Ti_2Ni. Meanwhile, 30 at.% of Fe observed in the grey phase indicates that Fe has diffused into the underlayer zone. The bright phase marked by the spot D gives a clear indication on the diffusion of Fe into the underlayer zone. The data obtained by EDX/EDS in Fig. 7.4(d) show that the spot D contains a high concentration of Fe atom which achieves 57.8 at.% as given in Table 7.2. The diffusion of Fe from the substrate to the underlayer can be caused by a local melting in the surface of the substrate due to the effect of the heat generated by induction heating and the heat released by multiple reactions in the Ni–Al–Ti–C system.

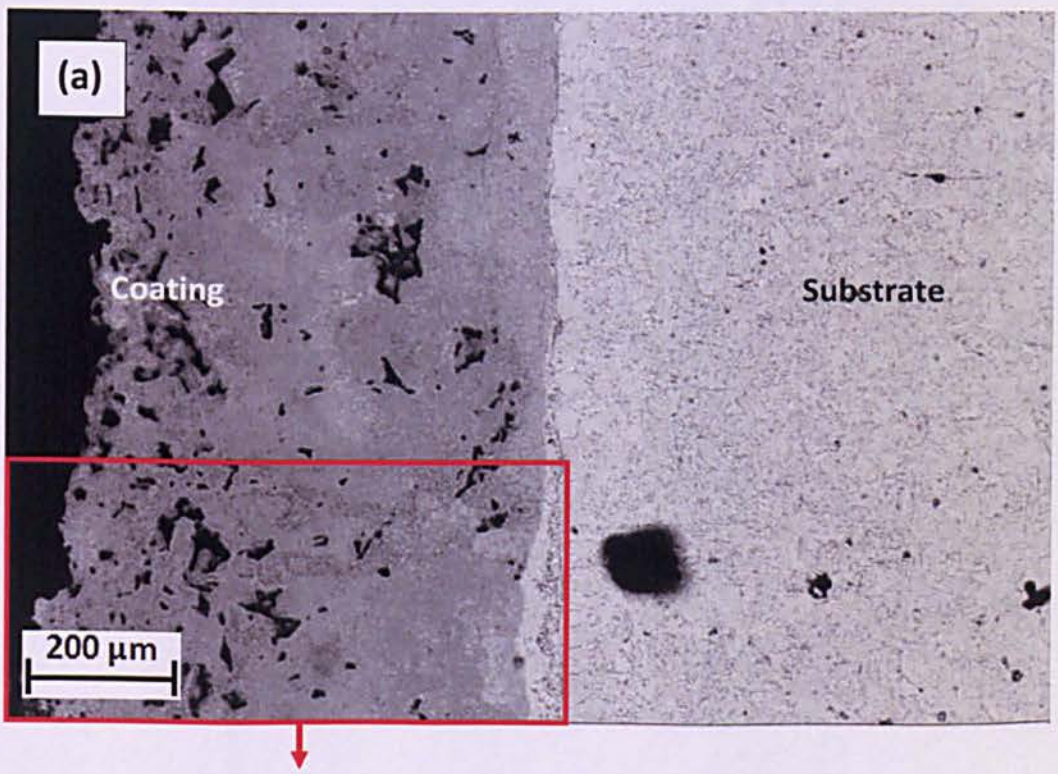

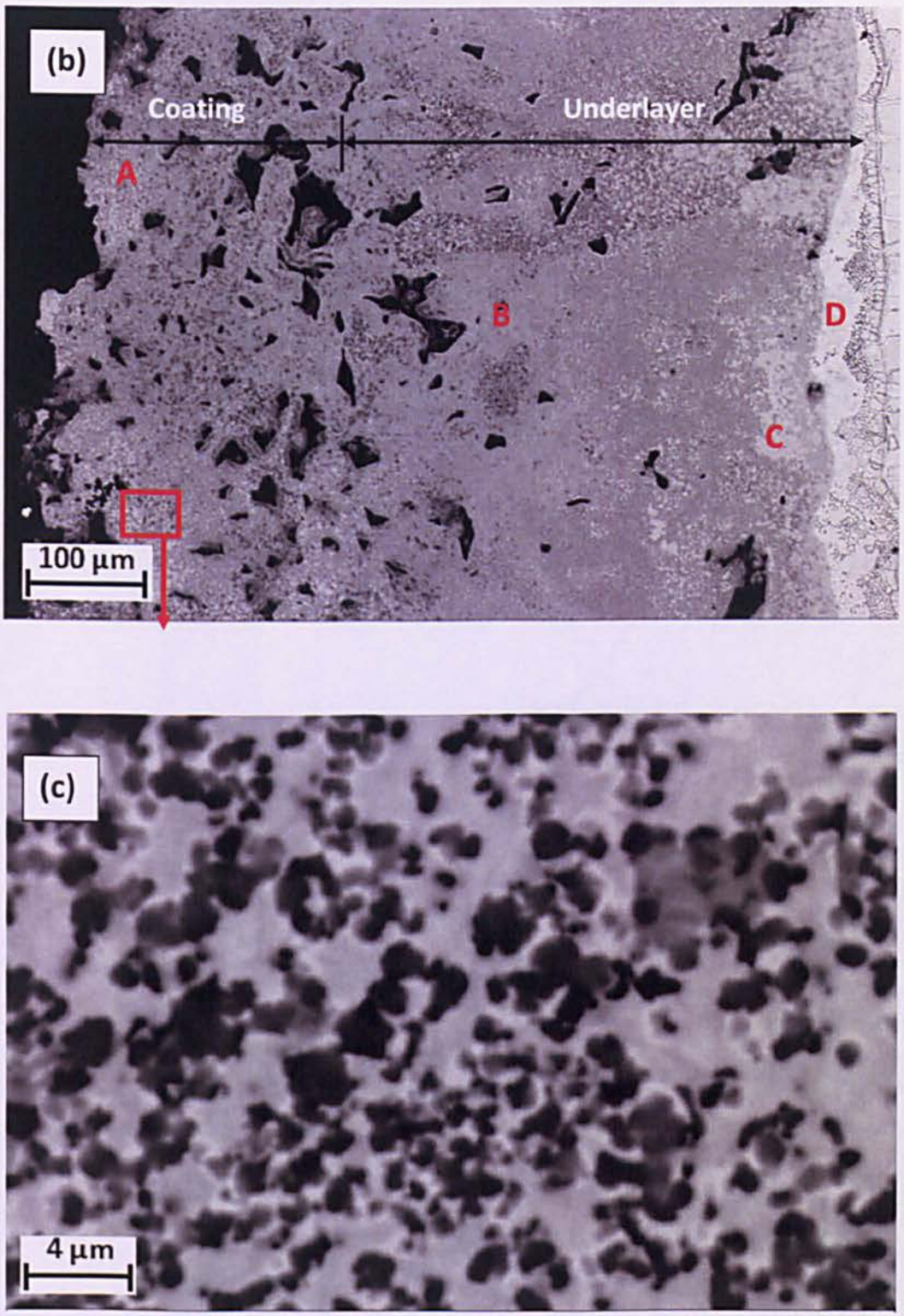

Fig. 7.3. Typical SEM micrograph of TiC composite coating: (a) image across the coating and substrate; (b) enlarge image of the coating; (c) high magnification image showing the particles in the coating surface

Table 7.1. Chemical composition (in wt.%) of the phases in Fig. 7.3(b)

Spectrum	Al	Ti	Mn	Fe	Ni	Total
A	10.84	57.36		0.79	24.64	93.63
B	10.71	58.81		3.95	22.19	95.67
C	5.78	48.09		33.07	12.64	99.59
D	2.99	28.27	0.41	62.02	5.97	99.66

Table 7.2. Chemical composition (in at.%) of the phases in Fig. 7.3(b)

Spectrum	Al	Ti	Mn	Fe	Ni	Total
A	19.77	58.89		0.69	20.64	100
B	19.15	59.21		3.41	18.23	100
C	10.57	49.57		29.24	10.62	100
D	5.77	30.73	0.39	57.82	5.29	100

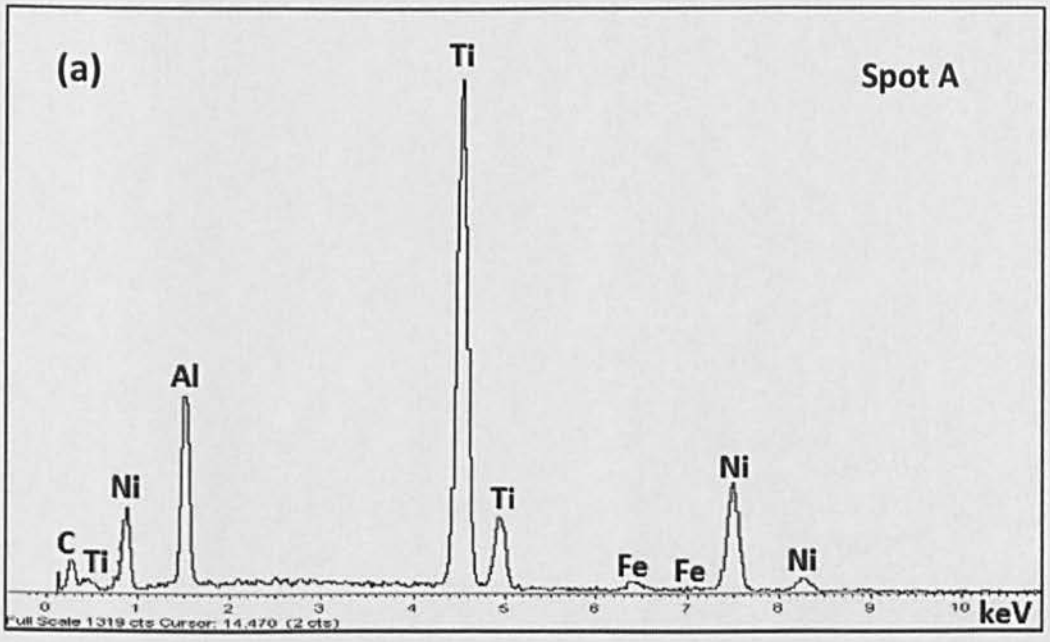

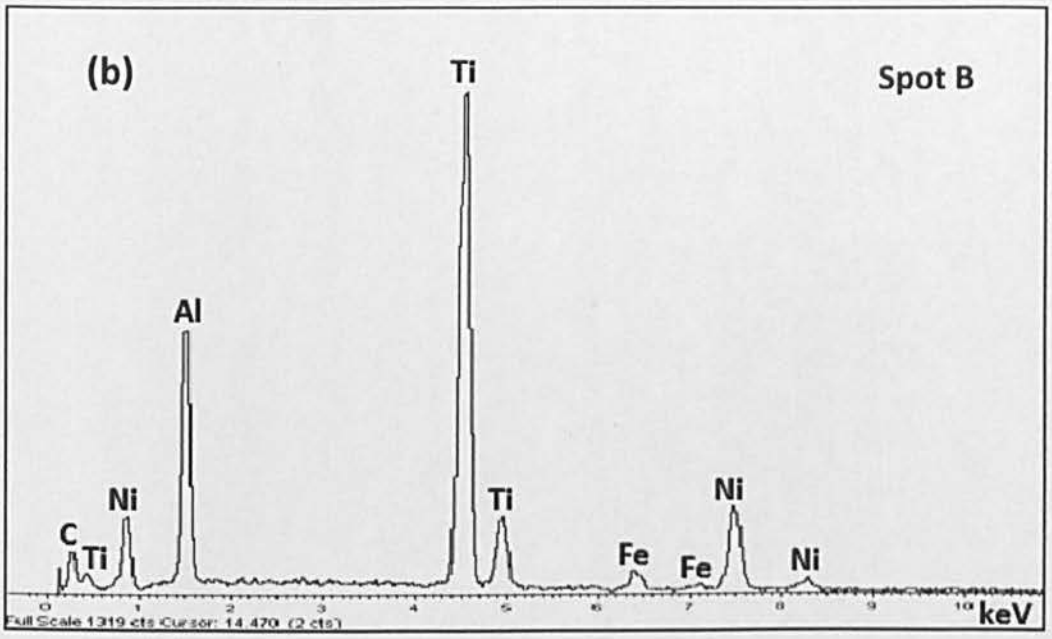
(b)
Spot B
Ti
Al
Ni
C
Ti
Ti
Fe
Fe
Ni
Ni
keV
Full Scale 1319 cts Cursor: 14.470 (2 cts)

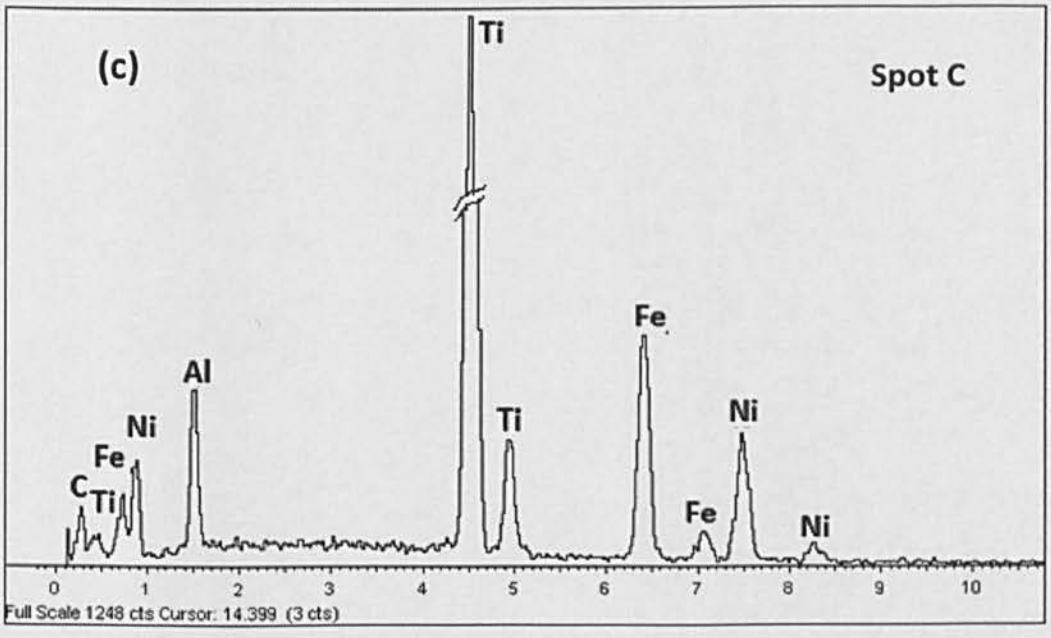
(c)
Spot C
Ti
Fe
Al
Ni
Ti
Ni
Fe
C
Ti
Fe
Ni
0
1
2
3
4
5
6
7
8
9
10
Full Scale 1248 cts Cursor: 14.399 (3 cts)

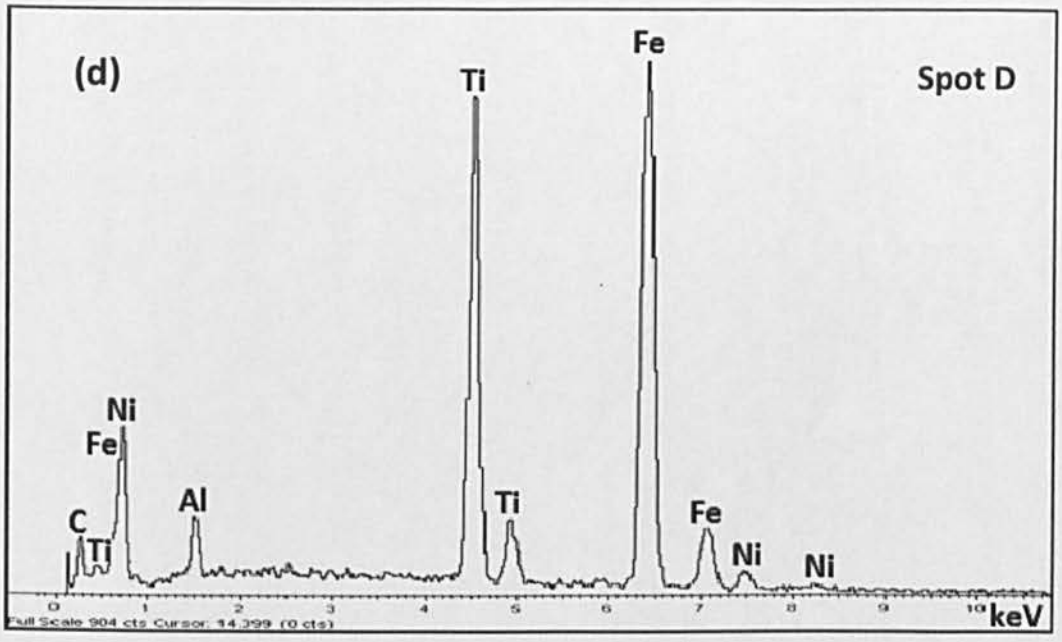

Fig. 7.4. EDX spectra of: (a) spot A; (b) spot B; (c) spot C; and (d) spot D shown in Fig. 7.3 (b)

In order to investigate the morphology and phases of the products at the interface of the substrate, an enlarged SEM micrograph and the EDX analysis are presented in Fig. 7.5 and Fig. 7.6, respectively. It can be seen that a diffusion layer is observed at the interface between the underlayer and the substrate. The formation of diffusion layer also indicates that the adhesion between coating and substrate was formed by metallurgical adhesion. The existence of diffusion layer in this system is surprising since it was absent during the fabrication of NiAl coatings with Ti underlayer. The higher combustion temperature of Ti/C reaction relative to that of Ni/Al reaction may be responsible for the formation of the diffusion layer adjacent to the substrate. It can also be observed that cracks propagate along the interface and partly to the diffusion layer. The formation of crack along the interface can be attributed to the effect of residual stress generated by the coefficient of thermal expansion (CTE) mismatch between the substrate and the reaction products in the diffusion layer. Meanwhile, the cracks observed across the layer can be associated with the formation of brittle phases of the diffusion layer. The EDX spectra of the diffusion area which marked by the spot E in Fig. 7.6

indicates a high atomic concentration of Fe and Ti. Thus, the diffusion layer may refer to the formation of intermetallic systems of Fe–Ti.

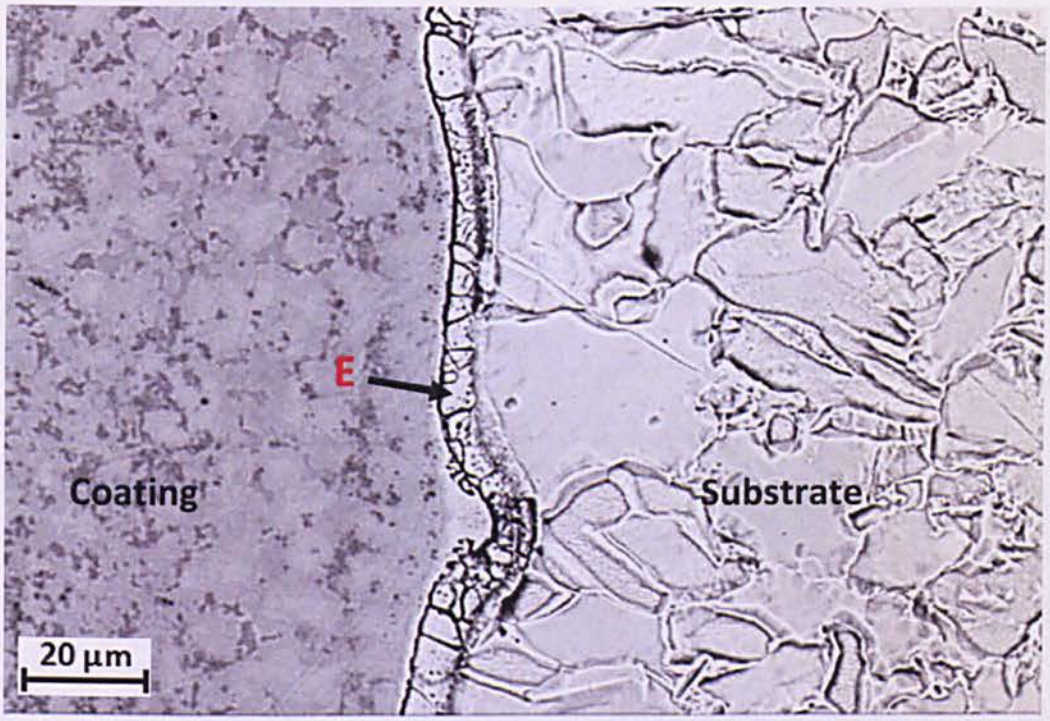

Fig. 7.5. Microstructure across the interface in the TiC system

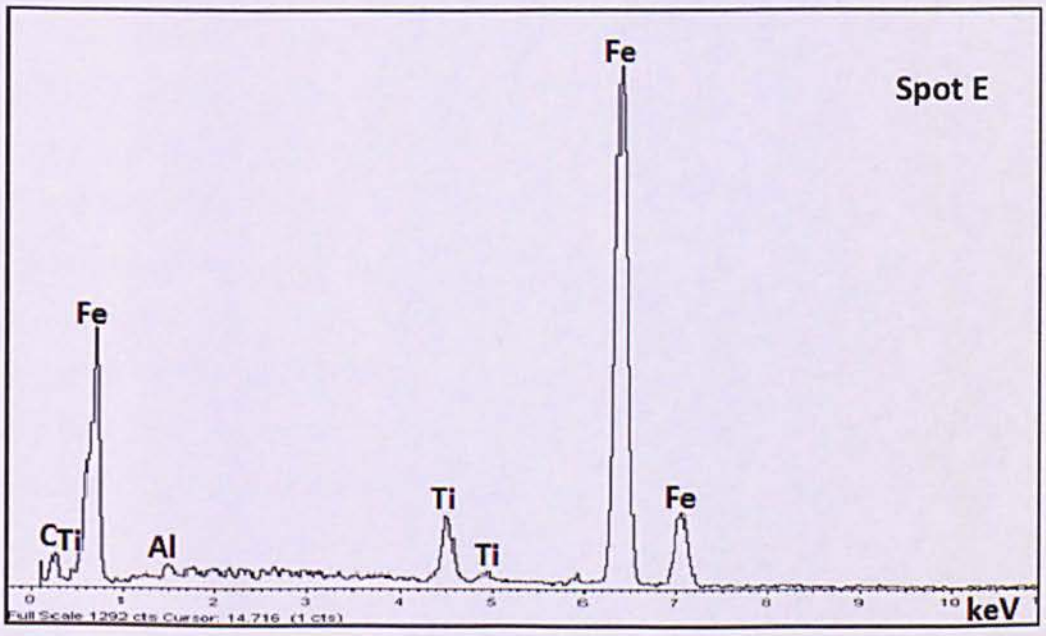

Fig. 7.6. EDX spectra of the spot E shown in Fig. 7.5

Considering the complexity of the phase distribution inside the product, line scans illustrating the element evolutions across the synthesized product were observed as presented in Fig 7.7 and Fig 7.8. It can be seen in Fig 7.7 that the interface of the difference layers in the synthesized product cannot be clearly identified. It means that there was a mixing between the layers. A confirmation can be found in the gradient evolution of the atomic concentrations from the coating surface to the substrate interface as shown in Fig 7.8. It can be observed that Ti atom is distributed along the product. The amount of Ti concentration increases progressively from the coating surface to the substrate. This shows that there was a diffusion of Ti across the underlayer. As observed in Fig 4.6 (Chapter 4), the temperature profile of Ti showed that Ti had melted during the combustion synthesis of NiAl/Ti due to the heat from Ni/Al reaction. Based on this finding, it can be though that the diffusion of Ti occurred after melting due to the heat released by Ni/Al reaction in the underlayer. The atomic concentrations of Ni and Al are also distributed along the product indicating that these elements have melted and spread during the synthesis reaction. This is also supported by the temperature profile of Ni/Al reaction as described in Fig 4.4 (Chapter 4) indicating that the synthesized product of NiAl formed a liquid phase during the reaction. The line scan EDS analysis in Fig 7.8 also shows that the intensity of Ni and Al is lower than that of Ti. This is due to the amount of Ti concentration in the underlayer which is higher than that of Ni and Al mixture in the underlayer. The evolution of Fe is also found in the underlayer. It can be seen that a small amount of Fe has diffused across the substrate interface which can still be observed at a distance of about 400 μm from the substrate. The diffusion of Fe can be attributed to the local melting of the substrate surface due to the high temperature of substrate surface after receiving the heat from the molten Ti or its reaction with Ni/Al and the heat generated by induction heating during the process.

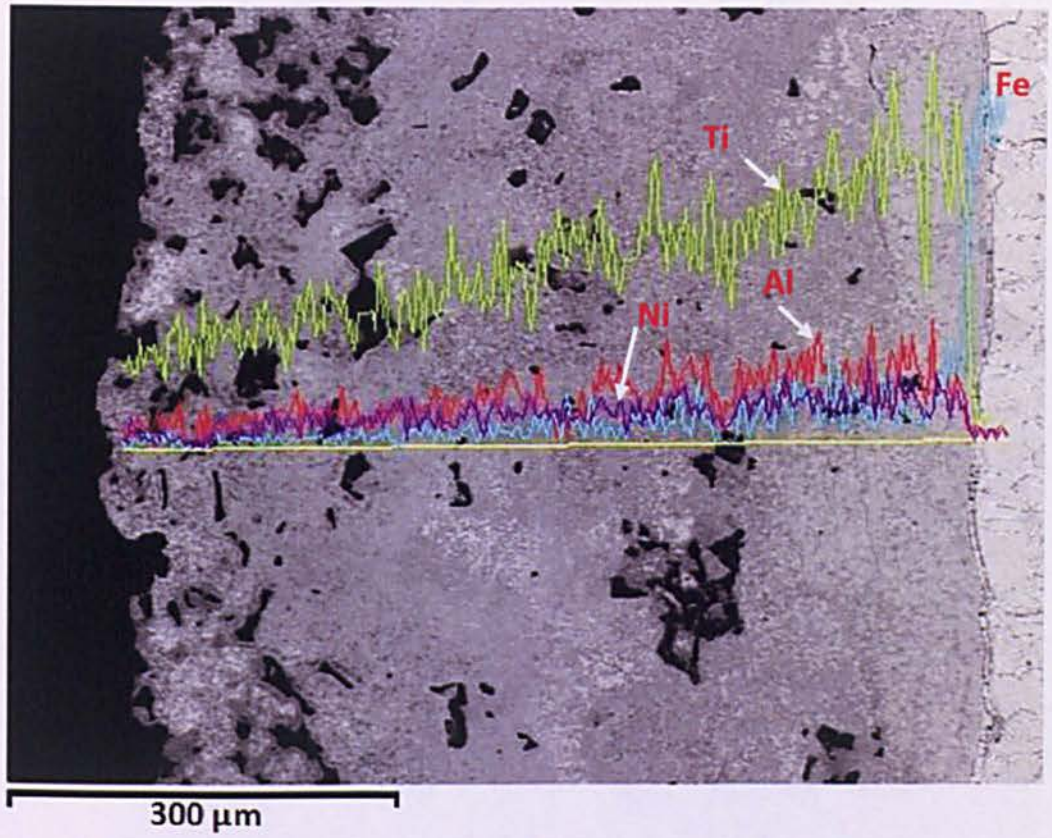

Fig. 7.7. Element distribution across the synthesized product of TiC system

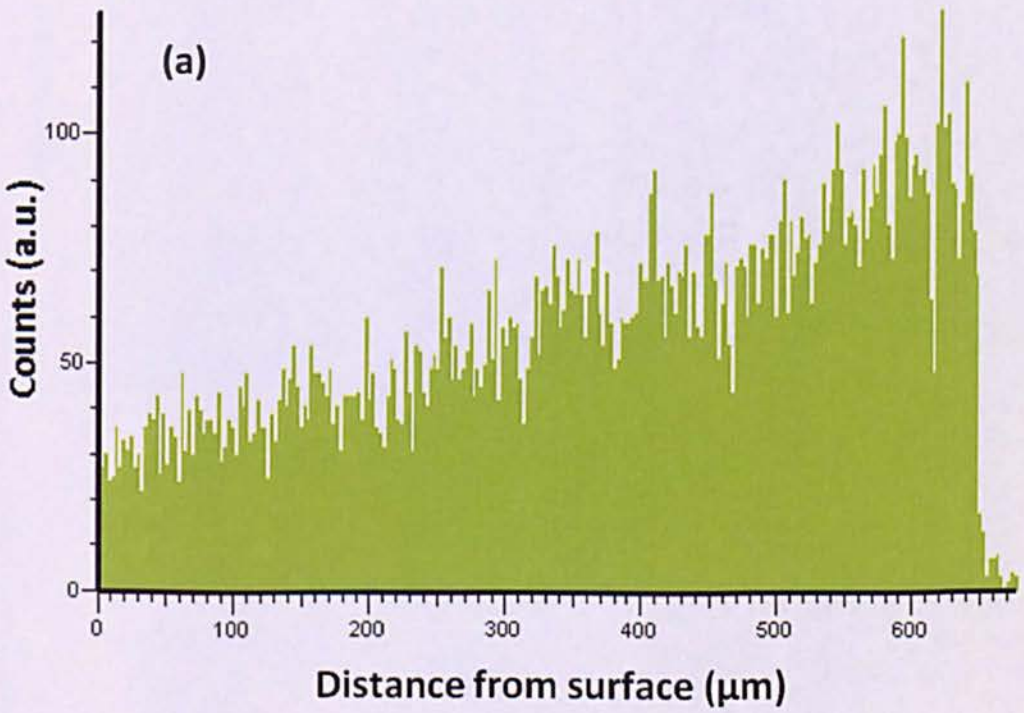

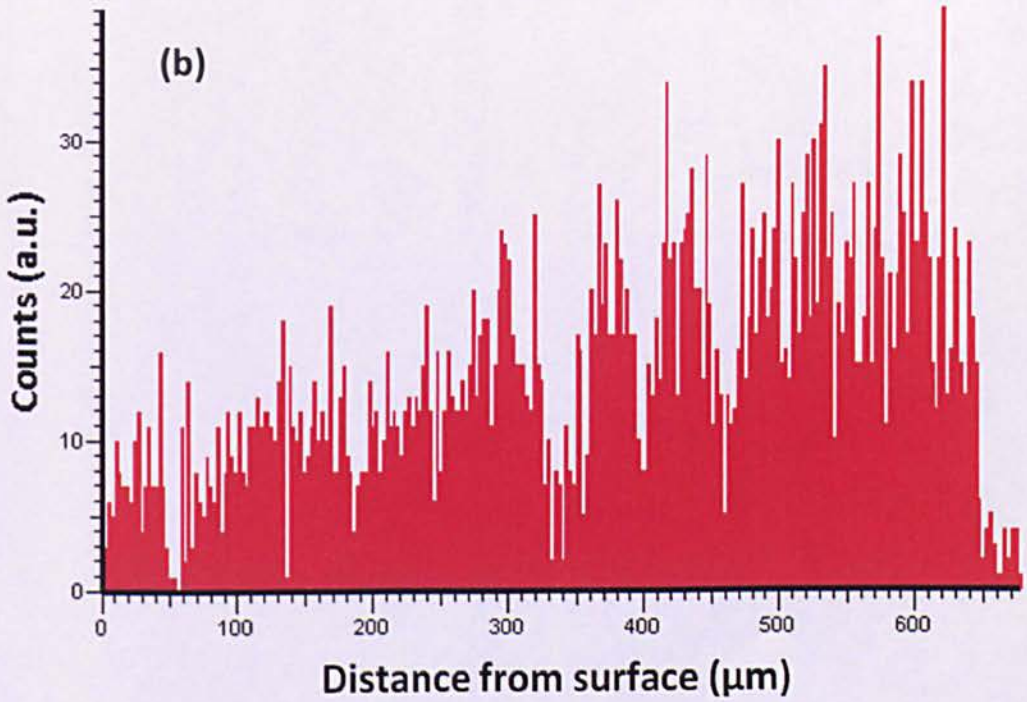
(b)
Counts (a.u.)
0
10
20
30
0
100
200
300
400
500
600
Distance from surface (µm)

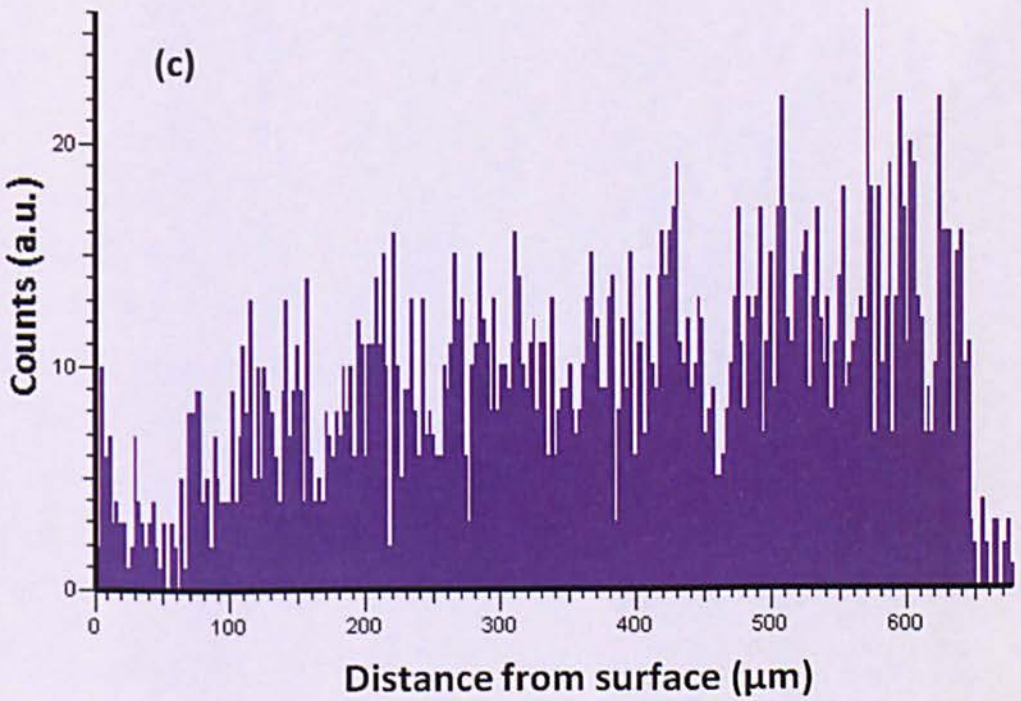
(c)
Counts (a.u.)
0
10
20
0
100
200
300
400
500
600
Distance from surface (µm)

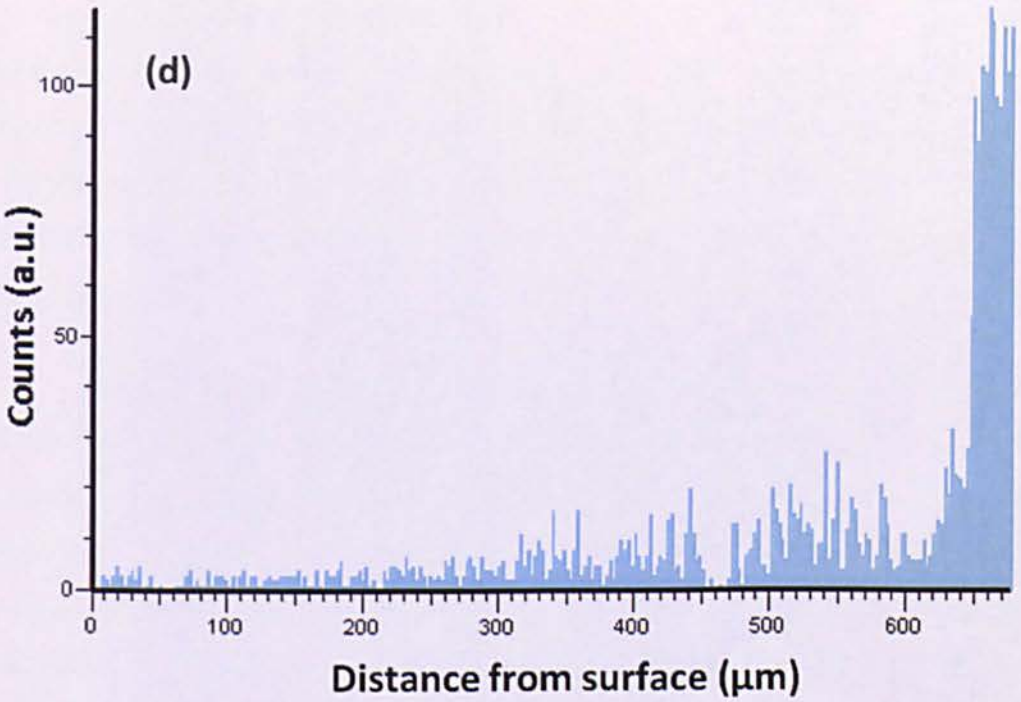

Fig. 7.8. Line scan EDS analysis of: (a) Ti; (b) Al; (c) Ni; and (d) Fe shown in Fig. 7.7

7.3.2. Formation mechanisms

From the microstructural transition as observed above, it can be concluded that Ti and Ni/Al in the underlayer have melted during the process. The formation of several intermetallic phases also indicates that there were reactions between Ni/Al and Ti. It is then proposed that the combustion synthesis in the preforms was initiated by the melting of Al in the underlayer as it is the substance with the lowest melting point (933 K). Since Al was located in the mixture of Ni/Al, the liquid Al then spread around Ni particles in the underlayer. A part of Al in the Ni/Al layer was also possible to disperse into Ti and Ti/C layers resulting in the contact of the liquid Al with Ti and C.

Following the melting of Al, the reactions of Al–Ti, Al–Ni and Al–C were all possible. The formation of TiC, Ti_2Ni, TiNi, Ti_3Al and TiO_2 in the sample as observed by XRD indicated that there were numerous binary compounds existed in the system. Thermodynamic analysis may be helpful to determine the possibilities of reaction sequence in these systems [194]. However, it is believed that the reaction

of Ni/Al occurred initially. The main reason is related to the position of Ni in the mixture of Ni/Al allowing Ni to have more contact with Al. In addition, previous study reported that the heating rate generated by induction heating in the reaction of Ni/Al was higher than that of Ti/C since Ti and C are magnetically nonconductive materials and could not be sufficiently heated using induction heating to initiate a TiC reaction [18].

During the Ni/Al reaction, the synthesized NiAl formed a liquid state which allowed it to spread across the sample. The temperature profile of Ni/Al reaction (in Chapter 4) confirmed that the combustion temperature of Ni/Al reaction achieved its melting point at approximately 1911 K. The effect of capillary force then caused the liquid NiAl in the underlayer to spread and infiltrate around the solid Ti/C in the upper layer and solid Ti in the underlayer, and formed a Ni–Al–Ti–C system. Further reactions in this system were possible to start. The temperature profile of Ti (in Chapter 4), however, indicated that the high heat released by the formation of NiAl (ΔH_f = −118.4 kJ/mol) ensured the melting of Ti and followed by phase transformation of Ti–Al and Ti–Ni system. The liquid of Ti then spread into NiAl and formed Ni–Al–Ti melt in the underlayer. The gradient concentration of Ti indicated by the line scan confirmed that Ti has melted and spread around NiAl.

After the melting of Ti, C particles dissolved into Ni–Al–Ti melt. The heat released by Ni/Al reaction was responsible for the ignition of the reaction between the liquid Ti and C particles to form a stable TiC. The formed TiC then precipitated in Ni–Al–Ti melt. Several literatures showed that the formation of TiC can be started by dissolution of carbon particles into Ti liquid, followed by precipitation of TiC [195]. Since the Ti/C reaction is highly exothermic (ΔH_f = −184.5 kJ/mol), it then maintained the reactions of the intermetallic Ti–Al and Ti–Ni systems to complete to form stable phases such as Ti_2Ni, TiNi and Ti_3Al. By referring to the phase diagram of Ti–Ni and Ti–Al systems given in Fig. 4.19 and Fig. 4.20 (Chapter 4), the presence of Ti_2Ni and Ti_3Al in the synthesized product indicates that the reaction occurred in Ti–rich zone since the formation of Ti_2Ni and Ti_3Al requires high titanium concentrations. Thus, the reaction of Ti–Al and Ti–Ni could be initiated initially to form intermediate phases in the underlayer, and the heat released by TiC

reaction then kept the Ni–Al–Ti reactions to complete. Further experimental evidence is needed to confirm the formation mechanism in these systems.

7.3.3. Mechanical properties

Although the present system was prepared using a multilayer structure, the microstructure analysis showed that the formed phases in the synthesized product were inhomogeneous. The XRD spectra given in Fig. 7.2 show that the surface of synthesized product is composed of TiC mixed with $Ti_3Al/TiNi/Ti_2Ni/TiO_2/C$. For convenience, the main products in the upper layer are referred to as $TiC/Ti_3Al/Ti_2Ni$ since TiO_2 is a secondary products, TiNi is also present in a small volume, while C is a residual product. Since the concern of this work was to fabricate TiC intermetallic coatings, the examination on the microhardness of synthesized products was carried out in a number of locations on the coating surface. The hardness of the synthesized product is described in Fig. 7.9. For comparison, the hardness of other systems such as NiAl, NiAl+40 wt.% (TiC/Al_2O_3) and Ti_2Ni/Ti_3Al as produced in previous works (Chapter 5 and 6) is also attached in the graph. It can be seen that the average hardness of $TiC/Ti_3Al/Ti_2Ni$ system (1135.48 ± 139.58) is higher than that of other systems. A wide range of the hardness value in the $TiC/Ti_3Al/Ti_2Ni$ system shows that the material is composed of heterogeneous phases with a variety of hardness values. It can be seen that the lowest value of the standard error is almost similar to the average hardness of Ti_3Al/Ti_2Ni system indicating the existence of Ti_3Al/Ti_2Ni phase in the $TiC/Ti_3Al/Ti_2Ni$ system.

Fig. 7.10 shows the picture of Vickers indentation on the surface of $TiC/Ti_3Al/Ti_2Ni$ system. It can be seen that the indentation sizes are varied. This shows a wide variety of the hardness values due to the presence of inhomogeneous phase. The small indentation size shows the higher hardness due to the existence of the hard phases, while the big indentation size shows the lower hardness which can be attributed to the matrix site. Since the surface of the sample contains many pores, Vickers indentations were only performed in the dense areas. It can be seen that the pores with sizes of 10–40 μm are found in the surface of synthesized product. According to a previous study, this is due to the capillary force was

insufficient to sustain the infiltration of the molten intermetallic with equal speed throughout the sample for producing completely a dense product [192]. Considering that the present product has high hardness with new compositions, further investigation on the melt infiltration of the intermetallic phase is required in order to control the density of synthesized product.

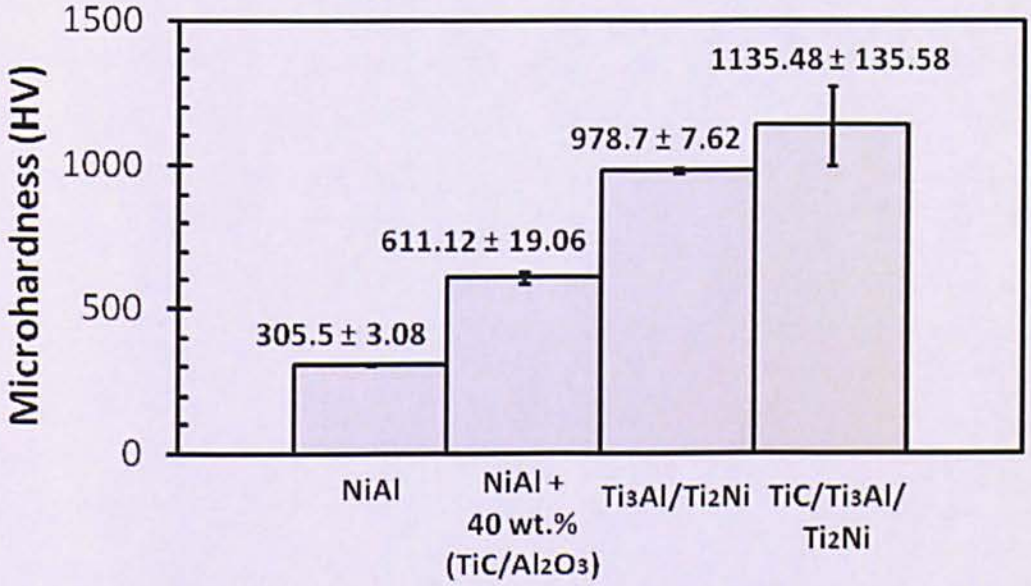

Fig. 7.9. Microhardness comparison of different systems

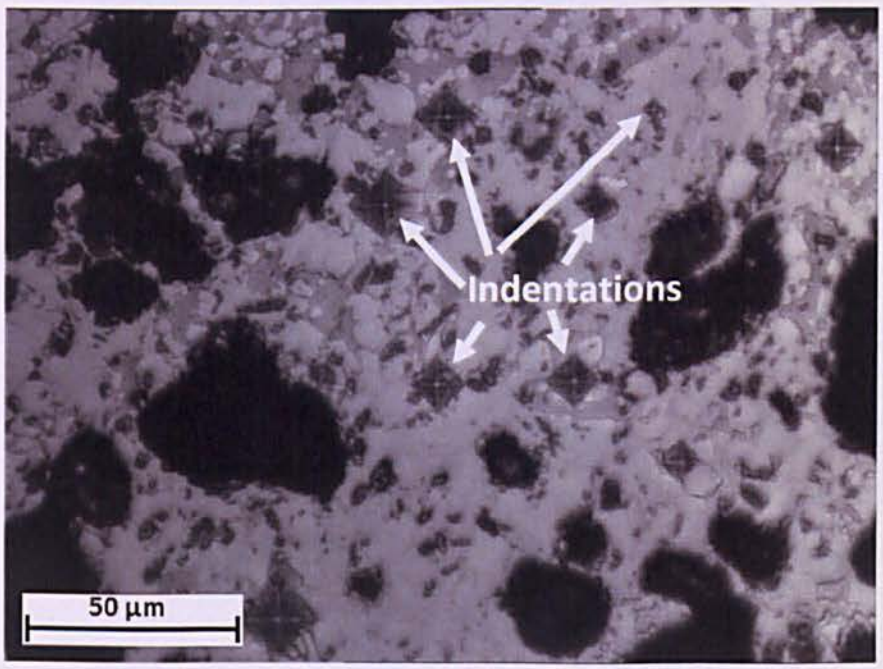

Fig. 7.10. Indentation on the coating surface of TiC composite coating

7.4. Summary

In this chapter, the fabrication of $TiC/Ti_2Ni/Ti_3Al$ composite coating prepared by multilayer Ti/C, Ni/Al, and Ti on a steel substrate is reported. The synthesized products were successfully formed using the SHS process which was ignited using induction heating. The results suggested that a good bonding between the coating and the substrate was achieved. The microstructure analysis showed that the synthesized product was composed of inhomogeneous phase of $TiC/Ti_3Al/Ti_2Ni$ mixed with a secondary product of TiO_2. Based on the microstructure, XRD and EDX analysis the formation mechanism of the synthesized products is discussed. Firstly, the heat supplied by induction heating melted Al and started to ignite the SHS process of Ni/Al. The Ni/Al reaction released a high heat which caused the melting of Ti and promoted further reactions between the molten Ti and liquid NiAl to form Ti_2Ni, TiNi and Ti_3Al as well as C to form TiC. The evaluation of mechanical property showed that the microhardness of $TiC/Ti_3Al/Ti_2Ni$ system is higher than that of the intermetallic Ti_3Al/Ti_2Ni and $NiAl/TiC/Al_2O_3$ composite. The present study shows that high performance intermetallic–ceramic composite coatings can be produced by the SHS process ignited by induction heating.

Chapter 8

Conclusions and Further Work

This chapter summarizes the results of this study which was aimed to develop a new method to fabricate high performance intermetallic and ceramic materials and coatings formed by the SHS process. This research work has shown that induction heating can be used to ignite the SHS process of Ni/Al and preheat the substrate in the coating fabrication, while Ti can be used as underlayer to improve the adhesion strength. The findings obtained from the experiments are summarized below. Several recommendations for future work are proposed for implementing the results.

8.1. Conclusions

Three systems were studied in this project. The following conclusions can be drawn based on the investigation.

(a). Fabrication of NiAl coating

In this study, the experiment was carried out to find a method to simultaneously synthesize and fabricate NiAl coating on a steel substrate. The objective of this study was to improve the adhesion between the coating and the substrate, particularly to study the combustion behaviour, analyze the microstructure and formation mechanism of synthesized products, and evaluate their mechanical properties and thermal shock behaviours. The preforms were prepared using two layer structures of Ni/Al mixture and Ti as underlayer, and were placed on the substrate inside a combustion chamber. The preforms were then heated using induction heating with various currents. The experimental results demonstrated that induction heating with currents of 200 A – 300 A were capable of igniting the SHS process of Ni/Al to produce a complete reaction. The temperature profile of Ni/Al reaction illustrated that the combustion temperature

increased from its initial condition at room temperature to an ignition point with different heating rates depending on the currents of induction heating. The heating rate of the initial heating with the currents of 200 A, 250 A and 300 A was 46.6 K/s, 57.0 K/s and 85.5 K/s, respectively. After reaching the ignition point, the combustion temperature increased sharply to achieve the maximum temperature. The maximum combustion temperature for all current variations was remained the same at approximately 1911 K, which indicates that the synthesized product has melted during the reaction. By referring to the thermodynamic calculation, the NiAl was fully melted during the reaction since induction heating could preheat the sample to a temperature above 834 K. Due to a capillary action, a part of the liquid Ni/Al which formed during the reaction spread into underlying Ti. The heat released by Ni/Al reaction then melted the titanium and promoted further reactions between the liquid Ni/Al and Ti.

As observed by SEM and XRD, Ti underlayer changed into new materials in the underlayer composed of Ti_2Ni–Ti_3Al composite and Ti alloy, in which their compositions mainly depended on the variation of the underlayer thickness. When using a thin underlayer of Ti (with a thickness of 0.31 mm), most of Ti were consumed and reacted to form new phases composed of Ti_2Ni–Ti_3Al composite in the underlayer. A small amount of $AlNi_2Ti$ phases was also observed in the interface of NiAl. In the sample with a thick underlayer (0.83 mm), there was only a part of Ti which reacted to form Ti_2Ni–Ti_3Al, while a large quantity of Ti was remained as unreacted Ti which formed an alloy with Ni/Al.

Interestingly, the evaluation of mechanical properties of synthesized product using Vickers microhardness tester showed that the average hardness of Ti_2Ni–Ti_3Al composite (978.7 ± 18.34 HV) was higher than that of NiAl (345.2 ± 18.34 HV), Ti alloy (479.1 ± 7.78 HV) and Fe substrate (166.2 ± 2.86 HV). Indentation tests using Vickers microhardness tester at the interface between underlayer and substrate showed that no cracks were observed after an indentation with 20 N, as the maximum load of the indenter, indicating that the coatings have good adhesion to the substrate. The microstructure analysis showed that the strong adhesion of coatings occurred due to the formation of metallurgical bonding between

underlayer and the substrate which caused by the melting of Fe during the process. It was revealed that the heat generated by induction heating and the heat released by Ni/Al reaction could preheat the substrate and promoted the melting of Fe and the reaction at the interface between Ti and Fe substrate.

After investigating the microstructure and analyzing the formation mechanism of the synthesized products, the performance of NiAl coatings was investigated by evaluating their thermal shock resistance and bonding to substrate after high temperature treatments. Thermal shock tests were repeated 8 times by heating the samples to 1173 K (900 °C) in an atmospheric furnace followed by water quenching for 5 minutes. The result showed that the thickness of underlayer significantly affected the thermal crack existed in the heated products. In the sample with thin underlayer, four types of cracks were observed in the products: continuous cracks which developed into crack networks at the surface, major/vertical cracks which propagated from the surface through the underlayer to the substrate, horizontal cracks which generated along the interface between the coating and underlayer, and minor cracks which grown in the interface of underlayer/substrate. The formation of these cracks was attributed to the formation of hard phases (Ti_2Ni–Ti_3Al) in the underlayer. In the sample with thick underlayer, no cracks were observed after thermal shock testes. One of the significant findings to emerge from this study is that no cracks were observed at the interface between the substrate and underlayer after indentation test. This finding was attributed to the formation of Ti alloy in the underlayer. The samples with thick underlayer thickness hence have higher thermal shock resistance and adhesion strength than that with thin underlayer thickness. These findings enhance our understanding on the role of underlayer.

(b). Fabrication of NiAl–TiC–Al_2O_3 obtained from a low cost TiO_2

In the second work, the fabrication of NiAl–TiC–Al_2O_3 composite using induction heating was investigated. This work was designed to study the effect of reactant compositions on the combustion behaviour, microstructure and mechanical properties of synthesized product. The preforms were prepared using

Ni, Al, C and TiO_2 powder which were weighed to form a composition of (1 – x)Ni/Al and (x)3TiO_2/4Al/3C with x equals to 10, 20, 30 and 40 wt.%. The phase identification using XRD showed that NiAl, TiC and Al_2O_3 were the main phases in the synthesized product, where their compositions depended on the reactant compositions. The identification of formed phases in the synthesized product obtained by XRD was confirmed by the use of laser Raman microspectroscopy. The temperature profile measured in this study indicated that two stages of reactions existed in the SHS process. The first stage which formed a peak temperature was attributed to the exothermic reaction of TiO_2/Al/C, while the second stage which formed a plateau corresponded to a phase transformation of NiAl. It was revealed that an increase in TiO_2/Al/C content by 10, 20, 30 and 40 wt.% increased the maximum temperature of the exothermic reaction to 1911 K, 2093 K, 2135 K and 2208 K, respectively. Although the maximum combustion temperature has increased significantly, they were still below the melting point of TiC (3210 K) and Al_2O_3 (2325 K) indicating that those phases were in the solid state during reactions. The microstructure analysis using SEM showed that an increase in the content of TiO_2/Al/C led to an increase in the porosity of synthesized products, which is due to the increase of the amount of solid TiC and Al_2O_3 particles rather than the amount of liquid NiAl in the synthesized product. The evaluation of mechanical properties proved that increasing the content of TiO_2/Al/C resulted in the increase of hardness which can be attributed to the increase of TiC–Al_2O_3 content in the synthesized product. The findings in the present study hence make noteworthy contribution to the formation of high performance NiAl–TiC–Al_2O_3 composite which obtained from low cost material (TiO_2). The result also showed that induction heating was able to initiate the reaction of Ni/Al and the heat released by Ni/Al reaction then promoted the reaction of TiO_2/Al/C to produce a NiAl–TiC–Al_2O_3 composite. The present study also provides additional information for the fabrication of NiAl–TiC–Al_2O_3 composite with respect to the relationship between the combustion temperature, the microstructure characterization and the mechanical properties of synthesized products.

(c). Fabrication of TiC intermetallic composite coating

In the third part of the research, the work was expanded to study the fabrication of TiC intermetallic matrix composite prepared using multilayer configurations of Ti/C, Ni/Al and Ti. The objective of this work was to assess microstructure and mechanical properties of the synthesized product formed by SHS process which was ignited by induction heating, and investigate the formation mechanism of the synthesized products. The result of this investigation showed that the synthesized product was composed of inhomogeneous phase of $TiC/Ti_3Al/Ti_2Ni$ mixed with secondary products TiO_2. The formation mechanism of the synthesized products was initiated by the melting of Al which followed by the ignition of Ni/Al reaction after receiving the heat from induction heating. The high heat released by Ni/Al reaction then caused the melting of Ti and triggered further reactions between the liquid Ni/Al and molten Ti to form Ti_2Ni, TiNi and Ti_3Al as well as C to form TiC. The main products in this system are $TiC/Ti_3Al/Ti_2Ni$ composite, while a small amount of TiO_2 and Ti_6O oxides were observed due to the presence of oxygen during the SHS process. The evaluation on the mechanical properties of this system showed that the hardness of $TiC/Ti_3Al/Ti_2Ni$ was 1135.48 ± 139.58 HV, which is higher than that of Ti_3Al/Ti_2Ni and $NiAl/TiC/Al_2O_3$ composite. The current findings therefore add substantially to our understanding in the production of hard TiC intermetallic composite coating formed by induction heating.

8.2. Further work

The evidence from the present study suggested that the application of Ti as underlayer combined with induction heating can be used to enhance the adhesion between the NiAl coating and the steel substrate. The application of Ti also resulted in the formation of new materials containing Ti_3Al in the underlayer. Considering the finding that the new material in the underlayer has a high hardness, the present result will serve as a base for future studies in the production of Ti_3Al through the combustion synthesis of NiAl and Ti. As can be found in many literatures, Ti_3Al is one of the intermetallics which offer significant advantages for high temperature applications such as high speed spacecrafts and automotive industries.

In the successful application of induction heating to initiate the Ni/Al reaction and simultaneously preheat the substrate in the coating fabrication, it was shown that metallurgical bonding was formed at the interface between the underlayer and the substrate. The result showed that the melting of the substrate surface is an important factor to produce metallurgical bonding by allowing the diffusion of Fe from the substrate to the underlayer. Due to the limited equipment, the quantity of the adhesion strength was not observed. Thus, further work is required to investigate this issue. In addition, the new technique developed in this work can also be expanded to explore the application of induction heating on other joining processes such as welding and brazing.

In the temperature profile of Ti during the combustion synthesis of Ni/Al, it was shown that the temperature of titanium achieved a maximum point at the melting point of Ti and followed by a plateau. This plateau indicates that there was a phase transformation after the melting of Ti. In the microstructure analysis, it was shown that there is a formation of Ti_3Al/Ti_2Ni composite in the underlayer, which was originally occupied by Ti. However, due to the limited data of the thermochemical properties of the materials, particularly the formation heat of Ti_3Al and Ti_2Ni, the calculation of adiabatic temperature for Ti_3Al and Ti_2Ni reactions could not be carried out. Further work needs to be done to establish whether the plateau represents the formation of Ti_3Al and Ti_2Ni. It was also revealed that the temperature of the plateau was decreased with an increase in the current of induction heating. Therefore, it would be interesting to assess the effect of induction heating current on the formation of the plateau.

In the NiAl coating with thick underlayer, it was proven that Ti alloy was formed in the underlayer due to the heat released by Ni/Al reaction which was insufficient to promote further reactions between the liquid Ni/Al and Ti. The evidence from the present study showed that the formation of Ti alloy has produced a higher thermal shock resistance compared with that in the sample with thin underlayer. On the contrary, the hardness of the underlayer with thin underlayer was higher than that of the underlayer with thick underlayer. In future investigations it might be possible to tailor the microstructure of the underlayer

whilst maintaining a high performance material with a high thermal shock resistance and high hardness. In addition, with the evidence of the high performance Ti alloy observed in the present work, future studies on the similar topic such as the fabrication of Al alloy are recommended.

In the phase identification of TiC, the data obtained by SEM was not transferable directly to confirm the existence of TiC due to the absence of C composition. The formation of Ti_3Al and Ti_2Ni could also not be determined in the fabrication of TiC coating described in Chapter 7. Further clarification using accurate techniques on this study is therefore suggested.

References

[1] C. Pascal, C. Merlet, and J. C. Tedenac, "Combustion synthesis: a new route for repair of gas turbine components - achievements and perspectives for development of SHS rebuilding," *Journal of Materials Processing technology*, vol. 135, pp. 2–11, 2003.

[2] K. Morsi, "Review: reaction synthesis processing of Ni–Al intermetallic materials," *Materials Science and Engineering: A*, vol. 299, no. 1–2, pp. 1–15, Feb. 2001.

[3] S. Vaucher, M. Stir, K. Ishizaki, J. M. Catala-Civera, and R. Nicula, "Reactive synthesis of Ti–Al intermetallics during microwave heating in an E-field maximum," *Thermochimica Acta*, vol. 522, no. 1–2, pp. 151–154, Aug. 2011.

[4] A. A. Hambardzumyan, S. S. Grigoryan, H. L. Khachatryan, and S. L. Kharatyan, "Combined effect of thermal and mechanical activation on the combustion and phase formation laws in the Cr–Si–C system," *Chemical Engineering Journal*, vol. 162, no. 3, pp. 1075–1081, 2010.

[5] C. L. Yeh, S. H. Su, and H. Y. Chang, "Effects of TiC addition on combustion synthesis of NiAl in SHS mode," *Journal of Alloys and Compounds*, vol. 398, no. 1–2, pp. 85–93, Aug. 2005.

[6] R. M. & P. J. D. C. M. Ward-Close, "Intermetallic-matrix composites - a review," *Intermetallics*, vol. 9795, no. 95, pp. 217–229, 1996.

[7] P. La, Q. Xue, and W. Liu, "A study of $MoSi_2$ - MoS_2 coatings fabricated by SHS casting route," *Materials Science and Engineering*, vol. 277, pp. 266–273, 2000.

[8] X. Cui, F. Wang, S. Wang, Z. Yang, M. Gao, and M. Wei, "In Situ Synthesis of Heat Resistant Gradient Composite on Steel Surface," *Journal of Iron and Steel Research, International*, vol. 16, no. 2, pp. 89–94, Mar. 2009.

[9] M. Masanta, S. M. Shariff, and A. R. Choudhury, "Tribological behavior of TiB_2–TiC–Al_2O_3 composite coating synthesized by combined SHS and laser technology," *Surface and Coatings Technology*, vol. 204, no. 16–17, pp. 2527–2538, May 2010.

[10] M. Masanta, P. Ganesh, R. Kaul, A. K. Nath, and A. Roy Choudhury, "Development of a hard nano-structured multi-component ceramic coating by laser cladding," *Materials Science and Engineering: A*, vol. 508, no. 1–2, pp. 134–140, May 2009.

[11] G. P. Cammarota, A. Casagrande, G. Poli, and P. Veronesi, "Ni–Al–Ti coatings obtained by microwave assisted SHS: Effect of annealing on microstructural and mechanical properties," *Surface and Coatings Technology*, vol. 203, no. 10–11, pp. 1429–1437, Feb. 2009.

[12] I. Boromei, A. Casagrande, F. Tarterini, G. Poli, P. Veronesi, and R. Rosa, "Ni–Al–Ti coatings obtained by microwave assisted SHS: Oxidation behaviour in the 750–900°C range," *Surface and Coatings Technology*, vol. 204, no. 11, pp. 1793–1799, Feb. 2010.

[13] P. La, M. Bai, Q. Xue, and W. Liu, "A study of NiAl coating on carbon steel surface via the SHS casting route," *Surface and Coatings Technology*, vol. 113, pp. 44–51, 1999.

[14] J. J. Moore and H. J. Feng, "Combustion synthesis of advanced materials: Part II. Classification, Applications and modelling," *Progress in Materials Science*, vol. 39, pp. 275–316, 1995.

[15] L. Y. Sheng, F. Yang, J. T. Guo, T. F. Xi, and H. Q. Ye, "Investigation on NiAl–TiC–Al_2O_3 composite prepared by self-propagation high temperature synthesis with hot extrusion," *Composites Part B: Engineering*, vol. 45, no. 1, pp. 785–791, Feb. 2013.

[16] A. K. Jadoon, B. Ralph, and P. R. Hornsby, "Metal to ceramic joining via a metallic underlayer bonding technique," *Journal of Materials Processing Technology*, vol. 152, no. 3, pp. 257–265, Oct. 2004.

[17] X. Zhu, T. Zhang, D. Marchant, and V. Morris, "The structure and properties of NiAl formed by SHS using induction heating," *Materials Science and Engineering: A*, vol. 528, no. 3, pp. 1251–1260, Jan. 2011.

[18] X. Zhu, T. Zhang, D. Marchant, and V. Morris, "Combustion synthesis of TiC–NiAl composite by induction heating," *Journal of the European Ceramic Society*, vol. 30, no. 13, pp. 2781–2790, Oct. 2010.

[19] X. Zhu, T. Zhang, V. Morris, and D. Marchant, "Combustion synthesis of NiAl/Al_2O_3 composites by induction heating," *Intermetallics*, vol. 18, no. 6, pp. 1197–1204, Jun. 2010.

[20] G. Sauthoff, *Basics of Thermodynamics and Phase Transitions in Complex Intermetallics*, Vol. 1. London: World Sceintific, 2008, p. 147.

[21] N. S. Stolo, C. T. Liu, and S. C. Deevi, "Emerging applications of intermetallics," *Intermetallics*, vol. 8, pp. 1313–1320, 2000.

[22] N. Cinca and J. M. Guilemany, "Thermal spraying of transition metal aluminides: An overview," *Intermetallics*, vol. 24, pp. 60–72, May 2012.

[23] D. Johnson, "Intermetallic-based composites," *Current Opinion in Solid State and Materials Science*, vol. 4, no. 3, pp. 249–253, Jun. 1999.

[24] P. Zhu, J. C. M. Li, and C. T. Liu, "Adiabatic temperature of combustion synthesis of Al–Ni systems," *Materials Science and Engineering: A*, vol. 357, no. 1–2, pp. 248–257, Sep. 2003.

[25] P. Lazar and R. Podloucky, "Ductility and magnetism: An ab-initio study of NiAl–Fe and NiAl–Mn alloys," *Intermetallics*, vol. 17, no. 9, pp. 675–679, Sep. 2009.

[26] S. K. Bhaumik, C. Divakar, L. Rangaraj, and A. K. Singh, "Reaction sintering of NiAl and TiB_2–NiAl composites under pressure," vol. 257, pp. 341–348, 1998.

[27] S. Djanarthany, J. Viala, and J. Bouix, "An overview of monolithic titanium aluminides based on Ti_3Al and TiAl," *Materials Chemistry and Physics*, vol. 72, pp. 301–319, 2001.

[28] R. Orru, G. Cao, and Z. A. Munir, "Mechanistic investigation of the field-activated combustion synthesis (FACS) of titanium aluminides," *Chemical Engineering Science*, vol. 54, pp. 3349–3355, 1999.

[29] H. Gao, Y. He, P. Shen, J. Zou, N. Xu, Y. Jiang, B. Huang, and C. T. Liu, "Porous FeAl intermetallics fabricated by elemental powder reactive synthesis," *Intermetallics*, vol. 17, no. 12, pp. 1041–1046, 2009.

[30] P. Z. Shen, Y. H. He, H. Y. Gao, J. Zou, N. P. Xu, Y. Jiang, B. Y. Huang, and C. T. Liu, "Development of a new graded-porosity FeAl alloy by elemental reactive synthesis," *Desalination*, vol. 249, no. 1, pp. 29–33, 2009.

[31] S. Azem, M. Nechiche, and K. Taibi, "Development of copper matrix composite reinforced with FeAl particles produced by combustion synthesis," *Powder Technology*, vol. 208, no. 2, pp. 515–520, 2011.

[32] H. Wang, C. Li, G. Yang, and C. Li, "Effect of heat treatment on the microstructure and property of cold-sprayed nanostructured FeAl/Al_2O_3 intermetallic composite coating," *Vacuum*, vol. 83, pp. 146–152, 2009.

[33] M. Salehi, F. Karimzadeh, and A. Tahvilian, "Formation of Ti–Ni intermetallic coatings on carbon tool steel by a duplex process," *Surface and Coatings Technology*, vol. 148, pp. 55–60, 2001.

[34] A. Bansiddhi, T. D. Sargeant, S. I. Stupp, and D. C. Dunand, "Porous NiTi for bone implants: A review," *Acta Biomaterialia*, vol. 4, pp. 773–782, 2008.

[35] G. Tosun, L. Ozler, M. Kaya, and N. Orhan, "A study on microstructure and porosity of NiTi alloy implants produced by SHS," *Journal of Alloys and Compounds*, vol. 487, no. 1–2, pp. 605–611, Nov. 2009.

[36] J. C. Schuster, "Critical data evaluation of the aluminium-nickel-titanium system," *Intermetallics*, vol. 14, pp. 1304–1311, 2006.

[37] H. Li, P. He, T. Lin, F. Pan, J. Feng, and Y. Huang, "Microstructure and shear strength of reactive brazing joints of TiAl/Ni-based alloy," *Transactions of Nonferrous Metals Society of China*, vol. 22, no. 2, pp. 324–329, Feb. 2012.

[38] B. Huang, L. D. Chen, and S. Q. Bai, "Bulk ultrafine binderless WC prepared by spark plasma sintering," *Scripta Materialia*, vol. 54, pp. 441–445, 2006.

[39] B. G. Kim, Y. Choi, J. W. Lee, Y. W. Lee, and G. M. Kim, "Characterization of a silicon carbide thin layer prepared by a self-propagating high temperature synthesis reaction," *Thin Solid Films*, pp. 82–86, 2000.

[40] D. Vallauri and I. C. At, "TiC–TiB_2 composites: A review of phase relationships, processing and properties," *Journal of the European Ceramic Society*, vol. 28, pp. 1697–1713, 2008.

[41] M. Razavi, M. Reza, and R. Mansoori, "Synthesis of TiC–Al_2O_3 nanocomposite powder from impure Ti chips, Al and carbon black by mechanical alloying," *Journal of Alloys and Compounds*, vol. 450, pp. 463–467, 2008.

[42] S. C. Tjong and Z. Y. Ma, "Microstructural and mechanical characteristics of in situ metal matrix composites," *Materials Science and Engineering*, vol. 29, no. July, pp. 49–113, 2000.

[43] C. L. Yeh and Y. L. Chen, "Combustion synthesis of TiC–TiB_2 composites," *Journal of Alloys and Compounds*, vol. 463, no. August 2007, pp. 373–377, 2008.

[44] M. A. C. Curfs, I.G. Cano, G.B.M. Vaughan, X. Turrillas, A. Kvick, Rodrigues, "TiC–NiAl composites obtained by SHS: a time-resolved XRD study," *Journal of the European Ceramic Society*, vol. 22, pp. 1039–1044, 2002.

[45] L. Z. Zhou, J. T. Guo, and G. J. Fan, "Synthesis of NiAl–TiC nanocomposite by mechanical alloying elemental powders," *Materials Science and Engineering: A*, vol. 249, no. 1–2, pp. 103–108, Jun. 1998.

[46] X. Q. You, T. Z. Si, N. Liu, P. P. Ren, Y. D. Xu, and J. P. Feng, "Effect of grain size on thermal shock resistance of Al_2O_3–TiC ceramics," *Ceramics International*, vol. 31, no. 1, pp. 33–38, Jan. 2005.

[47] Q. Dong, Q. Tang, and W. Li, "Al_2O_3–TiC–ZrO_2 nanocomposites fabricated by combustion synthesis followed by hot pressing," *Materials Science and Engineering: A*, vol. 475, no. 1–2, pp. 68–75, Feb. 2008.

[48] E. Mohammad Sharifi, F. Karimzadeh, and M. H. Enayati, "Mechanochemically synthesized Al_2O_3–TiC nanocomposite," *Journal of Alloys and Compounds*, vol. 491, no. 1–2, pp. 411–415, Feb. 2010.

[49] J. J. Moore and H. J. Feng, "Combustion synthesis of advanced materials: Part I. Reaction parameters," *Progress in Materials Science*, vol. 39, no. 4–5, pp. 243–273, Jan. 1995.

[50] L. Huang, H. Y. Wang, Q. Li, S. Q. Yin, and Q. C. Jiang, "Effect of Ni content on the products of Ni–Ti–B system via self-propagating high-temperature synthesis reaction," *Journal of Alloys and Compounds*, vol. 457, no. 1–2, pp. 286–291, Jun. 2008.

[51] B. A. I. Ling, G. E. Changchun, S. Weiping, M. A. O. Xiaodong, and Z. Ke, "Densification, microstructure, and fracture behavior of TiC/Si_3N_4 composites by spark plasma sintering," *Rare Metals*, vol. 27, no. 3, pp. 315–319, 2008.

[52] A. G. Merzhanov, "Combustion Processes That Synthesize Materials," *Journal of Materials Processing technology*, vol. 56, no. Elsevier, pp. 222–243, 1996.

[53] D. Atong and D. E. Clark, "Ignition behavior and characteristics of microwave-combustion synthesized Al_2O_3–TiC powders," *Ceramics International*, vol. 30, pp. 1909–1912, 2004.

[54] Y. X. Li, J. D. Hu, H. Y. Wang, Z. X. Guo, and A. N. Chumakov, "Thermodynamic and lattice parameter calculation of TiCx produced from Al-Ti-C powders by laser igniting self-propagating high-temperature synthesis," *Materials Science and Engineering: A*, vol. 458, no. 1–2, pp. 235–239, Jun. 2007.

[55] C. Sierra and A Vazquez, "NiAl coatings on carbon steel by self-propagating high-temperature synthesis assisted with concentrated solar energy: mass influence on adherence and porosity," *Solar Energy Materials and Solar Cells*, vol. 86, no. 1, pp. 33–42, Feb. 2005.

[56] R. Licheri, R. Orru, G. Cao, and A. Crippa, "Self-propagating combustion synthesis and plasma spraying deposition of TiC–Fe powders," *Ceramics International*, vol. 29, pp. 519–526, 2003.

[57] Q. Hu, P. Luo, and Y. Yan, "Influence of an electric field on combustion synthesis process and microstructures of TiC–Al_2O_3–Al composites," *Journal of Alloys and Compounds*, vol. 439, no. 1–2, pp. 132–136, Jul. 2007.

[58] Z. Du, H. Fu, H. Fu, and Q. Xiao, "A study of ceramic-lined compound copper pipe produced by SHS–centrifugal casting," *Materials Letters*, vol. 59, no. 14–15, pp. 1853–1858, Jun. 2005.

[59] B. Du, Z. Zou, X. Wang, and S. Qu, "Laser cladding of in situ TiB_2/Fe composite coating on steel," *Applied Surface Science*, vol. 254, no. 20, pp. 6489–6494, Aug. 2008.

[60] Y. Li, Y. Liu, H. Geng, and D. Nie, "Synthesis and cladding of Ni_3Al intermetallic on steel substrate by laser controlled reactive synthesis," *Journal of Materials Processing Technology*, vol. 171, no. 3, pp. 405–410, Feb. 2006.

[61] S. Chatterjee, P. Ganesh, R. Palai, J. A. Wu, R. Kaul, J. Dutta Majumdar, and A. Roy Choudhury, "Effect of h-BN addition on the properties of nanostructured Al_2O_3–TiB_2–TiN based coatings developed by combined SHS and laser surface alloying," *Surface and Coatings Technology*, vol. 204, no. 11, pp. 1702–1709, Feb. 2010.

[62] S. Chatterjee, J. D. Majumdar, K. Singaiah, S. M. Shariff, G. Padmanabham, and A. R. Choudhury, "Performance evaluation of laser surface alloyed hard nanostructured Al_2O_3–TiB_2–TiN composite coatings with in-situ and ex-situ reinforcements," *Surface and Coatings Technology*, vol. 205, no. 11, pp. 3478–3484, Feb. 2011.

[63] S. Chatterjee, S. M. Shariff, G. Padmanabham, J. D. Majumdar, and A. R. Choudhury, "Study on the effect of laser post-treatment on the properties of nanostructured Al_2O_3–TiB_2–TiN based coatings developed by combined SHS and laser surface alloying," *Surface and Coatings Technology*, vol. 205, no. 1, pp. 131–138, Sep. 2010.

[64] C. Sánchez Bautista, A. Ferriere, G. P. Rodríguez, M. López-Almodovar, A. Barba, C. Sierra, and A. J. Vázquez, "NiAl intermetallic coatings elaborated by a solar assisted SHS process," *Intermetallics*, vol. 14, no. 10–11, pp. 1270–1275, Oct. 2006.

[65] C. S. Bautista, G. P. Rodríguez, and A. Ferriere, "Numerical modelling of the solar cladding process," *Surface and Coatings Technology*, vol. 202, no. 9, pp. 1594–1605, Feb. 2008.

[66] A. Ferriere, C. Sanchez Bautista, G. P. Rodriguez, and A. J. Vazquez, "Corrosion resistance of stainless steel coatings elaborated by solar cladding process," *Solar Energy*, vol. 80, no. 10, pp. 1338–1343, Oct. 2006.

[67] C. Leonelli and T. J. Mason, "Microwave and ultrasonic processing: Now a realistic option for industry," *Chemical Engineering and Processing: Process Intensification*, vol. 49, no. 9, pp. 885–900, Sep. 2010.

[68] G. Poli, R. Sola, and P. Veronesi, "Microwave-assisted combustion synthesis of NiAl intermetallics in a single mode applicator: Modeling and optimisation," *Materials Science and Engineering: A*, vol. 441, no. 1–2, pp. 149–156, Dec. 2006.

[69] R. T. Mousavian, S. Sharafi, and M. H. Shariat, "Microwave-assisted combustion synthesis in a mechanically activated Al–TiO_2–H_3BO_3 system," *International Journal of Refractory Metals and Hard Materials*, vol. 29, no. 2, pp. 281–288, Mar. 2011.

[70] E. T. Thostenson and T. W. Chou, "Microwave processing: fundamentals and applications," *Composites Part A: Applied Science and Manufacturing*, vol. 30, no. 9, pp. 1055–1071, Sep. 1999.

[71] K. G. Krzyztof Naplocha, "Combustion synthesis of Al–Cr preforms activated in microwave field.pdf," *Journal of Alloys and Compounds*, vol. 480, pp. 369–375, 2009.

[72] J. R. Jokisaari, S. Bhaduri, and S. B. Bhaduri, "Microwave activated combustion synthesis of titanium aluminides," *Materials Science and Engineering: A*, vol. 394, no. 1–2, pp. 385–392, Mar. 2005.

[73] R. Kolleck, R. Veit, M. Merklein, J. Lechler, and M. Geiger, "Investigation on induction heating for hot stamping of boron alloyed steels," *CIRP Annals - Manufacturing Technology*, vol. 58, no. 1, pp. 275–278, Jan. 2009.

[74] H. Y. Lee, J. K. Roe, and A. Ikenaga, "Sliding wear properties for Ni–Al based intermetallic compound layer coated on ductile cast iron by combustion synthesis," *Wear*, vol. 260, no. 1–2, pp. 83–89, Jan. 2006.

[75] H. Y. Lee, A. Ikenaga, S. H. Kim, and K. B. Kim, "The effects of induction heating rate on properties of Ni–Al based intermetallic compound layer coated on ductile cast iron by combustion synthesis," *Intermetallics*, vol. 15, no. 8, pp. 1050–1056, Aug. 2007.

[76] H. Y. Liu, J. H. Huang, C. F. Yin, J. G. Zhang, and G. B. Lin, "Microstructure and properties of TiC–Fe cermet coatings by reactive flame spraying using asphalt as carbonaceous precursor," *Ceramics International*, vol. 33, no. 5, pp. 827–835, Jul. 2007.

[77] S. Tondu, T. Schnick, L. Pawlowski, B. Wielage, S. Steinha, and L. Sabatier, "Laser glazing of FeCr–TiC composite coatings" *Surface and Coatings Technology*, vol. 123, pp. 247–251, 2000.

[78] M. Jones, A. Horlock, P. Shipway, D. McCartney, and J. Wood, "A comparison of the abrasive wear behaviour of HVOF sprayed titanium carbide and titanium boride based cermet coatings," *Wear*, vol. 251, no. 1–12, pp. 1009–1016, Oct. 2001.

[79] B. Lotfi, P. H. Shipway, D. G. McCartney, and H. Edris, "Abrasive wear behaviour of Ni(Cr)–TiB_2 coatings deposited by HVOF spraying of SHS-derived cermet powders," *Wear*, vol. 254, no. 3–4, pp. 340–349, Feb. 2003.

[80] M. Jones, A. Horlock, P. Shipway, D. McCartney, and J.Wood, "Microstructure and abrasive wear behaviour of FeCr–TiC coatings deposited by HVOF spraying of SHS powders," *Wear*, vol. 249, no. 3–4, pp. 246–253, May 2001.

[81] Y. Zhou, C. J. Li, G. J. Yang, H. D. Wang, and G. Li, "Effect of self-propagating high-temperature combustion synthesis on the deposition of NiTi coating by cold spraying using mechanical alloying Ni/Ti powder," *Intermetallics*, vol. 18, no. 11, pp. 2154–2158, Nov. 2010.

[82] H. Wang, J. Huang, J. Zhu, H. Zhang, and X. Zhao, "Microstructure of cermet coating prepared by plasma spraying of Fe–Ti–C powder using sucrose as carbonaceous precursor," *Journal of Alloys and Compounds*, vol. 472, no. 1–2, pp. L1–L5, Mar. 2009.

[83] P. Kelly and R. Arnell, "Magnetron sputtering: a review of recent developments and applications," *Vacuum*, vol. 56, no. 3, pp. 159–172, Mar. 2000.

[84] D. Zhong, E. Sutter, J. Moore, G. G. Mustoe, E. Levashov, and J. Disam, "Mechanical properties of Ti–B–C–N coatings deposited by magnetron sputtering," *Thin Solid Films*, vol. 398–399, pp. 320–325, Nov. 2001.

[85] D. Zhong, J. Moore, B. Mishra, T. Ohno, E. Levashov, and J. Disam, "Composition and oxidation resistance of Ti–B–C and Ti–B–C–N coatings deposited by magnetron sputtering," *Surface and Coatings Technology*, vol. 163–164, pp. 50–56, Jan. 2003.

[86] O. Ozdemir, S. Zeytin, and C. Bindal, "A study on NiAl produced by pressure-assisted combustion synthesis," *Vacuum*, vol. 84, no. 4, pp. 430–437, Dec. 2009.

[87] H. Y. Wang, Q. C. Jiang, B. X. Ma, Y. Wang, and F. Zhao, "Reactive infiltration synthesis of TiB_2–TiC particulates reinforced steel matrix composites," *Journal of Alloys and Compounds*, vol. 391, no. 1–2, pp. 55–59, Apr. 2005.

[88] H. Y. Wang, Q. C. Jiang, Y. G. Zhao, and F. Zhao, "In situ synthesis of TiB_2/Mg composite by self-propagating high-temperature synthesis reaction of the Al–Ti–B system in molten magnesium," *Journal of Alloys and Compounds*, vol. 379, no. 1–2, pp. L4–L7, Oct. 2004.

[89] A. Azadmehr and E. Taheri-Nassaj, "An in situ (W,Ti)C–Ni composite fabricated by SHS method," *Journal of Non-Crystalline Solids*, vol. 354, no. 27, pp. 3225–3234, Jun. 2008.

[90] H. Weiss, "Adhesion of advanced overlay coatings : mechanisms and quantitative assessment," *Surface and Coatings Technology*, vol. 71, pp. 201–207, 1995.

[91] M. Schwartz, *Brazing for the engineering technologist*, Manufactur. London: Chapman & Hall, 1995.

[92] Y. S. Hong, S. H. Kwon, T. Wang, D. Kim, J. Choi, and K. H. Kim, "Effects of Cr underlayer on mechanical and tribological properties of Cr-Al-Si-N nanocomposite coating," *Transaction of Nonferroes Metals Society of China*, 2010.

[93] H. Ollendorf and D. Schneider, "A comparative study of adhesion test methods for hard coatings," *Surface and Coatings Technology*, vol. 113, no. 1–2, pp. 86–102, Mar. 1999.

[94] C. Wei and J. Y. Yen, "Effect of film thickness and underlayer on the adhesion strength of diamond like carbon films on different substrates," *Diamond and Related Materials*, vol. 16, no. 4–7, pp. 1325–1330, Apr. 2007.

[95] D. F. Diao, Y. Sawaki, and H. Suzuki, "Effect of underlayer on maximum contact stresses of hard coating under sliding contact," *Surface and Coatings Technology*, vol. 86–87, pp. 480–485, Dec. 1996.

[96] X. C. Zhang, B. S. Xu, H. D. Wang, Y. Jiang, and Y. X. Wu, "Application of functionally graded underlayer on reducing the residual stress discontinuities at interfaces within a plasma-sprayed thermal barrier coating," *Surface and Coatings Technology*, vol. 201, no. 9–11, pp. 5716–5719, Feb. 2007.

[97] M. X. Wei, S. Q. Wang, F. Wang, and X. H. Cui, "A thermal explosion process to fabricate an intermetallic matrix composite coating on a steel," *Materials & Design*, vol. 30, no. 8, pp. 3041–3047, Sep. 2009.

[98] Q. S. Meng, S. P. Chen, J. F. Zhao, H. Zhang, H. X. Zhang, and Z. A. Munir, "Microstructure and mechanical properties of multilayer-lined composite pipes prepared by SHS centrifugal-thermite process," *Materials Science and Engineering: A*, vol. 456, no. 1–2, pp. 332–336, May 2007.

[99] P. Mossino, "Some aspects in self-propagating high-temperature synthesis," *Ceramics International*, vol. 30, no. 3, pp. 311–332, Jan. 2004.

[100] S. Gennari, U. Anselmi-Tamburini, F. Maglia, and G. Spinolo, "Modeling the ignition of self-propagating combustion synthesis of transition metal aluminides," *Intermetallics*, vol. 18, no. 12, pp. 2385–2393, Dec. 2010.

[101] Y. F. Yang, H. Y. Wang, R. Y. Zhao, Y. H. Liang, L. Zhan, and Q. C. Jiang, "Effects of C particle size on the ignition and combustion characteristics of the SHS reaction in the 20wt.% Ni–Ti–C system," *Journal of Alloys and Compounds*, vol. 460, no. 1–2, pp. 276–282, Jul. 2008.

[102] M. Adeli, S. H. Seyedein, M. R. Aboutalebi, M. Kobashi, and N. Kanetake, "A study on the combustion synthesis of titanium aluminide in the self-

propagating mode," *Journal of Alloys and Compounds*, vol. 497, no. 1–2, pp. 100–104, May 2010.

[103] B. Zou, P. Shen, and Q. Jiang, "Dependence of the SHS reaction behavior and product on B_4C particle size in Al–Ti–B_4C and Al–TiO_2–B_4C systems," *Materials Research Bulletin*, vol. 44, no. 3, pp. 499–504, Mar. 2009.

[104] S. Miura, Y. Terada, T. Suzuki, C. T. Liu, and Y. Mishima, "Thermal conductivity of Ni-Al powder compacts for reaction synthesis," *Intermetallics*, vol. 8, pp. 151–155, 2000.

[105] Z. Huque and G. M. S. Azad, "Thermal conductivity effects on steady state propagation speed during self-propagating high-temperature synthesis of Ti+C green compacts," *Materials Science and Engineering: B*, vol. 147, no. 1, pp. 19–26, Jan. 2008.

[106] H. Amel-Farzad, J. Vahdati-Khaki, A. Haerian, and A. Youssefi, "Combustion wave stability in diluted TiO_2/Al/C system in atmospheric air," *Solid State Sciences*, vol. 10, no. 12, pp. 1958–1969, Dec. 2008.

[107] C. Zanotti, P. Giuliani, A. Terrosu, S. Gennari, and F. Maglia, "Porous Ni–Ti ignition and combustion synthesis," *Intermetallics*, vol. 15, no. 3, pp. 404–412, Mar. 2007.

[108] Y. H. Liang, H. Y. Wang, Y. F. Yang, R. Y. Zhao, and Q. C. Jiang, "Effect of Cu content on the reaction behaviors of self-propagating high-temperature synthesis in Cu–Ti–B4C system," *Journal of Alloys and Compounds*, vol. 462, no. 1–2, pp. 113–118, Aug. 2008.

[109] H. Y. Wang, Q. C. Jiang, X. L. Li, and F. Zhao, "Effect of Al content on the self-propagating high-temperature synthesis reaction of Al–Ti–C system in molten magnesium," *Journal of Alloys and Compounds*, vol. 366, no. 1–2, pp. L9–L12, Mar. 2004.

[110] M. S. Song, B. Huang, M. X. Zhang, and J. G. Li, "Study of formation behavior of TiC ceramic obtained by self-propagating high-temperature synthesis from Al–Ti–C elemental powders," *International Journal of Refractory Metals and Hard Materials*, vol. 27, no. 3, pp. 584–589, May 2009.

[111] W. N. Zhang, H. Y. Wang, P. J. Wang, J. Zhang, L. He, and Q. C. Jiang, "Effect of Cr content on the SHS reaction of Cr–Ti–C system," *Journal of Alloys and Compounds*, vol. 465, no. 1–2, pp. 127–131, Oct. 2008.

[112] Y. Wang, Z. Q. Zhang, H. Y. Wang, B. X. Ma, and Q. C. Jiang, "Effect of Fe content in Fe–Ti–B system on fabricating TiB_2 particulate locally reinforced steel matrix composites," *Materials Science and Engineering: A*, vol. 422, no. 1–2, pp. 339–345, Apr. 2006.

[113] Y. F. Yang, H. Y. Wang, R. Y. Zhao, Y. H. Liang, and Q. C. Jiang, "Effect of Ni content on the reaction behaviors of self-propagating high-temperature synthesis in the Ni–Ti–B_4C system," *International Journal of Refractory Metals and Hard Materials*, vol. 26, no. 2, pp. 77–83, Mar. 2008.

[114] J. Y. G. M. Castillo, J.J. Moore, F.D. Schowengerdt, R.A. Ayers, X. Zhang, M. Umakosho, H.Y. Yi, "Effects oF Gravity on Combustion Synthesis of Functionally Graded Materials," *Adv. Space Res.*, vol. 32, no. 2, pp. 265–270, 2003.

[115] A. G. Merzhanov, V. N. Sanin, and V. I. Yukhvid, "On a peculiarity of structure formation in combustion of high-caloric metallothermic compounds under microgravity conditions," *Doklady Physics*, vol. 45, no. 3, pp. 93–96, Mar. 2000.

[116] C. Unuvar, D. M. Fredrick, U. Anselmi-Tamburini, B. D. Shaw, A. Manerbino, J. Y. Guigne, and Z. A. Munir, "Gravity effects on reactive settling of transition metals in liquid aluminum under SHS conditions," *Acta Materialia*, vol. 55, no. 9, pp. 2965–2975, May 2007.

[117] A. S. Rogachev, V. N. Sanin, A. E. Sytschev, V. I. Yukhvid, E. Medda, and G. Cao, "Influence of graavity on self-propagating high-tempperature thermite reactions: The case of Cu_20-Al and Cu_20-Cu-Al systems," vol. 29, no. 4, pp. 505–510, 2002.

[118] G. Merzhanov, A. S. Rogachev, and A. E. Sychev, "Self-Propagating High-Temperature Synthesis: First Space Experiments," *Doklady Physics*, vol. 362, no. 2, pp. 299–303, 1998.

[119] D. R. Ragone, *Thermodynamics of materials*, The MIT Se. Wiley, 1995.

[120] O. Kubaschewsky, *Materials Thermochemistry*, 6th ed. Pergamon Press, 1993, p. 6.

[121] J. H. Lee, S. K. Ko, and C. W. Won, "Combustion characteristics of TiO_2/Al/C system," *Materials Research Bulletin*, vol. 36, pp. 1157–1167, 2001.

[122] H. Y. Wang, S. J. Lü, M. Zha, S. T. Li, C. Liu, and Q. C. Jiang, "Influence of Cu addition on the self-propagating high-temperature synthesis of Ti_5Si_3 in Cu–Ti–Si system," *Materials Chemistry and Physics*, vol. 111, no. 2–3, pp. 463–468, Oct. 2008.

[123] S. Gennari, U. A. Tamburini, F. Maglia, G. Spinolo, and Z. A. Munir, "A new approach to the modeling of SHS reactions: Combustion synthesis of transition metal aluminides," *Acta Materialia*, vol. 54, no. 9, pp. 2343–2351, May 2006.

[124] V. Rosenband and A. Gany, "Activated self-propagating high-temperature synthesis of aluminum and titanium nitrides," *Experimental Thermal and Fluid Science*, vol. 31, no. 5, pp. 461–467, Apr. 2007.

[125] D. Shtansky, E. Levashov, N. Glushankova, N. D'yakonova, S. Kulinich, M. Petrzhik, F. Kiryukhantsev-Korneev, and F. Rossi, "Structure and properties of CaO and ZrO_2-doped TiCxNy coatings for biomedical applications," *Surface and Coatings Technology*, vol. 182, no. 1, pp. 101–111, Apr. 2004.

[126] D. V Shtansky, N. A Gloushankova, A N. Sheveiko, M. A Kharitonova, T. G. Moizhess, E. A Levashov, and F. Rossi, "Design, characterization and testing of Ti-based multicomponent coatings for load-bearing medical applications.," *Biomaterials*, vol. 26, no. 16, pp. 2909–24, Jun. 2005.

[127] G. Xanthopoulou and G. Vekinis, "An overview of some environmental applications of self-propagating high-temperature synthesis," *Advances in Environmental Research*, vol. 5, no. 2, pp. 117–128, May 2001.

[128] N. Pradeilles, M. C. Record, and R. M. Marin-Ayral, "A modified SHS method for Si_2N_2O elaboration," *Journal of the European Ceramic Society*, vol. 26, no. 13, pp. 2489–2495, Jan. 2006.

[129] J. Davies, *Induction Heating Handbook*. McGraw-Hill Press, 1979.

[130] J. Chan, H. Jin, and B. Min, "The influence of induction heating on the microstructure of A356 for semi-solid forging," *Journal of Materials Processing technology*, vol. 87, pp. 46–52, 1999.

[131] T. Noda, T. Shimizu, M. Okabe, and T. Iikubo, "Joining of TiAl and steels by induction brazing," *Materials Science and Engineering: A*, vol. 239–240, pp. 613–618, Dec. 1997.

[132] F. Tummler and R. Oberacker, *An introduction to powder metallurgy*. London: Institute of Materials, 1993.

[133] C. A. Leon-Patiño and R. A. L. Drew, "Role of metal underlayers in the infiltration of metal–ceramic composites," *Current Opinion in Solid State and Materials Science*, vol. 9, no. 4–5, pp. 211–218, Aug. 2005.

[134] J. J. M. A.O. Kunrath, T.R. Strhaecher, "Combustion synthesis of metal-matrix composites: Part I, teh Ti-TiC-Al_2O_3 system," *Scripta Materialia*, vol. 34, no. 2, pp. 175–181, 1996.

[135] T. Sakurai, O. Yamada, and Y. Miyamoto, "Combustion synthesis of fine AlN powder and its reaction control," *Materials Science and Engineering: A*, vol. 416, no. 1–2, pp. 40–44, Jan. 2006.

[136] P. Zhu, J. C. Li, and C. T. Liu, "Reaction mechanism of combustion synthesis of NiAl," *Materials Science and Engineering: A*, vol. 329–331, pp. 57–68, Jun. 2002.

[137] P. Coppa and A. Consorti, "Normal emissivity of samples surrounded by surfaces at diverse temperatures," *Measurement*, vol. 38, no. 2, pp. 124–131, Sep. 2005.

[138] S. Marinetti and P. Giorgio Cesaratto, "Emissivity estimation for accurate quantitative thermography," *NDT & E International*, vol. 51, pp. 127–134, Jun. 2012.

[139] Z. Xiaomeng, "Combustion synthesis of NiAl and NiAl based composites," PhD Thesis, Kingston University, London, 2010.

[140] R. S. Das and Y. K. Agrawal, "Raman spectroscopy: Recent advancements, techniques and applications," *Vibrational Spectroscopy*, vol. 57, no. 2, pp. 163–176, Nov. 2011.

[141] I. Dreiling, A. Haug, H. Holzschuh, and T. Chassé, "Raman spectroscopy as a tool to study cubic Ti–C–N CVD coatings," *Surface and Coatings Technology*, vol. 204, no. 6–7, pp. 1008–1012, Dec. 2009.

[142] R. J. Anton and G. Subhash, "Dynamic Vickers indentation of brittle materials," *Wear*, vol. 239, no. 1, pp. 27–35, Apr. 2000.

[143] J. Lesage, M. H. Staia, D. Chicot, C. Godoy, and P. E. V. De Miranda, "Effect of thermal treatments on adhesive properties of a NiCr thermal sprayed coating," *Thin Solid Films*, vol. 377–378, pp. 681–686, 2000.

[144] L. M. Peng, J. H. Wang, H. Li, and M. Gong, "Microstructure and mechanical behavior of NixAly–Al_2O_3 in situ composites by pre-oxidation followed by hot-pressed reactive sintering," *Materials Science and Engineering: A*, vol. 425, no. 1–2, pp. 339–345, Jun. 2006.

[145] H. Y. Kim, D. S. Chung, and S. H. Hong, "Reaction synthesis and microstructures of NiAl/Ni micro-laminated composites," *Materials Science and Engineering: A*, vol. 396, no. 1–2, pp. 376–384, Apr. 2005.

[146] R. A. Bini, M. L. Santos, E. A. Filho, R. F. C. Marques, and A. C. Guastaldi, "Apatite coatings onto titanium surfaces submitted to laser ablation with different energy densities," *Surface and Coatings Technology*, vol. 204, no. 4, pp. 399–403, Nov. 2009.

[147] G. Cacciamani, A. Dinsdale, M. Palumbo, and A. Pasturel, "The Fe–Ni system: Thermodynamic modelling assisted by atomistic calculations," *Intermetallics*, vol. 18, no. 6, pp. 1148–1162, Jun. 2010.

[148] S. A. A. Akbarimousavi and M. GohariKia, "Investigations on the mechanical properties and microstructure of dissimilar cp-titanium and AISI 316L austenitic stainless steel continuous friction welds," *Materials & Design*, vol. 32, no. 5, pp. 3066–3075, May 2011.

[149] Z. Zhong, T. Hinoki, T. Nozawa, Y. H. Park, and A. Kohyama, "Microstructure and mechanical properties of diffusion bonded joints between tungsten and $F_{82}H$ steel using a titanium underlayer," *Journal of Alloys and Compounds*, vol. 489, no. 2, pp. 545–551, Jan. 2010.

[150] L. C. Hsiung and H. H. Sheu, "A comparison of the phase evolution in Ni, Al, and Ti powder mixtures synthesized by SHS and MA processes," *Journal of Alloys and Compounds*, vol. 479, no. 1–2, pp. 314–325, Jun. 2009.

[151] A. M. Locci, R. Orrù, G. Cao, and Z. A. Munir, "Field-activated pressure-assisted synthesis of NiTi," *Intermetallics*, vol. 11, no. 6, pp. 555–571, Jun. 2003.

[152] L. I. Hai-xin, H. E. Peng, L. I. N. Tie-song, P. A. N. Feng, F. Ji-cai, and H. Yu-dong, "Microstructure and shear strength of reactive brazing joints of TiAl/Ni-based alloy," *Transaction of Nonferroes Metals Society of China*, vol. 22, pp. 324–329, 2012.

[153] N. Bertolino, M. Monagheddu, A. Tacca, P. Giuliani, C. Zanotti, and U. Anselmi Tamburini, "Ignition mechanism in combustion synthesis of Ti–Al and Ti–Ni systems," *Intermetallics*, vol. 11, no. 1, pp. 41–49, Jan. 2003.

[154] K. Naplocha and K. Granat, "Microwave activated combustion synthesis of porous Al–Ti structures for composite reinforcing," *Journal of Alloys and Compounds*, vol. 486, no. 1–2, pp. 178–184, Nov. 2009.

[155] S. P. Gupta, "Intermetallic compounds in diffusion couples of Ti with an Al–Si eutectic alloy," *Materials Characterization*, vol. 49, no. 4, pp. 321–330, Nov. 2002.

[156] M. Kobashi, N. Inoguchi, and N. Kanetake, "Effect of elemental powder blending ratio on combustion foaming behavior of porous Al–Ti intermetallics and Al3Ti/Al composites," *Intermetallics*, vol. 18, no. 5, pp. 1039–1045, May 2010.

[157] M. Nassik, K. Mahdouk, and J. C. Gachon, "Calorimetric study of the aluminium–titanium system," *Journal of Alloys and Compounds*, vol. 350, pp. 151–154, 2003.

[158] M. Ghosh, S. Chatterjee, and B. Mishra, "The effect of intermetallics on the strength properties of diffusion bonds formed between Ti–5.5Al–2.4V and 304 stainless steel," *Materials Science and Engineering: A*, vol. 363, no. 1–2, pp. 268–274, Dec. 2003.

[159] B. Y. Tay, C. W. Goh, Y. W. Gu, C. S. Lim, M. S. Yong, M. K. Ho, and M. H. Myint, "Porous NiTi fabricated by self-propagating high-temperature synthesis of elemental powders," *Journal of Materials Processing Technology*, vol. 202, no. 1–3, pp. 359–364, Jun. 2008.

[160] H. Gao, Y. He, J. Zou, N. Xu, and C. T. Liu, "Pore structure control for porous FeAl intermetallics," *Intermetallics*, vol. 32, pp. 423–428, Jan. 2013.

[161] Y. Sun, Y. Zhao, D. Zhang, C. Liu, H. Diao, and C. Ma, "Multilayered Ti-Al intermetallic sheets fabricated by cold rolling and annealing of titanium and aluminum foils," *Transactions of Nonferrous Metals Society of China*, vol. 21, no. 8, pp. 1722–1727, Aug. 2011.

[162] X. Chen, Z. Zhang, Z. Qiu, C. Shi, and X. Li, "Hydrothermal fabrication and characterization of polycrystalline linneite (Co(3)S(4)) nanotubes based on the Kirkendall effect.," *Journal of colloid and interface science*, vol. 308, no. 1, pp. 271–5, Apr. 2007.

[163] T. Irisawa and H. Matsumoto, "Thermal shock resistance and adhesion strength of plasma-sprayed alumina coating on cast iron," *Thin Solid Films*, vol. 509, no. 1–2, pp. 141–144, Jun. 2006.

[164] M. Moonesan, A. Honarbakhsh raouf, F. Madah, and A. Habibollah zadeh, "Effect of alloying elements on thermal shock resistance of gray cast iron," *Journal of Alloys and Compounds*, vol. 520, pp. 226–231, Apr. 2012.

[165] J. C. Han and B. L. Wang, "Thermal shock resistance of ceramics with temperature-dependent material properties at elevated temperature," *Acta Materialia*, vol. 59, no. 4, pp. 1373–1382, Feb. 2011.

[166] A. Chávez-Valdez, J. M. Almanza-Robles, G. Vargas-Gutiérrez, and A. Arizmendi-Morquecho, "Adhesion strength and thermal shock resistance of fly ash cenospheres deposited on SiC," *Materials Characterization*, vol. 61, no. 11, pp. 1299–1303, Nov. 2010.

[167] M. Okazaki, S. Yamagishi, Y. Yamazaki, K. Ogawa, H. Waki, and M. Arai, "Adhesion strength of ceramic top coat in thermal barrier coatings subjected to thermal cycles: Effects of thermal cycle testing method and environment," *International Journal of Fatigue*, pp. 1–7, Mar. 2012.

[168] M. Li, X. Sun, W. Hu, and H. Guan, "Thermal shock behavior of EB-PVD thermal barrier coatings," *Surface and Coatings Technology*, vol. 201, no. 16–17, pp. 7387–7391, May 2007.

[169] K. Kokini, J. DeJonge, S. Rangaraj, and B. Beardsley, "Thermal shock of functionally graded thermal barrier coatings with similar thermal resistance," *Surface and Coatings Technology*, vol. 154, no. 2–3, pp. 223–231, May 2002.

[170] L. Gu, X. Chen, X. Fan, Y. Liu, B. Zou, Y. Wang, and X. Cao, "Improvement of thermal shock resistance for thermal barrier coating on aluminum alloy with various electroless underlayers," *Surface and Coatings Technology*, vol. 206, no. 1, pp. 29–36, Oct. 2011.

[171] R. Ahmadi-Pidani, R. Shoja-Razavi, R. Mozafarinia, and H. Jamali, "Improving the thermal shock resistance of plasma sprayed CYSZ thermal barrier coatings by laser surface modification," *Optics and Lasers in Engineering*, vol. 50, no. 5, pp. 780–786, May 2012.

[172] S. Rangaraj and K. Kokini, "Estimating the fracture resistance of functionally graded thermal barrier coatings from thermal shock tests," *Surface and Coatings Technology*, vol. 173, no. 2–3, pp. 201–212, Aug. 2003.

[173] A. Ozel and S. Gent, "Influence of underlayer material and geometry on stress levels in MgO.ZrO2-GG coatings subjected to thermal shock," vol. 18, no. 2, pp. 73–76, 1997.

[174] S. Simões, F. Viana, M. Koçak, A. S. Ramos, M. T. Vieira, and M. F. Vieira, "Diffusion bonding of TiAl using reactive Ni/Al nanolayers and Ti and Ni foils," *Materials Chemistry and Physics*, vol. 128, no. 1–2, pp. 202–207, Jul. 2011.

[175] A. Gorbunoff, A. A. Levin, and D. C. Meyer, "Low-temperature thermal expansion of metastable intermetallic Fe–Cr phases," *Journal of Alloys and Compounds*, vol. 480, no. 1, pp. 152–156, Jul. 2009.

[176] V. Chawla, R. Jayaganthan, and R. Chandra, "Finite element analysis of thermal stress in magnetron sputtered Ti coating," *Journal of Materials Processing Technology*, vol. 200, no. 1–3, pp. 205–211, May 2008.

[177] H. Latreche, G. Bozzolo, P. J. Masset, T. Weber, and M. Schütze, "Measurements of the coefficient of thermal expansion (CTE) of NiAlMo alloys and comparison with modelling predictions," *Materials Science and Engineering: A*, vol. 527, no. 21–22, pp. 5837–5843, Aug. 2010.

[178] M. Mohammadi, S. Javadpour, A. Kobayashi, S. A. Jenabali Jahromi, and K. Shirvani, "Thermal shock properties and microstructure investigation of LVPS and HVOF-CoNiCrAlYSi coatings on the IN738LC superalloy," *Vacuum*, no. 1000, pp. 2–7, Feb. 2012.

[179] R. Bhattacharya, G. Jha, S. Kundu, R. Shankar, and N. Gope, "Influence of cooling rate on the structure and formation of oxide scale in low carbon steel wire rods during hot rolling," *Surface and Coatings Technology*, vol. 201, no. 3–4, pp. 526–532, Oct. 2006.

[180] S. Hou, Z. Liu, and D. Liu, "The study of NiAl–TiB_2 coatings prepared by electro-thermal explosion ultrahigh speed spraying technology," *Surface & Coatings Technology*, vol. 205, no. 19, pp. 4562–4568, 2011.

[181] G. Gottstein, K. Reichert, K. Wen, R. Cremer, W. Hu, and D. Neuschu, "Influence of BN fiber coatings on the interfacial structure of sapphire fiber reinforced NiAl composites," *Applied Surface Science*, vol. 179, pp. 150–155, 2001.

[182] A. Makino, D. Ichikawa, a. Matsumoto, T. Kanda, and T. Watanabe, "Spontaneous ignition temperature for the compacted mixture of Ni–Al system: Experiment, theory, and comparisons," *Proceedings of the Combustion Institute*, vol. 34, no. 2, pp. 2197–2204, Jan. 2013.

[183] W. Xi, H. Wang, J. Li, and C. Shi, "A NiAl and TiC-reinforced Fe-based nanocomposite prepared by the rapid-solidification thermite process," *Materials Science and Engineering: A*, vol. 541, pp. 166–171, Apr. 2012.

[184] M. Ali-Rachedi, W. Ramdane, D. Vrel, A. Benaldjia, P. Langlois, and M. Guerioune, "The role of sintering additives on synthesis of cermets by auto-combustion," *Powder Technology*, vol. 197, no. 3, pp. 303–308, Jan. 2010.

[185] J. Guo, Z. Wang, L. Sheng, L. Zhou, C. Yuan, Z. Chen, and L. Song, "Wear properties of NiAl based materials," *Progress in Natural Science: Materials International*, vol. 22, no. 5, pp. 414–425, Oct. 2012.

[186] A. Ozel, V. Ucar, A. U. Mimaroglu, and I. Calli, "Comparison of the thermal stresses developed in diamond and advanced ceramic coating systems under thermal loading," pp. 437–440, 2000.

[187] I. Burlacov, J. Jirkovský, M. Müller, and R. B. Heimann, "Induction plasma-sprayed photocatalytically active titania coatings and their characterisation by micro-Raman spectroscopy," *Surface and Coatings Technology*, vol. 201, no. 1–2, pp. 255–264, Sep. 2006.

[188] R. Tomaszek, L. Pawlowski, J. Zdanowski, J. Grimblot, and J. Laureyns, "Microstructural transformations of TiO_2, Al_2O_3+13TiO_2 and Al_2O_3+40TiO_2 at plasma spraying and laser engraving," *Surface and Coatings Technology*, vol. 185, no. 2–3, pp. 137–149, Jul. 2004.

[189] S. Boullosa-Eiras, E. Vanhaecke, T. Zhao, D. Chen, and A. Holmen, "Raman spectroscopy and X-ray diffraction study of the phase transformation of ZrO_2–Al_2O_3 and CeO_2–Al_2O_3 nanocomposites," *Catalysis Today*, vol. 166, no. 1, pp. 10–17, May 2011.

[190] B. H. Lohse, A. Calka, and D. Wexler, "Raman spectroscopy sheds new light on TiC formation during the controlled milling of titanium and carbon," *Journal of Alloys and Compounds*, vol. 434–435, pp. 405–409, May 2007.

[191] P. K. Ajikumar, M. Vijayakumar, M. Kamruddin, S. Kalavathi, N. Kumar, T. R. Ravindran, and A. K. Tyagi, "Effect of reactive gas composition on the microstructure, growth mechanism and friction coefficient of TiC overlayers,"

International Journal of Refractory Metals and Hard Materials, vol. 31, pp. 62–70, Mar. 2012.

[192] M. X. Gao, Y. Pan, F. J. Oliveira, J. L. Baptista, and J. M. Vieira, "High strength TiC matrix $Fe_{28}Al$ toughened composites prepared by spontaneous melt infiltration," *Journal of the European Ceramic Society*, vol. 26, no. 16, pp. 3853–3859, Jan. 2006.

[193] G. Yoruk and O. Ozdemir, "The evaluation of NiAl and TiAl-based intermetallic coatings produced on the AISI 1010 steel by an electric current-activated sintering method," *Intermetallics*, vol. 25, pp. 60–65, Jun. 2012.

[194] H. Zhu, Y. Jiang, Y. Yao, J. Song, J. Li, and Z. Xie, "Reaction pathways, activation energies and mechanical properties of hybrid composites synthesized in-situ from Al–TiO_2–C powder mixtures," *Materials Chemistry and Physics*, vol. 137, no. 2, pp. 532–542, Dec. 2012.

[195] H. Boutefnouchet, C. Curfs, A. Triki, A. Boutefnouchet, and D. Vrel, "Self-propagating high-temperature synthesis mechanisms within the Ti–C–Ni system: A time resolved X-ray diffraction study," *Powder Technology*, vol. 217, pp. 443–450, Feb. 2012.